UNIVERSIDAD POLITÉCNICA DE MADRID
Escuela Técnica Superior de Ingenieros de Caminos, Canales y Puertos

Effect of grain boundaries on the deformation and fracture of metallic polycrystals

DOCTORAL THESIS

Submitted for the degree of Doctor by:

María Eugenia Nieto Valeiras
Master in Materials Engineering

Madrid, 2023

UNIVERSIDAD POLITÉCNICA DE MADRID
Escuela Técnica Superior de Ingenieros de Caminos, Canales y Puertos

Doctoral Degree in Engineering of Structures, Foundations and Materials

Effect of grain boundaries on the deformation and fracture of metallic polycrystals

DOCTORAL THESIS

Submitted for the degree of Doctor by:

María Eugenia Nieto Valeiras
Master in Materials Engineering

Under the supervision of:
Dr. Javier LLorca

Madrid, 2023

Title: Effect of grain boundaries on the deformation and fracture of metallic polycrystals
Author: María Eugenia Nieto Valeiras
Doctoral Programme: Engineering of Structures, Foundations and Materials

Thesis Supervision:

Dr. Javier LLorca, University Professor, Universidad Politécnica de Madrid

External Reviewers:

Thesis Defense Committee:

Thesis Defense Date:

Para Milocho.

Acknowledgements

I would like to acknowledge the financial support from the European Research Council under the European Union's Horizon 2020 research and innovation programme (Advanced Grant VIRMETAL, grant agreement No. 669141) and to the Grant Program for Research and Teaching Stays in the USA of the Polytechnic University of Madrid, for conceding me the grant for my research stay at Purdue University.

A PhD thesis is a long, tortuous way, and there are a lot of people who have accompanied me along this journey. However, I would rather express my gratitude in my mother tongue.

En primer lugar, quiero darle las gracias a mi supervisor, Javier LLorca. Dicen que la relación entre un doctorando y su supervisor es una de las grandes claves del éxito en la investigación académica. En mi caso, me siento tremendamente afortunada de haber recorrido este camino junto a Javier. Gracias por toda la confianza depositada, el inmenso conocimiento compartido y la formación del más alto nivel que he podido recibir. Gracias por creer en mí, por acompañarme en momentos difíciles y por organizar las millones de ideas en esta cabecita alocada. Ha sido un privilegio poder compartir tanto ratos de ecuaciones en la pizarra y conversaciones científicas, como nuestra pequeña rivalidad en cierto deporte de raqueta.

En segundo lugar, quiero agradecer a Nik Chawla y a su grupo de investigación por haberme acogido con tanto cariño en Purdue desde el primer momento. Gracias a Nik por involucrarme en todas las actividades, tanto académicas como no académicas, y por dejarme aprender y enseñar. Mi formación profesional no sería la que es si no hubiese pasado cinco meses como parte del Chawla Research Group. Gracias a todos mis compañeros del grupo, Eshan, Hamid, Swapnil, Daniel, Rahul, Amey, John, Ted, Ankit y Min, por acompañarme en mi aventura americana. En especial quiero darle las gracias a Eshan, con el que siempre es un placer trabajar o simplemente perderse en la ciencia con un café.

Esta tesis y el poso que deja en mí no serían lo mismo si no se hubiese llevado a cabo en IMDEA Materiales. Después de casi cinco años bajo ese techo acristalado echo la vista atrás y hay tantas personas a las que tengo que dar las gracias que no podría nombrarlas a todas. Recordando mis primeros años de tesis tengo que darles las gracias a Sarra Haouala y a Alberto Orozco, a los que he sentido como mentores desde el principio y de los que he aprendido tantísimo. A Bárbara, probablemente mi mejor compañera de mesa, a la que admiro profundamente. A los técnicos de IMDEA, que siempre han estado disponibles para echarme una mano, y en especial a Amalia, por su tiempo y por su inmensa paciencia. A mis compañeros del grupo de investigación, Abbas, Biaobiao, y especialmente a mi amiga Maral, que me ha acompañado en tantísimos momentos felices y no tan felices, y quién siempre ha tenido un hueco para mí. Gracias a toda la gente que trabaja en IMDEA, desde investigadores, postdocs, predocs, y gente de la cuarta planta, hasta el personal de limpieza, recepción y mantenimiento. Es muy fácil trabajar en algo tan frustrante como la ciencia cuando estás rodeada de personas tan estupendas y cariñosas. Además, quiero darle las gracias a la gente de la segunda planta porque gracias a ellos me siento como en

casa. Gracias también a todos los que se toman (o en algún momento se han tomado) el café a las 11, comen a las 2, y comen en Getafe los viernes, porque la rutina nunca es rutina con vosotros.

Finalmente quiero dedicarles unas palabras a esas personas que han sido un apoyo imprescindible para mí durante estos años de tesis. Gracias a mis compañeros de IMDEA que se han convertido en amigos del alma, Andrés, Ángela, Carmen, David, Guille, Jorge, Lola, Nacho Escobar, y Nacho Rodríguez. Por hacer los días infinitamente más divertidos, reír conmigo en los momentos alegres y acompañarme en los momentos difíciles. No puedo no dar una mención especial a mi gran apoyo y casi hermano Nacho Escobar, por no dejar de animarme y de creer en mí y por estar siempre ahí incondicionalmente. Esta tesis también es un poquito tuya. A mis amigos de Ourense y de Madrid, que tengo la fortuna de tener desde hace muchísimos años y que espero disfrutar, como mínimo, de otros tantos más. A Picu, porque ha sido un pilar fundamental durante muchos años a pesar de escuchar a diario un montón de datos innecesarios sobre bordes de grano. Por ser mi mejor amigo y hacerme reír hasta llorar, y llorar conmigo hasta reír. Por último, quiero darle las gracias a mi familia, que siempre me han creído capaz de todo lo que me proponga. Soy una privilegiada por tenerles a mi lado y por formar parte de una piña tan unida. Gracias a mis tías y a mis hermanos, de los que me siento profundamente orgullosa. Gracias a mis padres, por invertir tantísimo en mí, en mi educación y en mi felicidad, y por enseñarme que si estamos juntos podemos con todo. Gracias papá por ser mi fan número uno y por enseñarme a no darme nunca por vencida. Espero que estés orgulloso, te llevo conmigo.

Abstract

Metallic materials stand for the standard materials for structural applications in engineering. However, the strength of pure metals is rather limited due to the development of plastic deformation by dislocation slip. Different strengthening mechanisms have been employed to create obstacles that hinder dislocation motion through the crystalline lattice. Grain boundaries stand among the strongest barriers to dislocation slip in polycrystals, playing a critical role in their mechanical properties. However, grain boundaries can trigger damage, induce size effects such as the Hall-Petch effect, or weaken the material due to irradiation and hydrogen embrittlement. Designing materials with grain boundaries resistant to such effects is essential for increasing the lifespan and safety of critical components and requires understanding the interaction of dislocations with grain boundaries. The experimental evidence has revealed dislocations can transfer slip to the neighbor grain through the grain boundary in some cases, while dislocation pile-ups are formed in other grain boundaries. Nevertheless, there is still no general agreement on the criteria to predict slip transfer in polycrystalline materials.

This thesis aims to analyze the mechanisms of dislocation/grain boundary interaction in metallic polycrystals from the experimental and simulation viewpoints. The occurrence of slip transfer and blocking has been analyzed in thin pure nickel (face-centered cubic) and pure titanium (hexagonal close-packed) polycrystals. State-of-the-art experimental techniques, such as electron backscatter diffraction-based slip trace analysis, diffraction contrast tomography, and high-resolution digital image correlation, have been used to characterize the microstructure and determine the conditions for slip transfer. In particular, diffraction contrast tomography was employed to determine the effect of the three-dimensional grain boundary geometry on slip transfer, and high-resolution digital image correlation was used to account for the effect of the local stress state around grain boundaries. A large database of slip transfer/blocking events acquired in nickel and titanium was used to validate/disprove the accuracy of the geometrical criteria for slip transfer across grain boundaries available in the literature.

In addition, an existing crystal plasticity model was extended to include the strengthening effect of grain boundaries and the possibility of slip transfer on the mechanical behavior of face-centered cubic and hexagonal close-packed polycrystals. A variety of geometrical slip transfer criteria were successfully implemented and were used to simulate the effect of grain size on the flow strength of face-centered cubic and hexagonal close-packed polycrystals by means of computational homogenization. The simulations were validated against experimental data of the tensile response of well-annealed cubic and hexagonal polycrystals found in the literature. Subsequently, the effect of slip transfer on intergranular fracture was studied through the insertion of cohesive surfaces at the grain boundaries of polycrystalline foils to determine the effect of grain boundary character and geometry on the strength and fracture of metallic polycrystals.

The main results of Chapter 2 of this thesis have been published in

E. Nieto-Valeiras, J. LLorca,
Criteria for slip transfer across grain and twin boundaries in pure Ni,
Materialia **21**, 101303 (2022),
arXiv:2201.04936 [cond-mat.mtrl-sci]

The main results of Chapter 3 of this thesis have been published in

E. Ganju, E. Nieto-Valeiras, N. Chawla, J. LLorca,
A novel diffraction contrast tomography (DCT) acquisition strategy for capturing the 3D crystallographic structure of pure titanium,
Tomography of Materials and Structures **1**, 100003 (2023)

The main results of Chapter 4 of this thesis have been published in

E. Nieto-Valeiras, E. Ganju, N. Chawla, J. LLorca,
Assessment of slip transfer criteria for prismatic-to-prismatic slip in pure Ti from 3D grain boundary data,
Acta Materialia **262**, 119424 (2024),
arXiv:2310.06118 [cond-mat.mtrl-sci]

Part of the results of Chapter 6 of this thesis have been published in

E. Nieto-Valeiras, S. Haouala, J. LLorca,
On the effect of slip transfer at grain boundaries on the strength of FCC polycrystals,
European Journal of Mechanics - A/Solids **91**, 104427 (2022),
arXiv:2109.10791 [cond-mat.mtrl-sci]

Resumen

Los materiales metálicos suelen ser los materiales estándar para aplicaciones estructurales en ingeniería. Sin embargo, la resistencia de los metales puros es bastante limitada debido al desarrollo de la deformación plástica por deslizamiento de dislocaciones. Se han empleado distintos mecanismos de endurecimiento para crear obstáculos que dificulten el movimiento de las dislocaciones a través de la red cristalina. Los bordes de grano se encuentran entre las barreras más fuertes al deslizamiento de dislocaciones en policristales, desempeñando un papel crítico en sus propiedades mecánicas. Sin embargo, los bordes de grano pueden provocar daños, inducir efectos de tamaño como el efecto Hall-Petch o debilitar el material debido a la irradiación y la fragilización por hidrógeno. Diseñar materiales con bordes de grano resistentes a estos efectos es esencial para alargar la vida útil y la seguridad de los componentes críticos y requiere comprender la interacción entre las dislocaciones y los bordes de grano. Las pruebas experimentales han revelado que, en algunos casos, las dislocaciones pueden transferir deslizamiento al grano vecino a través del borde de grano (*slip transfer*), mientras que en otros bordes de grano se forman apilamientos de dislocaciones (*slip blocking*). Sin embargo, aún no existe un acuerdo general sobre los criterios para predecir el *slip transfer* en materiales policristalinos.

Esta tesis tiene como objetivo analizar los mecanismos de interacción dislocación/borde de grano en policristales metálicos desde el punto de vista experimental y de simulación numérica. Se ha analizado la ocurrencia de *slip transfer/blocking* en policristales delgados de níquel puro (red cúbica centrada en las caras) y titanio puro (red hexagonal compacta). Se han utilizado técnicas experimentales de última generación, como el análisis de trazas de deslizamiento basado en la difracción de electrones retrodispersados, la tomografía de difracción de contraste y la correlación digital de imágenes de alta resolución, para caracterizar la microestructura y determinar las condiciones para el *slip transfer*. En particular, la tomografía de difracción de contraste se empleó para determinar el efecto de la geometría tridimensional de los bordes de grano en el *slip transfer*, y la correlación digital de imágenes de alta resolución se utilizó para tener en cuenta el efecto del estado de tensiones locales alrededor de los bordes de grano. Se utilizó una amplia base de datos de eventos de *slip transfer/blocking* adquiridos en níquel y titanio para validar/desaprobar la precisión de los criterios geométricos de *slip transfer* disponibles en la bibliografía.

Además, se amplió un modelo existente de plasticidad cristalina para incluir el efecto endurecedor de los bordes de grano y la posibilidad de *slip transfer* en el comportamiento mecánico de policristales cúbicos centrados en las cara y hexagonales compactos. Se implementaron con éxito diversos criterios geométricos de *slip transfer* y se utilizaron para simular el efecto del tamaño de grano en la resistencia mecánica de los policristales mediante homogeneización computacional. Las simulaciones se validaron frente a datos experimentales de la respuesta a la tracción de policristales cúbicos y hexagonales encontrados en la bibliografía. Posteriormente, se estudió el efecto del *slip transfer* en la fractura intergranular mediante la inserción de superficies cohesivas en los bordes de grano de láminas policristalinas para determinar el efecto del carácter y la geometría de los bordes de grano en la resistencia y la fractura de policristales metálicos.

Los principales resultados presentados en el capítulo 2 de esta tesis han sido publicados en

E. Nieto-Valeiras, J. LLorca,
Criteria for slip transfer across grain and twin boundaries in pure Ni,
Materialia **21**, 101303 (2022),
arXiv:2201.04936 [cond-mat.mtrl-sci]

Los principales resultados presentados en el capítulo 3 de esta tesis han sido publicados en

E. Ganju, E. Nieto-Valeiras, N. Chawla, J. LLorca,
A novel diffraction contrast tomography (DCT) acquisition strategy for capturing the 3D crystallographic structure of pure titanium,
Tomography of Materials and Structures **1**, 100003 (2023)

Los principales resultados presentados en el capítulo 4 de esta tesis han sido publicados en

E. Nieto-Valeiras, E. Ganju, N. Chawla, J. LLorca,
Assessment of slip transfer criteria for prismatic-to-prismatic slip in pure Ti from 3D grain boundary data,
Acta Materialia **262**, 119424 (2024),
arXiv:2310.06118 [cond-mat.mtrl-sci]

Parte de los resultados presentados en el capítulo 6 de esta tesis han sido publicados en

E. Nieto-Valeiras, S. Haouala, J. LLorca,
On the effect of slip transfer at grain boundaries on the strength of FCC polycrystals,
European Journal of Mechanics - A/Solids **91**, 104427 (2022),
arXiv:2109.10791 [cond-mat.mtrl-sci]

Contents

Acknowledgements . . . iii
Abstract . . . v
Resumen . . . vii
List of Figures . . . xxiii
List of Tables . . . xxvi
Glossary . . . xxvii

1 Introduction **1**
1.1 Plastic deformation by dislocation slip . . . 2
1.2 Grain boundaries . . . 4
1.2.1 Geometrical description of grain boundaries . . . 4
1.2.2 Interactions between dislocations and grain boundaries . . . 5
1.3 Slip transfer criteria: state of the art . . . 6
1.4 Mesoscale modeling of grain boundaries . . . 13
1.5 Objectives . . . 17

2 Slip transfer at grain boundaries in Ni **19**
2.1 Introduction . . . 19
2.2 Material and experimental techniques . . . 21
2.3 Results and discussion . . . 23
2.4 Conclusions and limitations . . . 27

3 3D grain mapping by means of Diffraction Contrast Tomography (DCT) **31**
3.1 Introduction . . . 31
3.2 Materials and methods . . . 32
3.2.1 Titanium sample . . . 32
3.2.2 Diffraction Contrast Tomography (DCT) . . . 33
3.3 Results and discussion . . . 36
3.3.1 3D grain reconstructions from LabDCT data . . . 37

3.3.2 Comparison of LabDCT and EBSD orientation maps . . . 40
3.3.3 Comparison of LabDCT grain geometry with SEM micrographs . . . 40
3.4 Summary and conclusions . . . 45

4 Analysis of slip transfer in pure Ti through 3D GB characterization 51
4.1 Introduction . . . 51
4.2 Materials and experimental techniques . . . 51
4.3 Results . . . 53
4.3.1 3D grain and grain boundary characterization . . . 53
4.3.2 2D microstructural characterization . . . 55
4.3.3 Slip trace and slip transfer analysis . . . 56
4.3.4 Evaluation of slip transfer criteria . . . 59
4.4 Discussion . . . 64
4.5 Conclusions . . . 68

5 Analysis of slip transfer in pure Ti through HRDIC 71
5.1 Introduction . . . 71
5.2 Materials and methods . . . 72
5.2.1 Microstructural characterization . . . 72
5.2.2 High-resolution digital image correlation . . . 73
5.2.3 Mechanical testing . . . 76
5.3 Results and discussion . . . 76
5.3.1 Slip transfer assessment from HRDIC data . . . 76
5.3.2 When slip transfer geometrical criteria work . . . 82
5.3.3 When slip transfer geometrical criteria fail: the influence of local stress 84
5.4 Conclusions . . . 90

6 Simulation of polycrystal deformation including slip transfer/blocking at grain boundaries 93
6.1 Introduction . . . 93
6.2 Physically-based crystal plasticity model . . . 94
6.2.1 FCC metallic crystals . . . 94
6.2.2 HCP metallic crystals . . . 97
6.3 Polycrystal homogenization framework . . . 101
6.3.1 RVE generation . . . 101
6.3.2 Boundary conditions . . . 102
6.3.3 GB distance calculation . . . 103
6.3.4 Slip transfer criteria calculation . . . 105
6.4 Results and discussion . . . 106
6.4.1 RVE selection . . . 106
6.4.2 Effect of slip transfer on the flow strength of FCC metals . . . 106
6.4.3 Effect of slip transfer on the Hall-Petch law of FCC metals . . . 113
6.4.4 Comparison with experiments (FCC) . . . 115
6.4.5 Effect of slip transfer on the flow strength of HCP metals . . . 118
6.4.6 Comparison with experiments (HCP) . . . 122

6.5 Conclusions 124

7 Simulation of the deformation of polycrystals including intergranular fracture 127
7.1 Introduction 127
7.2 Constitutive behavior 128
7.2.1 Crystal plasticity model 128
7.2.2 Slip transfer/blocking at GBs 128
7.2.3 Intergranular fracture modeling 130
7.3 Numerical model 132
7.3.1 Finite element model 132
7.3.2 Cohesive surfaces 133
7.3.3 Boundary conditions 134
7.4 GB damage analysis 136
7.5 Results and discussion 138
7.5.1 Intergranular fracture of Al foils in tension 138
7.5.2 Intergranular fracture of Mg foils in tension (random texture) 144
7.5.3 Intergranular fracture of Mg foils in tension (basal texture) 150
7.6 Conclusions 158

8 General discussion, conclusions and future work 161
8.1 General discussion and conclusions 161
8.2 Future work 167

Bibliography 169

List of Figures

1.1 Most densely packed slip planes and directions within the FCC unit lattice. 3
1.2 Schematic diagram of the main slip systems in HCP lattices. 4
1.3 Five degrees of freedom to describe a planar GB. 5
1.4 Basic mechanisms of dislocation-GB interaction between two active slip systems A and B in adjacent grains separated by a GB. (a) Opaque GB, (b) translucent GB, and (c) transparent GB. 6
1.5 Schematic representation of the geometrical alignment between incoming and outgoing slip systems across a GB. 7
1.6 Different RVE discretizations for the same microstructure with 100 equiaxed grains generated with the open-source software Neper [146]. (a) RVE discretized with hexahedral or voxel elements. (b) RVE discretized with tetrahedral elements. 14

2.1 Schematic representation of two annealing twins in a Ni grain, where twin 1 is composed of two parallel coherent TBs (CTB) and twin 2 is composed of two parallel coherent TBs (CTB) and one incoherent TB (ICB). 20
2.2 Dogbone tensile specimen of Ni. dimensions in mm. 21
2.3 Microstructure of the as-received Ni foil, after metallographic preparation and chemical etching with Kalling's 2 reagent. 22
2.4 Stress-strain curve of the Ni sample deformed along the rolling direction (Fig. 2.5(a)). 22
2.5 (a) EBSD map of the surface of the dogbone specimen parallel to the rolling direction. TBs (which are associated with a misorientation angle Θ of 60°) are drawn with white lines, while regular GBs are drawn with black lines. (b) Inverse pole figure with respect to the z axis, where each grain mean crystallographic orientation is represented by a black dot. 23

2.6 Examples of slip transfer and slip blocking at different GBs (a) Slip transfer across a regular GB. (b) Blocked slip at two regular GBs, supported by the slip trace discontinuity and the presence of a ledge. (c) Slip transfer across a coherent TB. (d) Slip transfer across the end of the twin boundary (incoherent TB). The slip bands in the parent grain and the twinned grain are parallel to each other and parallel to the twin boundary. (d) Blocked slip at a TB supported by the discontinuity between slip bands across the boundary and the formation of micro volumes (marked by white arrows). The orientation of the trace of the active slip system in each grain according to slip trace analysis is marked by solid lines, colored according to the active slip plane as indicated in Table 1.1. 25
2.7 (a) Effect of the misorientation angle Θ on slip transfer for GBs and TBs. (b) Occurrence/absence of slip transfer across GBs and TBs as a function of the Luster-Morris parameter m' and the misorientation angle. 26
2.8 Geometrical criteria for slip transfer in Ni. (a) Regular GB. (b) Coherent and incoherent TBs. (c) Coherent TB. 28

3.1 Pure Ti sample prepared using electro-discharge machining followed by annealing in vacuum at 850°. 33
3.2 LabDCT acquisition set-up using a conical beam source. 35
3.3 Acquisition of Lab DCT using stitched conventional DCT (C-DCT) scans and Helical Phyllotaxis DCT scans (HP-DCT) showing positions on the sample exposed to x-rays during a DCT scan. 36
3.4 Forward modeling reconstruction approach for generation of 3D grain maps implemented in Xnovo GrainMapper3D. 37
3.5 3D grain reconstructions of the central region in the Ti sample: conventional DCT scan acquisition and helical phyllotaxis scan acquisition. The grains are colored according to the inverse pole figure color key along the y-direction. 38
3.6 Comparison of average grain completeness obtained from conventional and helical phyllotaxis DCT scans: (a) fraction of average grain completeness, (b) cumulative distribution of average grain completeness, and (c) average grain completeness vs. grain size (equivalent sphere diameter). 39
3.7 Grain maps and (0001) pole figures from (a) EBSD, (b) conventional DCT, and (c) helical phyllotaxis DCT. 41
3.8 GB misorientation distribution for the grain maps from (a) EBSD, (b) conventional DCT, and (d) helical phyllotaxis DCT. 41
3.9 Comparison of GB misorientations: (a) distribution of GB misorientation angles obtained from EBSD and LabDCT grain reconstructions, and (b) distribution of absolute difference (Δ) in GB misorientation between EBSD and LabDCT grain maps. 42
3.10 Grain maps for the central section of the Ti sample: (a) SEM micrograph, (b) Conventional DCT scan data, and (c) Helical phyllotaxis DCT scan data. . . 42

3.11 Comparison of grain size and morphology obtained from SEM and DCT scan data: (a) grain size distribution from SEM and DCT, (b) distribution of normalized grain size from DCT, (c) aspect ratio distribution from SEM and DCT, and (d) distribution of normalized aspect ratio from DCT. 44

3.12 Overlap of aligned GB maps: (a) SEM vs. helical phyllotaxis DCT scan, and (b) SEM vs. conventional DCT scan. 45

3.13 Comparison of the centroidal distance between corresponding grains in SEM and DCT grain maps: (a) distribution of centroidal distance between corresponding grain in the SEM and DCT grain maps (b) centroidal distance vs. 2D grain size, and (c) normalized centroidal distance (centroidal distance normalized by 2D grain size) vs. grain size. 46

3.14 Comparison of GB detection accuracy: overlap between SEM and DCT grain data. 47

3.15 Comparison of GB detection accuracy: euclidian distance transform (EDT) heatmap of SEM grain. 47

3.16 Comparison of GB detection accuracy through the heatmap of the distance between SEM and conventional DCT GB for the corresponding grain (left), and heatmap of the distance between SEM and helical phyllotaxis DCT GBs for the corresponding grain (right). 48

3.17 Comparison of average grain boundary distance between corresponding grains from SEM and DCT maps: (a) distribution of average grain boundary distance between SEM and DCT data, (b) average grain boundary distance vs. 2D grain size, and (c) normalized average grain boundary distance (average grain boundary distance normalized by 2D grain size) vs. grain size. . 49

4.1 Ti dogbone micro tensile specimen dimensions in mm (left) and sample dimensions compared to a coin (right). 52

4.2 Microstructural characterization by DCT. (a) Reconstructed DCT map of the sample gauge colored according to the inverse pole figure with respect to the screen plane (color key in Fig. 4.4 (b)). The left half corresponds to the reconstructed volume of the sample, and the right half corresponds to the surface mesh generated at the GBs. (b) Sample scanning strategy consisting of 7 overlapping sub-regions to map the full gauge length. (c) Detailed view of two neighboring grains (dashed squared area in (a)), where the reconstructed voxelized volume is shown in (c), and the corresponding surface mesh is shown in (d). In the latter, some GB surface normals are drawn in yellow. 54

4.3 Microstructural features of the Ti sample obtained by DCT. (a) Grain size distribution, (b) Grain boundary misorientation distribution, (c) Grain boundary inclination (β) distribution. 55

4.4 Microstructure of the gauge section of the sample from EBSD. (a) Raw EBSD map colored according to the inverse pole figure perpendicular to the surface in (b). White dots correspond to regions that were not indexed by EBSD. The loading axis is horizontal, as indicated by the arrow. (c) Post-processed EBSD map of the rectangular region indicated in (a) at higher magnification. GB are colored according to their misorientation angle in degrees, and the orientation of the hexagonal unit cell is shown at the center of each grain. (d) Basal plane (0001) pole figure. Intensity is marked in multiple of random distributions. 56

4.5 Prismatic-to-prismatic slip transfer/blocking across GB. The theoretical orientation of the slip traces of the active slip systems is indicated by the dashed lines. (a) Slip transfer. (b) Double slip transfer. (c) Slip blocking and ledge at the GB. (d) Partial slip transfer. The arrows indicate slip bands fading towards the grain interior. 58

4.6 Distribution of slip transfer events in the microstructure: (a) Classification of prismatic-to-prismatic perfect slip transfer (purple), partial slip transfer (orange), and slip blocking (dark blue) across GB in Ti, and (b) Influence of GB misorientation angle distribution on the occurrence of perfect slip transfer, partial slip transfer and slip blocking. 59

4.7 Dependence of slip transfer on κ, ψ, and θ: (a) Influence of κ and ψ on the occurrence of slip transfer/blocking across the GB. (b) Influence of κ and θ on the occurrence of slip transfer/blocking across the GB. (c) Influence of ψ and θ on the occurrence of slip transfer/blocking across the GB. 61

4.8 (a) Influence of angle κ on slip transfer, partial slip transfer, and slip blocking. A black vertical dashed line is drawn in $\kappa = 45^{\circ}$ to represent a potential threshold that divides the data in predicted slip events ($slip = 1$) to the left of the line and predicted blocking events ($slip = 0$) to the right of the line. (b) Schematic representation of a confusion matrix to compare the actual and predicted values slip transfer/blocking for any categorical variable. . . 62

4.9 F1 score matrix for slip transfer/blocking. The diagonal terms represent the performance of a single angle in terms of the F1 score, whereas the out-of-diagonal terms represent the F1 score obtained by the combination of two angles. The F1 score value is indicated in each box and represented as a heat map variable, ranging from yellow (lowest) to blue (highest). The threshold that leads to the maximum F1 for each angle is depicted in Table 4.1. 64

4.10 F1 score matrix for slip transfer/blocking. The diagonal terms represent the performance of a single slip transfer criterion in terms of the F1 score, whereas the out-of-diagonal terms represent the F1 score obtained by the combination of two slip transfer criteria. The F1 score value is indicated in each box and represented as a heat map variable, ranging from yellow (lowest) to blue (highest). The threshold that leads to the maximum F1 for each slip transfer criterion is depicted in Table 4.2. 65

5.1 Microstructural characterization by DCT. (a) Reconstructed DCT map of the sample gauge, where the grains of the ROI have been colored according to the inverse pole figure with respect to the screen plane (color key in (b)). The region outside the ROI corresponds to the surface mesh generated at the GB, colored according to an integer number given to each GB (GB identifier). (c) Detailed view of two neighbor grains in the ROI, where the reconstructed voxelized volume is shown on the left and the corresponding surface mesh on the right. 74

5.2 (a) Backscattered electrons image of the Au pattern on the Ti sample. The black background corresponds to the Ti substrate and the white speckles to the Au nano-sized pattern. (b) Au particle size distribution. 75

5.3 EBSD maps of the ROI surface. (a) EBSD map before deformation; the three dashed areas indicate the sub-regions where HRDIC maps were acquired. (b) EBSD map of sub-region two after 4.5% plastic strain. (c) Ex-situ tensile stress-plastic strain curve. The markers indicate the conditions in which the EBSD and the HRDIC maps were acquired. (d) EBSD map of sub-region one after 4.5% plastic strain. In the EBSD maps in (a), (b), and (d), the grains are colored according to the inverse pole figure with respect to the screen plane, shown at the top of the figure. The GBs are colored according to their misorientation angle Θ, ranging from low misorientations (blueish colors) to high misorientations (yellowish colors). The grains of interest have been labeled in (a). The non-indexed pixels have been colored in white in (b) and (d). 77

5.4 Effective shear strain maps acquired by HRDIC in the sample within sub-region 1. The correlated maps correspond to three deformation steps at (a) 1%, (b) 2.5%, and 4.5% plastic deformation. The white pixels in the maps correspond to non-correlated points caused by surface scratches and dirt deposited onto the gold nano-speckle pattern. The white arrows in (b) highlight strain concentrations close to GB and triple junctions. The red dashed lines in (c) delimit a macro-strain band. (d) GB map obtained from EBSD before deformation. The main grains and GB of study have been labeled, and the theoretical prismatic slip traces have been drawn at the center of the grains. 78

5.5 Effective shear strain maps, γ_{eff}, obtained by HRDIC in the ROI within sub-region 2. The correlated maps correspond to three deformation steps at (a) 1%, (b) 2.5%, and 4.5% applied plastic deformation. The white pixels in the maps correspond to non-correlated points caused by surface scratches and dirt deposited onto the gold nano-speckle pattern. The white arrows in (b) and (c) highlight different strain concentrations close to GBs and triple junctions. The red dashed lines in (b) delimit a macro-strain band. (d) GB map obtained from the EBSD map before deformation. The main grains and GB of study have been labeled, and the theoretical prismatic slip traces have been drawn at the center of the grains. 79

5.6 Effective shear strain maps acquired by HRDIC in the sample within sub-region 3. The correlated maps correspond to three deformation steps at (a) 1%, (b) 2.5%, and 4.5% plastic deformation. The white pixels in the maps correspond to non-correlated points caused by surface scratches and dirt deposited onto the gold nano-speckle pattern. The white arrows in (b) highlight strain concentrations close to GB and triple junctions. The red dashed lines in (c) delimit a macro-strain band. (d) GB map obtained from the EBSD map before deformation. The main grains and GB of study have been labeled, and the theoretical prismatic slip traces have been drawn at the center of the grains. 80

5.7 Influence of κ and ψ on slip transfer/blocking across the GBs as a function of the applied plastic deformation. (a) $\mathrm{def}_1 \approx 1\%$, (b) $\mathrm{def}_2 \approx 2.5\%$, and (c) $\mathrm{def}_3 \approx 4.5\%$. The GBs labeled with solid symbols will be analyzed in more detail in the next sections due to their unexpected slip transfer behavior. (d) Summary of the changes in the occurrence of slip transfer with plastic deformation in the selected GBs. 81

5.8 Influence of κ and θ on the occurrence of slip transfer/blocking across the analyzed GBs as a function of the applied plastic deformation. (a) $\mathrm{def}_1 \approx 1\%$, (b) $\mathrm{def}_2 \approx 2.5\%$, and (c) $\mathrm{def}_3 \approx 4.5\%$. 83

5.9 Effective shear strain maps of two GB that fulfill the classical slip transfer criteria. (a), (b), and (c): slip transfer across GB_4 after 1%, 2.5%, and 4.5% plastic deformation, respectively. (d), (e), and (f): slip blocking across GB_{27} after 1%, 2.5%, and 4.5% plastic deformation, respectively. The theoretical prismatic slip traces of the active slip systems have been drawn for each GB, and the GB trace has been indicated with a fine dashed gray line in the first deformation map. 85

5.10 Effective shear strain maps after 1%, 2.5%, and 4.5% plastic deformation in the neighborhood of three GBs that do not fulfill the classical slip transfer criteria. (a), (b), and (c): GB_{25}. (d), (e), and (f): GB_{14}. (g), (h), and (i): GB_{18}. The theoretical prismatic slip traces of the observed active slip systems have been drawn for each GB, and the GB trace has been indicated with a fine dashed gray line at the first deformation map. An additional first-order pyramidal theoretical slip trace has been added in G_{23}. 86

5.11 Detail shear strain HRDIC maps of two GBs that do not follow the classical slip transfer criteria. (a), (b), and (c): GB_{16} shear strain maps after 1%, 2.5%, and 4.5% plastic deformation, respectively. (d), (e), and (f): GB_2 shear strain maps after 1%, 2.5%, and 4.5% plastic deformation, respectively. For each GB, the theoretical prismatic slip traces of the observed active slip systems have been drawn, and the GB trace has been indicated with a translucent dashed gray line at the first deformation map. (g) and (h): G_2 EBSD and grain reference orientation deviation (GROD) maps after 4.5% plastic deformation, respectively. 89

6.1 RVE of the microstructure including 100 grains discretized with 150000-second order tetrahedra. The grains are colored according to the crystal orientation relative to the Z axis, as indicated in the inverse pole figure. . . . 103
6.2 Schematic of the calculation of the distance from a Gauss point to the nearest GB along one slip direction. 104
6.3 RVE selection analysis performed in Cu RVEs with 20 μm grain size and fully opaque GBs. (a) Effect of the number of grains on the tensile response. (b) Effect of the discretization on the tensile response. (c) Effect of the set of random orientations on the tensile response. 107
6.4 Engineering stress-strain curves of Al and Cu polycrystals as a function of grain boundary type: (a) Al $\bar{D}_g$ =10 μm, (b) Al $\bar{D}_g$ = 40 μm, (c) Cu $\bar{D}_g$ = 10 μm and (d) Cu $\bar{D}_g$ = 40 μm. 109
6.5 Spatial distribution of the total dislocation density (in m^{-2}) in a cross-section of the RVE of the Al and Cu polycrystals with an average grain size of 10 μm deformed up to 5%. (a) Al, opaque GBs. (b) Cu, opaque GBs. (c) Al, translucent GBs with $m' > 0.9$. (d) Cu, translucent GBs with $m' > 0.9$. (e) Al, translucent GBs with $m' > 0.75$. (f) Cu, translucent GBs with $m' > 0.75$. . 110
6.6 Spatial distribution of the Von Mises stress (in MPa) in a cross-section of the RVE of the Al and Cu polycrystals with an average grain size of 10 μm grain size deformed up to 5%. (a) Al, opaque GBs. (b) Cu, opaque GBs. (c) Al, translucent GBs with $m' > 0.9$. (d) Cu, translucent GBs with $m' > 0.9$. (e) Al, translucent GBs with $m' > 0.75$. (f) Cu, translucent GBs with $m' > 0.75$.111
6.7 Fraction of GBs in the RVE as a function of the number of transparent slip systems. (a) $m' > 0.9$. (b) $m' > 0.75$. (c) $m' > 0.5$. 112
6.8 Engineering stress-strain curves of polycrystals with an average grain size of 10 μm for opaque and transparent GBs as well as slip transfer criteria of $m' > 0.75$ or $\Delta b < 0.45b$. (a) Al. (b) Cu. 113
6.9 Fraction of GBs in the RVE as a function of the number of transparent slip systems. (a) $m' > 0.75$. (b) $\Delta b_{\alpha\beta} < 0.45b$. 114
6.10 Grain boundary strengthening in Al and Cu polycrystals as a function of the adimensional parameter $\bar{D}_g\sqrt{\rho_i}$. (a) Al, $\varepsilon = 1\%$. (b) Al, $\varepsilon = 5\%$. (c) Cu, $\varepsilon = 1\%$. (d) Cu, $\varepsilon = 5\%$. The results of the simulations with fully opaque GBs and with thresholds $m' > 0.9$ and $m' > 0.75$ for slip transfer are plotted in each figure. 115
6.11 Experimental data from the literature and simulation results of the flow stress of Al, Cu, Ni, and Ag polycrystals as a function of $\bar{D}_g^{-1}$ for different applied strains. (a) Al. (b) Cu. (c) Ni. (d) Ag. Experimental results are indicated by black circles, while simulation results without and with slip transfer are represented by open red and blue circles. The linear fittings for the simulated results are indicated in red (opaque GBs) and blue (translucent GBs) solid lines. 117
6.12 Engineering stress-strain curves of polycrystals with transparent GBs and opaque GBs with grain sizes between 10 and 80 μm for (a) Ti, and (b) Mg. . 119

6.13 Spatial distribution of the Von Mises stress in MPa and the total dislocation density (in m^{-2}) in a cross-section of the Ti polycrystals with transparent GBs (a) and (c), and opaque GBs with an average grain size of 10 μm (b) and (d) deformed up to 1% in tension. Notice the different legend ranges for the stresses and dislocation densities between transparent GBs and opaque GBs. The white arrows in (a) indicate some stress concentrations present at GBs for the simulation with fully transparent GBs. 120

6.14 Spatial distribution of the Von Mises stress in MPa and the total dislocation density (in m^{-2}) in a cross-section of the Mg polycrystals with transparent GBs (a) and (c), and opaque GBs with an average grain size of 10 μm (b) and (d) deformed up to 1% in tension. Notice the different legend ranges for the stresses and dislocation densities between transparent GBs and opaque GBs. The white arrows in (a) indicate some stress concentrations present at GBs for the simulation with fully transparent GBs. 121

6.15 Relative activity of the different slip systems to the accumulated plastic slip γ as a function of the applied strain for the 10 μm RVE with opaque GBs and the RVE with transparent GBs for (a) Ti, and (b) Mg. 122

6.16 Experimental data from the literature and simulation results of the flow stress of HCP polycrystals as a function of $\bar{\mathrm{D}}_{\mathrm{g}}^{-1/2}$ for different applied strains for (a) Ti and (b) Mg. The experimental results are indicated by black circles, and simulation results with opaque GBs are indicated by open purple squares. The linear fittings for the simulated results are indicated in purple solid lines. 123

7.1 Bilinear traction-separation law, where damage initiation is indicated by the superindex 0 and failure is indicated by the superindex f. 131

7.2 Thin foil with columnar grains to simulate the effect of GBs in FCC and HCP metals. The reference frame and the loading direction are indicated in (a), and the notation employed for the foil boundary faces is indicated in (b). 133

7.3 Thin foils used to simulate the effect of GBs in Al (FCC) (a)-(c). The grains within the foils are colored according to the inverse pole figure along z, provided in (d). Note that foils 1 and 2 have the same grain distribution (R_1) but different crystal orientations, while foil 3 has a different grain distribution (R_2). 134

7.4 Thin foils used to simulate the effect of GBs in Mg (HCP) (a)-(d). The grains within the foils are colored according to the inverse pole figure along z, provided in (e). Note that two different grain realizations were generated (R_1 and R_2), and two different sets of crystal orientations were used for each foil: random orientation and a strong basal texture. The basal pole figure for the microstructures with basal texture is shown in (f). 135

7.5 Example of thin foil polycrystal (left), together with the sample reference frame and loading direction, and cohesive surfaces generated at the GBs of the same polycrystal (right). 136

7.6 Schematic representation of Pearson correlation between two variables u and v: (a) strong positive correlation with $r > 0$, (b) no correlation with $r = 0$, and (c) strong negative correlation. 137

7.7 Engineering stress-strain curves of the Al (FCC) foils as a function of grain boundary type under (a) plane stress and (b) plane strain loading conditions. The solid lines correspond to the mechanical behavior without fracture, and the dashed lines correspond to simulations that include fracture at the GBs. 138

7.8 Contour plot of the Von Mises stress in MPa (left column) and of total dislocation density in m^{-2} (right column) at ε = 2% as a function of GB character in Al foil 1 under plane stress without fracture. The contour plots with fully opaque GBs are represented on the first row, with translucent GBs where slip transfer is allowed for $m' > 0.8$ on the second row and with transparent GBs on the third row. Note that a different scale is employed for the dislocation density for the foils with opaque and translucent GBs than that used for fully transparent GBs. 140

7.9 Contour plots of the Von Mises stress in MPa at ε = 2% without including fracture (left) and including intergranular fracture (right) as a function of GB character in Al foil 1 under plane stress. The contour plots with fully opaque GBs are represented on the first row, with translucent GBs where slip transfer is allowed for $m' > 0.8$ on the second row and with transparent GBs on the third row. Cracks are indicated by white arrows. 141

7.10 Crack path at the end of the simulations of Al foil 1 under plane stress (left column) and plane strain (right column) with fully opaque GBs (first row), translucent GBs where slip transfer is allowed for $m' > 0.8$ (second row), and transparent GBs (third row). The white arrows indicate the location of several intergranular cracks that are not evident in the figure. 142

7.11 Pearson correlation matrix for GB fracture in the Al foils. (a) Plane stress, (b) plane strain. 143

7.12 Engineering stress-strain curves of the Mg thin foils with random orientations (foils 1 and 3) as a function of GB type under (a) plane stress and (b) plane strain loading conditions. The solid lines correspond to the mechanical response of the foils without fracture, while the dashed lines include fracture at GBs. 144

7.13 Contour plot of the Von Mises stress in MPa (left column) and of total dislocation density in m^{-2} (right column) at ε = 2% as a function of GB character in Mg foil 1 (random texture) under plane stress without fracture. The contour plots with fully opaque GBs are represented on the first row, with translucent GBs where slip transfer is allowed for $m' > 0.8$ on the second row and with transparent GBs on the third row. Note that a different scale is used for the dislocation density of the foils with opaque and translucent GBs and for the fully transparent GBs. 146

7.14 Contour plots of the Von Mises stress in MPa at ε = 2% without intergranular fracture (left) and with intergranular fracture (right) as a function of GB character in the Mg foil 1 under plane stress. The contour plots with fully opaque GBs are represented on the first row, with translucent GBs where slip transfer is allowed for $m' > 0.8$ on the second row and with transparent GBs on the third row. The white arrows indicate the location of intergranular cracks. 147
7.15 Crack path at the end of the simulations of Mg foil 1 with random crystal orientations under plane stress (left column) and plane strain (right column) with fully opaque GBs (first row), translucent GBs where slip transfer is allowed for $m' > 0.8$ (second row), and transparent GBs (third row). 148
7.16 Pearson correlation matrix for GB fracture in the Mg foils with random crystal orientations. (a) Plane stress, (b) plane strain. 149
7.17 Engineering stress-strain curves of the Mg thin foils with basal texture (foils 2 and 4) as a function of GB type under (a) plane stress and (b) plane strain loading conditions. The solid lines correspond to the mechanical response of the foils without fracture, while the dashed lines include fracture at GBs. 150
7.18 Contour plot of the Von Mises stress in MPa (left column) and of total dislocation density in m^{-2} (right column) at ε = 2% as a function of GB character in Mg foil 2 (strong basal texture) under plane stress without fracture. The contour plots with fully opaque GBs are represented on the first row, with translucent GBs where slip transfer is allowed for $m' > 0.8$ on the second row and with transparent GBs on the third row. Note that a different scale is employed for the dislocation density for the foils with opaque and translucent GBs and for those with fully transparent GBs. 152
7.19 Contour plots of the Von Mises stress in MPa at ε = 2% without including fracture (left) and including intergranular fracture (right) as a function of GB character in Mg foil 2 under plane stress. The contour plots with fully opaque GBs are represented on the first row, with translucent GBs where slip transfer is allowed for $m' > 0.8$ on the second row and with transparent GBs on the third row. Intergranular cracks are indicated with white arrows. 153
7.20 Crack path at the end of the simulations of Mg foil 1 with basal texture under plane stress (left column) and plane strain (right column) with fully opaque GBs (first row), translucent GBs where slip transfer is allowed for $m' > 0.8$ (second row), and transparent GBs (third row). 154
7.21 (a) Engineering stress-strain curves of Mg thin foils with random crystal orientations (foils 1 and 3, in blue) and with strong basal texture (foils 2 and 4, in red) with opaque GBs under plane stress. The solid lines correspond to the foils without fracture, and the dashed lines correspond to the foils with fracture. (b) Relative contribution of the basal, prismatic, and pyramidal slip systems to the accumulated plastic slip γ as a function of the crystallographic texture in Mg thin foils 1 (random orientations, solid lines) and 2 (basal texture, dashed lines) with fully opaque GBs under plane stress conditions. 155

7.22 (a) Engineering stress-strain curves of Mg thin foils with random crystal orientations (foils 1 and 3, in blue) and with strong basal texture (foils 2 and 4, in red) with opaque GBs under plane strain. The solid lines correspond to the foils without fracture, and the dashed lines correspond to the foils with fracture. (b) Relative contribution of the basal, prismatic, and pyramidal slip systems to the accumulated plastic slip γ as a function of the crystallographic texture in Mg thin foils 1 (random orientations, solid lines) and 2 (basal texture, dashed lines) with fully opaque GBs under plane strain conditions. 156
7.23 Pearson correlation matrix for GB fracture in the Mg foils with strong basal texture. (a) Plane stress, (b) plane strain. 157

List of Tables

1 Recurrent acronyms used throughout this thesis (A-G). xxvii
2 Recurrent acronyms used throughout this thesis (H-Z). xxviii
3 Recurrent notations used throughout this thesis — Latin symbols. xxix
4 Recurrent notations used throughout this thesis — Greek symbols. xxx

1.1 Slip system notation in FCC metals, indicating the coloring of the four $\{111\}$ slip planes. 3
1.2 Main slip system families in HCP metals. 4

3.1 Summary of DCT acquisition and reconstruction approach followed in the current study: scanning and reconstruction times for conventional DCT (C-DCT) and helical phyllotaxis (HP-DCT) and achieved average grain completeness values. 34

4.1 Threshold angle (according to the F1 score) to predict slip transfer. 63
4.2 Optimum threshold (for maximum F1 score) for different well-known slip transfer criteria. 65

5.1 Geometrical parameters and slip transfer criteria between the active prismatic slip systems for GB_4, and GB_{27}. The rank of the SF of the active prismatic slip system among the three possible planes is indicated between parenthesis and the SF is colored according to the active slip systems indicated in the legend in Fig. 5.9. 84
5.2 Geometrical parameters and slip transfer criteria between the active prismatic slip systems for GB_{25}, GB_{14}, and GB_{18}. The rank of the SF of the active prismatic slip system among the three possible planes is indicated between parenthesis, and the SF is colored according to the active slip system indicated in the legend in Fig. 5.10. 87

5.3 Geometrical parameters and slip transfer criteria between the active prismatic slip systems for GB_{16} and GB_{2}. The rank of the SF of the active prismatic slip system among the three possible planes is indicated between parenthesis, and the SF is colored according to the active slip systems indicated in the legend in Fig. 5.10. 89

6.1 Parameters of the dislocation-based crystal plasticity model for FCC single crystals. 95
6.2 Parameters of the dislocation-based crystal plasticity model for FCC materials [78, 151] 97
6.3 Parameters of the dislocation-based crystal plasticity model for Ti and Mg (HCP) single crystals. The values of the stiffness constants (expressed in GPa) are taken from [81] for Ti and from [194], whereas the values of c/a are taken from [128] for Ti and from [23] for Mg. 98
6.4 Parameters of the dislocation-based crystal plasticity model for HCP Ti and Mg single crystals. 98
6.5 Lattice resistance and CRSS values for the Ti and Mg polycrystals, calculated with Eq. 6.8. The CRSS ratios with respect to prismatic slip are indicated between parenthesis for Ti, and the CRSS ratios with respect to basal slip are indicated between parenthesis for Mg. 100
6.6 Calculated and chosen critical annihilation distance between dislocations y_c^α for the Ti and Mg polycrystals, calculated with Eq. 6.11. The smallest y_c^α among basal and prismatic slip is highlighted in bold and will be chosen for both slip systems to account for basal-prismatic cross-slip. 101
6.7 Parameters of the dislocation-based crystal plasticity model depending on the slip systems for the Ti and Mg (HCP) crystals. 102
6.8 Flow stress slope error assessment between experimental data and simulation results for different strains for Al, Cu, Ag, and Ni (Fig. 6.11(a)-(d)). m_{exp}, m_{opaque}, and $m_{translucent}$ are the slopes of the scattered data for the experiments, opaque GBs simulation and translucent GBs simulation, respectively. $\mathrm{RE}_{\mathrm{opaque}}$ and $\mathrm{RE}_{\mathrm{translucent}}$ are the relative errors between the experiments and the opaque GBs simulation and between the experiments and the translucent GBs simulation, respectively. 118
6.9 Flow stress slope error assessment between experimental data and simulation results for different strains for Ti and Mg (Fig. 6.16(a) and (b)). m_{exp} and m_{opaque} are the slopes of the scattered data for the experiments, opaque GBs simulation and translucent GBs simulation, respectively. $\mathrm{RE}_{\mathrm{opaque}}$ is the relative error between the experiments and the opaque GBs simulation. 124

7.1 Latent-hardening coefficients for the dislocation interaction matrix $q_{\alpha\beta}$ for pure Mg [23]. 129
7.2 Interaction properties for the cohesive surfaces introduced at GBs in the Al and Mg thin foils. 132

Glossary

Acronym	Definition
AFM	Atomic Force Microscopy
BCC	Body-Centered Cubic
CBS	Circular Backscatter
C-DCT	Conventional Diffraction Contrast Tomography
CRSS	Critical Resolved Shear Stress
CSL	Coincident Site Lattice
DCT	Diffraction Contrast Tomography
DOF	Degrees Of Freedom
EBSD	Electron Backscatter Diffraction
EDT	Euclidean Distance Transform
FCC	Face-Centered Cubic
FFT	Fast Fourier Transformation
FIB	Focused Ion Beam
FN	False Negatives
FP	False Positives
GB(s)	Grain boundary(ies)
GNDs	Geometrically Necessary Dislocations
GROD	Grain Reference Orientation Deviation

Table 1: Recurrent acronyms used throughout this thesis (A-G).

Acronym	Definition
HCP	Hexagonal Close-Packed
HP-DCT	Helical Phyllotaxis Diffraction Contrast Tomography
HRDIC	High-Resolution Digital Image Correlation
LabDCT	Laboratory-scale Diffraction Contrast Tomography
LRB	Lee Robertson and Birnbaum
MFP	Mean Free Path
PCT	Phase Contrast Tomography
RDR	Relative Displacement Ratio
ROI	Region Of Interest
RSS	Resolved Shear Stress
RVE	Representative Volume Element
SEM	Scanning Electron Microscopy
SF	Schmid Factor
SGCP	Strain Gradient Crystal Plasticity
SSDs	Statistically Stored Dislocations
ST-MLRA	Slip Trace Modified Lattice Rotation Analysis
TB(s)	Twin Boundary(ies)
TEM	Transmission Electron Microscopy
TN	True Negatives
TP	True Positives
UMAT	User-Defined Material

Table 2: Recurrent acronyms used throughout this thesis (H-Z).

Symbol	Definition	Reference
$\boldsymbol{b}$	Slip system Burgers vector	Fig. 1.5
Δb	Residual Burgers vector	Sec. 1.3, Eqs. 1.1, 6.15
D	Damage at cohesive surfaces	Fig. 7.1
d_b	Distance to the nearest grain boundary	Sec. 6.3
$\overline{D}_g$	Average grain size	Ch. 6
F1	F1 score	Eq. 4.5
$\boldsymbol{G}$	Orientation matrix	Eq. 6.16
G_C	Energy of the cohesive surface	Sec. 7.2.3
K	Similitude coefficient	Eq. 6.6
K_{ii}	Cohesive surface stiffness constants	Fig. 7.1
K_s	Dislocation storage coefficient	Eqs. 6.5, 6.10
ℓ^α	Dislocation mean free path	Eq. 6.6
$\mathrm{L_{GB}}$	Grain boundary length	Sec. 7.4
LRB	Lee Robertson and Birnbaum parameter	Sec. 1.3, Eq. 1.3
m	Strain rate sensitivity coefficient	Eq. 5.1
m'	Luster Morris parameter	Sec. 1.3, Eqs. 1.4, 6.15
$\boldsymbol{n}$	Slip system normal vector	Fig. 1.5
N	Livingston and Chalmers parameter	Sec. 1.3, Eq. 1.2
$\mathrm{n_{Trs}}$	Number of transparent slip systems per grain boundary	Sec. 7.4
$q^{\alpha\beta}$	Dislocation interaction coefficients	Eqs. 6.3, 6.8
r	Pearson correlation coefficient	Sec. 7.4
SA	Slip activation factor	Sec. 7.4
t	Traction between cohesive surfaces	Fig. 7.1
t_i^0	Stress for damage initiation at the cohesive surface	Sec. 7.2.3
y_c	Critical annihilation distance between dislocations	Eqs. 6.5, 6.10, 6.11
y_e	Annihilation distance between edge dislocations	Eq. 6.11
y_s	Annihilation distance between screw dislocations	Eq. 6.11

Table 3: Recurrent notations used throughout this thesis — Latin symbols.

Symbol	Definition	Reference
α	Grain boundary trace angle	Fig. 1.3
α_x	Angle between grain boundary and loading axis	Sec. 7.4
β	Grain boundary inclination angle	Fig. 4.3 (c)
γ	Angle between incoming slip plane and outgoing Burgers vector	Fig. 1.5
γ	Accumulated plastic slip	Eq. 5.1
$\dot{\gamma}$	Shear strain rate	Eq. 5.1
$\dot{\gamma}_0$	Reference shear strain rate	Eq. 5.1
δ	Angle between incoming Burgers vector and outgoing slip plane	Fig. 1.5
δ	Angle between incoming Burgers vector and outgoing slip plane	Fig. 1.5
δ	Separation between cohesive surfaces	Fig. 7.1
δ_i^f	Maximum separation between cohesive surfaces	Sec. 7.2.3
ε	Applied strain	Ch. 2, 4, 5, 6, 7
ε_{dmg}^0	Strain for damage initiation	Sec. 7.4
φ_1	First Euler angle	Fig. 1.3
ϕ	Second Euler angle	Fig. 1.3
φ_2	Third Euler angle	Fig. 1.3
κ	Angle between incoming and outgoing Burgers vectors	Fig. 1.5
ψ	Angle between incoming and outgoing slip planes	Fig. 1.5
π	Pi	Eq. 6.11
σ_y	Yield strength of a polycrystal	Eq. 6.1
σ_∞	Flow strength of a polycrystal with infinite grain size	Eq. 6.1
θ	Twist angle	Fig. 1.5
Θ	Misorientation angle	Fig. 1.3
τ	Resolved shear stress	Eq. 5.1
τ_c	Critical resolved shear stress	Eq. 6.3
τ_{c0}	Lattice resistance	Eq. 6.8
μ	Shear modulus	Eqs. 6.3, 6.8
ρ	Dislocation density	Eq. 6.6
$\dot{\rho}$	Dislocation density rate	Eqs. 6.4, 6.5, 6.9, 6.10

Table 4: Recurrent notations used throughout this thesis — Greek symbols.

1 Introduction

Metallic materials stand as ideal candidates for many structural applications in the automotive, aerospace, chemical, construction, and biomedical sectors owing to their high stiffness, formability, and ductility. However, the strength of pure metals is very low due to the development of plastic deformation by dislocation slip. Hence, they have to be strengthened by obstacles that hinder dislocation motion.

Grain boundaries (GBs) stand among the strongest barriers to dislocation slip in polycrystals, playing a critical role in their mechanical properties [185]. Dislocations move through the crystal lattice when a metal undergoes plastic deformation by the application of an external load. GBs act as barriers to the motion of dislocations due to the lack of continuity between the lattice planes in neighbor grains, impeding the progress of dislocation motion. The interaction between dislocations and GBs allows to control the mechanical properties of metals, and GB engineering arises as a tool to deliberately manipulate the GB characteristics to enhance the performance of metallic materials. In fact, it is possible to tailor the mechanical properties to meet specific requirements by controlling the grain size, orientation, and distribution.

However, GBs are not just passive interfaces and can be sources of damage in metallic materials. They can act as sites for the initiation and propagation of cracks and voids in the presence of thermo-mechanical loads, leading to the premature failure of metallic components, particularly in the case of mechanical fatigue and/or creep deformation at high temperatures. Thus, understanding the behavior of GBs in the presence of thermo-mechanical loads is critical for designing materials with improved resistance to fatigue and creep [95, 193].

GBs also induce size effects during the plastic deformation of metals, leading to the classical Hall-Petch effect that relates the yield strength with the inverse of the square root of the average grain size [72, 143]. Moreover, metallic with nanoscale grains exhibit improved strength and hardness, as compared with their coarse-grained counterparts, but their strain hardening and ductility are dramatically reduced because dislocation storage within the grains is limited by their small size [43, 101, 174].

GBs also play a crucial role in the response of metallic materials to external factors such as irradiation and hydrogen exposure. In nuclear materials, irradiation can create defects and alter the GB structure, affecting their mechanical properties and integrity [18, 49]. Similarly, hydrogen embrittlement is a phenomenon where hydrogen atoms absorbed by GBs can lead to reduced ductility and catastrophic failure [21, 150]. Designing materials with GBs that are resistant to such effects is essential for ensuring the long-term performance and safety of critical components.

In conclusion, the behavior of GBs is one of the key factors to take into account for the design of metallic materials with improved mechanical properties. GB engineering offers a powerful tool to optimize material performance by tailoring these boundaries to meet specific requirements, and it is an essential aspect of physical metallurgy.

1.1 Plastic deformation by dislocation slip

Dislocation slip is a fundamental mechanism for plastic deformation in metals. Dislocations are line defects characterized by the Burgers vector $\boldsymbol{b}$, which represents the magnitude and direction of the lattice distortion caused by the dislocation. Dislocations move along crystallographic planes driven by the resolved shear stress acting on the slip plane along the slip direction, which is parallel to the Burgers vector [30]. There are three types of dislocations: edge, screw, and mixed dislocations. Edge dislocations are created by the insertion of an extra half-plane of atoms above the dislocation lines, and their Burgers vector is perpendicular to the dislocation line. Screw dislocations do not involve an extra half-plane of atoms, but the atomic planes are misaligned along the dislocation line, creating a spiral or helical pattern, and the Burgers vector is parallel to the dislocation line. Finally, mixed dislocations have components of both edge and screw dislocations [86, 142].

Following experimental observations and theoretical analyses, dislocation slip along crystallographic planes takes place when the shear stresses acting on the slip plane along the slip direction reach a certain critical value, denominated critical resolved shear stress (CRSS). The minimum CRSS in metallic materials is found in the most densely packed slip planes and along the orientations with the largest atomic density in these planes, which vary depending on the crystal lattice [86, 142].

In the case of face-centered cubic (FCC) crystal lattices (characterized by a lattice parameter a), dislocation slip takes place in four $\{111\}$ close-packed planes and three $<110>$ close-packed directions within these planes (Fig. 1.1 (b)). This leads to 12 different slip systems, characterized by the slip plane and the slip direction, which are presented in Table 1.1 and colored according to the active slip plane. Slip along these planes and directions is the primary mechanism for plastic deformation in FCC metals, and the CRSS is the same for all systems.

The hexagonal close-packed (HCP) crystal lattice is characterized by two lattice parameters: the basal plane hexagonal edge length a and the height between basal planes c (see Fig. 1.2 (a)). The c/a ratio has a direct impact on CRSS for dislocation motion along differ-

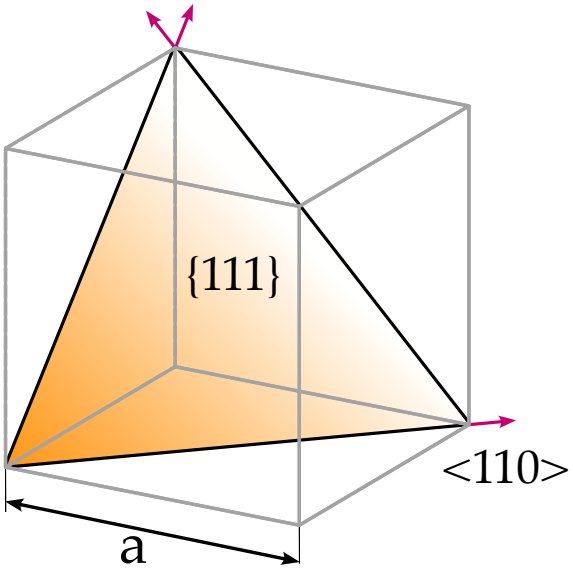

Figure 1.1: Most densely packed slip planes and directions within the FCC unit lattice.

Table 1.1: Slip system notation in FCC metals, indicating the coloring of the four $\{111\}$ slip planes.

Slip system	Plane	Direction
1	$(1\ 1\ 1)$	$[\bar{1}\ 1\ 0]$
2	$(1\ 1\ 1)$	$[1\ 0\ \bar{1}]$
3	$(1\ 1\ 1)$	$[0\ \bar{1}\ 1]$
4	$(\bar{1}\ 1\ 1)$	$[\bar{1}\ \bar{1}\ 0]$
5	$(\bar{1}\ 1\ 1)$	$[1\ 0\ 1]$
6	$(\bar{1}\ 1\ 1)$	$[0\ 1\ \bar{1}]$
7	$(\bar{1}\ \bar{1}\ 1)$	$[1\ \bar{1}\ 0]$
8	$(\bar{1}\ \bar{1}\ 1)$	$[\bar{1}\ 0\ \bar{1}]$
9	$(\bar{1}\ \bar{1}\ 1)$	$[0\ 1\ 1]$
10	$(1\ \bar{1}\ 1)$	$[1\ 1\ 0]$
11	$(1\ \bar{1}\ 1)$	$[\bar{1}\ 0\ 1]$
12	$(1\ \bar{1}\ 1)$	$[0\ \bar{1}\ \bar{1}]$

ent crystallographic directions because the spacing between crystal planes depends on it. The main slip systems in HCP lattices are schematically shown in Fig. 1.2, and the number of independent slip systems and their corresponding slip plane and slip direction families are displayed in Table 1.2.

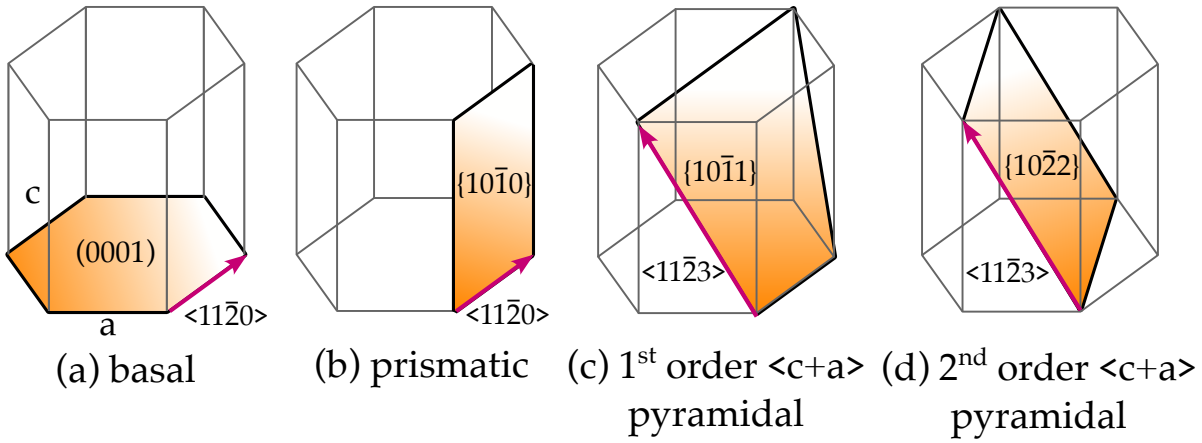

Figure 1.2: Schematic diagram of the main slip systems in HCP lattices.

Table 1.2: Main slip system families in HCP metals.

Slip family	Slip plane	Slip direction	Number of systems
Basal	(0001)	$<11\bar{2}0>$	3
Prismatic	$\{10\bar{1}0\}$	$<11\bar{2}0>$	3
1^{st} order pyramidal <c+a>	$\{10\bar{1}1\}$	$<11\bar{2}3>$	12
2^{nd} order pyramidal <c+a>	$\{10\bar{2}2\}$	$<11\bar{2}3>$	6

1.2 Grain boundaries

1.2.1 Geometrical description of grain boundaries

Polycrystalline materials are composed of an aggregate of single crystals or grains with different orientations. The different grains are separated by GBs, which are disordered regions where the crystallographic orientation abruptly changes from one grain to the next.

A planar grain boundary can be described by five macroscopic degrees of freedom (DOFs) [185]. Three DOFs are related to the relative crystallographic orientation between the neighboring grains, and the remaining two describe the geometry of the GB plane.

As depicted in Fig. 1.3, the crystallographic orientation of each crystal across the GB is determined by three Euler angles $(\varphi_1, \Phi, \varphi_2)$ per crystal. Then, the relative misorientation across the GB can be expressed as an axis-angle rotation that can be uniquely described by three parameters: two for the rotation axis ax determined by its direction cosines and one misorientation angle Θ. The other two remaining parameters deal with the orientation of the GB plane in the three-dimensional space and can be defined by the GB trace angle α and the GB inclination angle through the thickness β.

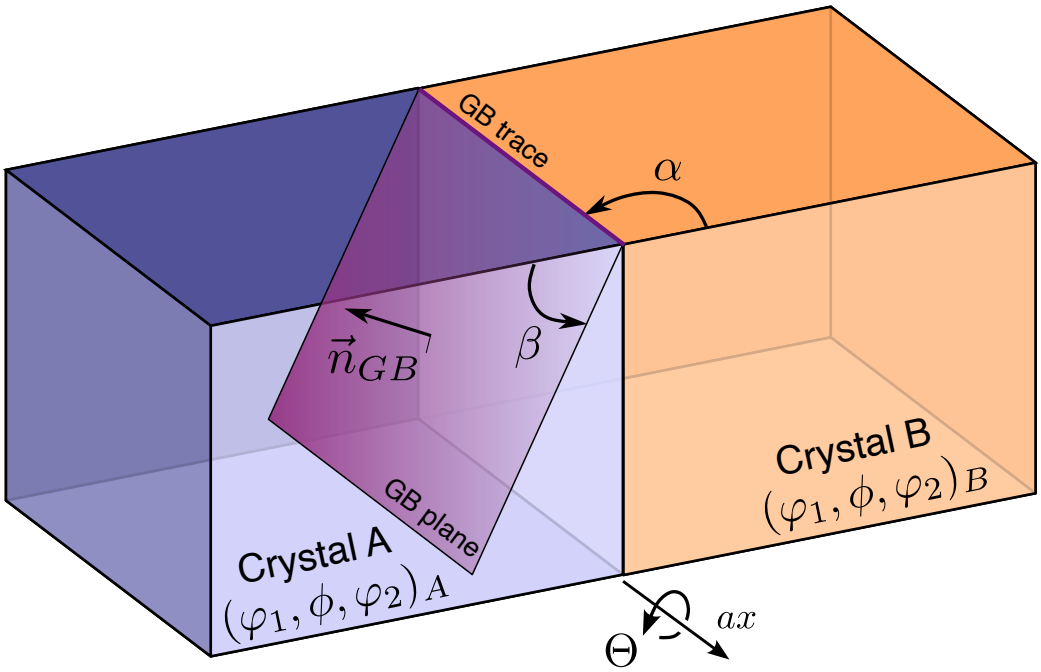

Figure 1.3: Five degrees of freedom to describe a planar GB.

1.2.2 Interactions between dislocations and grain boundaries

Grain boundaries play a key role in the plastic deformation of polycrystals because they constitute physical barriers to dislocation motion [83]. The interaction between dislocations and GBs was reviewed by Bayerschen *et al.* [19], and the most relevant mechanisms of dislocation-GB interactions are schematically illustrated in Fig. 1.4, where A stands for the incoming slip system in the blue grain and B stands for the outgoing slip system in the orange grain across the GB.

Slip transmission from the blue to the orange grain one is not possible in the case depicted in Fig. 1.4 (a) because of the differences in the orientation of the Burgers vector of the dislocations between both slip planes. Thus, the GB behaves as an impenetrable or opaque boundary that impedes dislocation slip to the adjacent grain, leading to the formation of dislocation pile-ups and local stress concentration at the GB. As a result, geometrically necessary dislocations (GNDs) are accumulated at the GB, which induce strong strain gradients in order to preserve the displacement continuity between neighbor grains [58, 85]. This stress concentration induced by the dislocation pile-up at the GB may lead to the activation of dislocation sources in the adjacent grain, thus promoting the emission of dislocations from the boundary [160].

Conversely, if the slip systems across the GB are suitably aligned, dislocations gliding along the slip system A in the blue grain can continue gliding in the slip system B in the orange grain (Fig. 1.4 (c)). Hence, this GB is transparent from the viewpoint of dislocation

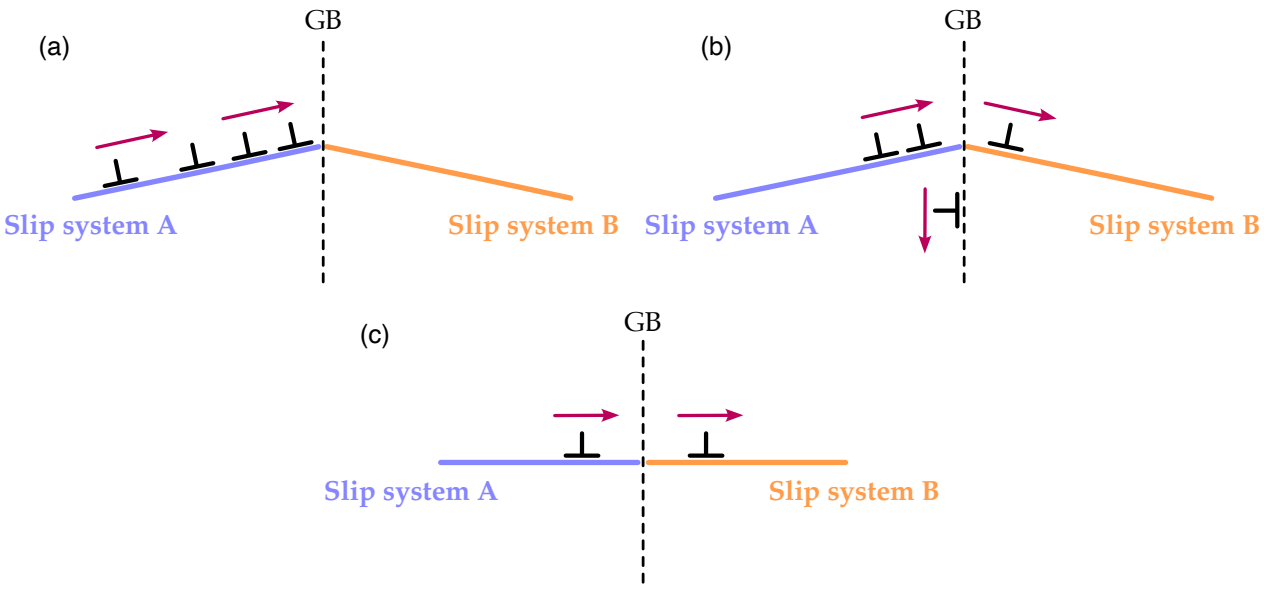

Figure 1.4: Basic mechanisms of dislocation-GB interaction between two active slip systems A and B in adjacent grains separated by a GB. (a) Opaque GB, (b) translucent GB, and (c) transparent GB.

motion and does not lead to any stress concentration [71]. The intermediate scenario is depicted in Fig. 1.4 (b)), which shows a translucent GB. Due to the misalignment between the incoming and outgoing Burgers vectors, slip transfer from the blue to the orange grain is necessarily accompanied by a residual dislocation at the GB to ensure the continuity of the Burgers vector [114]. This process is associated with a certain stress concentration that will depend on the misorientation between the slip planes across the boundary. Moreover, the accumulation of residual dislocations at the GB can also lead to grain boundary sliding and/or to the nucleation of dislocation sources in the adjacent grain.

1.3 Slip transfer criteria: state of the art

There is ample experimental evidence that different GBs present different slip transfer behavior. The empirical observations indicate that slip transfer occurs more easily in low-angle GBs, i.e., when the misorientation angle between adjacent grains is below $\approx 15°$ [149]. Nevertheless, slip transfer is not guaranteed by low-angle GBs, nor is impossible to occur for large GB misorientations.

The geometry of slip across a GB can be schematically described as shown in Fig. 1.5. The incoming slip system in crystal A is characterized by the Burgers vector $\boldsymbol{b}_A$ and the slip plane normal $\boldsymbol{n}_A$, whereas the outgoing slip system in crystal B is determined by the Burgers vector $\boldsymbol{b}_B$ and slip plane normal $\boldsymbol{n}_B$. $\boldsymbol{l}_A$ and $\boldsymbol{l}_B$ stand for the traces of the incoming and outgoing slip planes within the GB plane. This configuration gives rise to a series of angles that describe the geometrical alignment between incoming and outgoing slip systems across the GB. To begin with, the angle κ is the angle between Burgers vectors, and

ψ is the angle between slip plane normals. Next, δ and γ stand for the angles between the incoming Burgers vector and the outgoing slip plane normal and vice-versa, respectively. Finally, θ (often designated as the twist angle) represents the angle between the traces of the incoming ($\boldsymbol{l}_A$) and outgoing ($\boldsymbol{l}_B$) slip planes with the GB plane.

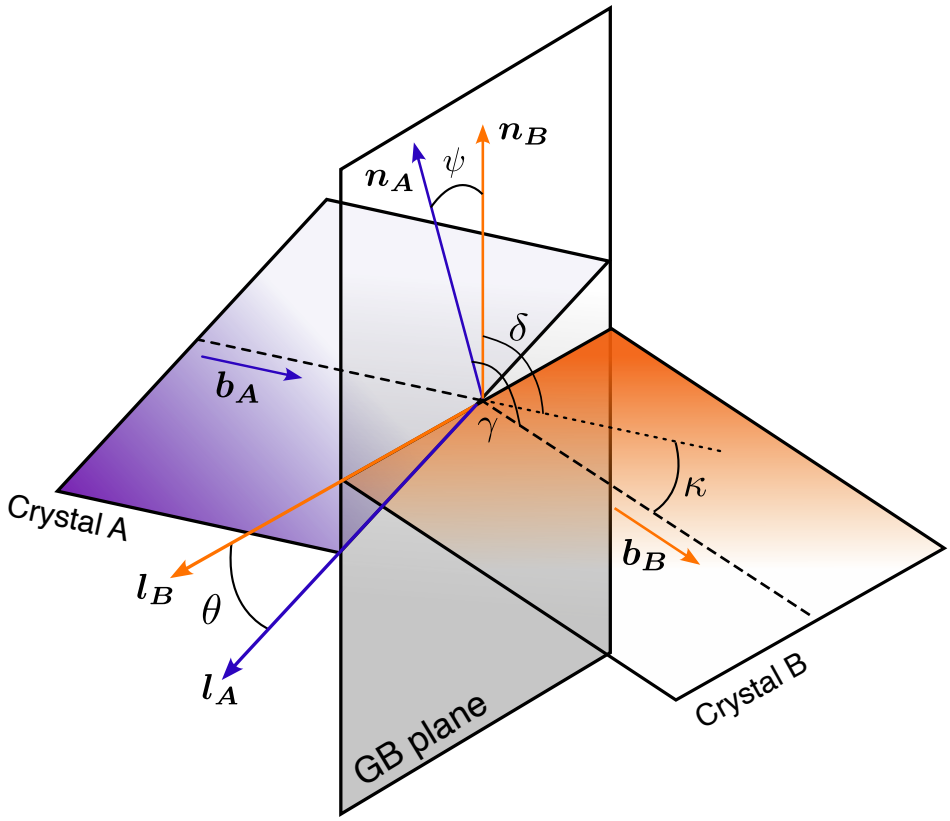

Figure 1.5: Schematic representation of the geometrical alignment between incoming and outgoing slip systems across a GB.

The occurrence of slip transfer across a GB has been extensively studied, and it has been associated with good geometrical alignment between the incoming and outgoing active slip systems [19]. Thus, criteria based on the angular parameters that characterize slip across GBs have been preferred (Fig. 1.5). Several investigations have attempted to define geometrical criteria to predict the likelihood of slip transfer across GBs.

Slip transfer is less likely to take place if the magnitude of the residual Burgers vector left at the GB Δb is very large [70, 71]. Δb is directly associated with the angle κ

$$\Delta b = |\boldsymbol{b}_A - \boldsymbol{b}_B| = 2 \cdot sin(\kappa/2). \tag{1.1}$$

Δb has been extensively used as an indicator for slip transfer when the κ angle between the slip systems is minimum [2, 3, 41, 140]. In that case, the local stress concentration caused by residual dislocations left at the GB is low [71]. Abuzaid *et al.* [2, 3] used a combination of electron back-scattered diffraction (EBSD) and digital image correlation to capture the formation of pile-ups at GB (indicative of slip blocked) or the transmission of

strains across GBs (indicative of slip transfer) in a Ni-based superalloy. Slip transfer was associated with small values of Δb, which seemed to be the best predictor of slip transfer, particularly for coherent twin boundaries where $\Delta b = 0$ was associated with slip transfer via cross-slip. Patriarca *et al.* [140] found a close correlation between the Δb and the local strain change across the GBs in a FeCr body-centered cubic (BCC) alloy. When the residual Burgers vector magnitude was large, the high strains on one side of the GB were paired with low strains across the GB, indicating the difficulties for dislocations to penetrate the interface. Conversely, smooth strain gradients were observed across the boundary when Δb was minimum because the resistance to slip transmission was negligible. Hence, their results suggested that the residual Burgers vector was closely related to the resistance to slip transfer.

Livingston and Chalmers [115] pioneered the use of geometrical criteria to predict the active slip system in a grain adjacent to a dislocation pile-up. This criterion was experimentally determined by means of transmission electron microscopy (TEM) after tensile deformation of several pure Al bicrystals. The geometrical criterion N was defined according to

$$N = \cos\psi \cos\kappa + \cos\gamma \cos\delta. \tag{1.2}$$

This criterion is based on the approximation that the stress state in the adjacent grain, resulting from the pile-ups of the incoming slip system at the GB, is of pure shear stress type. Thus, the shear stresses on the incoming and outgoing slip systems are related by the individual transmission factor, N. Using this approximation, given an incoming slip system A, the slip activation process will favor the operation of the slip system B with the highest N ($0 < N < 1$) in the adjacent grain. This criterion predicted additional (non-primary) active slip systems in the examined Al bicrystals and indicated that the higher N, the larger the probability of operation of an outgoing slip system B alongside the GB. Moreover, the slip traces of slip system B appeared clearly over nearly the entire crystal surface in the few cases where $N > 0.9$ [115]. This provided a more fundamental understanding of the bicrystal deformation process and constituted the first step toward the analysis of polycrystalline deformation.

However, as reviewed by Shen *et al.* [160], the N criterion alone is insufficient to predict the active slip system and more information is required regarding the geometry of the GB and the stress state around it. By means of dynamic TEM experiments performed in stainless steel, they concluded that the outgoing slip plane can be predicted by means of geometric factors that include the geometry of the GB plane, whereas the outgoing slip direction will be that with the maximum resolved shear stress. A year later, Lee, Robertson, and Birnbaum [108] proposed a combined criterion based on *in situ* transmission electron microscopy (TEM) deformation experiments as an extension of the work of Clark *et al.* [41] and Shen *et al.* [160]. They stated that slip transfer will take place under three conditions:

1. The geometrical condition: the angle between the lines of intersection between the active slip planes and the GB (the twist angle θ) should be minimized.
2. The resolved shear stress condition: the resolved shear stress (RSS) acting on the outgoing slip system should be maximized.

3. The residual GB dislocation condition: the Burgers vector of the dislocation left at the GB Δb, and thus the angle κ (Eq. 1.1) should be minimized.

Mathematically, this criterion was expressed as:

$$LRB = \cos\theta \cos\kappa. \tag{1.3}$$

Later, Lee *et al.* [109] proposed that the maximum resolved shear stress criteria and minimum Δb (conditions (2) and (3)) needed to be combined, as they are competitive in nature. This conclusion was also supported by Lim *et al.* [114], who suggested that the slip system with the maximum resolved shear stress may not be activated and could even operate only for a short period of time if Δb is very large.

The LRB factor has been used in previous investigations that indicate that not only a good alignment between the Burgers vectors according to κ is necessary for slip transfer, but also the slip planes must be well-aligned with the GB plane according to θ [26, 73, 154]. Several experimental investigations have revealed that the θ angle may affect the occurrence of slip transfer across GB even though the slip systems are well aligned. For instance, Lee *et al.* [109] performed a TEM-based study in which it was observed that the outgoing slip plane was that with the smallest twist angle in order to accommodate slip in FCC materials. In fact, the twin plane normal and the twist angle can be directly calculated in the case of $\Sigma 3$ annealing twin boundaries in Ni and Genée *et al.* [62], reported that $\theta \approx 0°$ appears as a necessary condition for slip transmission across coherent twin boundaries. Regarding HCP materials, slip blocking was observed in a few GBs in pure Mg, which were well-aligned for slip transfer but $\theta > 60°$ [154]. They measured the GB orientation within the sample by sequential milling with a focused ion beam. This technique has also been used in other investigations [45, 144], but it is destructive and very time-consuming, limiting the number of GBs that can be analyzed.

One of the most accepted criteria for slip transmission is the one proposed by Luster and Morris [118], who performed a detailed TEM analysis of the active slip systems in TiAl. They emphasized the importance of the good alignment between the incoming and outgoing slip systems through the geometric compatibility factor m', defined as

$$m' = \cos\psi \cos\kappa \tag{1.4}$$

which may vary between 0 and 1. $m' = 1$ indicates full compatibility between the active slip systems across the GB because the slip directions and the slip planes are perfectly parallel. Hence, dislocations should be easily transmitted across the GB to the adjacent grain. On the contrary, the slip systems are incompatible when $m' = 0$ because either the slip directions or the slip planes are orthogonal. This criterion has been used to assess slip transfer and blocking across GBs in various investigations [7, 24, 26, 88, 154]. For instance, Wang *et al.* [184] successfully related high m' values with the occurrence of a pop-in effect during indentation tests along selected GBs in pure Nb, which was associated with slip transfer across the GB. Later investigations showed that m' could also be employed to predict the nucleation of mechanical twins at GBs in pure Mg, Mg-rare-earth alloys, and pure Ti [179, 182]. Hémery *et al.* [82] studied slip transfer in a Ti-6Al-4V alloy and

found that the Luster-Morris parameter, combined with high resolved shear stresses in the outgoing slip system, was a good indicator of the probability of slip transfer. Bieler *et al.* [24] studied over 250 GBs to analyze the effect of the misalignment between the slip systems on either side of a GB in pure Al. It was observed that slip transfer across GBs is rare and only convincingly evident when $m' > 0.97$ across low-angle boundaries with $< 15°$ misorientation. Even though it was found that m' was effective when estimating the likelihood of slip transfer, they concluded that the alignment between slip plane normals and directions is not the only important metric to determine the threshold for slip transmission. Furthermore, a study carried out by Alizadeh *et al.* [7] in pure Al GBs by means of conventional slip trace analysis revealed that slip transfer was very likely to occur if the residual Burgers vector was below $0.3b$ and the Luster-Morris parameter was higher than 0.9. Moreover, the ratio of $m'/\Delta b$ also presented a threshold above which slip transfer was very probable.

The validity of these geometrical slip transfer criteria has been assessed in recent years thanks to the information provided by EBSD in combination with slip transfer/blocking evidence at GBs from slip trace analysis in the scanning electron microscope (SEM). The slip traces left by the active slip systems on the grain surface can be observed by SEM imaging. The theoretical orientation of the slip traces in each grain can be obtained from the grain orientation before deformation provided by EBSD. Thus, the active slip plane can be identified by comparing the orientation of the slip traces observed via SEM imaging with the theoretical slip traces of the possible slip systems obtained by EBSD.

This experimental strategy does not indicate the active slip system when several slip systems with different slip directions share the same slip plane (such as FCC lattices or basal slip in HCP lattices). Thus, the slip system that presents the highest resolved shear stress on the slip plane is assumed to be active. This is normally assessed through the Schmid factor (SF), a geometrical parameter that gives the ratio of the resolved shear stress on the slip plane along the slip direction to the applied stress. The maximum resolved shear stress occurs when both the slip plane and the slip direction are oriented at $45°$ to the applied stress, and thus, the maximum SF equals 0.5.

Slip trace analysis in combination with EBSD and the assumption that the slip system with the highest SF is active has been employed in different investigations to assess slip transmission and slip activity in Al [7, 24, 26], Ni-based superalloys [62, 169], Ti and Ti alloys [70, 82, 179, 182], and Mg and Mg alloys [35, 88, 154, 200]. According to these investigations, slip transfer is associated with low misorientation angles between adjacent grains and also with low values of the residual Burgers vector, Δb, and high values (close to 1) of the N, and m' compatibility factors. Nevertheless, a non-negligible number of instances of slip blocking was reported in all cases where slip transfer should occur because the incoming and outgoing slip systems showed good alignment. And vice versa, slip transfer was sometimes found when the incoming and outgoing slip systems were not well aligned. These inconsistencies may be caused by the limitations of EBSD-based slip trace analysis:

1. *Slip traces can only be identified for slip systems that lead to a slip trace on the specimen surface.* Thus, slip bands will not appear in the grain surface if the Burgers vector of the active slip system is parallel or nearly parallel to the sample surface.

2. *This method can only identify the active slip plane, not the slip direction.* There are three different slip directions for each $\{111\}$ plane of the FCC lattice as well as three different slip directions in the (0001) basal planes of the HCP lattice. In addition, the second-order pyramidal slip systems in the HCP lattice comprise six $\{10\bar{1}\bar{2}\}$ pyramidal planes with two possible $<11\bar{2}3>$ directions each. The slip system with the highest SF is assumed to be active among the different possibilities. This may be a reasonable assumption for FCC crystals, in which plastic deformation is rather isotropic, but it is not guaranteed and may be far away from reality in HCP metals, which present a large plastic anisotropy during deformation. This could lead to the activation of a different slip system from that with the highest global SF and even to the activity of several slip systems within the same slip plane [102, 119, 201].

   Lately, complementary techniques have developed to solve this issue, such as the slip trace modified lattice rotation analysis (ST-MLRA) [190] or the relative displacement ratio (RDR) [39]. The ST-MLRA technique tracks the crystal lattice rotation induced by slip after plastic deformation by means of EBSD. The crystallographic orientation of the grain after deformation is compared to the theoretical rotation of the crystal caused by slip along the different slip directions that share the same slip plane, and the actual slip plane(s) can be identified. This strategy was recently employed by Sarebanzadeh *et al.* [154], who identified the active basal slip system(s) in pure Mg after tensile deformation. Using this method, multiple basal slip could be identified for grains with coarser grain sizes, whereas single slip was dominant for small grain sizes. Moreover, the slip system with the highest SF was not active in $\approx 30\%$ of the grains, and hence, the basal slip system with the highest SF cannot be assumed to be the only active slip system in Mg.

   Alternatively, the RDR method uses high-resolution digital image correlation to determine the ratio between the x and y components of the displacement at both sides of a slip band. They are compared to the ratio between the x and y components of the different theoretical Burgers vectors of the slip systems in the slip plane to identify the active one [39]. This method has been successfully employed to identify the active slip system in several works [166, 189], yet requires the presence of sharp and discrete slip traces.

3. *Lack of information about the GB inclination beneath the sample surface.* The conventional slip trace analysis technique is surface-based, and thus, it can only determine the GB trace angle α but not the GB inclination β (Fig. 1.3). The twist angle θ (see Fig. 1.5) is directly related to the GB plane geometry, so its effect on slip transfer can only be assessed by 3D characterization techniques except for special GBs such as twin boundaries, where the parent/child orientation relationship is well-known.

   The 3D GB geometry has to be determined to overcome this limitation for general GBs. This can be achieved by serial sectioning via mechanical polishing or focused ion beam (FIB) milling, and this technique has been used to assess the role of the twist angle on slip transfer during deformation in Mg and Mg alloys [154, 200]. Nevertheless, this strategy is rather time-consuming, and only a limited number of GBs can be analyzed. Given the experimental difficulties in measuring the GB orientation

through the thickness, several studies have assumed that GB is perpendicular to the sample surface [38, 62] to study the effect of θ on the likelihood of slip transmission. However, this hypothesis may lead to large errors in the evaluation of θ [62].

4. *Lack of information about the local stress state after deformation* which may be very different from the global stress state induced by the external forces. In this context, high-resolution digital image correlation (HRDIC) appears as a powerful tool to quantify strain heterogeneity in plastically deformed polycrystalline materials. Several works have attempted to correlate the dislocation-GB interactions with the plastic strain heterogeneity at the GB neighborhoods via HRDIC. They have attempted to correlate the classical geometrical slip criteria with the pile-up stresses and the slip transfer behavior observed via HRDIC. Abuzaid *et al.* [2] concluded that higher strains across some GBs in a Ni-based superalloy with low Δb were associated with lower GB resistance against slip transfer while lower strains across GBs with high Δb were attributed to higher resistance against slip transfer. The shear strain maps also revealed cross slip in a large number of $\Sigma 3$ GBs with $\Delta b \approx 0$. Sperry *et al.* [167] correlated the pile-up stresses observed at GBs in a Ni-based superalloy with the occurrence of slip transfer across GBs and did not observe clear correlations between GB misorientation or the m' factor with the GB pile-up stress. Harte *et al.* [79, 80] observed the slip band characteristics and the local deformation mechanisms at the microscale level in a precipitation-strengthened Ni-based superalloy via HRDIC. They were able to quantify the number of active slip planes, slip planarity, the presence of cross slip, slip band bifurcation, slip band fading towards a GB, and slip band impingement upon a GB. These investigations concluded that the high slip intensity and slip band impingement on GBs create diffuse strain regions, causing local hardening.

   The heterogeneity in the plastic strain accommodation at GBs was observed through HRDIC in AZ31 Mg alloy by Orozco *et al.* [136] and Yavuzyegit *et al.* [191], where a large extent of the deformation was accommodated at GBs whereas lower plastic strain was accommodated by basal slip in the bulk. Both investigations agreed that there is very strong evidence that the local stresses have a major effect on both slip activity and twinning. [65] performed an HRDIC analysis of the strain transfer phenomena across GBs in TiAl alloys, where slip transfer was observed at low-angle GBs, as extensively reported in the literature. Nevertheless, they observed a different strain transfer mechanism at certain high-angle GBs, where the crystal lattice rotated locally to geometrically restore a compatible deformation across the GB. A region of accumulated slip was found perpendicular to the active slip plane in the adjacent grain across the GB due to slip band impingement. The slip gradients through the boundary enabled a localized lattice rotation that accommodates the shear strain in the incoming band, preventing the build-up of interfacial stresses. This strain transfer mechanism could only be detected after large deformations, unlike slip transfer, which is often observed at the onset of plastic deformation.

   Thus, HRDIC can provide extra information about the local plastic strains near GBs that can be used to elucidate other factors –besides good alignment– that control slip

transfer at GBs. Due to the limited number of HRDIC investigations on slip transfer, the local stresses are not considered in the slip transfer criteria, which nowadays rely only on the geometrical alignment of the slip systems across the boundary.

1.4 Mesoscale modeling of grain boundaries

Numerical simulations of the mechanical behavior of polycrystals have progressed rapidly in recent years through the combination of computational homogenization and crystal plasticity constitutive models [158]. This strategy is able to determine the effective properties of a polycrystal by solving a boundary value problem of a microstructural representative volume element (RVE) of the microstructure under homogeneous boundary conditions. Normally, algorithms based on either the finite element method or the fast Fourier transform are used to solve the boundary value problem.

An RVE is a statistical representation of the microstructure of a polycrystal, usually described by the grain size and shape distributions and the crystallographic orientations of the single crystals. RVEs have to be large enough to provide an accurate statistical representation of the polycrystalline microstructure that leads to effective properties that are independent of the size of the RVE. The RVE discretizations can be classified according to the finite element type employed for meshing the microstructure geometry into voxel-based (hexahedral elements) and tessellated (tetrahedral elements) RVEs. Traditionally, the polycrystals have been commonly discretized by voxels or cubic elements, which generally provide higher accuracy and convergence rates. However, as shown in Fig. 1.6 (a), this discretization leads to a stair-stepped appearance at GBs. Conversely, Voronoi tessellation consists of a subdivision of the 3D space into convex polyhedra that intersect at their flat boundaries. Hence, tetrahedral elements can more naturally adapt to curved and irregular surfaces providing a smoother interpolation of the GB geometry, as shown in 1.6 (b). For this reason, when comparing simulation results to experimental observations of GBs, using tetrahedral elements can lead to a closer alignment in terms of surface geometry and appearance. However, Voronoi tessellations are not always able to reproduce the actual grain size distribution, and weighted Voronoi tessellations are used instead.

Crystal plasticity models are based on the multiplicative decomposition of the deformation gradient, $\mathbf{F}$, into its elastic ($\mathbf{F^e}$) and plastic ($\mathbf{F^p}$) components as follows,

$$\mathbf{F} = \mathbf{F}^e \cdot \mathbf{F}^p \tag{1.5}$$

where $\mathbf{F^p}$ is called the intermediate or relaxed configuration. The velocity gradient can be decomposed as

$$\mathbf{L} = \dot{\mathbf{F}} \cdot \mathbf{F^{-1}} = \mathbf{L^e} + \mathbf{F^e} \cdot \mathbf{L^p} \cdot \mathbf{F^{e^{-1}}} \tag{1.6}$$

where $\dot{\mathbf{F}}$ represents the total derivative of the deformation gradient with respect to time. Writing $\mathbf{L^e}$ and $\mathbf{L^p}$ in the form of Eq. 1.6 leads to:

$$\mathbf{L^e} = \dot{\mathbf{F}}^\mathbf{e} \cdot \mathbf{F^{e^{-1}}}, \ \mathbf{L^p} = \dot{\mathbf{F}}^\mathbf{p} \cdot \mathbf{F^{p^{-1}}}. \tag{1.7}$$

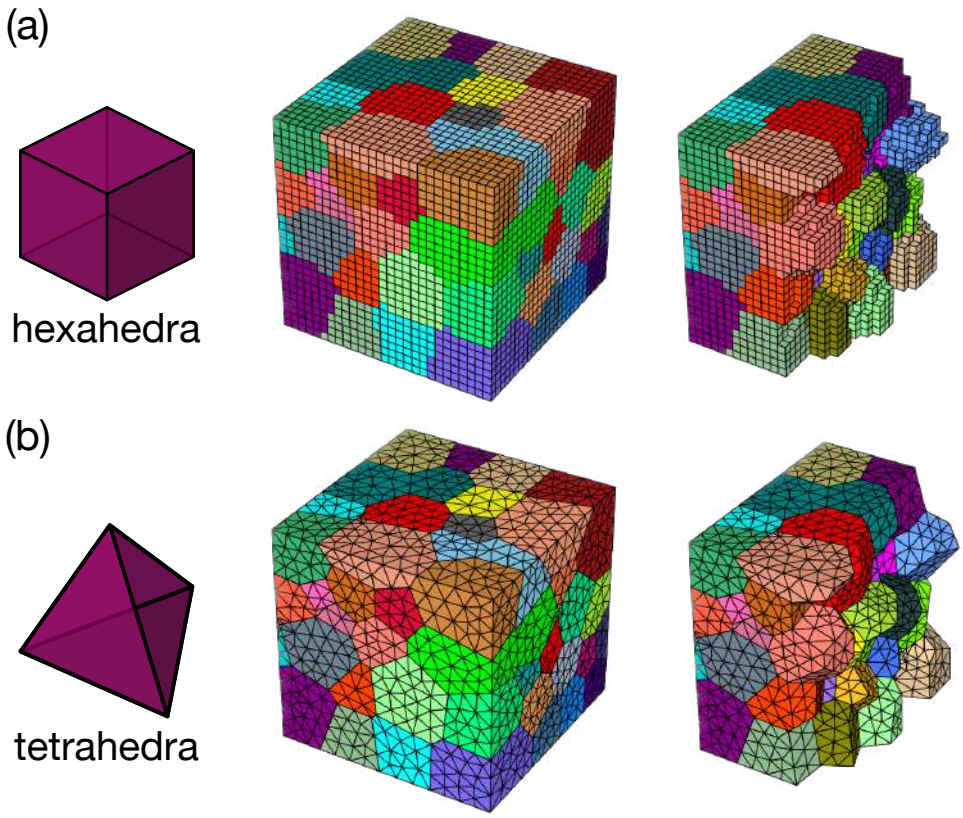

Figure 1.6: Different RVE discretizations for the same microstructure with 100 equiaxed grains generated with the open-source software Neper [146]. (a) RVE discretized with hexahedral or voxel elements. (b) RVE discretized with tetrahedral elements.

The evolution of the plastic deformation gradient $\mathbf{F}^{\mathrm{P}}$ is assumed to arise only from dislocation slip. Thus, the rate of the plastic velocity gradient $\mathbf{L}^{\mathrm{P}}$ in a grain depends on the sum of the slip rates $\dot{\gamma}^{\alpha}$ from all the slip systems α according to

$$\mathbf{L}^{\mathrm{P}} = \sum_{\alpha} \dot{\boldsymbol{\gamma}}^{\alpha} (\boldsymbol{s}^{\alpha} \otimes \boldsymbol{m}^{\alpha}) \tag{1.8}$$

where $\mathbf{s}^{\alpha}$ and $\mathbf{m}^{\alpha}$ denote the unit vectors in the slip direction and in the perpendicular direction to the slip plane, respectively.

Crystal plasticity models usually use phenomenological expressions to define the slip rates and the evolution of the internal variables. The evolution of plastic slip in a slip system α is commonly defined by a power-law dependency according to

$$\dot{\gamma^{\alpha}} = \dot{\gamma}_0 \left(\frac{|\tau^{\alpha}|}{\tau_c^{\alpha}} \right)^{\frac{1}{m}} sgn(\tau^{\alpha}) \tag{1.9}$$

where $\dot{\gamma}_0$ stands for the reference shear strain, m is the strain rate sensitivity parameter, ${\tau_c}^{\alpha}$ is the CRSS, and τ^{α} is the resolved shear stress on the slip system α. The latter can be

expressed as the projection of the Piola-Kirchhoff stress, $\mathbf{S}$, on the current slip system α, given by

$$\tau^{\alpha} = \mathbf{S} : (\mathbf{s}^{\alpha} \otimes \mathbf{m}^{\alpha}) \tag{1.10}$$

The boundary conditions applied to the RVE constitute a crucial aspect of full-field computational homogenization. Periodic boundary conditions are often applied because they reproduce the mechanical behavior of an infinite media constructed by a periodic arrangement of the RVE, assuming that it deforms as a jigsaw puzzle.

Nevertheless, the standard crystal plasticity models assume that GBs are transparent for slip transfer, and thus, the effect of GBs on the mechanical behavior of polycrystals has not been usually considered. Two strategies have been employed to account for the effect of GBs in crystal plasticity simulations through the increase of dislocation density near GBs: strain gradient crystal plasticity (SGCP) and physically based crystal plasticity.

The effect of the plastic heterogeneities in the mechanical response of a crystal was first rationalized by Nye and Ashby [9, 133] as a result of the interaction between statistically stored dislocations (SSDs), which evolve from random trapping processes during plastic deformation, and geometrically necessary dislocations (GNDs) induced by the presence of plastic strain gradients. The contribution of GNDs depends on the grain size and concentrates at GBs, whereas the density of SSDs is size-independent. Other theoretical approaches also provided a rational explanation of the Hall-Petch law [72, 143] with a grain representation formed by a soft core surrounded by a hard shell around the GB [83, 96]. From the modeling viewpoint, the most common approach to account for the effect of plastic strain heterogeneities in the material response is by introducing the influence of some plastic strain gradient measure in the constitutive equation, leading to the so-called strain gradient plasticity. Thus, strain gradient crystal plasticity simulations can account for the effect of GBs through the density of GNDs generated near the boundaries due to deformation incompatibility between grains with different crystallographic orientations. Different investigations have used this approach to analyze the effect of grain size on the strength of polycrystals [4, 17, 20, 40, 53, 105]. A recent investigation carried out by Haouala *et al.* [77] predicted the effect of grain size on the flow stress of various FCC polycrystals by means of strain gradient crystal plasticity and fast Fourier transformation (FFT) homogenization. Even though these simulations could capture the Hall-Petch effect on the flow stress due to the generation of GNDs, these simulations assume that all GBs behave as fully opaque to dislocations, so the slip transfer phenomenon at low-angle GBs is not taken into account.

Physically-based crystal plasticity models introduce the effect of GBs through the increase of dislocation density near the GB due to the accumulation of dislocations. In particular, the model developed by Haouala *et al.* and Rubio *et al.* for FCC polycrystals ([78], [151]), succeeded in predicting the grain size effect on the mechanical response of Cu, Al, Ag, and Ni polycrystals. The mechanical behavior of the crystals was modeled by a dislocation-based, rate-dependent crystal plasticity model in which the hardening of the slip systems follows the Taylor model [175]. The dislocation generation and annihilation in each slip system were controlled by a modified Kocks-Mecking model [97], which took into account the distance to the nearest GB in each slip system, so the dislocation density

increased near GBs. Interestingly, despite this model was able to capture the Hall-Petch effect in polycrystals, the predictions overestimated the strength of the polycrystals when the average grain size was < 20 μm. It was argued that the differences between experimental data and simulation results arose because all GBs were assumed to be opaque to dislocations. Haouala *et al.* updated this dislocation-based crystal plasticity model in order to account for slip transfer in pure Al bicrystals [76]. Different bicrystal orientations were studied in grains oriented for single and double slip, including fully transparent, fully opaque, and partially transparent GBs in the simulations. The addition of the slip transfer criteria in the model led to stress relaxation at the GB when it was suitably oriented for slip transfer ($m' > 0.95$), whilst high stress and dislocation densities were still observed when the alignment was poor.

1.5 Objectives

The present thesis aims to provide a quantitative understanding of the effect of grain boundaries (GBs) on the mechanical properties of metallic polycrystals through a combination of experiments and numerical simulations. From the experimental viewpoint, the experimental evidence has not yet provided robust criteria that can accurately predict slip transfer in polycrystalline materials due to the existence of a non-negligible number of outliers that do not follow the predictions from the classical geometrical criteria. These limitations are associated with the difficulties of assessing the actual active slip system, the GB geometry in 3D, and the local stress state. From the simulation viewpoint, the most widely used strategy to model polycrystal deformation is based on crystal plasticity simulations, which usually assume that all the GBs are transparent. Recent works have assumed that all GBs are opaque to predict the flow stress of polycrystals [76, 77], but models that include slip transfer and blocking are not available.

These limitations have been addressed as follows:

1. Experimental analysis of slip transfer was performed in pure Ni (FCC) and pure Ti (HCP) thin foils to avoid the effect of alloying elements or second phases in the dislocation-GB interactions. A large number of GBs were analyzed after plastic deformation, and the occurrence of slip transfer/blocking was registered. In order to overcome the main limitations of the standard slip transfer analysis procedures, the experiments were performed through a combination of different techniques, such as EBSD-based slip trace analysis, laboratory-scale diffraction contrast tomography (LabDCT), and high-resolution digital image correlation (HRDIC). LabDCT was employed to include the effect of 3D GB geometry on slip transfer, and HRDIC was used to account for the effect of the local stress state around GBs. The large and accurate database of slip transfer/blocking events was used to validate/disprove the accuracy of the geometrical criteria for slip transfer across GBs available in the literature.

2. An existing crystal plasticity model [76] was extended to include the effect of slip transfer on the mechanical behavior of FCC and HCP polycrystals. Different geometrical slip transfer criteria were successfully implemented and provided better agreement against experimental data of the tensile response of well-annealed polycrystals found in the literature. Subsequently, the effect of slip transfer on intragranular fracture was studied through the insertion of cohesive surfaces at the GBs of thin foil RVEs.

This thesis is structured as follows. After the introduction, the experimental work is presented in Chapters 2-5. Chapter 2 deals with the experimental analysis of slip transfer in pure Ni. Chapter 3 shows the potential of the LabDCT technique to assess the microstructure of polycrystals in 3D. Chapters 4 and 5 present the slip transfer analysis in pure Ti introducing the effect of 3D GB geometry through LabDCT (Chapter 4), and of local stresses through HRDIC (Chapter 5). The modeling part of this work is presented in Chapters 6 and 7. Chapter 6 presents the extension of the dislocation-based crystal plasticity model to account for slip transfer at GBs in FCC and HCP materials and the

validation of the simulations against experimental data. Chapter 7 presents the workflow to include intragranular fracture in the crystal plasticity simulations and the influence of GBs in damage nucleation and propagation. Finally, the main conclusions and the future work and perspectives are summarized in Chapter 8.

2 Slip transfer at grain boundaries in Ni

2.1 Introduction

The microstructure of annealed Ni polycrystals presents two types of grain boundaries: regular GBs and twin boundaries (TBs). The presence of annealing twin boundaries provides more obstacles for dislocation glide, making plastic deformation more challenging. As reported by some works, TBs can have a strong effect on the localization of plastic deformation that can lead to premature fatigue crack initiation in Ni-based superalloys [168, 170, 195]. Annealing twins in nickel (Ni) exhibit a distinctive $60°$ rotation around the $<111>$ axis, creating a fixed crystallographic relationship between the twin and the matrix. These twins, which are essentially $\Sigma 3$ GBs, are induced by the low stacking fault energy in Ni and appear during solidification and annealing. TBs are low-energy GBs, and thus, they are thermodynamically favorable in comparison with regular GBs.

The matrix-twin interface in TBs can be coherent or incoherent [28, 138, 164]. Coherent TBs maintain a consistent crystallographic orientation with the Ni matrix, resulting in a seamless lattice alignment with mirror symmetry across the boundary. The continuous alignment between the atomic planes across a coherent TB typically results in straight-sided bands that run across grains (see twin 1 in Fig. 2.1). These bands have a twinned orientation relative to their neighboring grain, and the parallel boundaries coincide with a $\{111\}$ twinning plane. In contrast, incoherent TBs appear at the twin ends when the annealing twins do not sufficiently grow to go through the entire parent grain size. As shown in Fig. 2.1, the perpendicular segment that joins the two coherent parallel TBs in twin 2 is incoherent with the lattice matrix and leads to a high lattice misfit and high boundary free energy.

Slip transfer in Ni-based superalloys has been analyzed in several investigations. A combination of EBSD and HRDIC was employed by Abuzaid *et al.* [2] to capture the formation of pile-ups at GBs (indicative of slip blocking) or the transmission of strains across the GB (indicative of slip transfer). This latter behavior was associated with small values of Δb, which seemed to be the best predictor of slip transfer, particularly for coherent TBs where $\Delta b = 0$ was associated with slip transfer via cross-slip. Genée *et al.* [62] analyzed

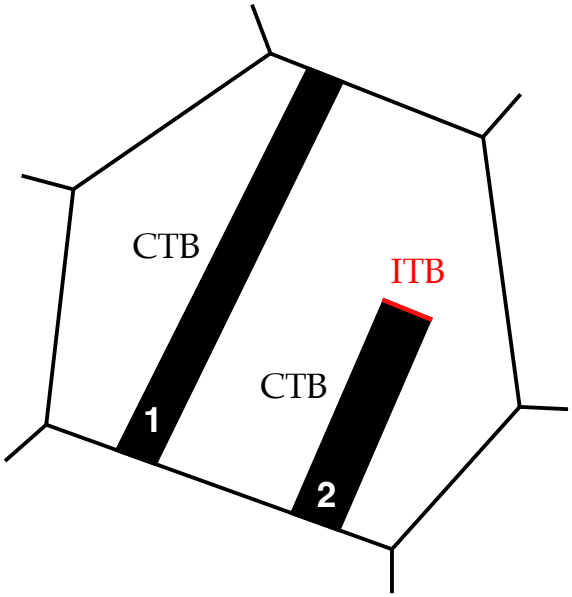

Figure 2.1: Schematic representation of two annealing twins in a Ni grain, where twin 1 is composed of two parallel coherent TBs (CTB) and twin 2 is composed of two parallel coherent TBs (CTB) and one incoherent TB (ICB).

slip transfer in another Ni-based superalloy using EBSD and concluded that the necessary condition for slip transfer at coherent TB was given by θ = 0° (as opposed to the other possibility θ = 60°). Regarding regular GB, they observed that slip transfer was favored by small values of κ and ψ. They could not, however, provide a criterion because of the experimental scatter, which was attributed to the influence of the twist angle θ, which cannot be determined from the EBSD information for regular GBs. Finally, Sperry *et al.* [167] also combined EBSD with HRDIC to study slip transfer in another Ni-based superalloy. They concluded that slip transfer in regular GBs was associated with low misorientation angles, and it was maximum when $m' = 0.78$ in twin boundaries.

These investigations on slip transfer in various Ni-based superalloys have not provided a quantitative unified geometrical criterion, possibly due to the choice of different slip transfer criteria and the differences between the alloys used in each investigation. Moreover, the strengthening effect provided by the alloying elements in Ni-based superalloys hinders the development of slip bands compared to pure Ni, where larger datasets of slip blocking/transmission events can be obtained.

To overcome the limitations of previous investigations, slip transfer/blocking was analyzed in more than 200 regular and twin boundaries of pure Ni foils. The standard conventional slip trace analysis workflow was employed as a starting point for the experimental slip transfer assessment. The objective was to rationalize the previous results obtained in Ni-based superalloys and to provide robust geometrical criteria for slip transfer that can be later incorporated within the framework of crystal plasticity simulations.

2.2 Material and experimental techniques

Slip transfer across GBs and TBs was analyzed in high purity (99.999%) Ni foils of 1 mm in thickness manufactured by rolling, which were purchased from Goodfellow. Two dogbone micro-tensile specimens with a central gauge section of 6×2 mm^2 were manufactured by electro-discharge machining (Fig. 2.2), with the tensile axis oriented at 0° and 45° from the foil rolling direction.

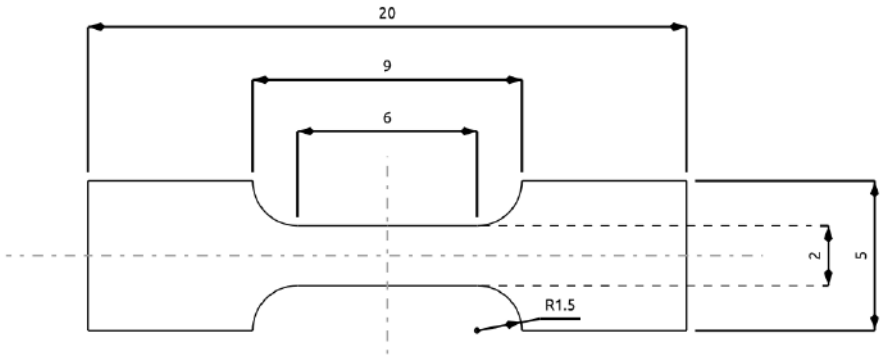

Figure 2.2: Dogbone tensile specimen of Ni. dimensions in mm.

The as-received foil was manually polished with synthetic cloths and 6-3-1 μm diamond paste and etched with Kalling's 2 reagent to reveal the microstructure (Fig. 2.3). The average grain size was 186 ± 31 μm. The as-received microstructure was irregular with wavy GBs, and thus the samples were heat treated to promote grain growth and homogenize the grain shape. To this end, they were encapsulated in quartz tubes filled with high-purity Ar (to prevent oxidation) and annealed at 800 °C for 30 minutes in a tubular vacuum furnace. EBSD maps of the gauge section were obtained after metallographic preparation of the surface of the samples by manual grinding followed by electropolishing using a nitric acid-methanol solution (20% volume of HNO_3) at -30°C and 20 V. Four micro indentations were placed in the central region of the gauge to ease the orientation and alignment of the samples inside the microscope.

EBSD maps were acquired at the upper and bottom surfaces of the gauge length of the sample. The crystallographic orientations were obtained in a FEI Helios NanoLab 600i dual-beam microscope equipped with an Oxford Instruments EBSD detector. The whole gauge length was mapped with 3×5 overlapping maps, followed by stitching in AZtec. The EBSD maps were acquired at 20 kV and 2.7 nA, with a step size of 3.4 μm, in order to accurately resolve the microstructural features. The overall quality of the EBSD maps was above 95% indexing. The maps were post-processed with the MTEX Matlab Toolbox [14] with a grain boundary misorientation threshold of $5°$.

The samples were tested *ex-situ* under uniaxial tension in a Kammrath and Weiss microtensile testing machine using a 10 kN load cell up to $\approx 5\%$ strain at a strain rate of $\approx 10^{-3}$ s^{-1}. The micro tensile test of the sample along the rolling direction is plotted in Fig. 2.4.

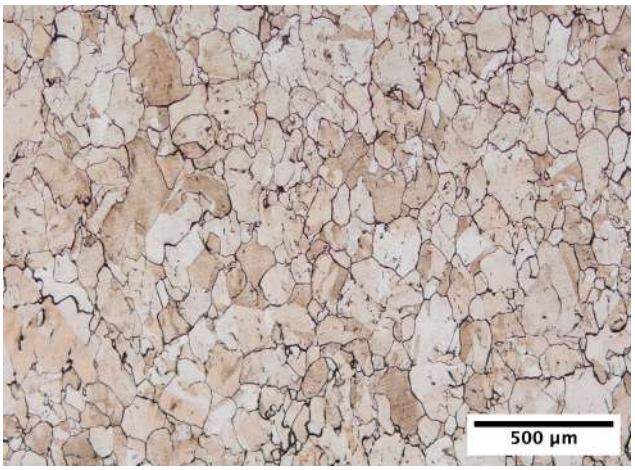

Figure 2.3: Microstructure of the as-received Ni foil, after metallographic preparation and chemical etching with Kalling's 2 reagent.

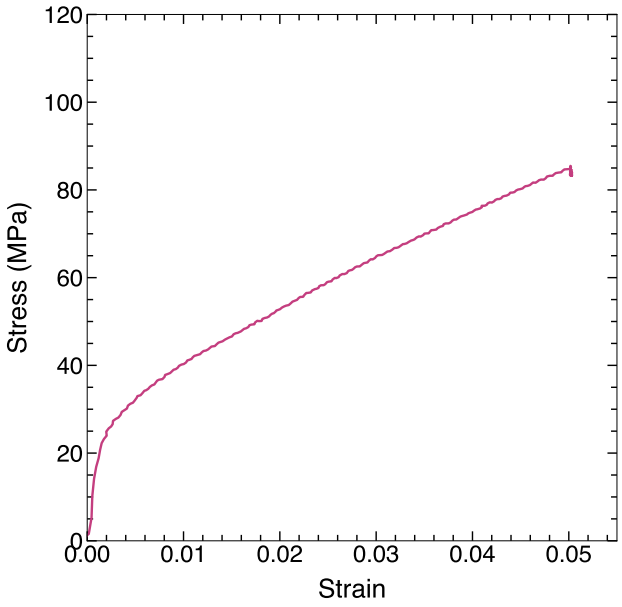

Figure 2.4: Stress-strain curve of the Ni sample deformed along the rolling direction (Fig. 2.5(a)).

SEM imaging was performed after deformation all over the sample surface employing the circular backscatter detector (CBS) to obtain the optimum balance between brightness and contrast to resolve slip traces and identify slip transfer/blocking across GBs. The active slip systems in the grains after deformation were identified by means of conventional slip trace analysis [7, 24]. This technique compares the spatial orientation of the theoretical slip bands calculated from the crystal orientation before deformation (obtained by EBSD) with the experimental ones shown by SEM. The theoretical slip traces were calculated from the EBSD crystal orientations with a Matlab code [24]. In the case of Ni, slip takes place on the $\{111\}$ close-packed planes along the $<110>$ close-packed directions, which results in

12 possible slip systems, as depicted in Table 1.1. Since each of the directions is common to two $\{111\}$ planes, three possible slip systems exist within the four possible slip planes. The deviations in the orientations between the theoretical and the experimental slip traces were always $< 5°$.

2.3 Results and discussion

The EBSD maps of the Ni foils after annealing revealed random texture and a very wide grain size distribution comprised of very large grains (of the order of mm) and clusters of smaller grains (Fig. 2.5). The average grain size was 240 ± 250 μm. In addition, many annealing twins were found throughout the microstructure. There were no significant differences between the samples mechanized at $0°$ and $45°$ from the rolling direction, and hence, no further distinction is made between both specimens

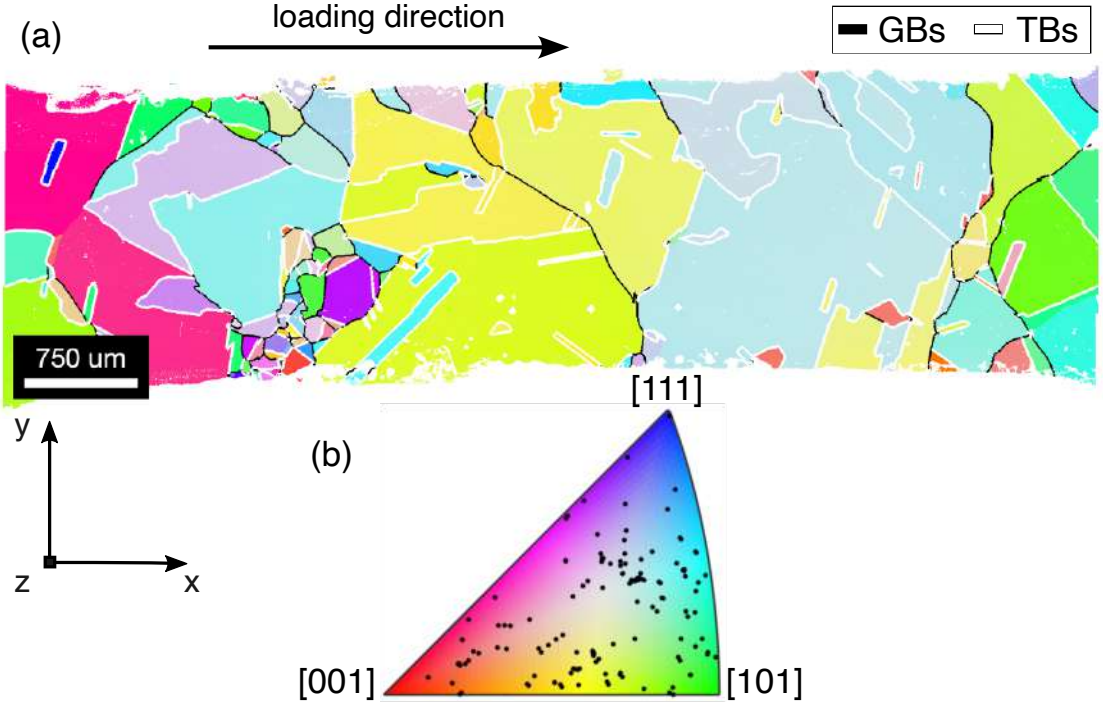

Figure 2.5: (a) EBSD map of the surface of the dogbone specimen parallel to the rolling direction. TBs (which are associated with a misorientation angle Θ of 60°) are drawn with white lines, while regular GBs are drawn with black lines. (b) Inverse pole figure with respect to the z axis, where each grain mean crystallographic orientation is represented by a black dot.

Slip transfer was analyzed in more than 200 GBs. After deformation and inspection of the slip traces in each grain, GBs were classified into two groups: boundaries where slip transfer was convincingly observed and boundaries where slip transfer was not observed. Convincing slip transfer was considered when the incoming and outgoing slip traces across a GB were continuous and clearly correlated, while negligible topography along the GB was observed, indicating relatively homogeneous deformation between the grains (Figs.

2.6 (a), (c) and (d)). Furthermore, the large number of annealing twins promotes the activation of the slip parallel to the TB in the so-called parallel slip configuration near TB [168, 169] (Fig. 2.6 (d)). The annealing twins can span the whole parent grain beginning at one boundary and ending at the opposite one, so the associated TBs are fully coherent with the matrix. However, sometimes the annealing twin does not reach the opposite boundary, leading to the formation of another TB (perpendicular to the coherent TB), which is incoherent [138, 164]. This is the case of Fig. 2.6 (d), in which the slip traces are parallel to the coherent TB (and, thus, neither slip transfer nor slip blocking occurs), and slip transfer is registered at the incoherent TB. Conversely, the slip blocking at GBs or TBs was indicated by the lack of continuity between the observed slip bands across the boundary, and this observation was reinforced by the existence of ledges or topography at the boundary, which is indicative of incompatibility of deformation between both grains (Fig. 2.6 (b)). In some cases, the impingement of the slip traces on a GB leads to the formation of micro volumes of deformation (Fig. 2.6 (e)), which appear due to a high density of dislocations, local crystalline rotations and/or grain boundary shearing, and also indicate that slip transfer is not possible [62].

The traces of the different {111} slip planes in each Ni grain on the specimen surface were obtained from a Matlab code from the crystallographic orientation of the grain provided by the EBSD scans obtained before deformation. It was assumed that the small lattice rotations induced by the applied deformation were negligible. To this end, the slip systems were rotated from the crystal to the sample reference frame using the orientation matrix computed from the Euler angles of the grain in Bunge convention. The trace orientation was computed from the cross-product between the slip plane normal and the z axis of the specimen in the sample reference frame.

The orientation of the traces for different slip systems was compared with the experimental slip traces (Fig. 2.6) to identify the active slip plane. Then, the SF for the possible slip directions in the active slip plane were determined assuming uniaxial tension from the stress tensor rotated to the crystal reference frame. Among the three possible slip systems sharing the active slip plane, it was assumed that deformation occurred in the one with the highest SF, which is a reasonable assumption given the absence of any information regarding the stress state in the microstructure [25, 197]. Once the two active slip systems across the GB or TB were identified, different metrics can be determined to assess whether they are able to predict slip transfer or blocking. Among them, the Luster-Morris parameter m' and the residual Burgers vector Δb have been used previously [2, 7, 82, 167] in metallic polycrystals. It should be noted that if slip traces were only visible in one grain across the boundary but not in the other, these GBs or TBs were not included in the analysis because it was not possible to identify the active slip plane in the latter grain.

The analysis of slip transfer/blocking included 133 regular GBs and 99 TBs (75 coherent and 24 incoherent). They showed that slip transfer mainly took place at GBs with low misorientation angle ($\Theta < 20°$) and in TBs, which present a misorientation angle of $\Theta = 60°$ (Fig. 2.7 (a)). The experimental results of slip transfer/blocking at boundaries are plotted in Fig. 2.7 (b) as a function of the Luster-Morris parameter m' and the misorientation angle. They show that slip transfer is strongly correlated with high values of m' and that slip

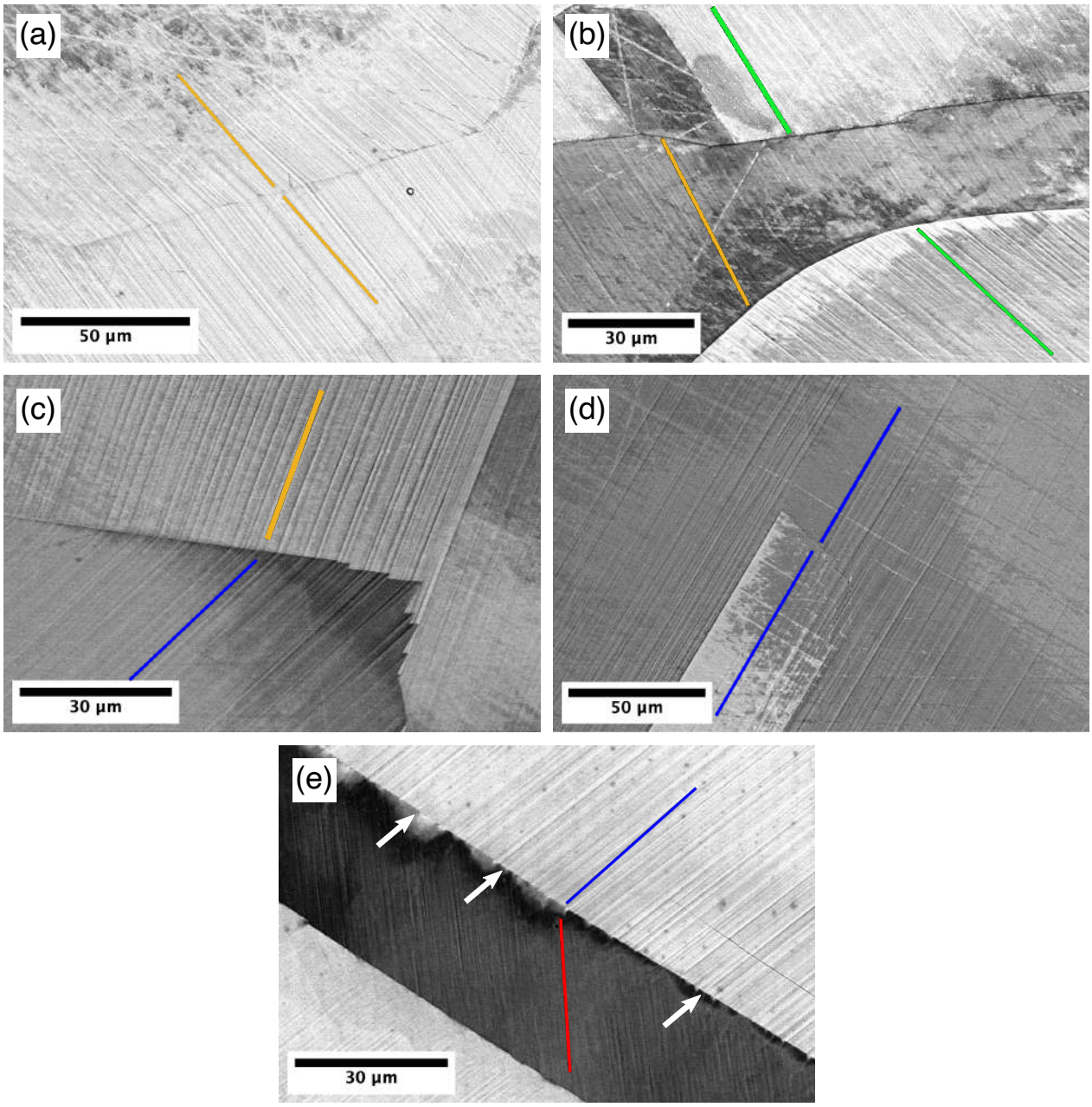

Figure 2.6: Examples of slip transfer and slip blocking at different GBs (a) Slip transfer across a regular GB. (b) Blocked slip at two regular GBs, supported by the slip trace discontinuity and the presence of a ledge. (c) Slip transfer across a coherent TB. (d) Slip transfer across the end of the twin boundary (incoherent TB). The slip bands in the parent grain and the twinned grain are parallel to each other and parallel to the twin boundary. (d) Blocked slip at a TB supported by the discontinuity between slip bands across the boundary and the formation of micro volumes (marked by white arrows). The orientation of the trace of the active slip system in each grain according to slip trace analysis is marked by solid lines, colored according to the active slip plane as indicated in Table 1.1.

transfer in GBs with a high misorientation angle (in the range $20° < \Theta < 60°$) was always associated with high m', which indicates a good alignment between the slip systems. However, it should be noted that slip blocking was observed in high-angle GBs even when m' was high. On the contrary, slip transfer was never observed when $m' < 0.65$. Thus, high m' seems to be a necessary condition for slip transfer at regular GBs but not sufficient, and this may be due to the influence of the twist angle θ that is unknown because it depends on the actual orientation of the GB across the sample thickness. However, the limited number of instances of slip blocking with high m' seems to indicate that the influence of θ is of second order compared to m'.

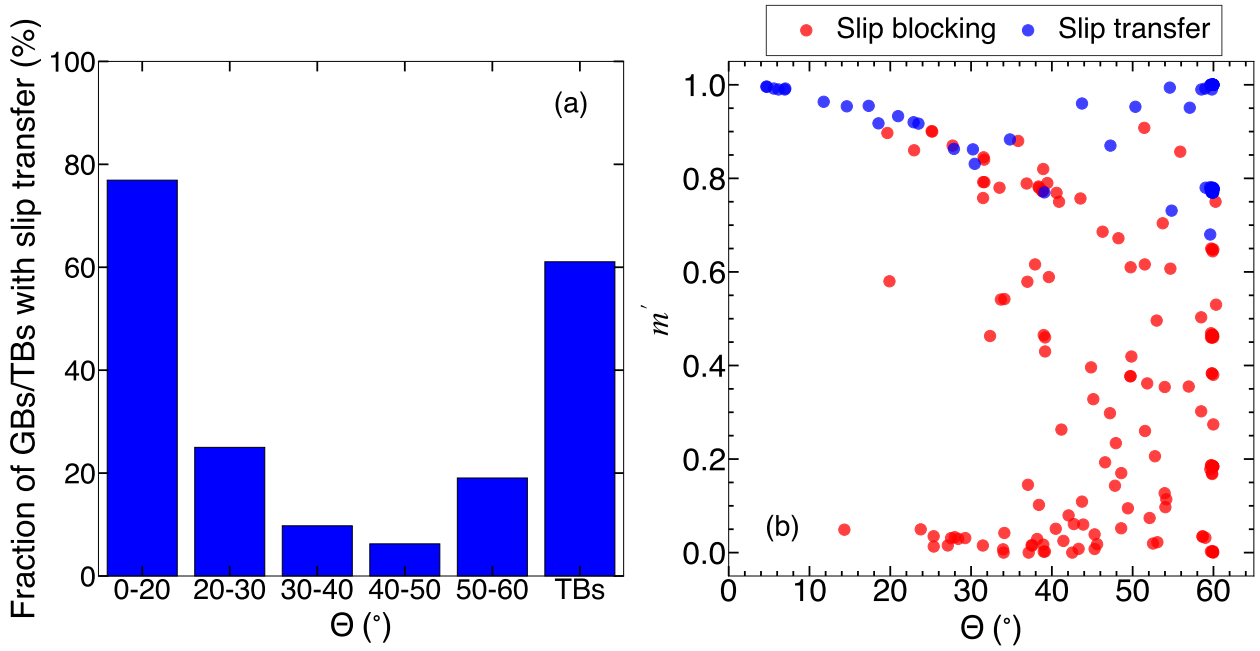

Figure 2.7: (a) Effect of the misorientation angle Θ on slip transfer for GBs and TBs. (b) Occurrence/absence of slip transfer across GBs and TBs as a function of the Luster-Morris parameter m' and the misorientation angle.

Regarding annealing TBs, slip transfer was observed in approximately 60%, and m' was either equal to 1 (32% out of the slip transfer instances across TBs) or 0.77 (remaining 68%). $m' = 1$ corresponds to slip transfer across an incoherent TB when the slip traces were parallel to the coherent TB (Fig. 2.6 (d)) while $m' = 0.77$ indicates that slip transfer took place at coherent TB between slip systems oblique to the TB (Fig. 2.6 (c)). The clustering of the slip transfer instances around these values of m' is a result of the limited number of combinations between incoming and outgoing slip systems across TBs due to the 60° rotation around <111>.

The performance of m' and Δb as metrics to predict slip transfer/blocking across GBs and TBs in Ni is depicted in Fig. 2.8. In the case of GBs, the evidence of slip transfer and slip blocking in 133 GBs is plotted in Fig. 2.8 and as a function of κ (which is related to Δb) and ψ (angle between the incoming and outgoing slip planes). Practically all the slip transfer instances are found in the lower-left corner of the figure, indicating that high values of

m' indicate a great likelihood of slip transfer. For instance, the criterion of $m' \geq 0.9$ for slip transfer (represented by a circular line in Fig. 2.8 (a)) correctly predicts 73% and 97% of the slip transfer and slip blocking events, respectively. If $m' \geq 0.75$ is chosen as the slip transfer criterion, 92% and 76% of slip transfer and slip blocking events are predicted correctly. Thus, $m' > 0.8$ seems to be an accurate criterion for slip transfer across regular GBs in Ni, similar to the results previously reported for Al [7]. The few experimental data about slip transfer/blocking that do not fulfill this criterion may be attributed to GBs with a very large twist angle θ, which impedes the slip transfer from one grain to the neighbor, but this factor seems to be of second order as compared with the role played by m'.

In the case of coherent and incoherent TBs (Fig. 2.8 (b)), slip transfer seems to be controlled by the angle between slip directions κ or, in other words, by the residual Burgers vector Δb. Slip transfer was found in 43 coherent ($\psi \approx 39°$) and 21 incoherent TBs ($\psi \approx 0°$) when $\Delta b \approx 0$, and slip blocking was found in 35 coherent and incoherent TBs when $\Delta b > 0$. When ψ and κ were close to zero, slip transfer took place across the incoherent TB present in unfinished annealing twins by the nearly perfect alignment of the active slip systems in the parent and the twinned regions (Fig. 2.6 (d)). When the angle between slip plane normals ψ was not zero, slip transfer was only observed when κ (and, thus, Δb) was close to zero. Hence, slip transfer was independent of the angle between slip system normals ψ, indicating that the incoming and outgoing slip planes may have very different orientations. Obviously, this abrupt change in the slip plane orientation, together with a negligible residual Burgers vector, is indicative of slip transfer by dislocation cross-slip at the TB [2, 52]. In addition, the role played by the twist angle θ on slip transfer can be analyzed in the case of coherent TBs because the orientation of the boundary between parent grain and twin is perfectly defined from crystallographic rotation measured by means of EBSD. This angle was calculated as the angle between the projections of the slip plane traces onto the twin boundary plane as indicated by Zhai *et al.* [193].

$$\theta = \cos^{-1}(\boldsymbol{n}_{TB} \times \boldsymbol{n}_A \cdot \boldsymbol{n}_{TB} \times \boldsymbol{n}_B) \tag{2.1}$$

where $\boldsymbol{n}_{TB}$ is the normal to the coherent TB and $\boldsymbol{n_A}$ and $\boldsymbol{n_B}$ stand for the slip plane normals to the incoming and outgoing slip systems, respectively.

As shown in Fig. 2.8 (c), only two twist angles, θ = 0° and 60° can be found in these coherent TBs. Slip blocking was found in the 24 TBs with θ = 60° while 43 of the 51 TBs with θ = 0° showed slip transfer. The latter corresponds to those TBs whose residual Burgers vector is close to 0, indicating that small values of Δb stand for the necessary condition for slip transfer in annealing TBs in Ni, and cross-slip is the physical mechanism responsible for slip transfer.

2.4 Conclusions and limitations

Slip transfer/blocking was analyzed in more than 200 GBs in two polycrystalline pure Ni samples by means of conventional slip trace analysis. The workflow for slip transfer assessment coupling EBSD orientation mapping and SEM imaging was successfully

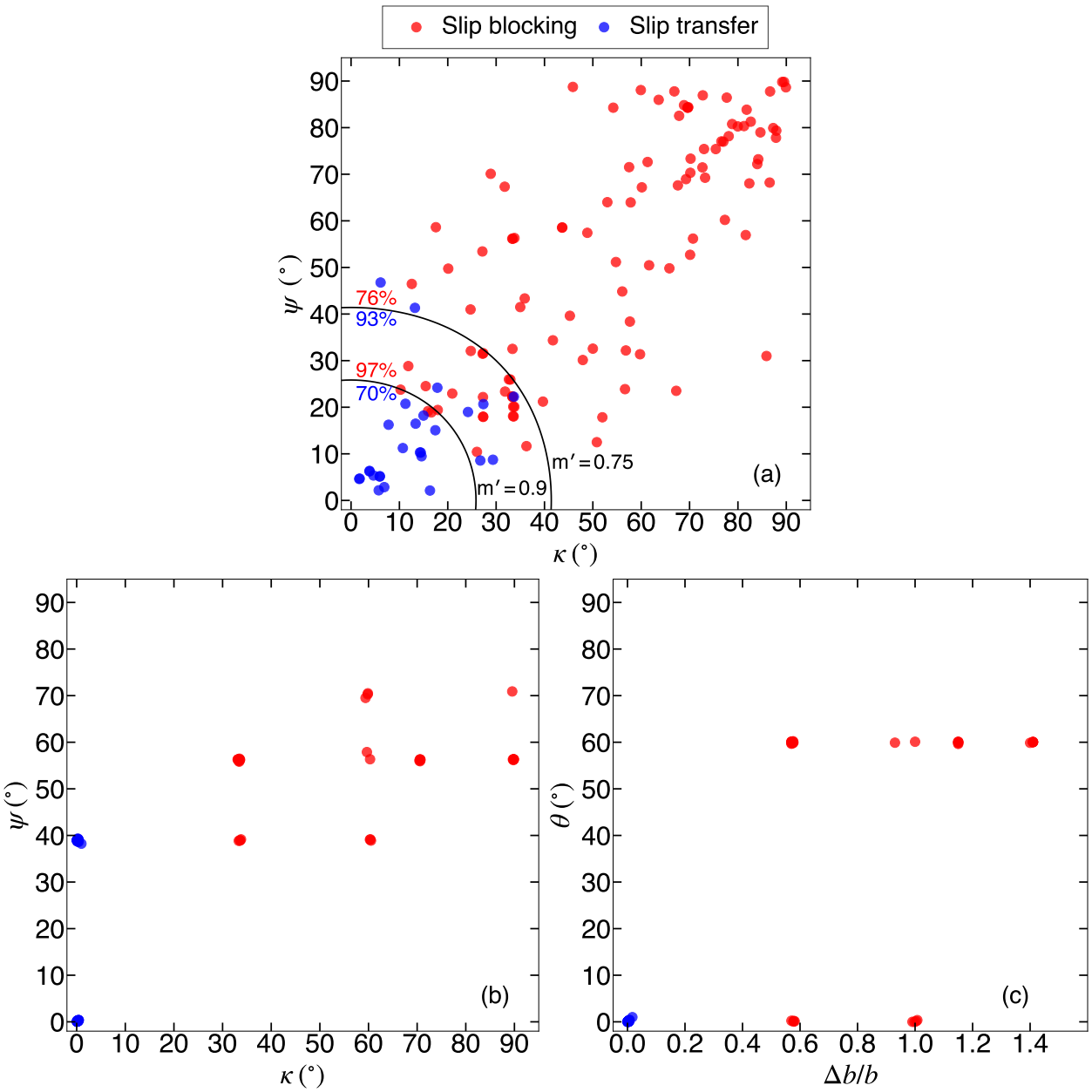

Figure 2.8: Geometrical criteria for slip transfer in Ni. (a) Regular GB. (b) Coherent and incoherent TBs. (c) Coherent TB.

established. The main conclusions of this chapter read as follows:

- Slip transfer at coherent and incoherent TBs is controlled by the residual Burgers vector and takes place when $\Delta b \approx 0$, regardless of the angle between slip normals and the twist angle between the incoming and outgoing slip planes. In this latter case, slip transfer seems to be controlled by dislocation cross-slip.
- In the case of regular GBs, slip transfer is very likely to occur across low-angle regular GBs if the Luster–Morris parameter $m' > 0.8$, and it is unlikely to take place

otherwise.

Nonetheless, although m' seems to be a good predictor for slip transfer across regular GBs in pure Ni (Fig. 2.8 (a)), there is a significant number of slip blocking instances when $0.75 < m' < 0.9$. Moreover, slip can transfer in some cases where the misorientation angle is rather high ($\Theta > 30°$) (Fig. 2.7). This behavior could be caused by different reasons that arise from the main limitations of the slip trace analysis technique, as stated in Sec. 1.3. Firstly, the active slip system is assumed to be that with the highest SF among the three possible slip systems in each slip plane. This is a reasonable assumption, especially in FCC metals whose plastic deformation is rather isotropic, but it is not guaranteed and may lead to errors.

Secondly, the lack of knowledge about the 3D GB geometry across the thickness of the sample impedes the assessment of the effect of the twist angle θ on slip transfer across regular GBs. Some experimental investigations have revealed that the θ angle may affect the occurrence of slip transfer across GBs even though the slip systems (between incoming and outgoing grains) are well aligned.

Finally, the conventional slip trace analysis does not provide information regarding the local stresses or the local strain heterogeneity in the microstructure during plastic deformation, which may also play an important role in promoting or impeding slip transfer.

3

3D grain mapping by means of Diffraction Contrast Tomography (DCT)

3.1 Introduction

The lack of knowledge about the 3D GB geometry across the thickness of a polycrystalline sample significantly biases the studies that assess the occurrence of slip transfer across GBs. As mentioned in the previous chapters, the GB inclination can affect the likelihood of slip transfer in FCC and HCP metals [108, 154]. However, most of the experimental techniques available to three-dimensionally characterize microstructures are destructive and very time-consuming, thus limiting the number of GB that can be examined.

X-ray Diffraction Contrast Tomography (DCT) has emerged as an alternative novel technique to map the crystal orientation of the grain in 3D in a non-destructive manner. DCT has been widely used to obtain grain orientations with a parallel beam (synchrotron source) [89, 117], and with a cone beam (X-ray tube source) at the lab scale [56, 93, 123, 132, 198]. More recently, Lab-based DCT (LabDCT) has proven to be an attractive option since it is more accessible than synchrotron-based DCT, and it lends itself to experiments requiring longer timescales.

The LabDCT technique was first used by King *et al.* [93] to capture the grain shape, location, and orientation in a metastable β-titanium alloy Ti21S (Tiβ21S) sample. The 3D grain maps obtained from the LabDCT technique were compared to the grain maps obtained from Phase Contrast Tomography (PCT) data, and a good agreement was reported between the two approaches. These findings led to a great amount of interest in the development of the LabDCT experimental setup. A few years later, McDonald *et al.* [123] used the LabDCT technique to map grain shape and orientations in a similar Tiβ21S sample. The authors also compared the grain orientations obtained from LabDCT scans with those obtained from EBSD data for a small polished region near the top surface of the sample. While the EBSD-DCT comparison was limited to a total of five grains, the results showed great promise for the analyses of grain maps using lab-scale X-ray equipment.

The unique combination of a lab-scale commercial X-ray computed tomography (XCT)

setup and the LabDCT technique made 3D grain maps available to a wider range of researchers. In the following years, the LabDCT technique was used to study the sintering of copper metal powder [122], recrystallization of production steel [172], grain orientation and shape in non-metallic materials [84], impurities in polycrystalline silicon [92], liquid metal embrittlement and grain growth mechanisms in steel samples [173], and corrosion in Al alloys [196, 198]. Bachman *et al.* [13] further advanced the LabDCT analyses technique and developed a fast and more accurate geometric indexing algorithm to capture the grain orientation and morphology from the diffraction data, and Niverty *et al.* [132] presented a new forward-modeling approach for the refinement of LabDCT grain reconstructions via an iterative reconstruction process thereby increasing fidelity of grain maps obtained from LabDCT. Recent developments in advanced LabDCT acquisition approaches have brought larger and more challenging geometries within the reach of LabDCT [134, 171]; however, no studies exist in the literature that systematically and quantitatively assess the use of these advanced LabDCT acquisition strategies and compare them to the conventional LabDCT approaches.

In this chapter, a detailed analysis of the grain maps is presented for a pure Ti sample by means of the tried-and-tested conventional LabDCT (C-DCT) acquisition approach and the more recent helical phyllotaxis LabDCT (HP-DCT) acquisition approach. The DCT-based grain maps were compared with those obtained on the surface from ground-truth EBSD and SEM data. Furthermore, the quality of grain reconstructions, grain orientations, GB misorientations, grain shapes, and grain morphology have been quantitatively assessed.

3.2 Materials and methods

3.2.1 Titanium sample

The sample used in this study was obtained from a 99.99% pure Ti foil with a thickness of 0.25 mm (purchased from Goodfellow). A micro-tensile specimen with a $5 \times 1\ mm^2$ central gauge section was machined by electro-discharge machining. The sample was subsequently annealed at 850° for eight hours to promote grain growth in a tubular vacuum furnace under continuum vacuum to prevent oxidation.

The central region of the gauge section was characterized using both SEM and EBSD. The EBSD map of the central gage section was obtained after metallographic preparation of the sample surface by electropolishing using Struers A3 electrolyte at room temperature and 38 V. The EBSD map was acquired using a FEI Helios NanoLab 600i dual beam microscope equipped with an Oxford Instruments EBSD detector at a voltage of 20 kV and a current of 2.7 nA. The step size was 3 μm to obtain good geometrical accuracy, and the overall indexing was above 95%. The EBSD map was post-processed using the open-source MATLAB toolbox MTEX [14], and the data was cleaned using a spline filter to fill non-indexed points. The threshold misorientation for grain reconstruction was set to 0.5°. In addition to the EBSD map, a lower resolution full field of view SEM scan of the central gauge region was also acquired using a Thermo Scientific Apreo 2 SEM at 20 kV and 1.6

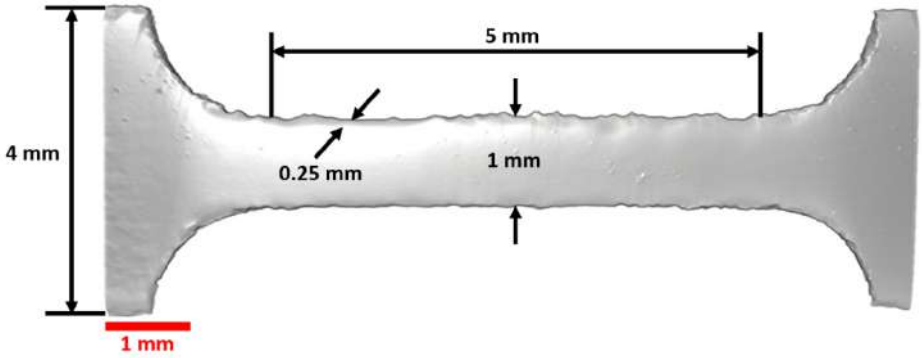

Figure 3.1: Pure Ti sample prepared using electro-discharge machining followed by annealing in vacuum at $850°$.

nA with the concentric backscatter detector (CBS) to resolve the grain boundaries on the surface of the sample.

3.2.2 Diffraction Contrast Tomography (DCT)

The DCT scans of the Ti sample were carried out in a lab-scale X-ray microscope (Zeiss Xradia Versa 620) equipped with DCT capabilities [122–124, 132, 198]. The schematic of the LabDCT setup is shown in Fig. 3.2. The sample was illuminated with a W lab source. The diffraction spots emanating from the sample were captured using a near-field detector. The Ti sample used in this study was positioned in such a manner that it was equidistant from the X-ray source and the detector (Laue Focusing Geometry) with both a source-to-sample (L_{ss}) and sample-to-detector (L_{sd}) distance of 14 mm. The spots created in a LabDCT setup with Laue Focusing Geometry tend to be shaped like elongated streaks due to astigmatic magnification caused by the polychromatic beam with a conical geometry [93]. This allows us to get a high photon count for each diffraction spot at the detector, thereby reducing the exposure time needed for each projection. Conventional DCT (C-DCT) scans are generally carried out by illuminating different orientations of the sample ($0 - 360°$) while keeping the samples fixed at a given height. In the case of a vertically extended sample (such as the one shown in Fig. 3.1), this process is repeated for different vertical sections of the sample by moving the sample vertically in discrete vertical steps, followed by a $360°$ rotation to obtain the diffraction projections at each vertical position (see Fig. 3.3). Generally, 181 diffraction projections at $2°$ interval rotation are captured for each vertical position. The combination of vertical movement followed by a $360°$ rotation is repeated until the entire region of interest is scanned. This approach, after the reconstruction of the grains, results in multiple grain maps, which are then stitched together to obtain the grain map of the entire sample.

In contrast, the sample is rotated and vertically translated to capture the entire sample in a single scan in helical phyllotaxis DCT (HP-DCT) scans. This scanning approach is ideal for the Ti sample used in this research since the central gauge section of the tensile sample is narrow enough to fit in the letterbox aperture's field of view but long enough that a

single C-DCT scan cannot capture the entire region of interest [134]. The different regions of the sample are illuminated by moving the sample in a helical phyllotaxis motion (see Fig. 3.3), which results in uniform angular coverage of the sample over the entire vertical extent. The sample is rotated by an increment of 137.5° and vertically translated following the recommendations by Xnovotech [188] for a minimum number of projections needed in the illuminated region of the sample for the forward modeling reconstruction analysis [13, 132]. Unlike the C-DCT scanning approach, the HP-DCT scanning approach allows the capture of grain maps of more challenging sample geometries without the need for stitching of individual grain maps. Furthermore, more uniform illumination of the sample is achieved with the incident x-rays due to the helical phyllotaxis motion, leading to a more efficient data collection than the C-DCT approach.

Table 3.1 presents a summary of the DCT scans carried out for this study. Both C-DCT and HP-DCT scans were carried out on the Ti sample at a source voltage of 160 kV and a source power of 15 W. A letter box aperture 250×750 μm in size was used to shape the incident x-rays on the sample. Each projection was captured with an exposure time of 180 s, which ensured a good signal-to-noise ratio for the diffraction spots. The C-DCT scan was carried out with 181 projections for each vertical position, and a total of 5 scans were performed to cover the central region of the sample (approximately 1 mm in length), with adjacent scans having an overlap of approximately 15%. This resulted in a total of 905 diffraction contrast projections for the conventional DCT scan. The same central region was also scanned with the HP-DCT approach with 680 projections.

Approach	Nb of segments	Source voltage (kV)	Source power (W)	Exposure time (s)	Nb of projections	Total scan time (h)[a]	Average grain completeness (%)
C-DCT	5	160	15	180	905[b]	45.25	81
HP-DCT	1				680	34	86

[a] Total scan time computed as the number of projections $\times$ exposure time per projection (180 s).

[b] Each section of the conventional scan was carried out with 181 projections, making the total number of projections for the targeted volume to be 905. An overlap of 15% was used between the adjacent scans to ensure enough space for alignment during stitching.

Table 3.1: Summary of DCT acquisition and reconstruction approach followed in the current study: scanning and reconstruction times for conventional DCT (C-DCT) and helical phyllotaxis (HP-DCT) and achieved average grain completeness values.

Once the scans were completed, the grain reconstructions from the captured diffraction data were carried out following the forward modeling approach [1, 13] using the fast geometric indexing reconstruction technique developed by Bachmann *et al.* [13] as implemented in GrainMapper3D 3.0 [188]. Fig. 3.4 shows a brief outline of the forward modeling approach. The same reconstruction approach was used for both conventional and helical phyllotaxis DCT reconstructions. For the filtration process, a rolling median filter was applied to the projections to enhance the contrast of the diffraction spots, followed by a grey level-based thresholding for segmentation of the diffraction spots. The four strongest lattice planes of the HCP Ti crystal structure with a c/a ratio of 1.587 were

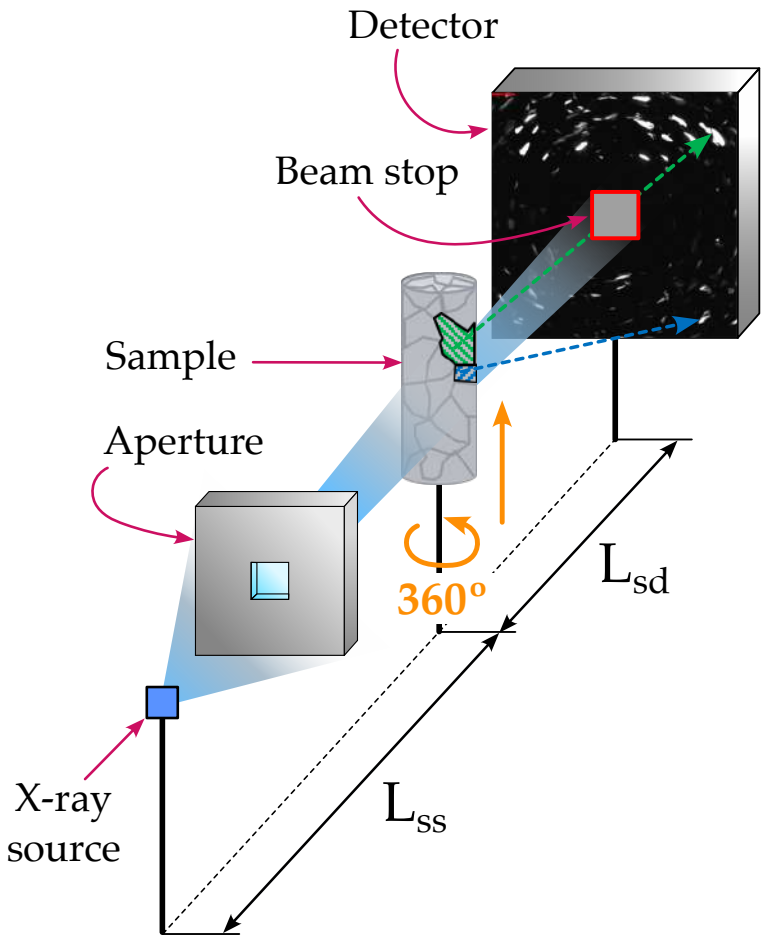

Figure 3.2: LabDCT acquisition set-up using a conical beam source.

used for the grain indexing. The initial reconstructions were iteratively refined by adjusting the source and detector distances in the forward model to minimize the horizontal and vertical distances between the observed and predicted diffraction spots (residuals). The iterations were carried out until no subsequent improvements were observed in the quality of the reconstructed grains (quantified using the completeness parameter). The number of iterations needed to refine the grain reconstructions was found to be similar for the C-DCT and HP-DCT datasets. The final grain reconstruction was carried out at a resolution of 5 $\mu m/\text{voxel}$. The total volume of the reconstructed sample was approximately 0.2 mm^3, while each section of the C-DCT scan had a volume of 0.045 mm^3.

Each conventional DCT scan took approximately 9 hours of acquisition time, while the reconstruction for each of these scans took approximately 10 hours. Therefore, each scan and reconstruction pair took approximately 19 hours to complete. The reconstructions were carried out using GrainMapper3D 3.0 on a Windows PC, with an Intel Xeon Silver 4144 processor with a clock speed of 2.19 GHz and a total RAM of 128 GB. Table 3.1 presents a summary of the scan and analysis time for the two acquisition strategies followed in this investigation. While the scan and analyses can be staggered in the case of the C-DCT approach, the iterative reconstruction process still requires significant manual input prior to

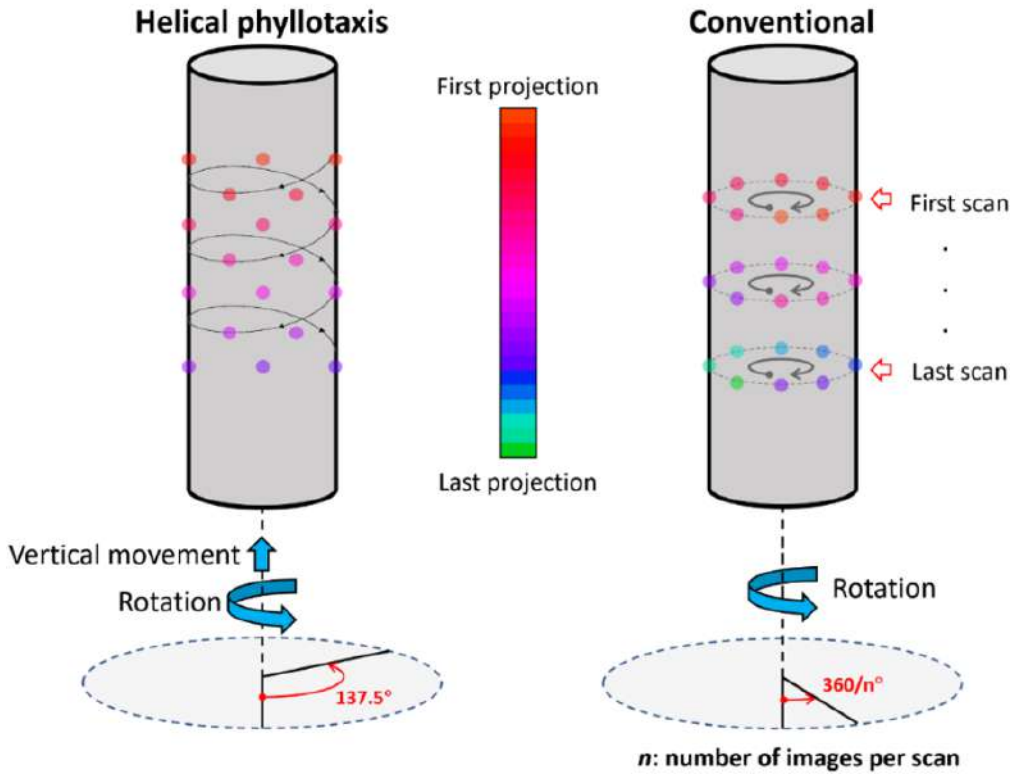

Figure 3.3: Acquisition of Lab DCT using stitched conventional DCT (C-DCT) scans and Helical Phyllotaxis DCT scans (HP-DCT) showing positions on the sample exposed to x-rays during a DCT scan.

the final reconstruction. Furthermore, due to the computationally intensive nature of the reconstruction process, only one reconstruction could be carried out at once. Additionally, the time needed for reconstruction optimization tends to be user-dependent, and it generally takes 30-40% of the entire reconstruction time, with the final reconstruction taking 60-70% of the reconstruction time. While the acquisition times were comparable for the C-DCT and HP-DCT scans in this study, the total reconstruction and analysis time for the C-DCT scan was found to be approximately 5 times that of the HP-DCT scan.

3.3 Results and discussion

The 3D grain reconstructions obtained from the HP-DCT and C-DCT scans are compared in this section, and the accuracy of the grain maps obtained from the two approaches is discussed. The grain orientations obtained from the DCT scans are compared with the ground-truth orientations on the surface of the sample obtained from EBSD data. The differences in GB misorientations between corresponding grains in the DCT and EBSD grain maps are also quantified. Finally, the grain size, morphology, and GB locations obtained from the DCT data are systematically compared with those from SEM micrographs for the corresponding grains.

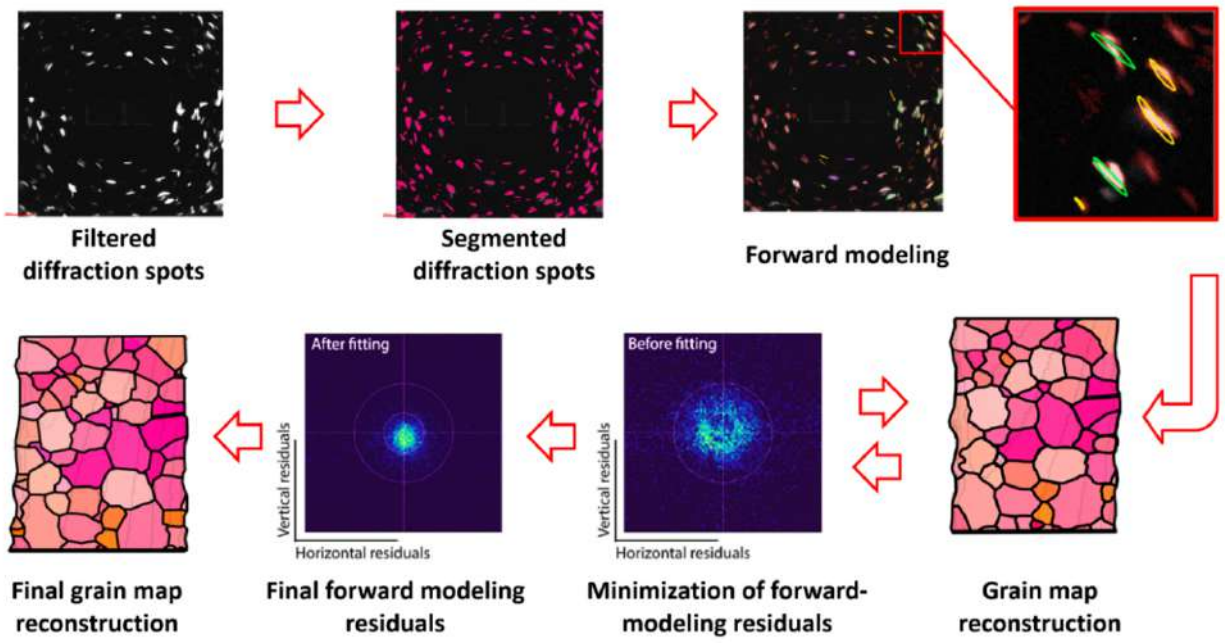

Figure 3.4: Forward modeling reconstruction approach for generation of 3D grain maps implemented in Xnovo GrainMapper3D.

3.3.1 3D grain reconstructions from LabDCT data

Fig. 3.5 shows a 3D rendering of the reconstructed grain map obtained from the C-DCT and HP-DCT scans. The grain maps indicate that the grains obtained from the conventional and helical DCT scans show similar sizes, shapes, and locations. To assess the quality of the DCT reconstructions, a completeness parameter C [13, 110] is generally used:

$$C = \frac{N_0}{N_p} \tag{3.1}$$

where N_0 is the number of observed diffraction spots for a given grain, and N_p is the number of predicted diffraction spots for a given grain from the forward modeling approach [132]. In the forward modeling approach, the mismatch between the predicted and observed diffraction spots is first separated into vertical and horizontal residuals (vertical and horizontal distance between the centers of the predicted and observed spots), and then an auto-fitting process is employed to iteratively update the instrumental parameters (relative positions of source, sample, and detector) in the analysis to minimize the vertical and horizontal residuals. Higher C values indicate higher confidence in the reconstructed grain. shows the average C values for the grains reconstructed using the HP-DCT and C-DCT data. These values indicate that the C-DCT performs slightly better than the HP-DCT scan in terms of the reliability of the reconstruction for an average grain. This observation may be explained by the larger number of total projections captured in the C-DCT scans compared to the HP-DCT scan. A larger number of projections implies that the diffraction spots for a given grain will be captured more frequently in the data, leading to a more robust grain reconstruction.

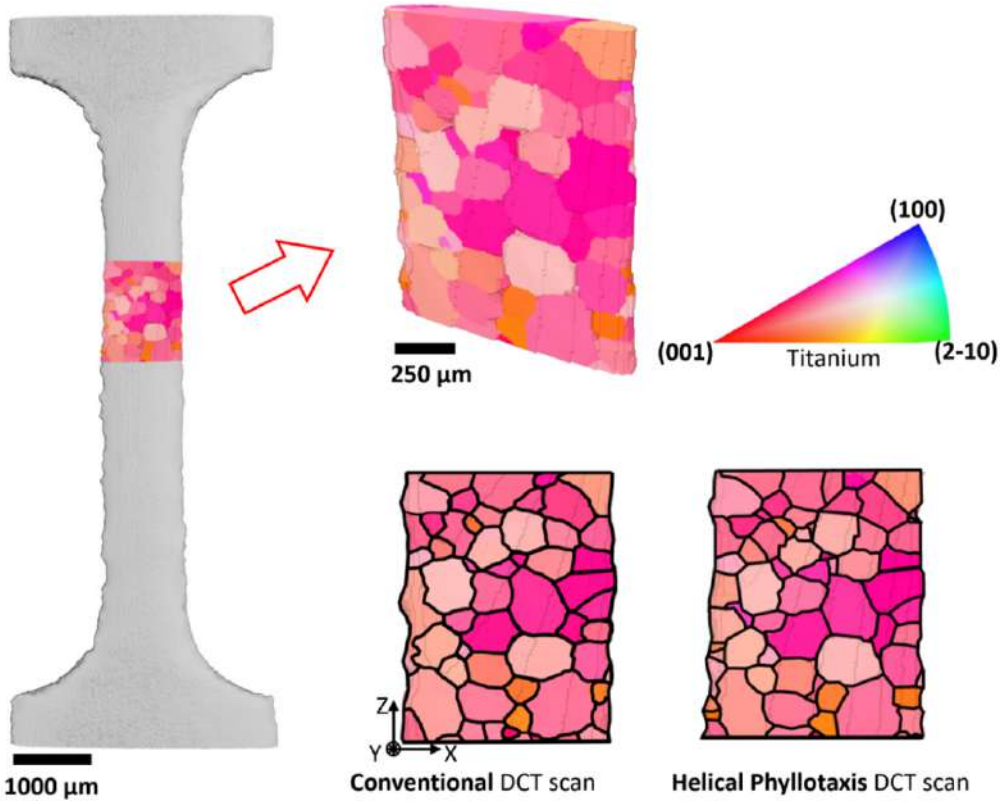

Figure 3.5: 3D grain reconstructions of the central region in the Ti sample: conventional DCT scan acquisition and helical phyllotaxis scan acquisition. The grains are colored according to the inverse pole figure color key along the y-direction.

To better quantify the robustness of the grain reconstruction, it is important to look at individual grain completeness values. While an average grain completeness value is useful to assess the overall quality of the sample, it does not give any information about local grain completeness, e.g., grain completeness as a function of 3D grain size. Fig. 3.6 (a) shows the distribution of average grain completeness, and Fig. 3.6 (b) shows the cumulative distribution of the average grain completeness for the C-DCT and HP-DCT scans. The cumulative distribution in Fig. 3.6 (b) also presents the distribution of the average grain completeness of individual sections of the conventional scans as solid lines. While the average completeness is higher for the C-DCT scans, the distribution of cumulative grain completeness is comparable to the HP-DCT scans in two sections in the C-DCT scans. This may be explained by the occurrence of smaller grains in those regions, which tend to result in lower grain completeness values.

The correlation between the grain size and the average grain completeness for the two scanning strategies is depicted in Fig. 3.6 (c). While the conventional scan plots have a slightly higher average grain completeness compared to the HP-DCT scan, the distributions are quite comparable, and the difference becomes smaller for the larger grains. It is also observable that grain completeness strongly depends on the grain size until a threshold of about 30 μm, after which an increase in grain size does not significantly affect the

grain completeness in both the C-DCT and HP-DCT scans. This observation is aligned with the findings in literature [13, 54, 55] that LabDCT tends to capture grains of the order of >20-40 μm with reasonable accuracy. For the current data, grains smaller than 30 μm have a completeness value less than 75%, whereas grains larger than 30 μm have a completeness value higher than 75%. Furthermore, the difference in completeness values between HP-DCT and C-DCT for grains larger than 30 μm is less than 10%, whereas, for the grains smaller than 30 μm, the difference in completeness values is 10-15% on average. Therefore, for the current sample, the C-DCT scan exhibits better overall grain completeness values, especially for grains smaller than 30 μm.

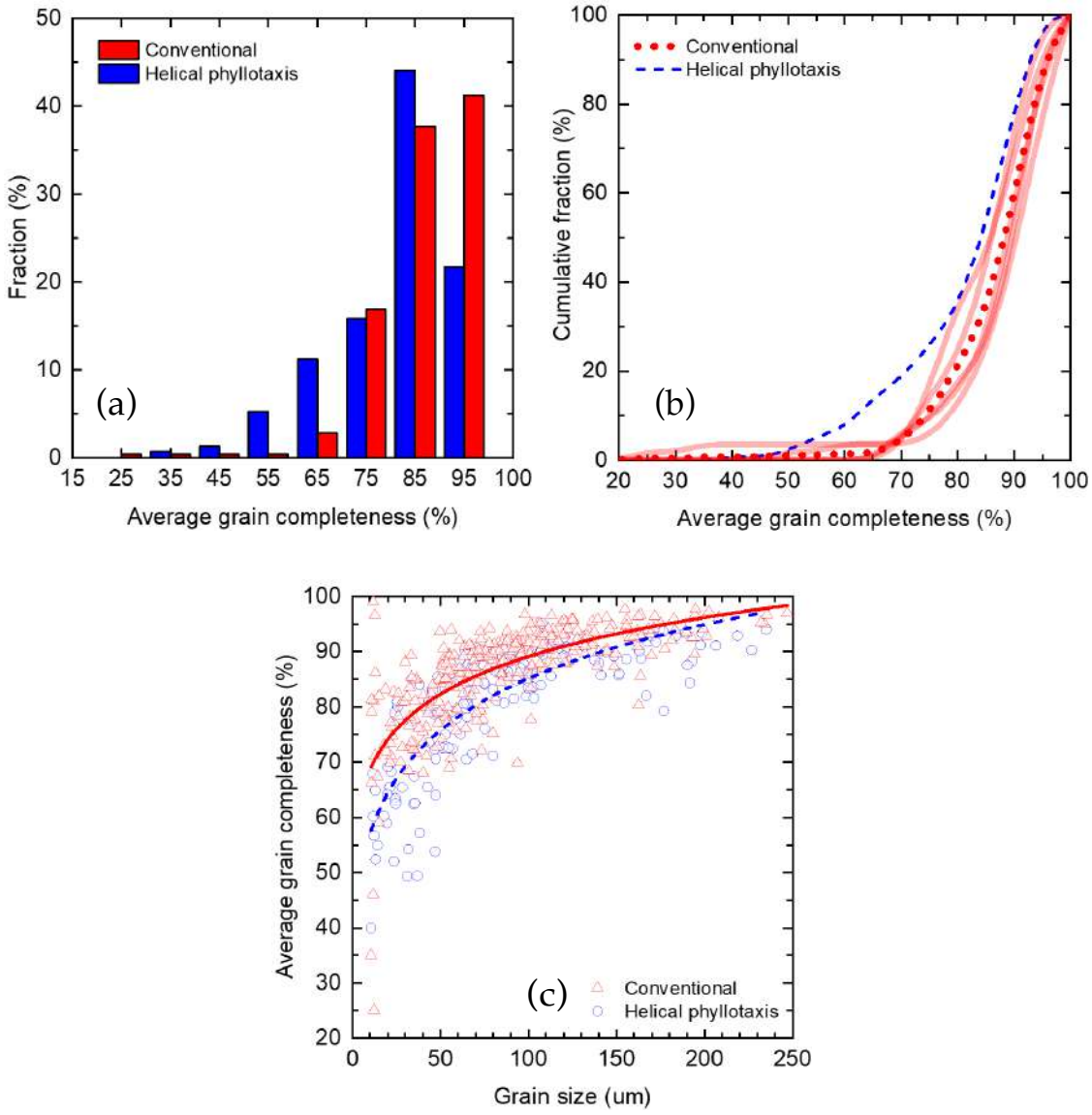

Figure 3.6: Comparison of average grain completeness obtained from conventional and helical phyllotaxis DCT scans: (a) fraction of average grain completeness, (b) cumulative distribution of average grain completeness, and (c) average grain completeness vs. grain size (equivalent sphere diameter).

3.3.2 Comparison of LabDCT and EBSD orientation maps

While a comparison of grain completeness is a good indicator of the robustness of the grain reconstruction from the forward modeling approach, the grain maps obtained from the DCT scans have to be compared to the "ground truth" provided by EBSD data to assess the accuracy of the grain orientations. DCT scans provide 3D maps of the grain, but non-destructive EBSD is limited to 2D grain maps on the surface of the sample. Therefore, to carry out a fair comparison between the EBSD (and later SEM) grain maps, the surface grains of the 3D DCT grain maps were projected on a flat surface parallel to the central plane of the sample. This approach projects the locations of the grain boundaries; however, it does not affect the grain orientation and GB misorientation values.

The grain orientation maps, (0001) pole figures, and GB misorientation maps from EBSD, C-DCT, and HP-DCT scans of the Ti sample can be found in Fig. 3.7 and 3.8, respectively. The EBSD maps show equiaxed grains and a strong bimodal texture typical of rolled commercially pure Ti [64]. The grain maps and GB misorientation maps from the DCT and EBSD show reasonably good agreement. The distribution of GB misorientation angles from EBSD and the DCT is depicted in Fig. 3.9 (a). The bimodal nature of the GB misorientation distribution is captured quite well by the DCT scans, and the two peaks in the distribution are observed at misorientation angles of 65° and 10°. The absolute difference, Δ, between the GB misorientation angles obtained by EBSD and DCT is plotted in Fig. 3.9 (b). The maximum value for Δ is below 0.6°, and 90% of the absolute differences in misorientation angle are below 0.3° for both the conventional and helical phyllotaxis DCT scans. The distribution in Fig. 3.9 (b) demonstrates quantitatively the high quality of the grain reconstructions obtained from both helical phyllotaxis and conventional DCT scans in this study.

3.3.3 Comparison of LabDCT grain geometry with SEM micrographs

In addition to the grain orientations, the accuracy of grain shapes obtained from DCT reconstructions also needs to be assessed. In the case of the grain shape, the ground truth was taken as an SEM image of the central region of the sample, depicted in Fig. 3.10 (a), which clearly shows the different grains in the Ti sample. To assess the grain shapes and locations, the SEM data was used instead of the EBSD data since the EBSD maps were cropped on the upper section due to issues with data collection. The grain maps from the conventional and helical phyllotaxis DCT scans are shown in Fig. 3.10 (b) and (c), respectively. Qualitatively, the grains from the DCT scans show good correspondence with the grains observed in the SEM image. A systematic comparison of the grain size, shape, centroidal grain distances, and average GB distance between corresponding grains in the SEM and DCT grain maps was performed to assess quantitatively the quality of the grain shape and GB locations in the DCT slice.

A comparison of the size and shape of the grains observed from SEM and DCT is presented in Figure 10. The grain size is determined from the equivalent circular diameter d:

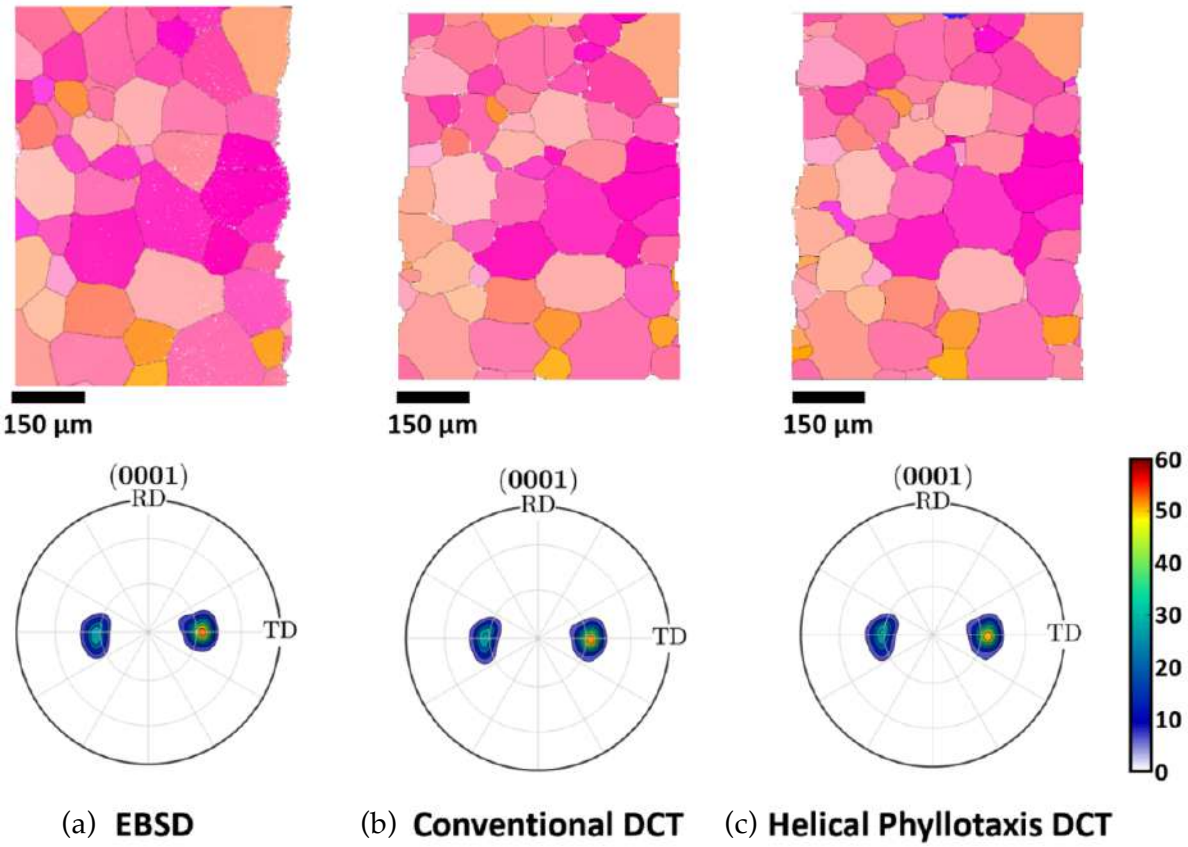

Figure 3.7: Grain maps and (0001) pole figures from (a) EBSD, (b) conventional DCT, and (c) helical phyllotaxis DCT.

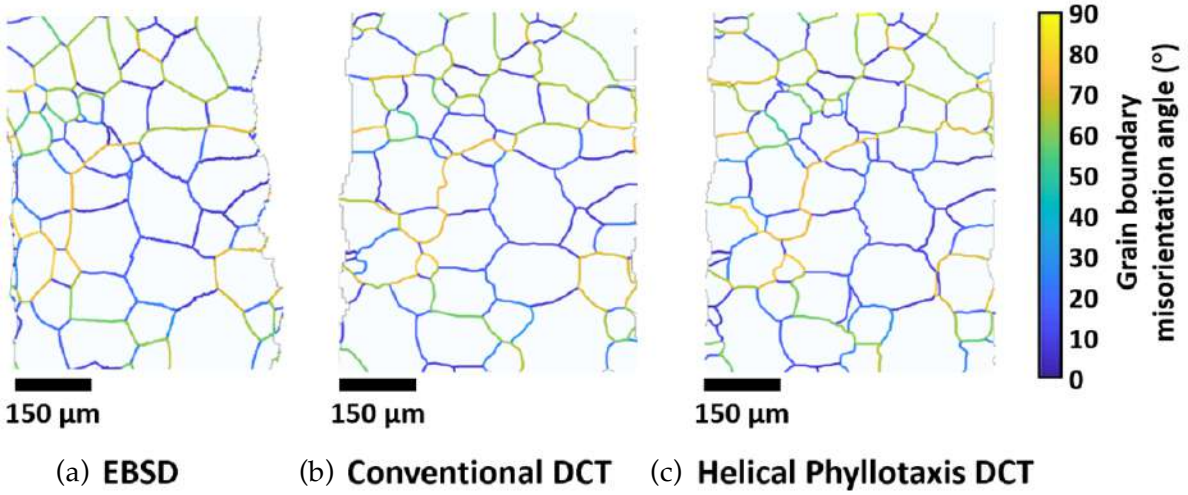

Figure 3.8: GB misorientation distribution for the grain maps from (a) EBSD, (b) conventional DCT, and (d) helical phyllotaxis DCT.

$$d = \sqrt{\frac{4A}{\pi}} \tag{3.2}$$

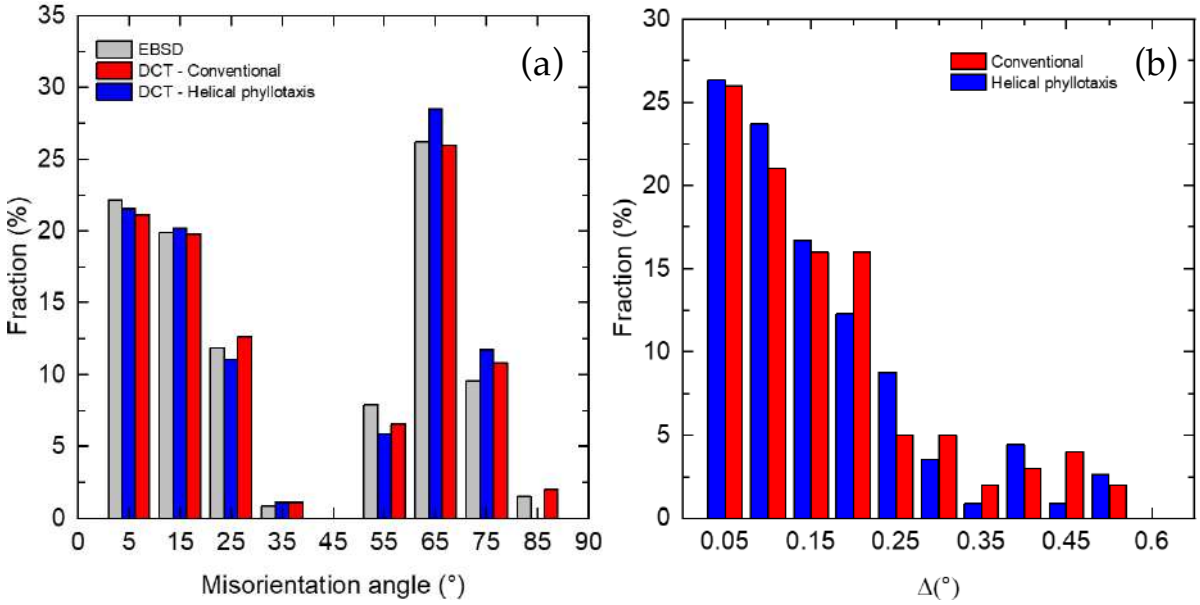

Figure 3.9: Comparison of GB misorientations: (a) distribution of GB misorientation angles obtained from EBSD and LabDCT grain reconstructions, and (b) distribution of absolute difference (Δ) in GB misorientation between EBSD and LabDCT grain maps.

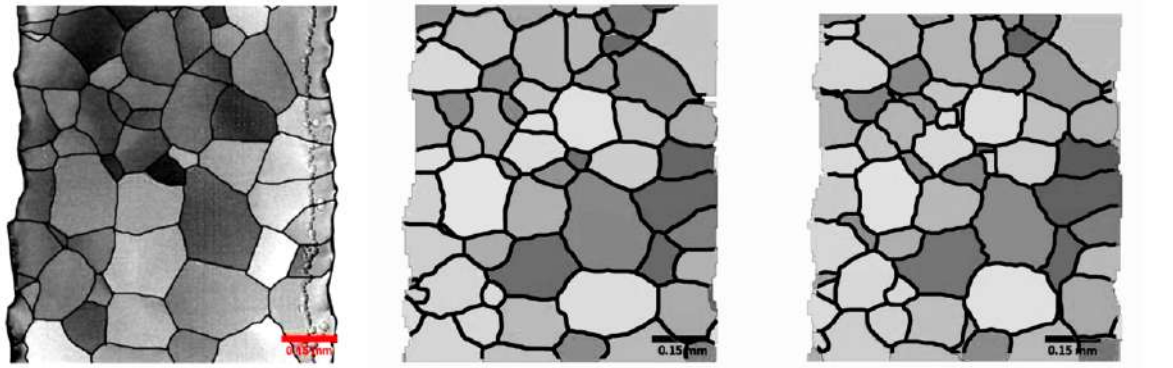

Figure 3.10: Grain maps for the central section of the Ti sample: (a) SEM micrograph, (b) Conventional DCT scan data, and (c) Helical phyllotaxis DCT scan data.

where A is the area of the grain in the 2D grain map. The grain size distributions obtained from DCT and SEM are plotted in Fig. 3.11 (a), and they show reasonable agreement. Furthermore, the grain size distribution from DCT scans normalized by the size of the corresponding grain in the SEM grain map is plotted in Fig. 3.11 (b). A value of 1 for this ratio indicates perfect agreement between the grain size of corresponding grains in the DCT and SEM maps. A value of less than 1 indicates that the DCT grain map underestimates the size of the corresponding grain in the SEM grain map. On average, the conventional DCT scans have a normalized grain size of 0.98 while the helical phyllotaxis DCT scan has a value of 1.02, indicating that the helical phyllotaxis scan slightly overesti-

mated and the conventional scan slightly underestimated the grain size as compared with the grain size measured by SEM.

Fig. 3.11 (c) shows the distribution of the 2D aspect ratio of the grains obtained from SEM and DCT. A normal distribution appears in both SEM and DCT data with an average aspect ratio of 1.4. The normalized aspect ratio, defined as the aspect ratio of the grain in the DCT scan normalized by the aspect ratio of the corresponding grain in the SEM scan, also shows a normal distribution with an average value close to 1, indicating that both the helical and conventional DCT scans capture the 2D aspect ratio of the grain with reasonable accuracy.

The results presented above indicate that both C-DCT and HP-DCT scans accurately capture the grain morphology. The next question that arises is in regard to the accuracy of the location of the grains. To compare the location of the centroids of the grains between the DCT and SEM data, the grain maps obtained from the DCT scans with the grain map obtained from the SEM image were first aligned by maximizing the overlap of the grain boundaries using an in-house Python code. The Python code overlaps the DCT and SEM GB maps and then iteratively moves the DCT GB map while keeping the SEM GB map stationary until maximum overlap between the grain boundaries is achieved, thereby aligning the two maps. The aligned and overlapped maps are shown in Fig. 3.12. The overlapped GB maps show excellent correspondence between the grain boundaries from both DCT scans with those in the SEM image. Afterward, the centroidal distance, defined as the absolute distance between the centroids of corresponding grains in the SEM and DCT grain maps, is computed for each grain in the sample using another in-house Python code. It should be noted that the centroidal distances are obtained after the global alignment of the DCT GB maps to the SEM data and not from the physical alignment of the samples.

The distribution of the centroidal distances between corresponding grains in the SEM and DCT grain maps is depicted in Fig. 3.13 (a). On average, the centroidal distance for the C-DCT scans is about 8 μm, whereas it is 12 μm for the HP-DCT scan. The largest centroidal distances were of the order of 27 μm for the HP-DCT scan and 22 μm for the C-DCT scan. The centroidal distances as a function of grain size are plotted in Fig. 3.13 (b), and no clear trends are apparent in the data. However, if the centroidal distance is normalized by the grain size (see Fig. 3.13 (c)), the error is a significant fraction of the grain size in small grains, whereas it only reaches a small fraction of the grain size in large grains. This trend is more prominent in the HP-DCT scan data than in the C-DCT scan data.

While the centroidal distance gives us a good sense of the correspondence between the grain positions from SEM and DCT data, it is also important to assess how well the DCT maps capture the GB locations. To assess the accuracy of the GB locations, the average GB distance between corresponding grains in the DCT and SEM grain maps was estimated following the method proposed by Ludwig *et al.* [116] and Bachmann *et al.* [13]. The GB maps from the SEM were first binarized - see Fig. 3.14 - and then a Euclidean distance transform (EDT) was computed for each grain in the SEM data.

The EDT of the GB map creates a heatmap of the distance to the nearest GB. In the EDT map, the regions near the GB have a small value (small distance to the nearest GB),

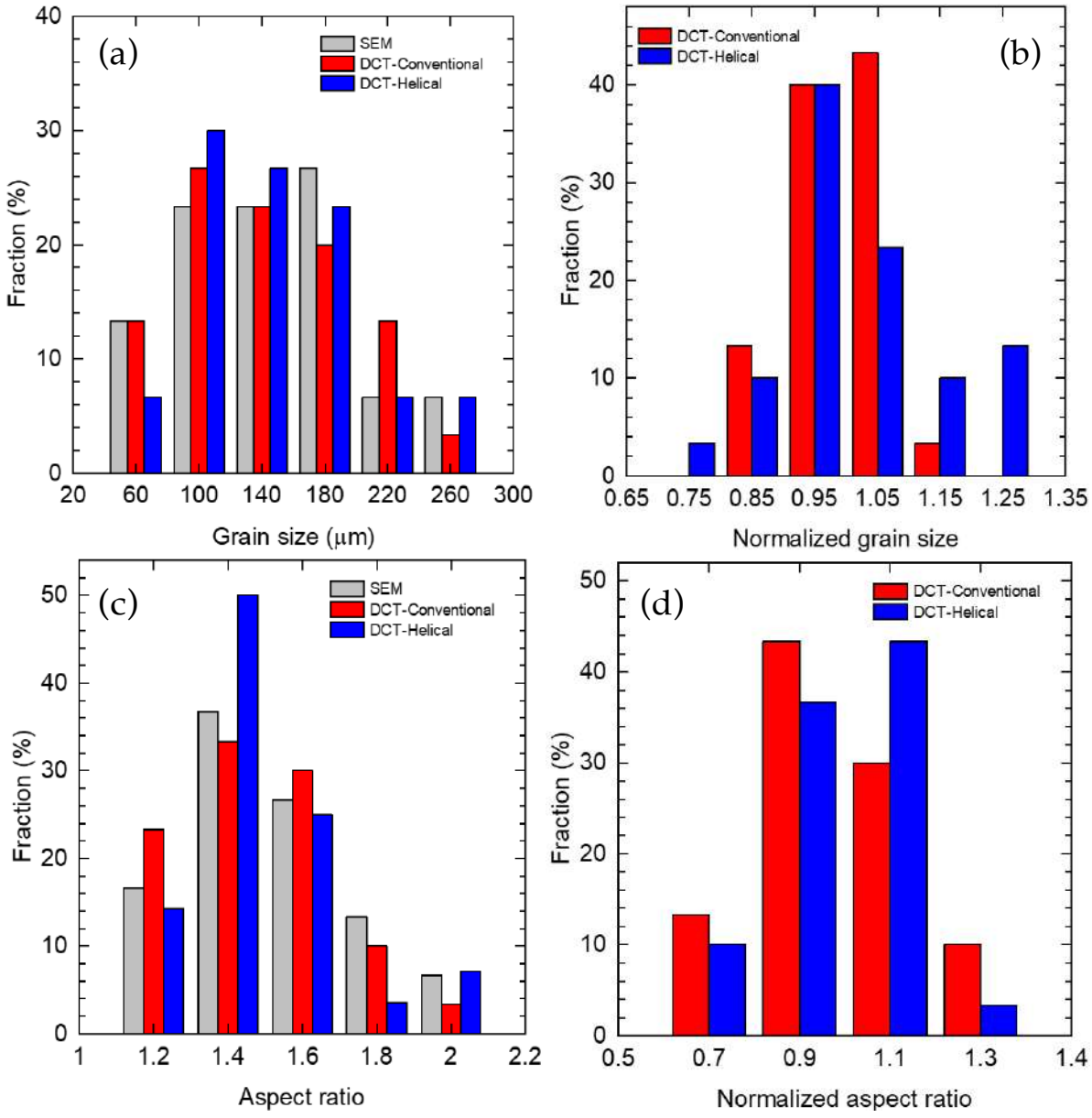

Figure 3.11: Comparison of grain size and morphology obtained from SEM and DCT scan data: (a) grain size distribution from SEM and DCT, (b) distribution of normalized grain size from DCT, (c) aspect ratio distribution from SEM and DCT, and (d) distribution of normalized aspect ratio from DCT.

whereas regions away from the GB have a large value. An EDT heat map of a central grain from the SEM data is shown in Fig. 3.15. To obtain a heatmap of the distance between the grain boundaries from DCT and SEM maps, the EDT map of the SEM grain was multiplied with the GB map (boundary pixels have a value of 1 and non-boundary pixels have a value of 0) of the corresponding grain in the aligned DCT grain map. Fig. 3.15 and 3.16 depicts an example of the GB distance heatmap for a central grain in the DCT grain maps. These heatmaps clearly show how far the DCT grain boundaries are

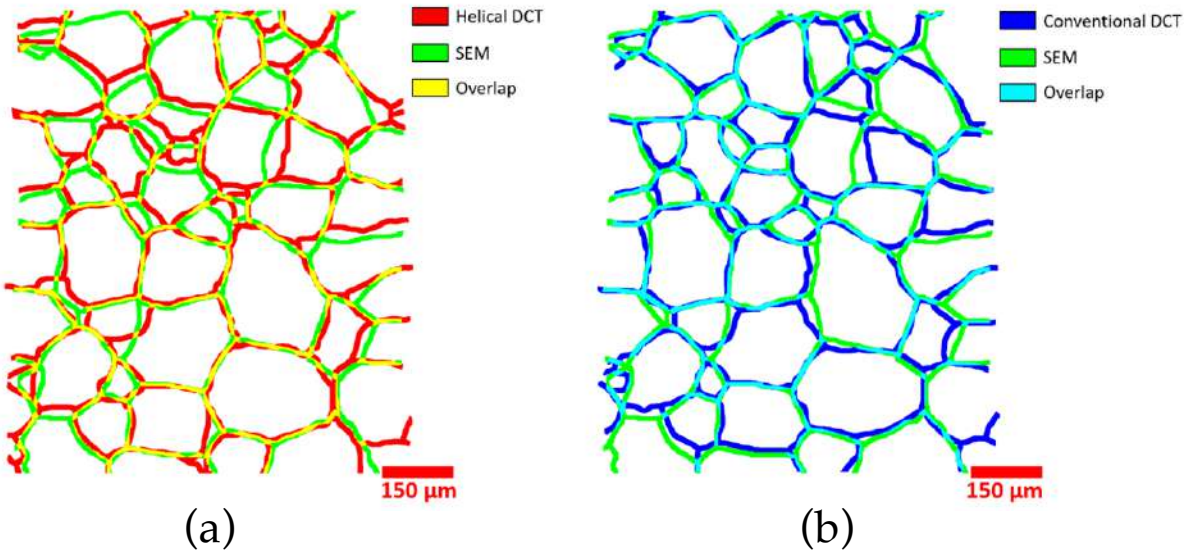

Figure 3.12: Overlap of aligned GB maps: (a) SEM vs. helical phyllotaxis DCT scan, and (b) SEM vs. conventional DCT scan.

from the SEM grain boundaries, and the average distance between the grain boundaries of corresponding grains in the SEM and DCT data can be quantified.

The process outlined above was repeated for each grain in the sample, and the distribution of the average GB distance for the grains in the DCT grain maps is presented in Fig. 3.15. The average GB distance is quite similar for the conventional and helical phyllotaxis scans, with the conventional scan having a slightly smaller value (6 μm) than the helical phyllotaxis scans (8 μm). The largest average GB distances were of the order of 15 μm for the HP-DCT scan and 12 μm for the C-DCT scan. Similar to the centroidal distance, the plot of the average GB distance shows no clear trends with the grain size. However, when the average GB distance is normalized by the grain size, the error in the GB is a larger fraction of the grain size in the case of small grains. This observation is especially true for the helical phyllotaxis scan, where the average GB distance can be as large as 20% of the grain diameter for the small grains. For applications where smaller grains play significant roles, such as in a corrosive environment [137, 148, 165], the inability to accurately capture the grains' morphology and orientation may have a non-negligible impact on our understanding of the underlying phenomena (Fig. 3.17).

3.4 Summary and conclusions

A commercially pure annealed Ti sample was characterized by LabDCT to obtain 3D crystallographic grain maps that were obtained from conventional (C-DCT) and helical phyllotaxis (HP-DCT) acquisition strategies. The quality of the 3D grain maps from both acquisition strategies was assessed, and grain shape and orientation statistics were compared against the grain maps obtained from EBSD and SEM scans of the same Ti sample. Since EBSD and SEM scans are restricted to near-surface grain information, only the sur-

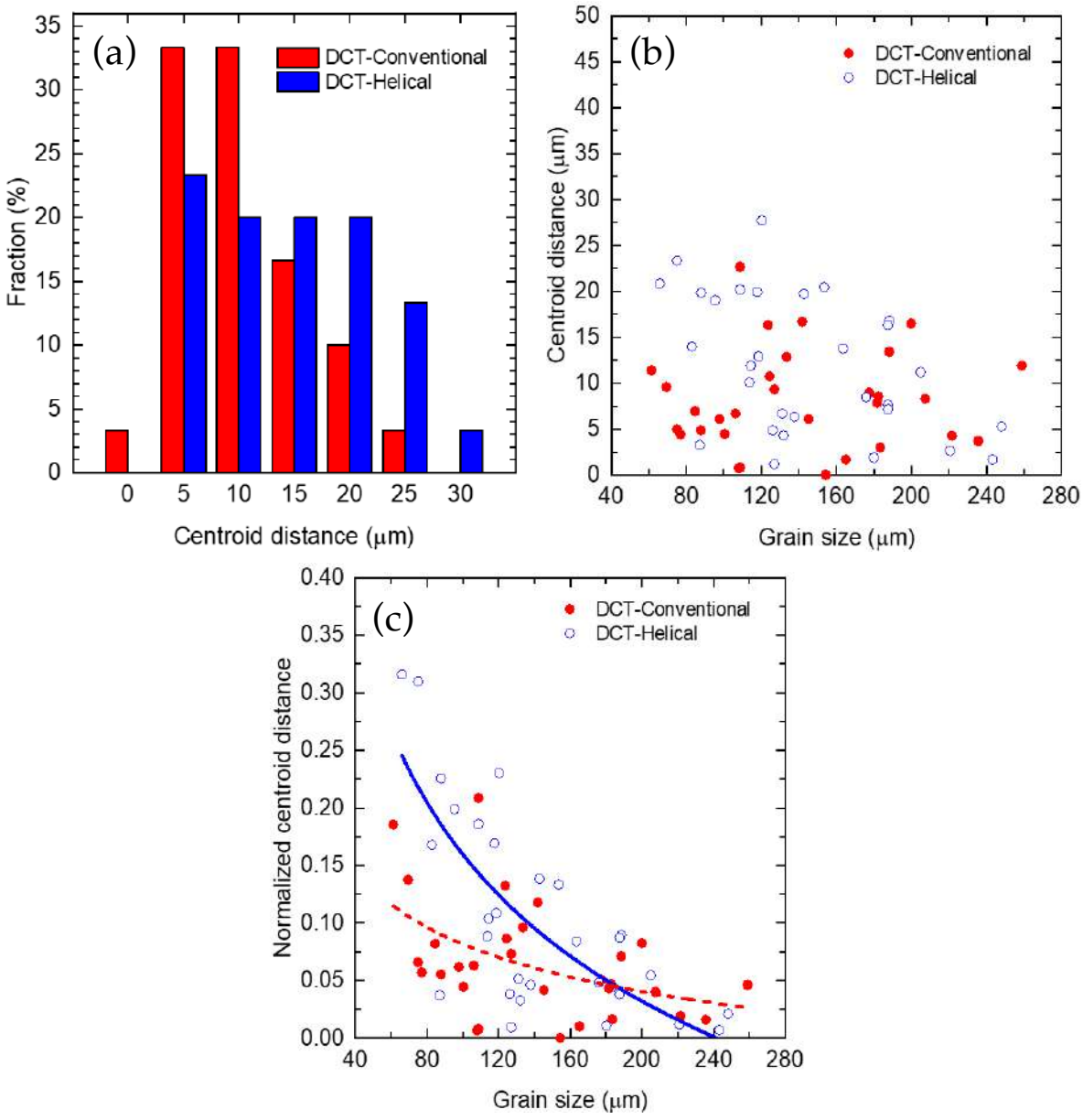

Figure 3.13: Comparison of the centroidal distance between corresponding grains in SEM and DCT grain maps: (a) distribution of centroidal distance between corresponding grain in the SEM and DCT grain maps (b) centroidal distance vs. 2D grain size, and (c) normalized centroidal distance (centroidal distance normalized by 2D grain size) vs. grain size.

face grains in the 3D grain maps from the DCT scans were extracted and compared to the EBSD and SEM data. The main findings from this investigation are the following:

1. Total scan times for HP-DCT and C-DCT scans were comparable for the samples scanned in the present study. However, the total reconstruction and analysis time for the C-DCT scans was five times longer than that of the HP-DCT scan.

2. The reliability of the grain reconstructions from the DCT scans was quantified using

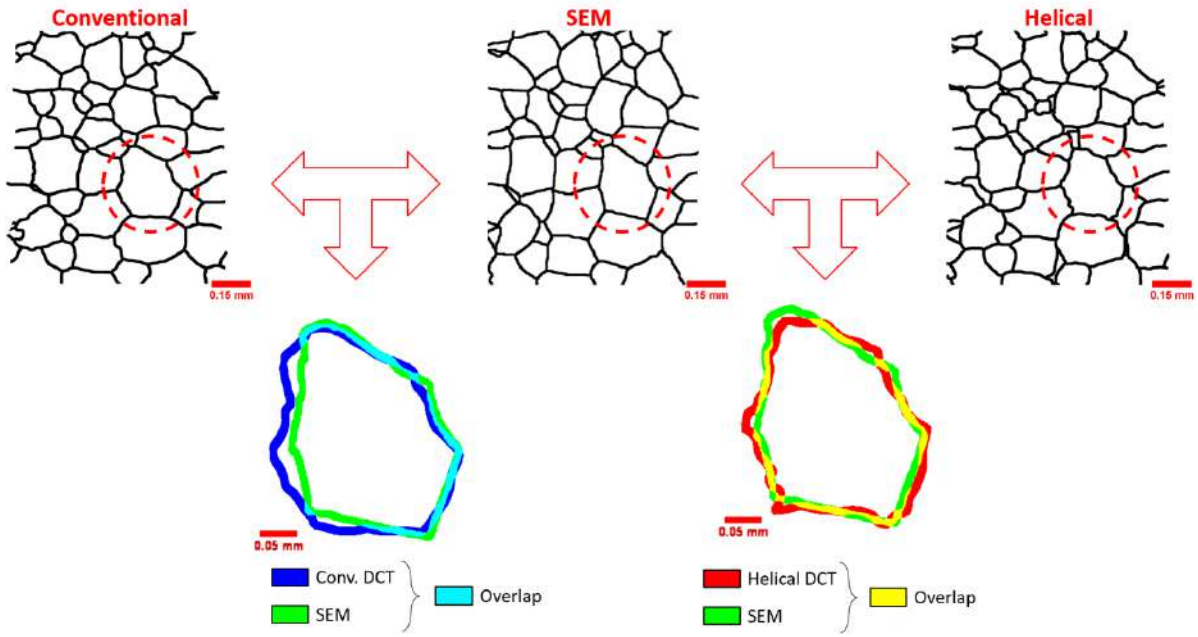

Figure 3.14: Comparison of GB detection accuracy: overlap between SEM and DCT grain data.

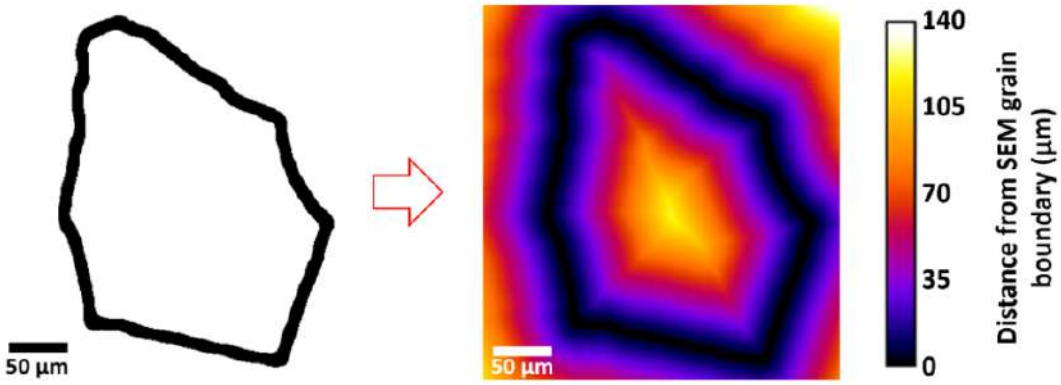

Figure 3.15: Comparison of GB detection accuracy: euclidian distance transform (EDT) heatmap of SEM grain.

a completeness parameter. It was found that the average grain completeness for both acquisition strategies was comparable with the average grain completeness, with the one from the C-DCT being marginally (5%) higher than that of the HP-DCT.

3. The grain orientation and GB misorientation maps obtained from DCT scans showed excellent agreement with the grain orientations from the EBSD data. The absolute difference between grain boundary misorientations was below $0.6°$, and 90% of the differences were below $0.3°$ for both conventional and helical scans.

4. The grain shape and morphology of the grains from the DCT grain maps were com-

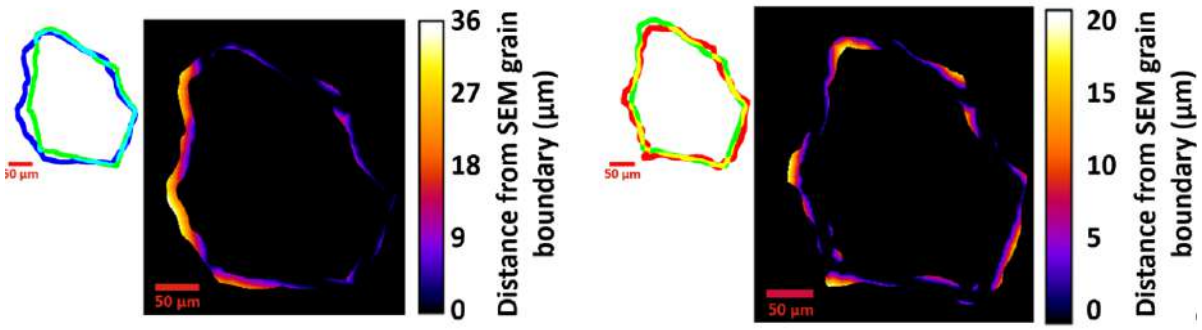

Figure 3.16: Comparison of GB detection accuracy through the heatmap of the distance between SEM and conventional DCT GB for the corresponding grain (left), and heatmap of the distance between SEM and helical phyllotaxis DCT GBs for the corresponding grain (right).

pared with those obtained from SEM grain maps. It was found that, on average, the HP-DCT scan slightly overestimated the 2D grain size by 2% while the C-DCT scan slightly underestimated the grain size from the SEM data (also by 2%). The grain aspect ratios were captured quite accurately by both acquisition strategies.

5. The position of the grain centroids obtained by DCT and SEM was compared. The differences in the positions were very small in the case of C-DCT (average difference of 8 μm) and slightly higher (12 μm) in the case of HP-DCT.

6. The average grain boundary distance for corresponding grains in the DCT and SEM scans was found to be 6 µm for the conventional DCT scans and 8 µm for the helical DCT scans, with the error being a larger fraction of the grain size for the smaller grains.

It should be noted that the analysis presented here is limited to samples with average 3D grain size in the range of 90-100 µm, and further exploration is needed to assess how these advanced DCT acquisition strategies will perform in samples with a finer grain structure. From the current data, it is clear that C-DCT scans result in higher fidelity grain maps compared to HP-DCT. However, the analysis time of the C-DCT approach for elongated sample geometries comes at a significantly higher time cost. This study demonstrates that, regardless of the scanning approach, DCT is a very useful technique for non-destructive 3D grain mapping, providing extremely valuable information that can be incorporated into the study of plastic deformation of polycrystals.

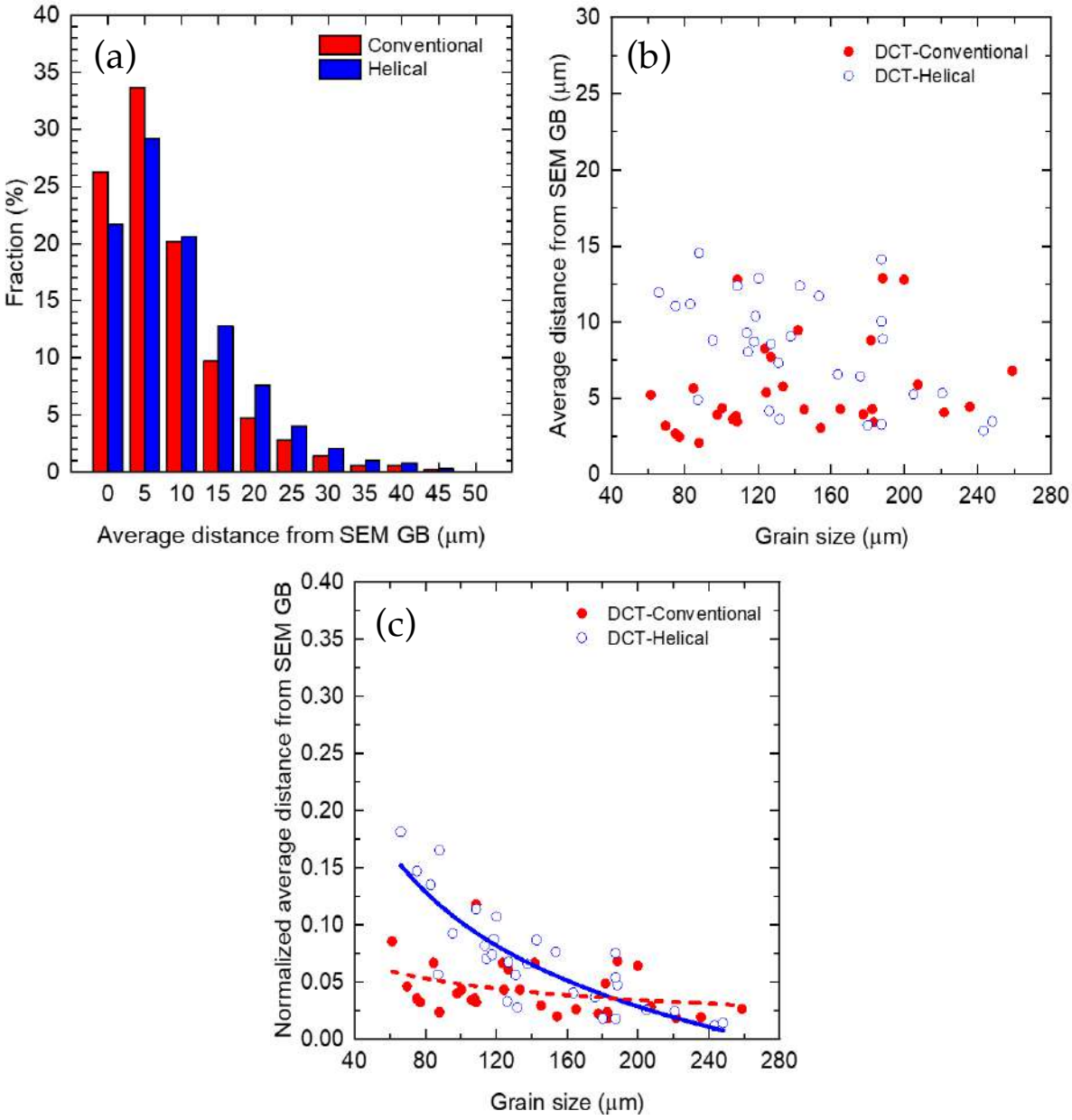

Figure 3.17: Comparison of average grain boundary distance between corresponding grains from SEM and DCT maps: (a) distribution of average grain boundary distance between SEM and DCT data, (b) average grain boundary distance vs. 2D grain size, and (c) normalized average grain boundary distance (average grain boundary distance normalized by 2D grain size) vs. grain size.

4 Analysis of slip transfer in pure Ti through 3D GB characterization

4.1 Introduction

The standard strategies to study slip transfer across GBs present two main drawbacks, namely the lack of information about the 3D GB geometry and the actual knowledge of the active slip system when several slip systems share the same slip plane. It is often argued that the limitations of the geometrical slip transfer criteria based on Δb or m' to predict slip transfer/blocking at GBs have to be associated with these uncertainties while the role played by the twist angle θ (and, thus, the accuracy of the LRB criterion) remains unknown. For instance, slip blockage was observed in five GBs in pure Mg where m' was close to 1, but $\theta > 60°$ [154]. The GB orientation within the sample was measured by sequential milling with FIB in five GBs, but it was not possible to analyze a large dataset of GBs to obtain definitive conclusions because this technique is very time-consuming.

As presented in Chapter 3, LabDCT has become a powerful tool to perform non-destructive, high-fidelity characterization of the 3D grain structure in polycrystals [123]. Notably, the accuracy of LabDCT has been extensively validated against EBSD data [60, 132, 195], and hence, it can help assess the role that the 3D geometrical features of the grains and GBs play in slip transfer. This technique is used in this chapter to assess the GB geometry of Ti foils that were later subjected to tensile deformation. Conventional slip trace analysis was used to ascertain the active prismatic slip systems and the occurrence or absence of slip transfer at several hundreds of GB. This unique data set was then used to validate/disprove the different slip transfer criteria proposed in the literature using the information on the GB orientation in 3D.

4.2 Materials and experimental techniques

High purity (99.99%) cold-rolled Ti foils of 0.25 mm in thickness were purchased from Goodfellow. A micro tensile dog-bone sample with a uniform central region of $5 \times 1\ mm^2$

was machined from the foil by electro-discharge machining. The sample was heat-treated at 850°C for 8 hours in a tubular vacuum furnace under argon atmosphere to minimize oxidation. The sample was gently ground with 1200 grit paper to remove the fine oxidation layer on the surface after the heat treatment. Afterward, it was electropolished to mirror finish on both surfaces of the central gauge section using a Struers A3 electrolyte at 27 V and room temperature.

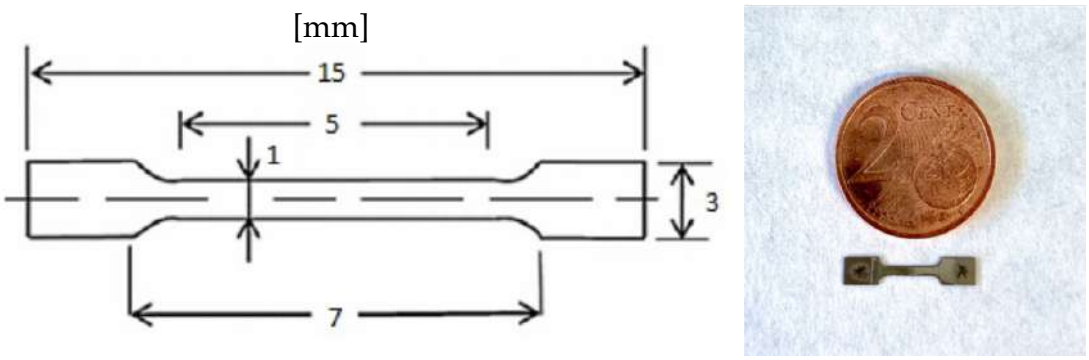

Figure 4.1: Ti dogbone micro tensile specimen dimensions in mm (left) and sample dimensions compared to a coin (right).

EBSD maps were acquired from both surfaces of the gauge length of the sample. The crystallographic orientations were obtained in a FEI Helios NanoLab 600i dual-beam microscope with an Oxford Instruments EBSD detector. The whole gauge length was mapped with several overlapping maps, followed by stitching in AZtec. The EBSD maps were acquired at 20 kV and 2.7 nA, with a step size of 3 μm, in order to accurately resolve the microstructural features. The overall quality of the EBSD maps was above 95% indexing. The maps were post-processed with the MTEX Matlab Toolbox [14] with a grain boundary misorientation threshold of 2° to capture low-angle grain boundaries.

The 3D grain structure was mapped using a Zeiss Xradia Versa 620 X-ray microscope with DCT capabilities. The sample was positioned at equal distance from the X-ray source and the detector (14 mm) (Fig. 3.2), keeping the Laue focusing geometry and a source voltage and power of 160 kV and 15 W, respectively, were used. A 4X DCT detector with a transmission beam stop was used to capture the diffraction spots during the scan. A conventional DCT (C-DCT) scanning approach, such as that presented in Chapter 3, was employed for this sample. In order to map the full gauge length with the selected aperture, seven overlapping scans were needed, followed by stitching, resulting in a total scan time of 63 h. The acquired DCT projections were iteratively reconstructed with GrainMapper3D (Xnovo Technology) using the forward modeling approach [132] until the average completeness values (Eq. 3.1) reached at least 90%. Then, Dream3D [69] was used to segment the volume into grains and grain boundaries, and Paraview [12] was used for visualization purposes.

The sample was deformed in uniaxial tension in a Kammrath and Weiss micro tensile testing machine equipped with a 1 kN load cell at a quasi-static strain rate of $\approx 10^{-3}\, s^{-1}$ to a strain of about 2%. The combination of SEM imaging and grain orientation before

deformation by EBSD was used to identify the active slip systems in the grains after deformation. The active slip system identification by conventional slip trace analysis is based on the comparison between the orientation of the experimentally observed slip bands with that obtained from the crystal orientation, as measured by EBSD [7, 24, 130]. It is worth mentioning that the crystal orientations provided by DCT could have also been used instead of EBSD to determine the theoretical orientation of the slip traces. However, the spatial resolution of EBSD at the sample surface is better than that of DCT, improving the accuracy in the case of very small grains.

4.3 Results

4.3.1 3D grain and grain boundary characterization

The DCT data reconstructed in GrainMapper3D was imported into Dream3D [69] to characterize the microstructure in 3D. Each voxel contained information about the Euler angles and the completeness value attained after the forward-modeling process. The data were denoised using a minimum completeness value of 0.1 and misorientation threshold of 2° for grain segmentation. Any spurious data were filled using an erode/dilate process with two iterations. Fig. 4.2 (a) shows the reconstructed sample gauge after post-processing in Dream3D, where the left half shows the voxelized volume. The sample was composed of approximately 24 million voxels and 588 grains, and the information about grains' positions, sizes, shapes, and misorientations was exported for the 3D microstructural analysis. A detailed view of two neighbor grains reconstructed with 5 μm voxel size is provided in Fig. 4.2 (c).

Once the volume of the sample was reconstructed, a triangular surface mesh was generated over the inner (GBs) and outer surfaces of the sample. The initial triangular surface mesh was smoothed using a Laplacian algorithm to minimize any stair-stepped appearance, and the resulting triangle data (triangle identifier, centroid, area, curvature, misorientation, and normal direction) were exported for further analysis. The right half of Fig. 4.2 (a) shows the generated surface mesh, composed of roughly 1.5 million triangles and 2319 GBs, where the outer surfaces of the sample have been removed for the sake of GB visualization. Fig. 4.2 (d) shows the surface mesh at the GBs of the grains in Fig. 4.2 (c), where the shared GB normals have been plotted as yellow arrows.

The lognormal grain size distribution obtained from DCT data is plotted in Fig. 4.3 (a). The average grain size is 111 ± 58 μm. The GB misorientation angle (also provided by DCT data after grain segmentation) is plotted in Fig. 4.3 (b) and presents a bimodal distribution with peaks at $\approx 15°$ and $\approx 70°$.

The normal vector to each triangle in the surface mesh was directly obtained from the surface mesh, and the GB normal direction, $\boldsymbol{n}_{GB}$, was estimated. To this end, a different subset was generated for every GB from the triangular mesh, so only the corresponding triangle normals were selected. The triangle winding was carefully checked and corrected so that all normal directions were pointing in the same direction. Given that the mean curvature of the studied GBs is close to 0, the GB normal was taken as the mean of the triangle

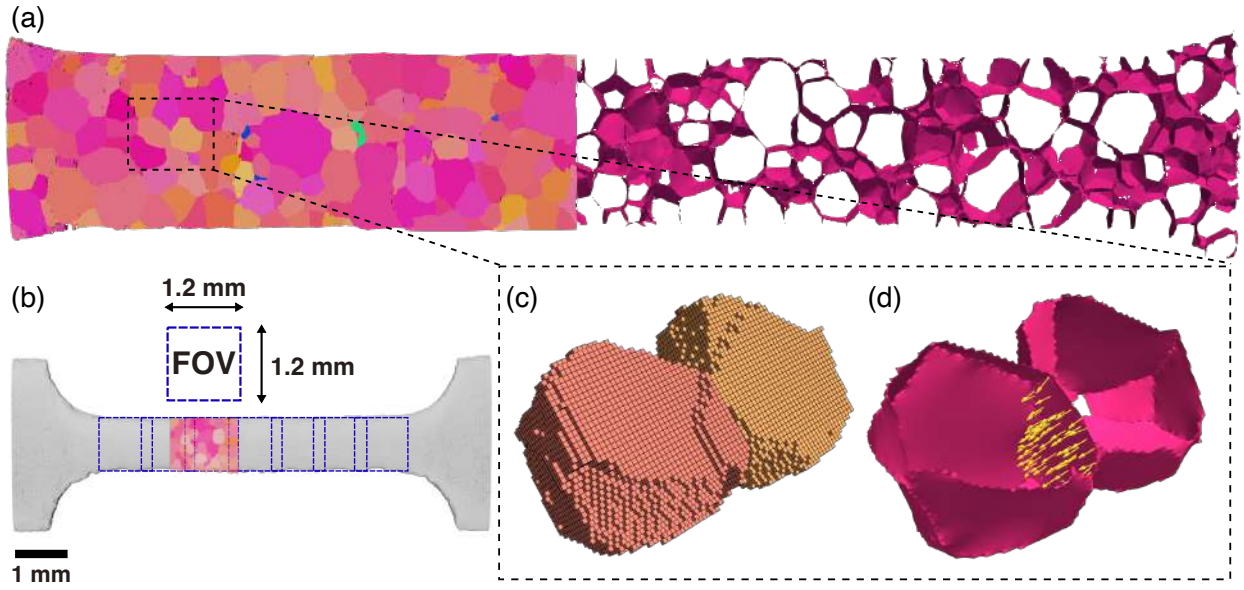

Figure 4.2: Microstructural characterization by DCT. (a) Reconstructed DCT map of the sample gauge colored according to the inverse pole figure with respect to the screen plane (color key in Fig. 4.4 (b)). The left half corresponds to the reconstructed volume of the sample, and the right half corresponds to the surface mesh generated at the GBs. (b) Sample scanning strategy consisting of 7 overlapping sub-regions to map the full gauge length. (c) Detailed view of two neighboring grains (dashed squared area in (a)), where the reconstructed voxelized volume is shown in (c), and the corresponding surface mesh is shown in (d). In the latter, some GB surface normals are drawn in yellow.

normals included in the surface. From this information, it was possible to calculate the GB inclination β, defined as the angle between the GB plane, characterized by the GB normal $\boldsymbol{n}_{GB}$, and the plane perpendicular to the sample surface and oriented along the length of the sample. Thus, vertical GBs (perpendicular to the sample surface) are characterized by high β (close to 90°). The GB inclination distribution β is plotted in Fig. 4.3 (c). As observed in Fig. 4.2 (a), there is a significant fraction ($\approx$ 20%) of vertical or close to vertical GBs with $\beta > 80°$ that grew very likely during the heat treatment due to the small thickness of the sample. Nevertheless, approximately 55% of the GB have an inclination $< 65°$.

The calculated GB normals, together with the observed active slip systems at both neighboring grains, also allowed the calculation of the twist angle θ associated with two slip planes across a GB according to (Fig. 1.5)

$$\theta = tan^{-1}\left(\frac{||\boldsymbol{l}_A \times \boldsymbol{l}_B||}{\boldsymbol{l}_A \cdot \boldsymbol{l}_B}\right) \tag{4.1}$$

where $\boldsymbol{l}_A$ and $\boldsymbol{l}_B$ stand for the traces of the incoming and the outgoing slip planes with the

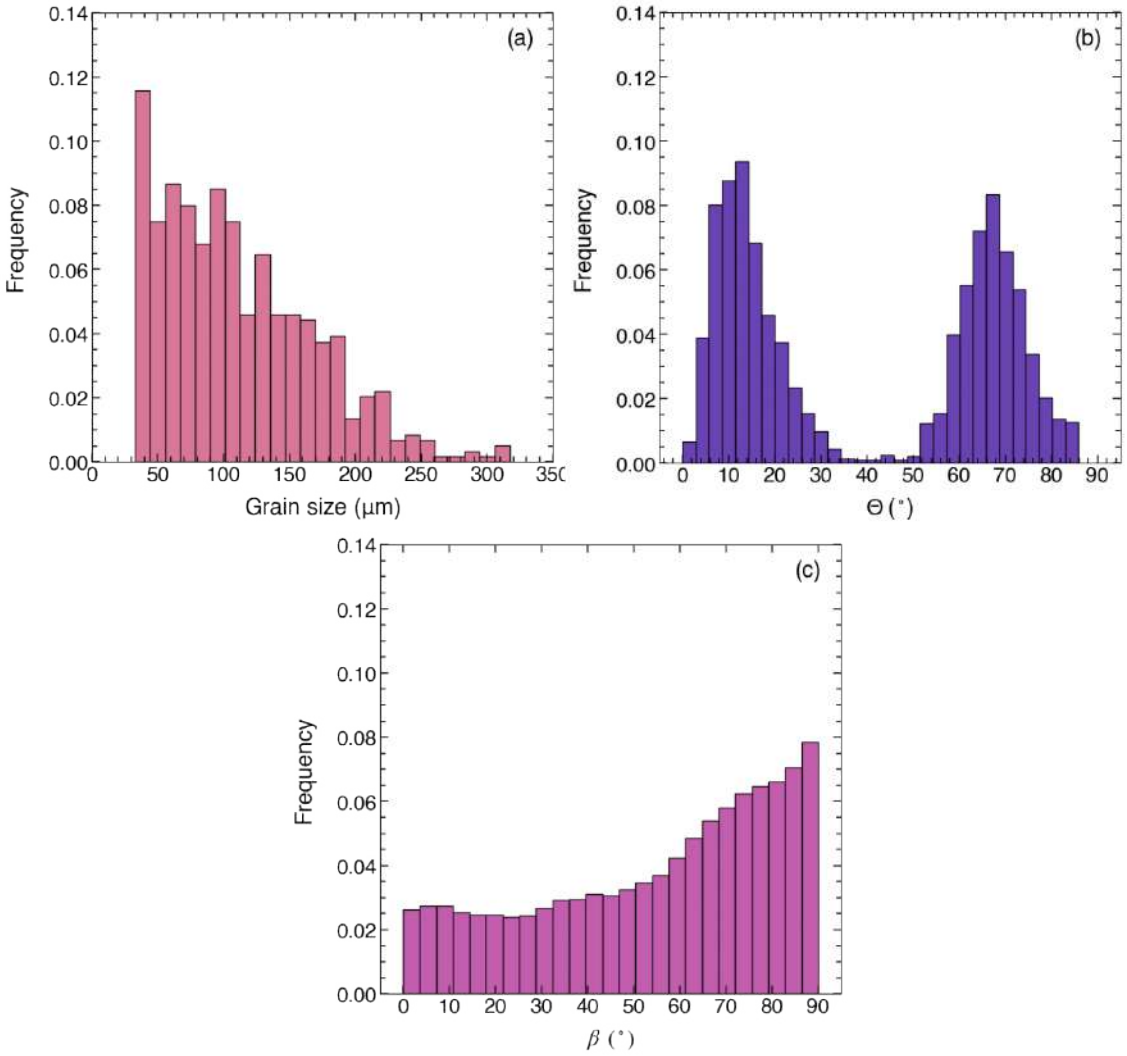

Figure 4.3: Microstructural features of the Ti sample obtained by DCT. (a) Grain size distribution, (b) Grain boundary misorientation distribution, (c) Grain boundary inclination (β) distribution.

GB plane, respectively, (Fig. 1.5) that can be calculated as follows:

$$\begin{aligned} \boldsymbol{l}_A &= \boldsymbol{n}_{GB} \times \boldsymbol{n}_A \\ \boldsymbol{l}_B &= \boldsymbol{n}_{GB} \times \boldsymbol{n}_B \end{aligned} \tag{4.2}$$

4.3.2 2D microstructural characterization

The microstructure within the surface of the sample obtained by EBSD is shown in Fig. 4.4. The grains have been colored according to the inverse pole figure perpendicular to the surface, and the color key is provided by the inverse pole figure color code in Fig. 4.4 (b). The raw EBSD map displayed in Fig. 4.4 (a) shows a good indexing rate with equiaxed grains throughout the sample gauge. The post-processed EBSD map of the rectangular region on

the left side of the sample is shown at higher magnification in Fig. 4.4(c). The GBs are colored according to their misorientation angle, ranging from very low misorientation GBs (blue) to high misorientation GBs (yellow). The relative orientation of the hexagonal unit cells is shown in the center of each grain and reveals a marked texture. The basal plane pole figure in Fig. 4.4 (d) shows a strong inclined basal texture, with the c-axes tilted about $\pm 30^{\circ}$ from the Z axis (perpendicular to the surface). This texture is typical of cold-rolled commercially pure Ti [64] and agrees with the bimodal misorientation angle distribution obtained from the DCT data (Fig. 4.3 (b)). As a result of this texture, tensile deformation will favor the activation of two of the three prismatic <a> slip systems in the hexagonal unit cell, whose SF are close to 0.5 (Fig. 4.4 (c)).

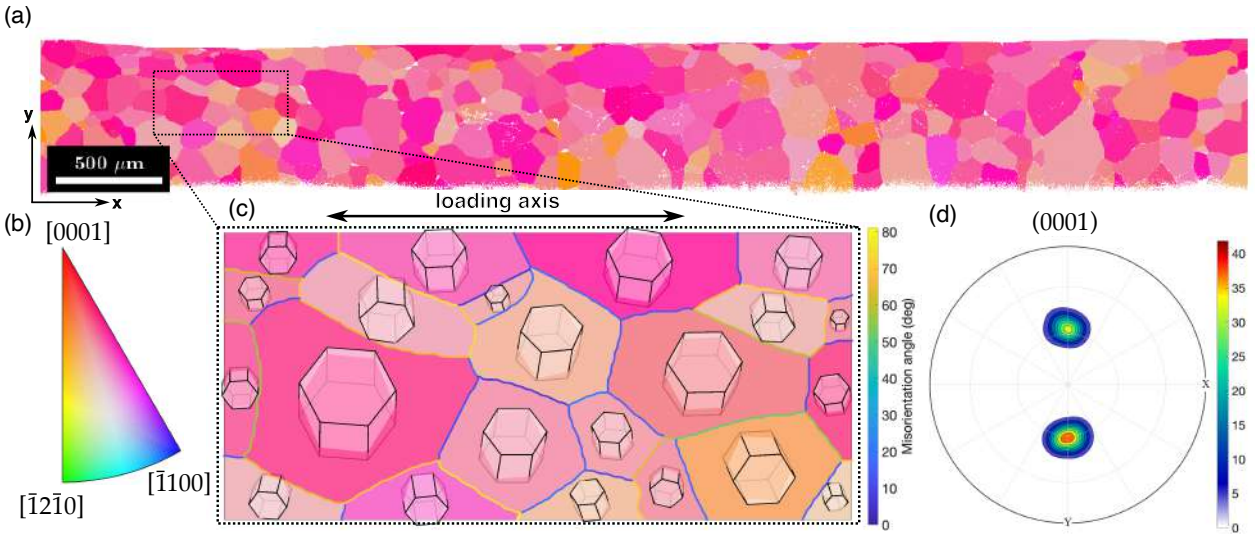

Figure 4.4: Microstructure of the gauge section of the sample from EBSD. (a) Raw EBSD map colored according to the inverse pole figure perpendicular to the surface in (b). White dots correspond to regions that were not indexed by EBSD. The loading axis is horizontal, as indicated by the arrow. (c) Post-processed EBSD map of the rectangular region indicated in (a) at higher magnification. GB are colored according to their misorientation angle in degrees, and the orientation of the hexagonal unit cell is shown at the center of each grain. (d) Basal plane (0001) pole figure. Intensity is marked in multiple of random distributions.

4.3.3 Slip trace and slip transfer analysis

The analysis of 233 grains in the SEM revealed that only prismatic <a> slip took place in the sample, favored by the strong texture. The lack of activation of other basal <a> or pyramidal <c+a> slip systems facilitates the unique identification of the active slip system (slip plane and direction) since the three prismatic planes lead to slip traces with different orientations on the sample surface. It should be noted that the active slip system identification through conventional slip trace analysis is not effective if the slip plane or the Burgers vector is parallel to the sample surface. To avoid this problem, the material and texture were carefully selected for this investigation to limit the number of active slip

systems to avoid the noise and complexity introduced by the activation of many (and different) slip systems [178]. In particular, (1) the prismatic planes are always oblique to the loading direction, and only one or two of them were suitably oriented for slip, and (2) the basal planes (which may be parallel to the sample surface) are very poorly oriented for plastic deformation given the geometry of the hexagonal lattice. Thus, it is very unlikely that other slip systems (besides prismatic) could be active, and any slip traces different from prismatic were not observed throughout the sample. The low CRSS of prismatic slip in pure Ti and the only observation of prismatic slip traces after deformation indicate that prismatic slip is enough to accommodate the plastic deformation in the sample.

Moreover, the deviation between the theoretical slip trace (calculated from the grain orientations obtained from the EBSD of the undeformed sample) and the observed slip trace was always $<5^{\circ}$. These small deviations between the observed and theoretical slip traces can be explained by the change in crystal orientation caused by the plastic deformation of the sample. Once one active prismatic slip system was impinging onto a GB, a number of parameters were measured for that GB. In the case of multiple slip in one or both grains across a GB, the best combinations in terms of the geometrical alignment between the active slip systems were chosen. This means that the two that provide the lowest κ and ψ were chosen in case that double prismatic slip was observed at both sides of a GB among the four possible combinations between the slip systems. The recorded parameters include GB misorientation Θ, the SF of the incoming and outgoing slip systems across the GB, and the four angles that characterize the geometrical alignment between the incoming and outgoing slip systems at the GB on the surface of the sample (κ, ψ, δ, γ) (Fig. 1.5). This information was recorded for 361 GBs considered reliable due to their similitude between EBSD and DCT, and was used to assess the slip transfer criteria.

The active prismatic slip systems were identified on either side of each GB, and they were classified according to the occurrence or absence of slip transfer in three distinct groups. The first group included those GBs in which slip transfer was convincingly observed, as revealed by the visible and unequivocal continuity between all or most of the slip traces at both sides of the boundary (Figs. 4.5 (a) and (b)). In some cases, only one slip system was active in both grains across the GB (Fig. 4.5 (a)), while double slip transfer along two different pairs of slip systems took place in other cases (Fig. 4.5 (b)). Slip transfer in these cases was confirmed by the absence of any changes in surface topography at the GB, indicating that deformation between the neighboring grains was homogeneous.

The second group included those GBs where slip blocking was observed, or in other words, where slip transfer was not observed (Fig. 4.5 (c)). The slip traces were stopped at the GB or did not match at both sides of the GB and, sometimes, feather-shaped microvolumes of deformation appeared near the boundary, indicating the presence of stress concentrations associated with heterogeneous plastic deformation [62, 70, 71]. The presence of a ledge or significant change in the topography at a GB is also indicative of heterogeneous deformation at both sides of the GB, and it is often associated with uncertain or poor slip transfer conditions [26, 185].

The third and last group corresponds to what we define as partial slip transfer (Fig. 4.5 (d)). These cases show slip transfer to some extent but were different from the perfect slip

transfer cases depicted in Fig. 4.5 (a) and (b). For instance, just a few slip bands matched across a GB, or some traces matched but faded away a few micrometers away from the GB.

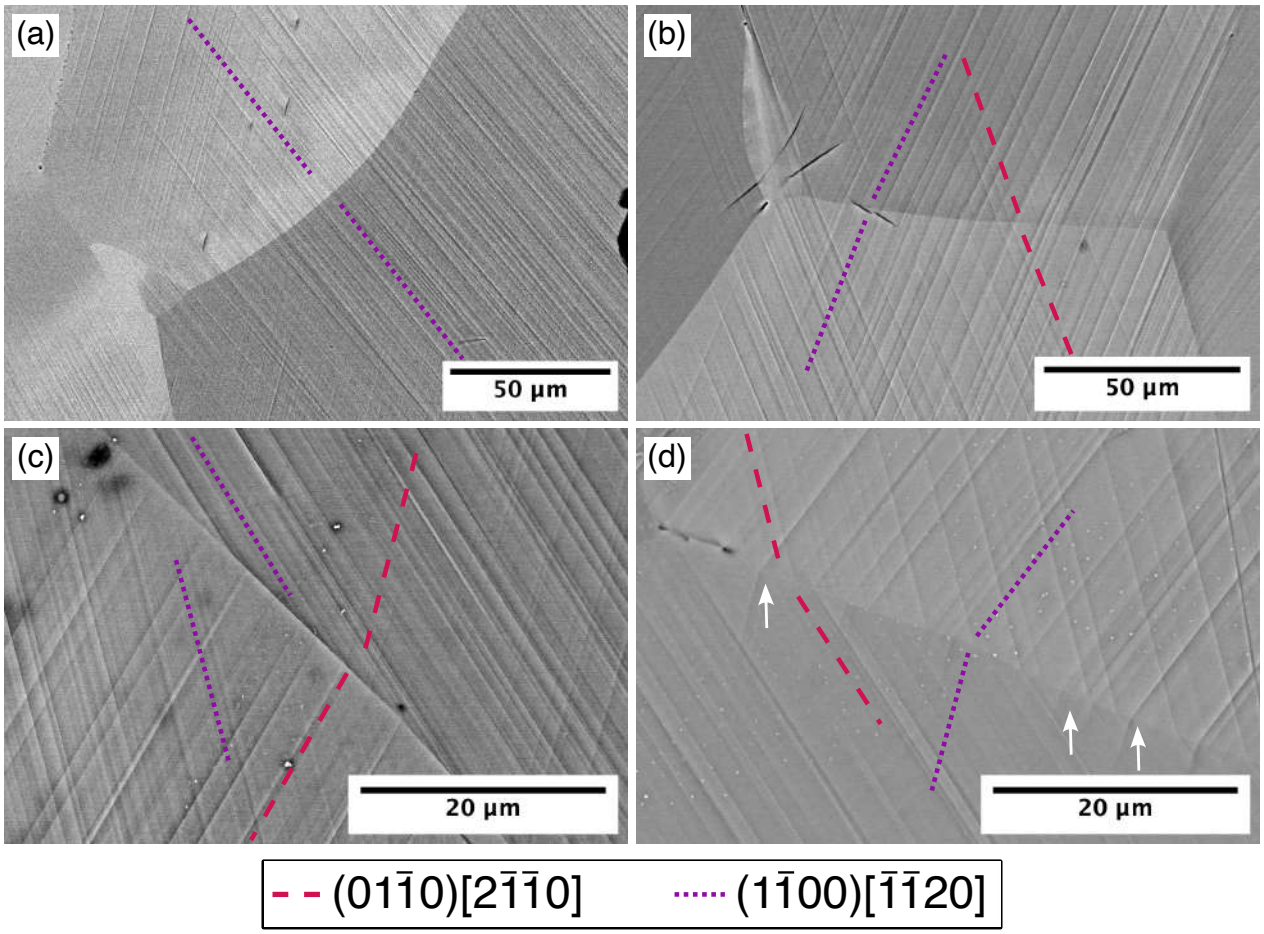

Figure 4.5: Prismatic-to-prismatic slip transfer/blocking across GB. The theoretical orientation of the slip traces of the active slip systems is indicated by the dashed lines. (a) Slip transfer. (b) Double slip transfer. (c) Slip blocking and ledge at the GB. (d) Partial slip transfer. The arrows indicate slip bands fading towards the grain interior.

Out of the 362 analyzed GB, convincing slip transfer was observed in 43.9% and partial slip transfer in 11.6% of the cases, leaving a remaining 44.5% of slip blocking instances (see Fig. 4.6 (a)). Therefore, the likelihood of slip transfer in this sample is distributed in approximately 50-50 fashion, i.e., 50% for partial + full slip transfer and 50% for slip blockage. The relationship between slip transfer, partial slip transfer, and slip blocking with GB misorientation angle is plotted in Fig. 4.6 (b). It shows that slip transfer (either perfect or partial) occurs at low misorientation GBs ($< 30°$). Nevertheless, there are still slip blocking events located at low misorientation GB, suggesting that the GB misorientation angle is not sufficient to predict prismatic-to-prismatic slip transfer across GBs in pure Ti. With a comprehensive database of the geometrical characteristics of the grains and grain boundaries, we can now assess how the different slip transfer criteria perform

for the current Ti sample.

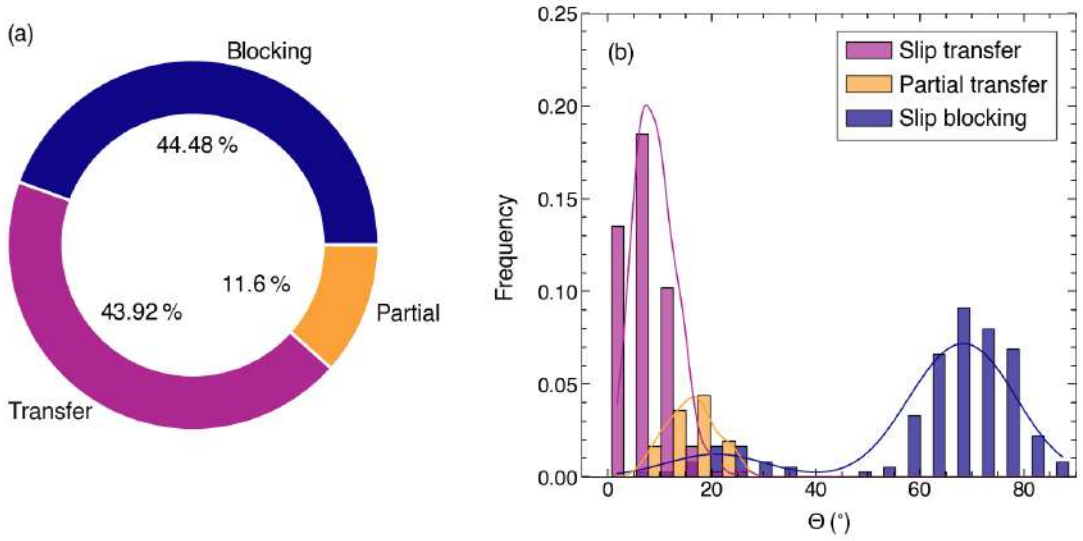

Figure 4.6: Distribution of slip transfer events in the microstructure: (a) Classification of prismatic-to-prismatic perfect slip transfer (purple), partial slip transfer (orange), and slip blocking (dark blue) across GB in Ti, and (b) Influence of GB misorientation angle distribution on the occurrence of perfect slip transfer, partial slip transfer and slip blocking.

4.3.4 Evaluation of slip transfer criteria

The slip transfer criteria presented in the introduction rely on the angles κ, ψ, γ, δ, and θ, in addition to the misorientation angle. All of them can be determined for each GB from the EBSD information of the neighboring grains except for θ, which requires 3D information about the orientation of the GB within the sample, given by $\boldsymbol{n}_{GB}$. This information was determined from the DCT data for 266 GBs out of the 362 analyzed by slip trace analysis (74%). This difference is due to the limitations of the DCT technique to accurately capture the shape and orientation of small grains [60]. Only GBs whose shape was accurately determined by both LabDCT and EBSD were included in the analysis. The twist angle θ was calculated using Eqs. (4.1) and (4.2), which take as input the grain boundary normal, $\boldsymbol{n}_{GB}$, obtained from LabDCT data, and the normals of the active slip planes across the GB, $\boldsymbol{n}_A$ and $\boldsymbol{n}_B$, obtained from the combination of SEM imaging and EBSD crystallographic information.

Traditionally, κ (that determines the residual Burgers vector) and ψ (that captures the misorientation between the incoming and outgoing slip planes) have been considered the most relevant angles to assess slip transfer [26, 82], following the Luster-Morris parameter m'. Their ability to predict slip transfer is shown in Fig. 4.7 (a), which shows that the majority of slip transfer events were found when κ and ψ were $< 20°$, in agreement with previous investigations [7, 24, 130, 154]. In these cases, the incoming and outgoing slip systems are well aligned because the magnitude of the residual dislocation left at the GB is small, and the resolved shear stress acting on the incoming slip system is easily

transmitted to the outgoing slip system because ψ is also small. Moreover, all partial slip transfer instances are located at low to moderate values of these angles ($< 30°$), and all the blocking events are shifted towards higher angles, except for three outliers where there is a ledge at the GB, indicating that plastic deformation at these GBs was not homogeneous. Two of these three outliers correspond to the GB shown in Fig. 4.5 (c), which presents a significant change in topography between the adjacent grains. In this case, two slip blocking instances are observed between both pairs of active slip systems (purple-to-purple and pink-to-pink) despite presenting, in principle, suitable geometrical alignment for slip transfer. The information provided by the conventional slip trace analysis technique is not sufficient to explain why slip transfer is not observed across this GB. Nevertheless, other techniques, such as HRDIC, could be employed to assess the heterogeneous distribution of the deformation and the effect of the local stress on the occurrence of slip transfer.

The occurrence of slip transfer/blocking is plotted in Fig. 4.7 (b) as a function of κ and θ. Perfect slip transfer is associated with low values ($< 20°$) of both angles, but no instances of slip transfer are found if $\kappa > 30°$, regardless of θ. Low values of θ only lead to slip transfer if they are associated with low values of κ. Moreover, many perfect or partial slip transfer instances are found if $\kappa < 25°$ even for very large values of θ. Finally, the occurrence of slip transfer/blocking is plotted in Fig. 4.7 (c) as a function of ψ and θ. Slip transfer is mainly associated with low values of ψ, but there is no obvious trend with θ. Moreover, it should be noted that large values of θ ($< 30°$) can be found even when the incoming and outgoing slip planes are well aligned and $\psi < 20°$. Theoretically, when ψ is small, the slip planes are well aligned, and thereby θ is very small and independent of the GB inclination angle β (Fig. 1.5). However, as ψ increases, the twist angle θ is more sensitive to the GB inclination. Thus, it cannot be concluded that –in general– good alignment between the active slip planes leads to low twist angles, and it is necessary to obtain this information experimentally. Overall, these results seem to indicate that θ plays a secondary role in determining slip transfer/blocking, compared with κ and ψ for the current prismatic-dominated slip transfer. This can be an effect of the strong texture in the sample, where all plastic deformation can be accommodated through prismatic slip. The influence of θ in a randomly oriented sample is still not well understood and could affect slip transfer between prismatic and non-prismatic slip systems.

To obtain more quantitative information, a categorical model was used to assess the influence of the different angles (κ, ψ, θ, δ and γ in Fig. 1.5, together with the GB misorientation Θ calculated from the crystal orientation of the neighbor grains) on the likelihood of slip transfer. To this end, all the data were divided into two categories: slip transfer (including partial slip transfer) and slip blocking. This is a reasonable assumption since partial slip transfer instances do transfer slip to some extent. The occurrence or absence of slip transfer for each GB was characterized by the categorical variable *slip* that can only take the values of 1 or *true* (slip transfer) or 0 or *false* (slip blocking).

The next step was to determine the optimum value of each angle that is able to discriminate slip transfer from slip blocking for each angle. The procedure is schematically shown in Fig. 4.8 (a) for κ. For any value of κ (such as $\kappa = 45°$ in Fig. 4.8 (a)), the data set will be divided into two groups, with $slip = 1$ (slip transfer) to the left of κ and $slip = 0$ (slip

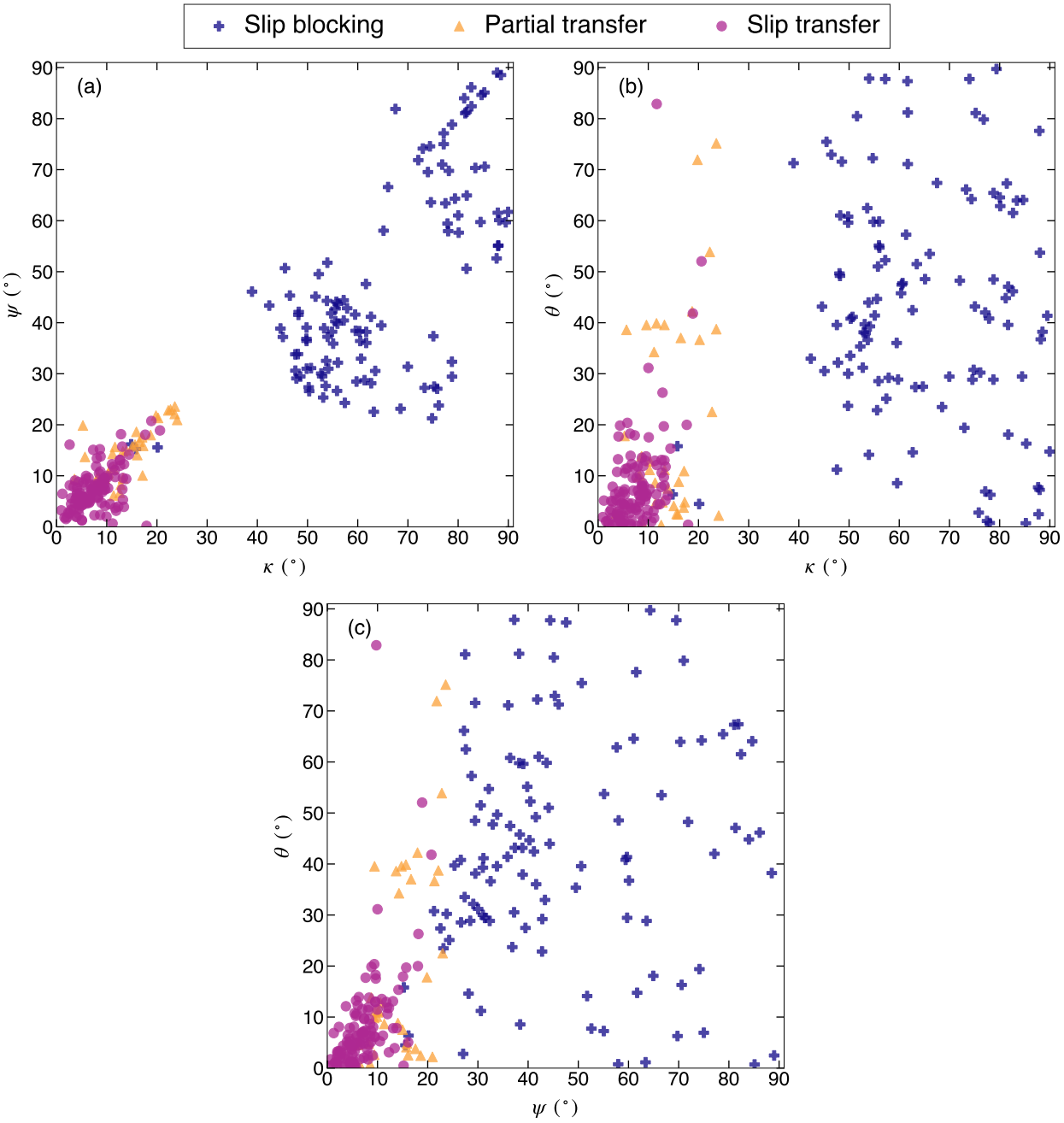

Figure 4.7: Dependence of slip transfer on κ, ψ, and θ: (a) Influence of κ and ψ on the occurrence of slip transfer/blocking across the GB. (b) Influence of κ and θ on the occurrence of slip transfer/blocking across the GB. (c) Influence of ψ and θ on the occurrence of slip transfer/blocking across the GB.

blocking) to the right of κ. This leads to a binary categorical model, where the data can be arranged in a confusion matrix including the true positives (TP), true negatives (TN), false positives (FP), and false negatives (FN), as depicted in Fig. 4.8 (b). Different model classification metrics, such as Precision (Eq. (4.3)) and Recall (Eq. (4.4)) [145, 176], can be

defined as

$$\text{Precision} = \frac{\text{TP}}{\text{TP} + \text{FP}} \tag{4.3}$$

$$\text{Recall} = \frac{\text{TP}}{\text{TP} + \text{FN}}. \tag{4.4}$$

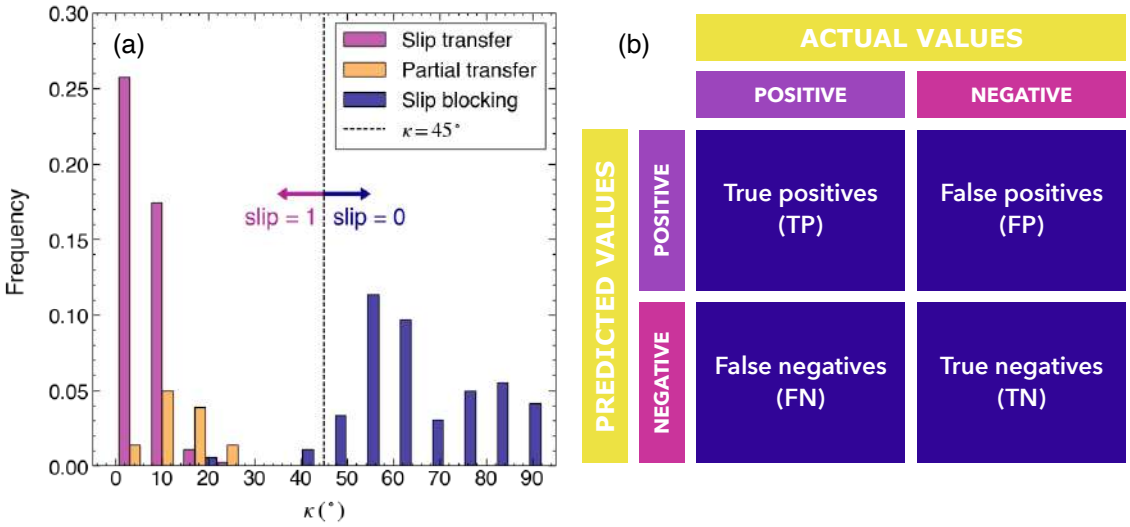

Figure 4.8: (a) Influence of angle κ on slip transfer, partial slip transfer, and slip blocking. A black vertical dashed line is drawn in $\kappa = 45°$ to represent a potential threshold that divides the data in predicted slip events ($slip = 1$) to the left of the line and predicted blocking events ($slip = 0$) to the right of the line. (b) Schematic representation of a confusion matrix to compare the actual and predicted values slip transfer/blocking for any categorical variable.

Precision or confidence deals with the "Predicted positive" row of the confusion matrix, determining how accurate the model is in predicting the positive outcomes out of all the predicted outcomes. Recall, or sensitivity, deals with the "Actual positive" column of the confusion matrix and measures the completeness of the positive predictions or how accurately the model was able to identify the positive outcomes out of all positive outcomes that were actually present. In other words, Precision indicates the accuracy of the positive predictions, whereas Recall refers to the percentage of positive values correctly classified by the model. In a model with 100% Precision, there are no false positives, and every positive prediction is correct, whereas with 100% Recall, there are no false negatives, and every negative prediction is correct.

Any of these metrics can be used to evaluate the performance of any categorical model, depending on the specific purpose of the model. However, they have to be combined into a single metric when precision and recall are equally important. This is normally achieved through the F1 score [176]

$$\mathrm{F1} = 2 \cdot \frac{\mathrm{Precision} \cdot \mathrm{Recall}}{\mathrm{Precision} + \mathrm{Recall}} \tag{4.5}$$

that can be interpreted as a measure of overall model performance ranging from 0 (worst) to 1 (best).

The threshold value for slip transfer for all the angles that characterize the GB was assessed from the maximum value of F1, and the results are summarized in Table 4.1. They show very similarly low values for the GB misorientation Θ, κ, ψ, and θ, and very similarly high values for δ and γ. However, the predictions for each angle are not similarly accurate; the higher the optimum F1, the better this angle can predict slip transfer/blocking. This information is summarized in the F1 score matrix (Fig. 4.9), which shows the maximum value of F1 for each angle in the diagonal of the matrix as well as the maximum F1 that can be obtained by choosing any pairwise combination of two angles with their respective thresholds presented in Table 4.1. The F1 score has been used as a heat map variable; therefore, the colors of each box in the matrix represent the magnitude of F1 compared to the other boxes.

According to the data in Fig. 4.9, the best indicator of slip transfer is $\kappa < 24.5°$, with F1 = 0.993. The F1 values for all the out-of-diagonal terms are smaller than this value, which means that the combination of two angles does not lead to better predictive performance for the current microstructure. It is also worth mentioning that combining three or more angular parameters leads to worse results than those presented in Fig. 4.9. The next best performances are attained by the pairwise combinations of misorientation Θ, κ, and ψ, whereas the performance of criteria based on the θ angle always attains the poorest performances to predict slip transfer/blocking. It should be noted that these findings may differ for a more random microstructure, and further exploration is needed to assess more diverse cases.

Table 4.1: Threshold angle (according to the F1 score) to predict slip transfer.

Angle	*Threshold angle*
Θ	$< 24.5°$
κ	$< 24.5°$
ψ	$< 23°$
θ	$< 23°$
δ	$> 74°$
γ	$< 78.5°$

A similar analysis was carried out to assess the performance of the slip transfer criteria presented in the introduction of this paper, namely GB misorientation angle Θ, Luster-Morris parameter m', normalized Burgers vector $\Delta b/b$, LRB, and N. The corresponding threshold values of each parameter for slip transfer that led to the highest F1 score are shown in Table 4.2. These thresholds were used as the best possible separation between the slip

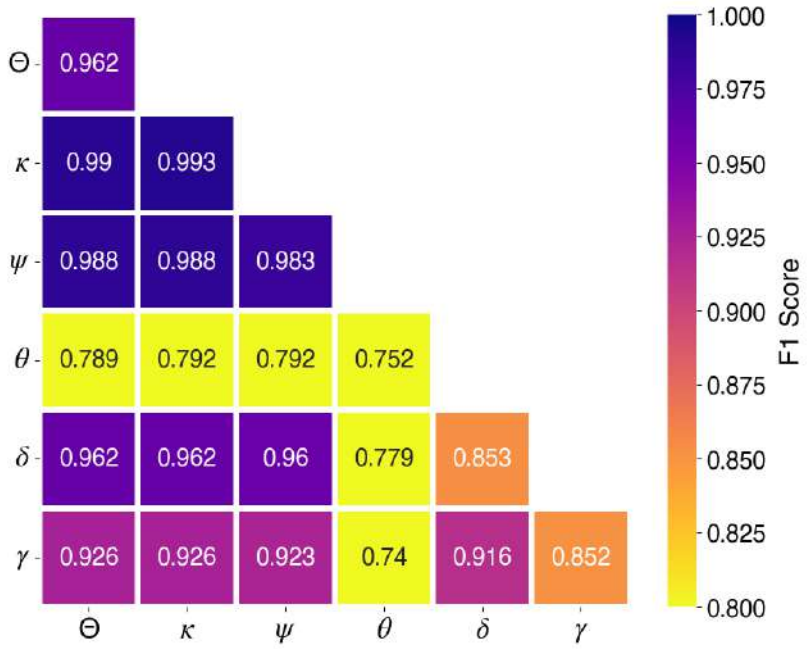

Figure 4.9: F1 score matrix for slip transfer/blocking. The diagonal terms represent the performance of a single angle in terms of the F1 score, whereas the out-of-diagonal terms represent the F1 score obtained by the combination of two angles. The F1 score value is indicated in each box and represented as a heat map variable, ranging from yellow (lowest) to blue (highest). The threshold that leads to the maximum F1 for each angle is depicted in Table 4.1.

transfer and blocking populations, and the corresponding F1 score matrix is presented in Fig. 4.10.

Besides low misorientation angles, slip transfer is likely to occur for low $\Delta b/b$ and high m' and N. The accuracy of these thresholds to predict the slip transfer/blocking, according to the F1 score, is shown in Fig. 4.10. The best performance is obtained with either $\Delta b/b$ or m', which leads to F1 = 0.993. Other slip transfer criteria (N and Θ) lead to lower F1 scores, while the LRB criterion gives the lowest F1 metric, indicating that it is not a good criterion to predict prismatic-to-prismatic slip transfer/blocking at GBs in Ti. The combination of two slip transfer criteria (for instance, $\Delta b/b$ and m', $\Delta b/b$ and N, m' and N) improves the F1 score up to the values obtained with only $\Delta b/b$ or m' but not more. On the contrary, the F1 score of LRB or any combination of LRB with another criterion is much lower, indicating that LRB is not a reliable criterion for slip transfer/blocking for this particular system.

4.4 Discussion

The results presented in the previous section provide the first assessment of slip transfer across GBs in polycrystalline metals in which a) the active slip systems across the GB

Table 4.2: Optimum threshold (for maximum F1 score) for different well-known slip transfer criteria.

Parameter	*Threshold*
Θ	$< 24.5°$
m'	> 0.8
$\Delta b/b$	< 0.45
LRB	> 0.65
N	> 0.9

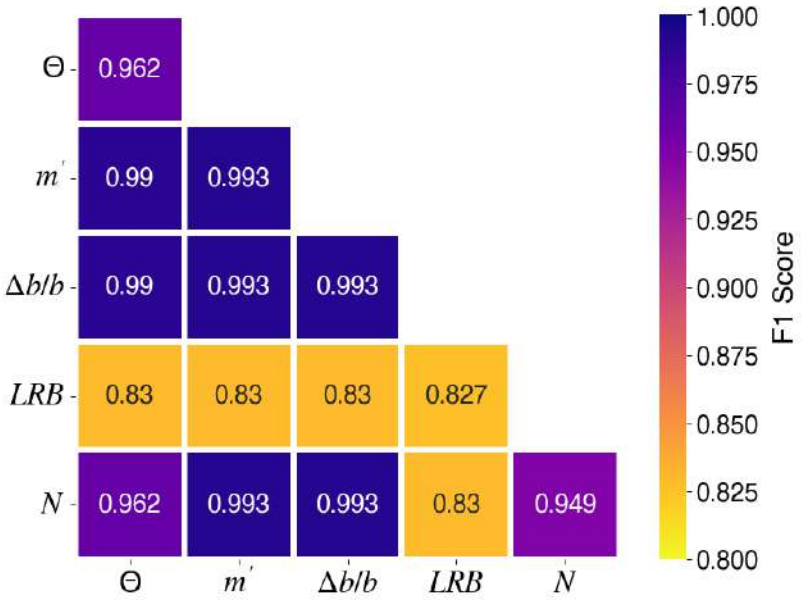

Figure 4.10: F1 score matrix for slip transfer/blocking. The diagonal terms represent the performance of a single slip transfer criterion in terms of the F1 score, whereas the out-of-diagonal terms represent the F1 score obtained by the combination of two slip transfer criteria. The F1 score value is indicated in each box and represented as a heat map variable, ranging from yellow (lowest) to blue (highest). The threshold that leads to the maximum F1 for each slip transfer criterion is depicted in Table 4.2.

are actually identified, b) the GB geometry is fully characterized in 3D and c) slip transfer/blocking data are obtained in a statistically significant number of GBs. These unique advantages allow us to robustly identify the governing geometrical parameters that impact the slip transfer in our prismatic slip-dominated Ti sample.

One of the primary conclusions of the analysis of the data is that the normalized residual Burgers vector across the GB, $\Delta b/b$, appears to be the best criterion to predict slip transfer, which is likely to occur if $\Delta b/b < 0.45$ (or $\kappa < 24.5°$) while slip blocking will be dominant otherwise. Similar scores are obtained in the case of m', which includes information about the residual Burgers vector and the angle ψ between the normals of the incoming and the

outgoing slip planes, which are related to the resolved shear stresses in both planes.

It should be noted, however, that the particular texture of the Ti sample leads to the presence of two prismatic planes in each grain with very high SF. Thus, if $\Delta b/b$ is small and there is no large barrier for slip transfer, the incoming dislocations will likely find another slip system with a high resolved shear stress in the neighbor grain that will be available to accommodate slip transfer. Thus, it is possible that m' (that includes the information about the residual Burgers vector) becomes a better predictor of slip transfer/blocking in other microstructures. These results generally agree with previous investigations based on surface observations in different polycrystalline metals [7, 24, 26, 82, 130].

The second main conclusion of this analysis is that the twist angle θ (and, thus, the LRB criterion) does not appear to be a good predictor of slip transfer/blocking for the grain orientations in the prismatic slip-dominated Ti sample tested here. Many instances of perfect and partial slip transfer were found for high values of θ, and slip transfer never occurred for low values of θ unless the residual Burgers vector was also small (Fig. 4.7 (b). This result is, to some extent, surprising because the limited information available in the literature seemed to indicate that θ played a major role in slip transfer. Zhou *et al.* [200] studied basal-to-prismatic and basal-to-pyramidal slip transfer in a Mg alloy. The actual basal slip system was determined using lattice-rotation analyses, and slip transfer was reported in 23 cases, corresponding to high m' in 16 cases and low $\Delta b/b$ in 21 cases. The GB orientation was measured by sectional grinding in one of the cases with slip transfer and low m', and it was found that $\theta = 26°$. Nevertheless, θ was not measured (but estimated) in other cases with slip transfer and low m', and solid conclusions could not be reached. Besides that, low $\Delta b/b$ seems to be a very good predictor of basal-to-prismatic and basal-to-pyramidal slip transfer in Mg.

Furthermore, Sarebanzadeh *et al.* [154] recently carried out a detailed analysis of basal-to-basal slip transfer in pure Mg. The actual active basal slip system in each grain was carefully identified by means of slip trace - modified lattice rotation analysis [190] and slip blocking when $m' < 0.45$ and $\Delta b/b < 0.6$ was only found in a few cases, that were analyzed in detail. They corresponded to situations in which basal slip was almost parallel to the GB (and, thus, slip lines did not cross the boundary) or to five cases in which the GB orientation was measured through the thickness through sequential FIB. $\theta > 60°$ in all these cases, and it was concluded that high twist angles may hinder basal to-basal slip transfer in Mg. In fact, the actual slip transfer mechanism for high twist angles is not known, and it has been suggested [73] that the activation of secondary slip systems (such as <a> basal or pyramidal slip in Ti) is needed near the GB to accommodate slip transfer between the primary prismatic slip systems when θ is high. While this is possible in Ti, because the critical resolved shear stress for <a> basal slip is not far away from that for <a> prismatic slip, this is unlikely to happen in Mg, in which the critical resolved stress for <a> basal slip is much lower than for other slip systems, blocking slip transfer for high twist angles. Zhou *et al.* [200] measured subsurface dislocation activity by differential aperture X-ray microdiffraction in five grains and found that <c+a> dislocations were active, but their activity did not appear at the surface. This observation implies that other unexpected dislocation sources may be assisting the slip transfer process under the

surface.

In the case of special GBs, such as twin boundaries, the effect of the twist angle can be assessed because the GB normal can be directly determined from the known crystallographic rotation between the parent and the twin. Genée *et al.* [62] analyzed slip transfer across $\Sigma 3$ annealing twin boundaries in a Ni-based superalloy and reported that the θ was the main geometrical parameter determining slip transmission across twin boundaries, where $\theta = 0°$ appeared as a necessary condition for slip transfer. Chen *et al.* [38] performed uniaxial tensile testing at $650°C$ in Inconel 718 Ni-based superalloy and also reported that $\theta = 0°$ and $\Delta b < 0.6b$ are sufficient conditions to ensure slip transfer across twin boundaries. However, the actual pair of active slip systems across the twin boundary was dictated by the maximum Schmid factor and was not conclusively established. Nieto-Valeiras and LLorca [130] acquired a significant number of slip transfer/blocking occurrences across grain and twin boundaries in a pure Ni sample deformed in tension. Slip transfer across twin boundaries was only observed when $\Delta b \approx 0$, regardless of the twist angle θ, which pointed out that slip transfer across annealing twins seems to be controlled by dislocation cross slip. Regarding regular grain boundaries, the effect of θ was not assessed due to the lack of information about the GB normal, but slip transfer was generally observed when $m' > 0.8$.

It should be finally noted that - given the experimental difficulties in measuring the GB orientation through the thickness of polycrystalline samples - some studies have assumed that GB is perpendicular to the sample surface [38, 62, 103] to study the effect of θ on the likelihood of slip transmission. Under this assumption, Genée *et al.* [62] determined that slip transfer was mostly observed for $\theta < 30°$, although it was also found for higher twist angles $> 40°$. Similarly, Chen *et al.* [38] stated that slip transfer was likely to occur when $\mathrm{LRB} > 0.82$, but several slip blocking instances were found at high LRB values while slip transfer was also observed below such threshold. However, this hypothesis may lead to large errors in the evaluation of θ and thus on LRB.

Thus, the experimental information obtained in this work provides -for the first time- sound evidence that prismatic-to-prismatic slip transfer across regular GBs in Ti is favored by a minimum magnitude of the residual Burgers vector and also by the good alignment between the incoming and outgoing slip planes, while the twist angle plays a secondary role in the process. However, it is important to mention that the negligible effect of the twist angle, in this case, could be affected by the strong texture present in the sample, which could lead to easier plastic deformation accommodation. The influence of the twist angle could still be important for slip transfer between non-prismatic slip systems in randomly oriented Ti samples.

This investigation showed that some of the simple geometrical slip transfer criteria (i.e., those based in Δb and m') can be used to assess slip transfer/blocking in > 99% of the GBs and, thus, are suitable to be incorporated into crystal plasticity models to simulate the behavior of polycrystals. In addition, large twist angles do not hinder prismatic-to-prismatic slip in Ti. However, there are a few GBs within the analyzed dataset whose behavior does not follow these geometrical criteria. These outliers could be caused by the local stress distribution in the GB neighborhoods, which may change the local SF, hindering slip transfer.

As mentioned in the introduction (1.3), conventional slip trace analysis does not provide any information about the strain heterogeneity within the sample, and other techniques, such as HRDIC, are required in order to assess the effect of the local stress state around GBs on the likelihood of slip transfer.

4.5 Conclusions

In this chapter, slip transfer across GBs was analyzed by means of SEM-based slip trace analysis and electron backscatter diffraction in a thin Ti sample which presented a strong rolling texture. The two-dimensional microstructural analysis was combined with three-dimensional grain maps, procured through LabDCT, which allowed for the determination of 3D grain shapes and the orientation of grain boundaries within the sample. After a thorough characterization, the sample was loaded in tension, which resulted in the activation of its <a> prismatic slip systems. The orientation of the active prismatic slip system(s) in each grain was determined from the orientation of the slip traces, and slip transfer/blocking was analyzed in > 300 GBs on the sample surface. The likelihood of slip transfer/blocking as a function of the main angles that characterize the incoming and outgoing slip systems and the grain boundary (misorientation angle Θ, κ, ψ, θ, γ and δ) was assessed by means of the "F1 score" within the framework of categorical models. The analysis was further extended to assess the efficacy of widely used slip transfer criteria available in the literature (Θ, $\Delta b/b$, m', LRB, and N). Via a thorough analysis of the various geometric characteristics of grains and grain boundaries, we arrived at the following observations:

1. For the current prismatic slip-dominated Ti sample, the best angle to predict slip transfer was the angle between the incoming and outgoing slip directions, with $\kappa < 24.5^\circ$ as the threshold for slip transfer with an F1 score of 0.993.
2. The next best performances were attained by the pairwise combinations of grain boundary misorientation angle Θ and the angles between incoming and outgoing Burgers vectors and slip planes, κ, and ψ.
3. Interestingly, the predictions for slip transfer based on the twist angle θ resulted in the poorest performance for the current prismatic slip-dominated system.
4. From the slip transfer criteria available in the literature, the best performance was obtained with either $\Delta b/b$ or m' slip transfer criteria (that lead to an F1 score of 0.993) while other slip transfer criteria (based on N and or the misorientation angle), led to lower F1 scores, with the LRB criterion giving the lowest F1 metric.
5. The combination of two slip transfer criteria (for instance, $\Delta b/b$ and m', $\Delta b/b$ and N, m' and N) improved the F1 score up to the values obtained with only $\Delta b/b$ or m', but not more.
6. In contrast, any combination of LRB with another criterion led to much lower F1 scores, indicating that LRB was not a reliable criterion to predict prismatic-to-prismatic slip transfer/blocking at GBs in the current Ti sample.

The results of this analysis highlight the effectiveness of combining established characterization techniques like EBSD and SEM with newer methods, like LabDCT, in thoroughly decoding the mechanisms of slip transfer in metals. The study has delivered substantial evidence that, in the case of the prismatic-slip dominated Ti sample, prismatic-to-prismatic slip transfer across regular GBs in Ti is facilitated by a minimal residual Burgers vector and a favorable alignment between the incoming and outgoing slip planes. The methodology demonstrated in this chapter could assist in shedding light on the comparative influence of the different geometrical parameters in more diverse slip systems.

Nevertheless, a few GBs in the dataset presented slip blocking when slip transfer should be active according to the geometrical criteria. This abnormal slip transfer phenomenon could be caused by the local stress state near those GBs, and HRDIC will be used in the next chapter to assess this behavior.

5 Analysis of slip transfer in pure Ti through HRDIC

5.1 Introduction

The geometrical slip transfer criteria have been successfully used to predict slip transfer/blocking across GBs in metallic materials [19, 91]. Nevertheless, they are not always accurate, and slip blocking is sometimes found in GBs with good geometrical alignment and vice versa [70, 88, 131, 154]. These deviations from the regular behavior were attributed to two main reasons: the precise identification of the active slip systems across the GB and the influence of the twist angle θ that cannot be obtained from surface information. These limitations were overcome in the previous chapter (Chapter 4) through the choice of a Ti sample with only prismatic slip activity and the use of LabDCT to scan the microstructure in 3D. Thus, the active slip system was uniquely identified, and the twist angle θ was calculated.

Nevertheless, several outliers were still found within the data, and slip blocking or partial slip transmission (i.e. just a few slip bands matched across a GB or some traces matched but then faded away a few micrometers away from the GB) was found in GBs that were suitably oriented for slip transfer. These results point out the complexity of the slip transfer process in which good alignment between incoming and outgoing slip systems seems to be necessary, but no sufficient condition and other factors may be relevant. For instance, the applied stress (that controls the driving force for slip activation) may lead to slip transfer once a minimum threshold is overcome, or the activation of cross-slip may be necessary to allow slip transfer when the twist angle is high [73]. This latter mechanism would explain why θ angles impede basal-to-basal slip transfer in Mg (because cross-slip from prismatic or pyramidal is very difficult due to the large critical resolved shear stresses) but nor prismatic-to-prismatic slip transfer in Ti.

HRDIC appears as a powerful tool for quantifying the strain heterogeneity near GBs in polycrystalline metals and ascertaining other processes that affect slip transfer/blocking at GBs. Unlike conventional EBSD-based slip trace analysis, HRDIC can capture the surface strains at the sub-grain scale, where plasticity is localized at individual slip bands, GBs, and triple junctions. Different investigations have used this technique to examine

the spatial distribution and the slip characteristics in Ni-based superalloys [79, 167], and others have attempted to correlate the dislocation-GB interactions with the plastic strain heterogeneity at the GB neighborhood. Other works have analyzed slip transfer and the plastic strain concentrations via HRDIC in Ni-based superalloys [2], FeCr BCC alloys [140], or TiAl alloys [65]. Thus, HRDIC can provide extra information about the local plastic strains near the GB that can be used to elucidate other factors –besides good alignment– that control slip transfer at GBs.

In this chapter, HRDIC has been used to assess slip transfer/blocking in a pure Ti foil as a function of the applied strain. The microstructure of the sample was characterized in 3D using DCT to have all the geometrical parameters that describe the slip configuration across a GB, especially the twist angle θ. The occurrence or absence of slip transfer at different deformations was ascertained from the observation of the slip bands in the shear strain HRDIC maps, which also provided information about the strain heterogeneity in the specimen after plastic deformation. Then, the well-known geometrical slip transfer criteria were tested for every GB analyzed to evaluate their performance to predict the likelihood of slip transmission, and particular attention was paid to those GBs in which the geometrical criteria failed.

5.2 Materials and methods

A similar sample to that used in Chapter 4 (Fig. 4.1) was employed, with identical heat treatment and sample preparation.

5.2.1 Microstructural characterization

EBSD maps of the gauge section of the sample were acquired before and after mechanical deformation. The crystallographic orientations were collected in an FEI Helios NanoLab 600i dual-beam microscope with an Oxford Instruments EBSD detector. The whole gauge length was mapped by the serial acquisition of several overlapping maps, followed by stitching in AZtec. The EBSD maps were acquired at 20 kV and 2.7 nA, with 3 μm step size for the maps before deformation (in which the whole gauge was mapped) and 0.6 μm after deformation in the selected region to accurately capture the crystallographic orientation gradients. The overall quality of the EBSD maps was above 95% indexing. The maps were post-processed with the MTEX Matlab Toolbox [14], and the GB misorientation threshold was set to 2° to capture low-angle GBs.

The microstructure of the sample was characterized in 3D using a Zeiss Xradia Versa 620 X-ray microscope with a DCT pro module [13]. The diffraction contrast data was collected following a helical phyllotaxis high aspect ratio tomography strategy, where the vertical and the rotational motion are combined to capture the entire sample in a single scan, as explained in Chapter 3. The flat panel detector was used to capture the diffraction spots, and a projection geometry was employed for this scan by positioning the source 14.5 mm from the sample and the detector 245 mm from the sample. The source voltage and power were set to 110 kV and 10 W, respectively. An exposure time of 15 seconds was used per

projection to ensure a good signal-to-noise ratio. The different regions of the sample were illuminated with a polychromatic beam through a letterbox aperture of 250×750 μm^2. A total of 3032 diffraction projections were collected to cover the entire gauge section, resulting in a total scan time of 13 hours. The advantages of helical phyllotaxis as compared with conventional DCT scanning have been recently reported [60, 134], and explained in Chapter 3.

The acquired DCT projections were reconstructed with GrainMapper3D (Xnovo Technology) using the forward modeling approach [132] until the average completeness values reached at least 90%. Then, Dream3D [69] was used to segment the volume into grains and GBs, and Paraview [12] was used for visualization purposes. The DCT acquisition strategy and post-processing workflow are detailed in Chapter 3.

The reconstructed sections were denoised and segmented in Dream3D using a minimum completeness value of 0.1 and a GB misorientation threshold of 2° to characterize the GBs in 3D. Then, the spurious data were filled using an erode/dilate process with two iterations. Once the volume of the sample was reconstructed, a triangular surface mesh was generated over the inner GBs and outer surfaces of the samples. The initial triangular surface mesh was smoothed using a Laplacian smoothing algorithm to avoid the stair-stepped appearance, and the resulting triangle data (triangle id, centroid, area, curvature, misorientation, and normal direction) were exported for further analysis. The reconstructed volume of the sample is shown in Fig. 5.1 (a), where the region of interest (ROI) is displayed along with the smooth surface mesh generated at the GBs. The surfaces within the triangular mesh are colored according to the GB numerical identifier. The grains within the studied ROI are colored according to the inverse pole figure plotted in Fig. 5.1 (b). Fig. 5.1 (c) shows a close-up view of a pair of grains within the ROI, where the volume reconstructed with voxels (cubic elements) is shown on the left, and the smoothed GBs are shown on the right.

The normal vector to each triangle in the surface mesh was directly obtained from the surface mesh, and the GB normal direction was estimated. To this end, a different subset was generated for every GB from the triangular mesh, so only the corresponding triangle normals were selected. The triangle winding was carefully checked and corrected so that all normal directions were pointing in the same direction. Given that the mean curvature of the studied GBs is close to 0, the GB normal was taken as the mean of the triangle normals included in the surface.

5.2.2 High-resolution digital image correlation

HRDIC was used to capture the heterogeneous strain distribution and assess slip transfer at different applied strains in the sample. An Au nano-speckle pattern was created on the surface of the gauge section of the sample- To this end, a fine Au layer of ~ 15 nm was deposited by sputtering on the electropolished surface, followed by remodeling in a saturated water vapor environment for 3 hours at 350 °C, as indicated in [66]. A small ROI was mapped in the SEM, followed by tile stitching and further correlation. The individual images were acquired in a Thermo Scientific Apreo 2S scanning electron microscope at 5

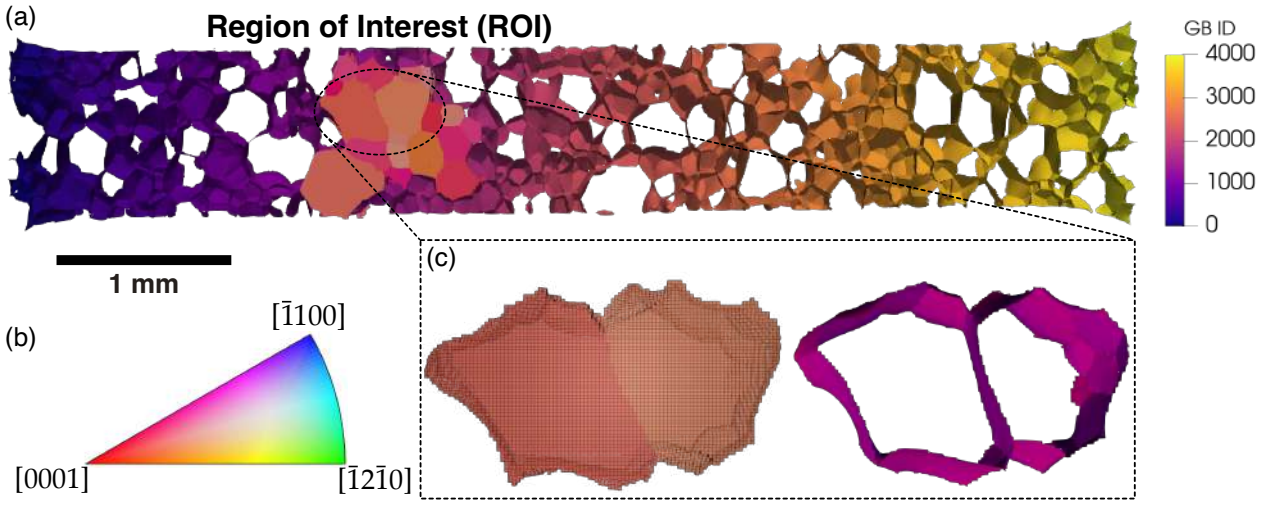

Figure 5.1: Microstructural characterization by DCT. (a) Reconstructed DCT map of the sample gauge, where the grains of the ROI have been colored according to the inverse pole figure with respect to the screen plane (color key in (b)). The region outside the ROI corresponds to the surface mesh generated at the GB, colored according to an integer number given to each GB (GB identifier). (c) Detailed view of two neighbor grains in the ROI, where the reconstructed voxelized volume is shown on the left and the corresponding surface mesh on the right.

kV voltage and 1.6 nA probe current to maximize spatial resolution. Moreover, the image quality was improved using the in-lens backscatter detector to achieve optimum contrast between the Ti substrate and the Au pattern. The working distance was set to 4.5 mm to maximize the signal-to-noise ratio, and every tile had a resolution of 1536×1024 pixels and a pixel size of ~ 65 nm. A representative SEM image of the Au pattern on the Ti sample for HRDIC is shown in Fig. 5.2 (a), where the nano-sized Au pattern (white particles) is homogeneously distributed onto the sample surface (black background). The particle size distribution was calculated using ImageJ standard particle size analysis procedures, depicted in Fig. 5.2 (b). The diameter of most Au particles is below 150 nm, thereby providing a suitable pattern to resolve microstructural features such as slip bands.

HRDIC provides the 2D full-field displacement tensor, which allows the calculation of the in-plane strain tensor. However, the effective shear strain, γ_{eff}, is a suitable metric of the heterogeneous strain in the metallic samples since plastic deformation in metals at room temperature occurs mainly dislocation slip [66]. It can be expressed as follows,

$$\gamma_{eff} = \sqrt{\left(\frac{\frac{\partial u}{\partial x} - \frac{\partial v}{\partial y}}{2}\right)^2 + \left(\frac{\frac{\partial u}{\partial y} - \frac{\partial v}{\partial x}}{2}\right)^2} \tag{5.1}$$

where u and v represent the horizontal and vertical components of the displacement field, respectively.

The background noise induced by the SEM operation was also assessed under the same

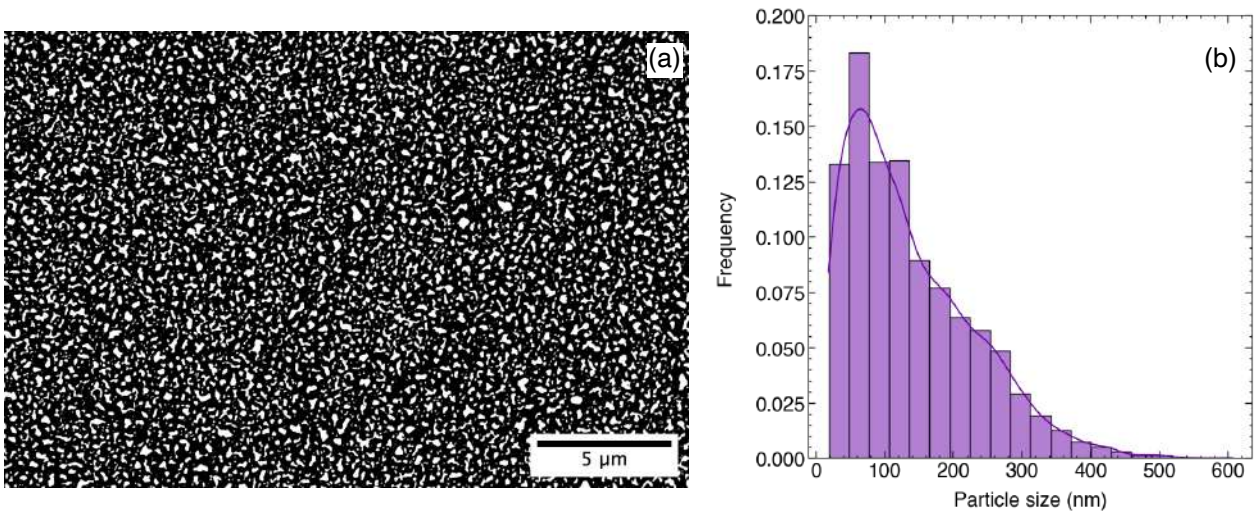

Figure 5.2: (a) Backscattered electrons image of the Au pattern on the Ti sample. The black background corresponds to the Ti substrate and the white speckles to the Au nano-sized pattern. (b) Au particle size distribution.

imaging conditions described above. The stage movement error was determined by the correlation between two images taken at the exact location after random movement of the SEM stage. The error was estimated as the mean shear strain in the correlated map and was below 0.98%. The error induced by the raster scanning during the image acquisition process was assessed by the consecutive acquisition of two images at the exact location. The correlation of these maps leads to an error of 0.74%. This means that the errors induced by the SEM were below 1% shear strain for any HRDIC maps taken under these imaging conditions. Finally, the out-of-plane pseudo-strain error –the error introduced by the movement of the grains out of the sample plane– can also be estimated. To this end, several images were acquired at the exact location for different defocusing conditions, ranging from -30 to 30 μm, to simulate an out-of-plane state. The images were correlated with the image at the focus condition pairwise, and the average effective shear strain was recorded for each of them and plotted against the defocus distance. This representation leads to a u-shaped curve, where the maximum error is located at the extreme defocus distances of -30 and 30 μm, keeping the symmetry along the y-axis from the focus condition at 0 defocus. The primary outcome of this error determination was that any out-of-plane displacement below $\pm 10\ \mu m$ leads to an average shear strain of a maximum of 1% under these imaging conditions. There are no expected out-of-plane displacements above 10 μm for the small applied deformations in this investigation, and hence, the induced systematic pseudo-strains will be negligible. It should be mentioned that no spatial drifts were observed in the error distribution measured by these three methods.

Three different areas of study were mapped as grids of 6×6 individual images or tiles acquired with a 15% overlap to enable seamless stitching into a larger map. The images of the gold nano-speckle pattern after deformation were obtained after unloading. The total field of view of the stitched map was $\sim 525 \times 350 \mu m^2$, and the tiles were stitched together with a linear blending fusion algorithm provided by the Grid/Collection stitching plugin

included in the Fiji distribution of ImageJ [156]. The stitched maps after deformation were correlated with the map in the undeformed state with LaVision's commercial software DaVis 10 [104] using an interrogation window of 6×6 which corresponds to a sub-region size of 390×390 nm^2. The correlated maps obtained from DaVis 10 were post-processed and analyzed with the DefDAP deformation data analysis Python package [10].

5.2.3 Mechanical testing

The sample was deformed in tension in a Kammrath and Weiss micro-testing module equipped with a 1 kN load cell at a quasi-static strain rate of $\approx 10^{-3}\ s^{-1}$ and sequentially deformed three times *ex-situ* until approximately 1%, 2.5%, and 4.5% plastic deformation. After each deformation step, the sample was removed from the machine, and three different HRDIC maps within the ROI were acquired in the SEM.

5.3 Results and discussion

5.3.1 Slip transfer assessment from HRDIC data

The identification of the active slip systems from the HRDIC maps relies on the crystal orientations before plastic deformation provided by EBSD. The theoretical slip traces of the different slip systems in the crystal lattice of HCP-Ti are compared to those observed in the HRDIC maps to identify the active slip system(s) in each grain. The EBSD maps acquired within the ROI are presented in Fig. 5.3, (a) before plastic deformation, and (b) and (d) after 4.5% plastic deformation.

The crystal orientations before deformation are homogeneous, whereas orientation gradients are visible within several grains (G_{19}, G_{22} or G_{23} in 5.3 (b), or G_{11} and G_{12} in 5.3 (d)) after deformation. The EBSD maps acquired after plastic deformation present some non-indexed pixels, which in the case of G_{27} correspond to deformation twins. On the contrary, the non-indexed points in the EBSD map displayed in 5.3 (d) are caused by surface scratches and dirt deposited onto the Au speckle pattern. The *ex-situ* tensile test stress-plastic strain curve is presented in 5.3 (c), where the relevant steps of the experimental process have been labeled as def_i for the HRDIC maps and EBSD_i for the EBSD maps.

As shown in Fig. 5.3 (a), three HRDIC maps were acquired within the ROI after each applied deformation and correlated with the undeformed map. The effective shear strain maps (calculated from Eq. 5.1) acquired by HRDIC within the first sub-region of the ROI are depicted in Fig. 5.4. The slip traces of the active slip systems active 1% plastic deformation are visible and identified as prismatic slip bands in all cases, as revealed by the comparison with the theoretical slip traces (Fig. 5.4 (d)). The slip band intensity and the number of active slip bands generally increase while the slip band spacing decreases as plastic deformation increases. Furthermore, double prismatic slip can be observed in some cases from the first applied deformation (G_{12} in Fig. 5.4 (a)), while the secondary prismatic slip systems get activated after certain deformation in other cases (G_{11} in Fig. 5.4 (b)). After 2.5% plastic deformation, strain concentrations arise at GBs and triple junc-

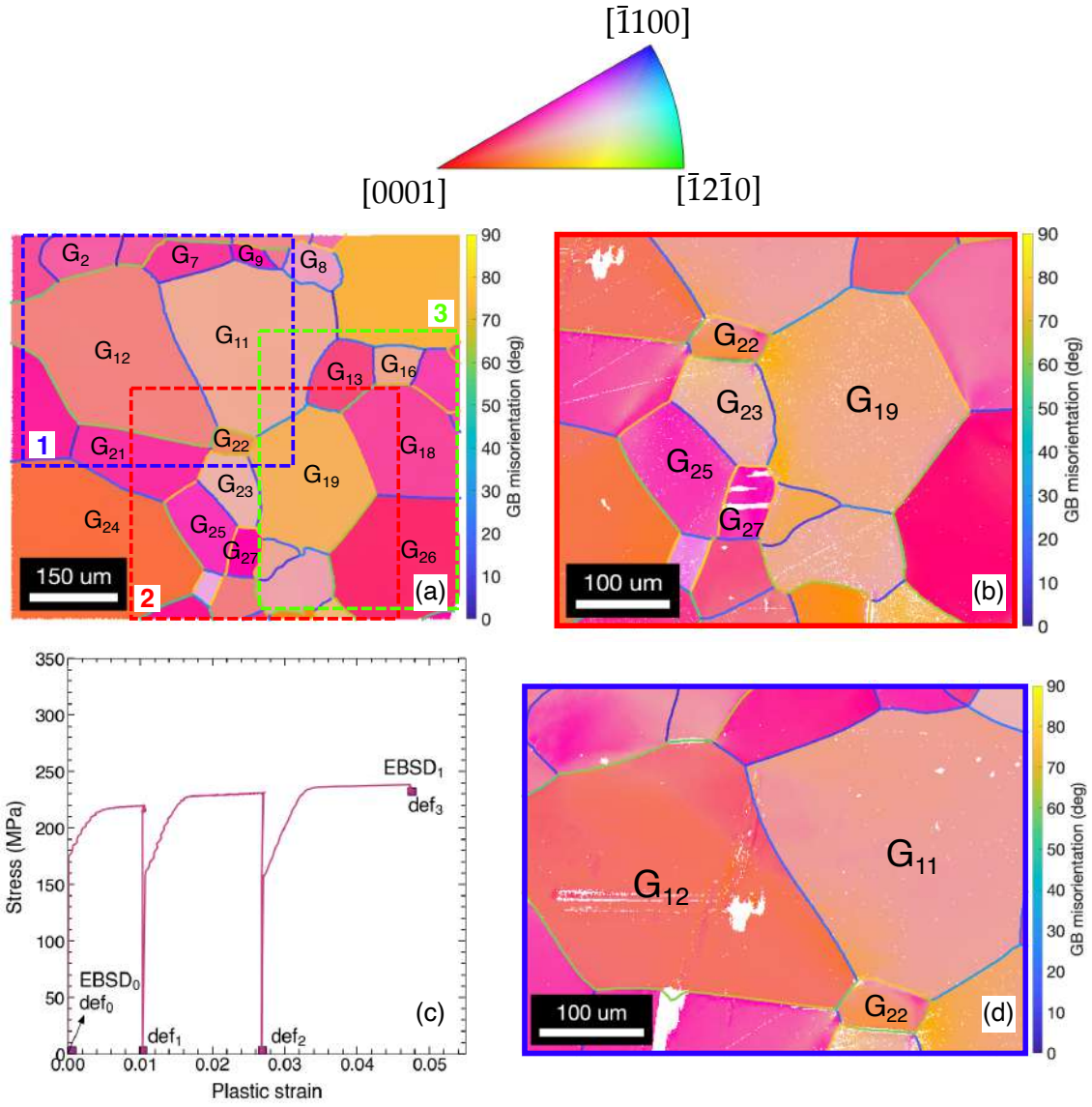

Figure 5.3: EBSD maps of the ROI surface. (a) EBSD map before deformation; the three dashed areas indicate the sub-regions where HRDIC maps were acquired. (b) EBSD map of sub-region two after 4.5% plastic strain. (c) Ex-situ tensile stress-plastic strain curve. The markers indicate the conditions in which the EBSD and the HRDIC maps were acquired. (d) EBSD map of sub-region one after 4.5% plastic strain. In the EBSD maps in (a), (b), and (d), the grains are colored according to the inverse pole figure with respect to the screen plane, shown at the top of the figure. The GBs are colored according to their misorientation angle Θ, ranging from low misorientations (blueish colors) to high misorientations (yellowish colors). The grains of interest have been labeled in (a). The non-indexed pixels have been colored in white in (b) and (d).

tions, as indicated by white arrows in Fig. 5.4 (b). When the strain reaches 4.5%, the shear strain levels and the strain concentrations at GBs and triple points drastically increase (Fig. 5.4 (c)). The shear strain distribution shows a macro-strain band that goes through G_{12}, de-

limited by the two red dashed lines in Fig. 5.4 (c) in which the shear strain is localized. As a result, the contrast between the effective strain levels within and outside the macro-band is huge.

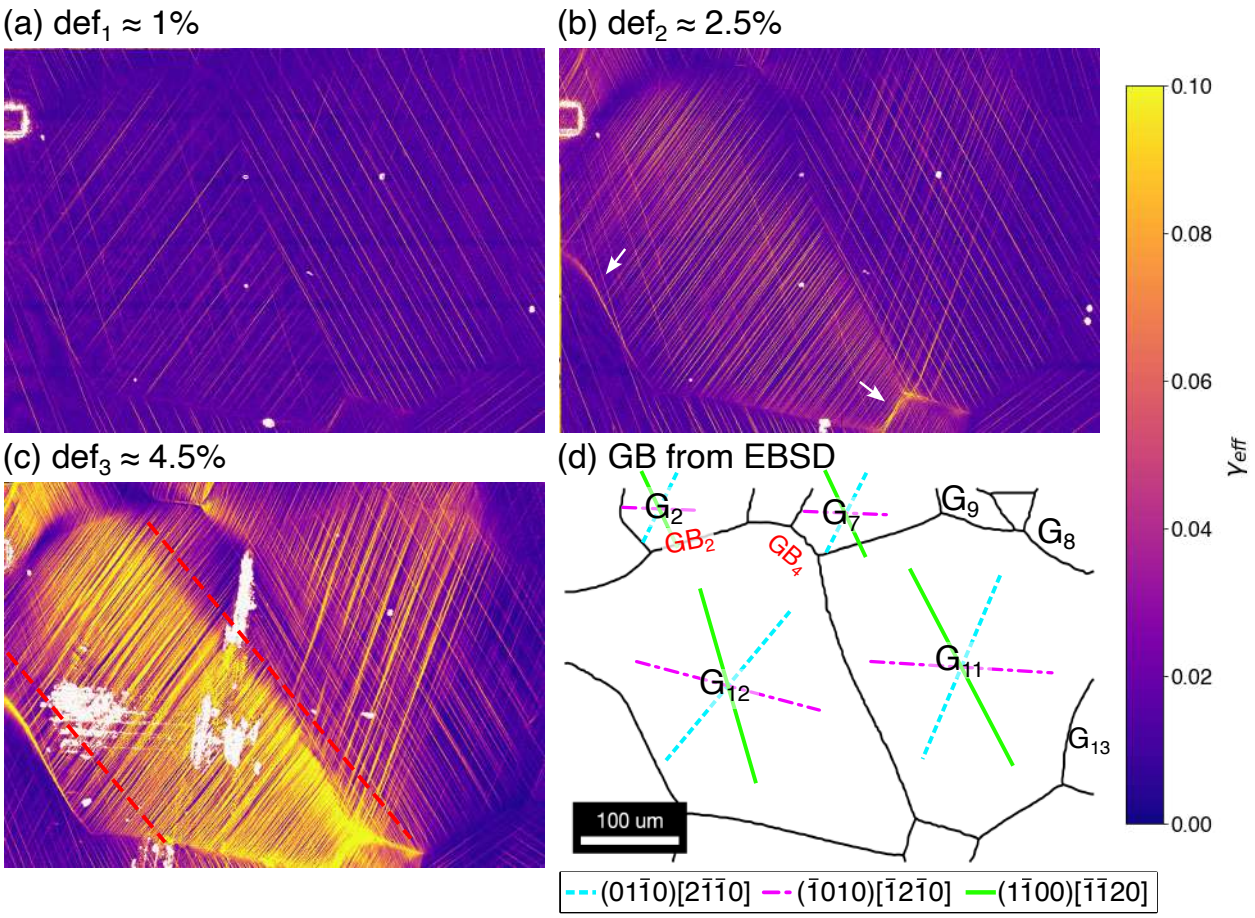

Figure 5.4: Effective shear strain maps acquired by HRDIC in the sample within sub-region 1. The correlated maps correspond to three deformation steps at (a) 1%, (b) 2.5%, and 4.5% plastic deformation. The white pixels in the maps correspond to non-correlated points caused by surface scratches and dirt deposited onto the gold nano-speckle pattern. The white arrows in (b) highlight strain concentrations close to GB and triple junctions. The red dashed lines in (c) delimit a macro-strain band. (d) GB map obtained from EBSD before deformation. The main grains and GB of study have been labeled, and the theoretical prismatic slip traces have been drawn at the center of the grains.

The effective shear strain distribution acquired in sub-region 2 is displayed in Fig. 5.5 for the three plastic strains of 1% (a), 2.5% (b) and 4.5% (c), whereas (d) presents a GB map with labeled grains and GBs of study in which the theoretical prismatic slip traces have been drawn at the center of the grains.

As observed in Fig. 5.5 (d), all slip bands are identified as prismatic, and the slip activity and intensity increase with plastic deformation. Several strain concentrations appear at 2.5% plastic deformation, especially at the triple junctions, and they are highlighted

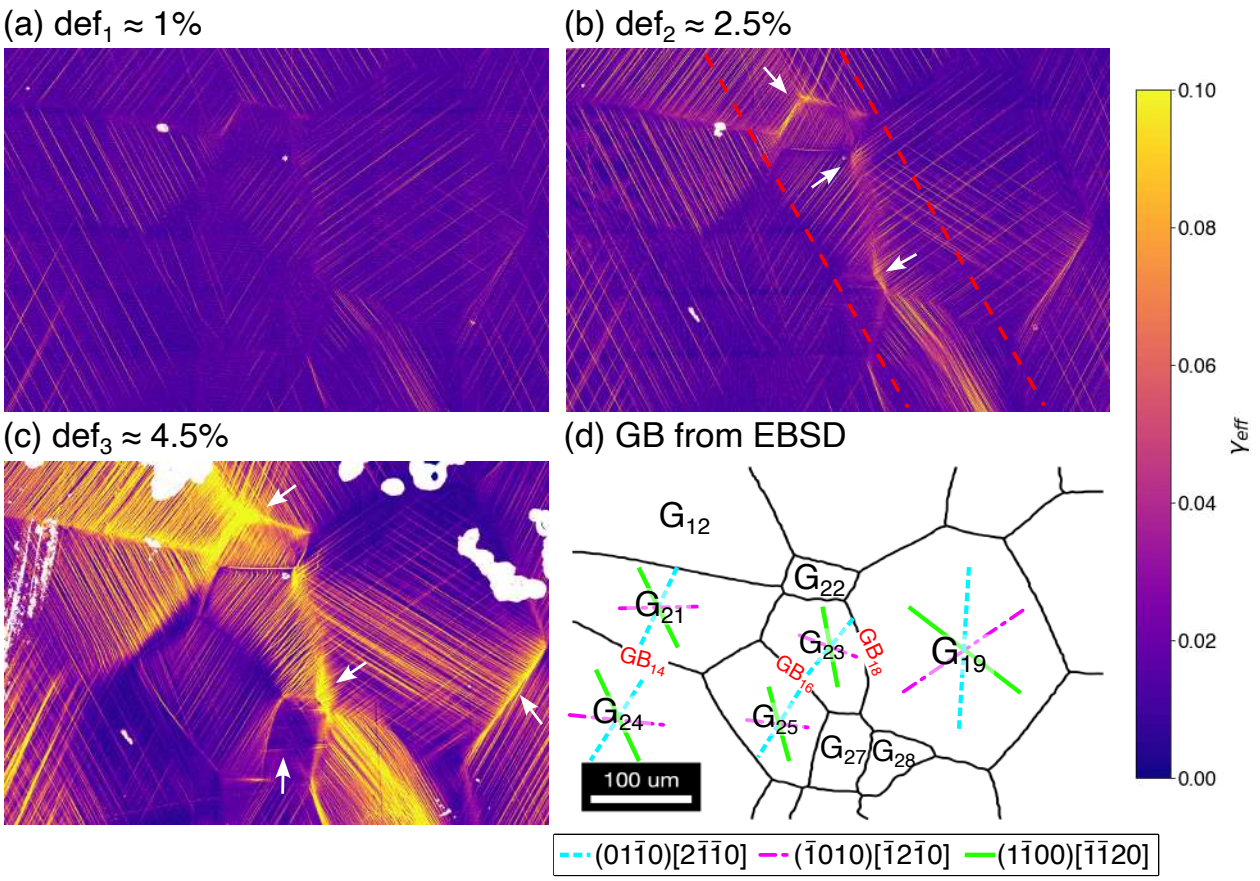

Figure 5.5: Effective shear strain maps, γ_{eff}, obtained by HRDIC in the ROI within subregion 2. The correlated maps correspond to three deformation steps at (a) 1%, (b) 2.5%, and 4.5% applied plastic deformation. The white pixels in the maps correspond to non-correlated points caused by surface scratches and dirt deposited onto the gold nanospeckle pattern. The white arrows in (b) and (c) highlight different strain concentrations close to GBs and triple junctions. The red dashed lines in (b) delimit a macro-strain band. (d) GB map obtained from the EBSD map before deformation. The main grains and GB of study have been labeled, and the theoretical prismatic slip traces have been drawn at the center of the grains.

with white arrows in Fig. 5.5 (b). The shear strain distribution shows the localization of the plastic deformation along a strain band that goes through grains G_{22}, G_{23}, and G_{28}, delimited by the two red dashed lines in Fig. 5.5 (b). The strain localization within the band increases with the applied strain, as shown in Fig. 5.5 (c), while the strain did not increase that much in the neighborhood of the macro band and in the surrounding grains (i.e. G_{25}). Furthermore, G_{22} undergoes an out-of-plane displacement to accommodate plastic deformation, as evidenced in the HRDIC maps after 2.5% and 4.5% deformation due to its small size and position within the macro-strain band. In contrast, G_{27} barely experienced plastic deformation at 2.5%, but deformation twinning was observed after 4.5% plastic deformation. This seems to indicate that G_{27} could not accommodate all plastic deformation within the macro-strain band region by slip, and thus twinning was activated

between 2.5% and 4.5% plastic deformation, leading to a relaxation in the shear strain, as observed in the third deformation map (Fig. 5.5 (c)).

The HRDIC maps acquired within the third sub-region of the ROI are presented in Fig. 5.6. Once again, all observed slip traces belong to prismatic planes, which increase in intensity and activity with applied deformation. Some shear strain concentrations at GBs are observed from the second deformation.

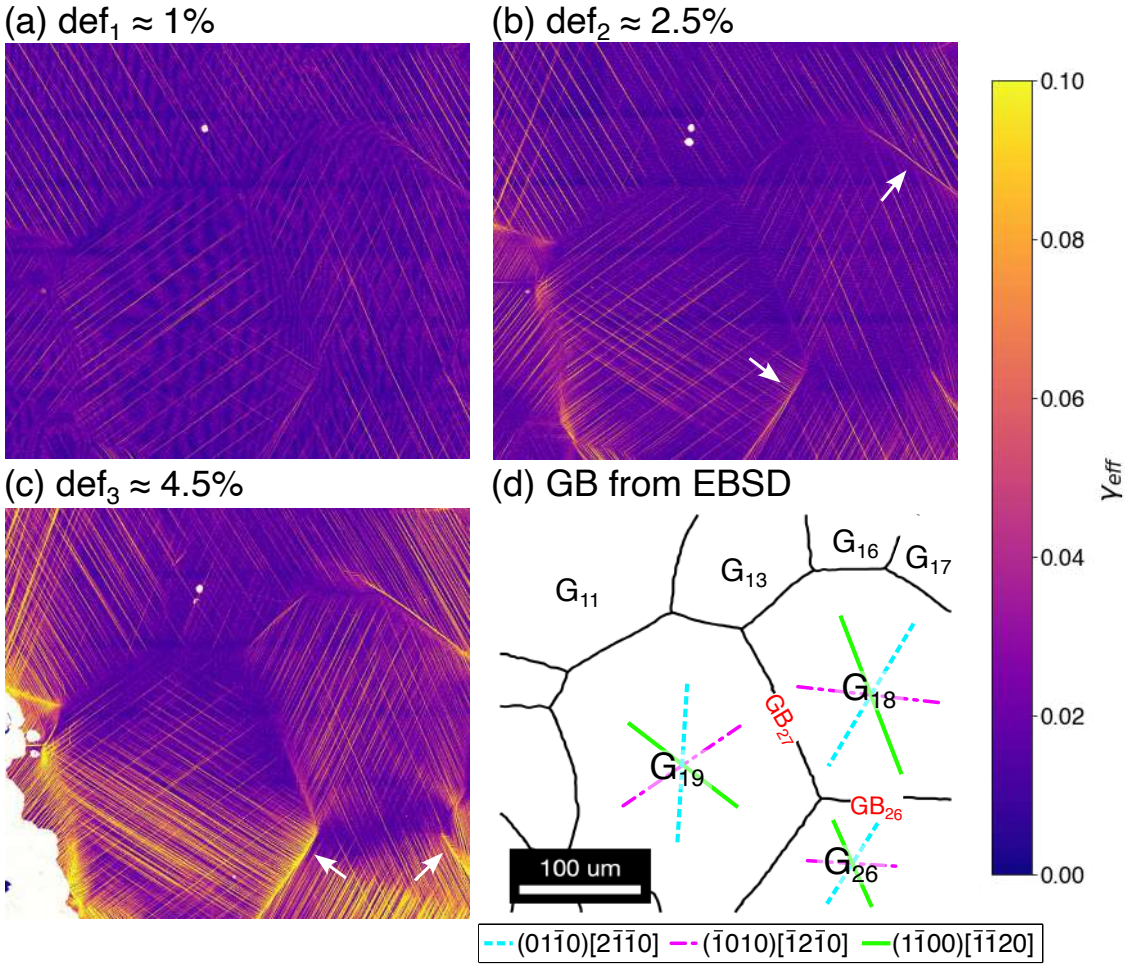

Figure 5.6: Effective shear strain maps acquired by HRDIC in the sample within sub-region 3. The correlated maps correspond to three deformation steps at (a) 1%, (b) 2.5%, and 4.5% plastic deformation. The white pixels in the maps correspond to non-correlated points caused by surface scratches and dirt deposited onto the gold nano-speckle pattern. The white arrows in (b) highlight strain concentrations close to GB and triple junctions. The red dashed lines in (c) delimit a macro-strain band. (d) GB map obtained from the EBSD map before deformation. The main grains and GB of study have been labeled, and the theoretical prismatic slip traces have been drawn at the center of the grains.

The occurrence of slip transfer/blocking across 28 GBs within the ROI was analyzed from the three effective shear strain maps for the three applied strain levels. The clear observation of the slip bands from the effective shear strain maps allowed us to reveal whether slip

transfer occurred at the GB, as revealed by the continuity between the slip traces across a GB. On the contrary, the discontinuity between the slip bands or the absence of slip traces at the GB region indicates slip blocking, and this conclusion can be supported by the presence of a strain concentration at the GB. Partial slip transfer can also be observed when just some slip bands are continuous across the GB or when the intensity of the slip bands significantly decreases a few microns away from the GB.

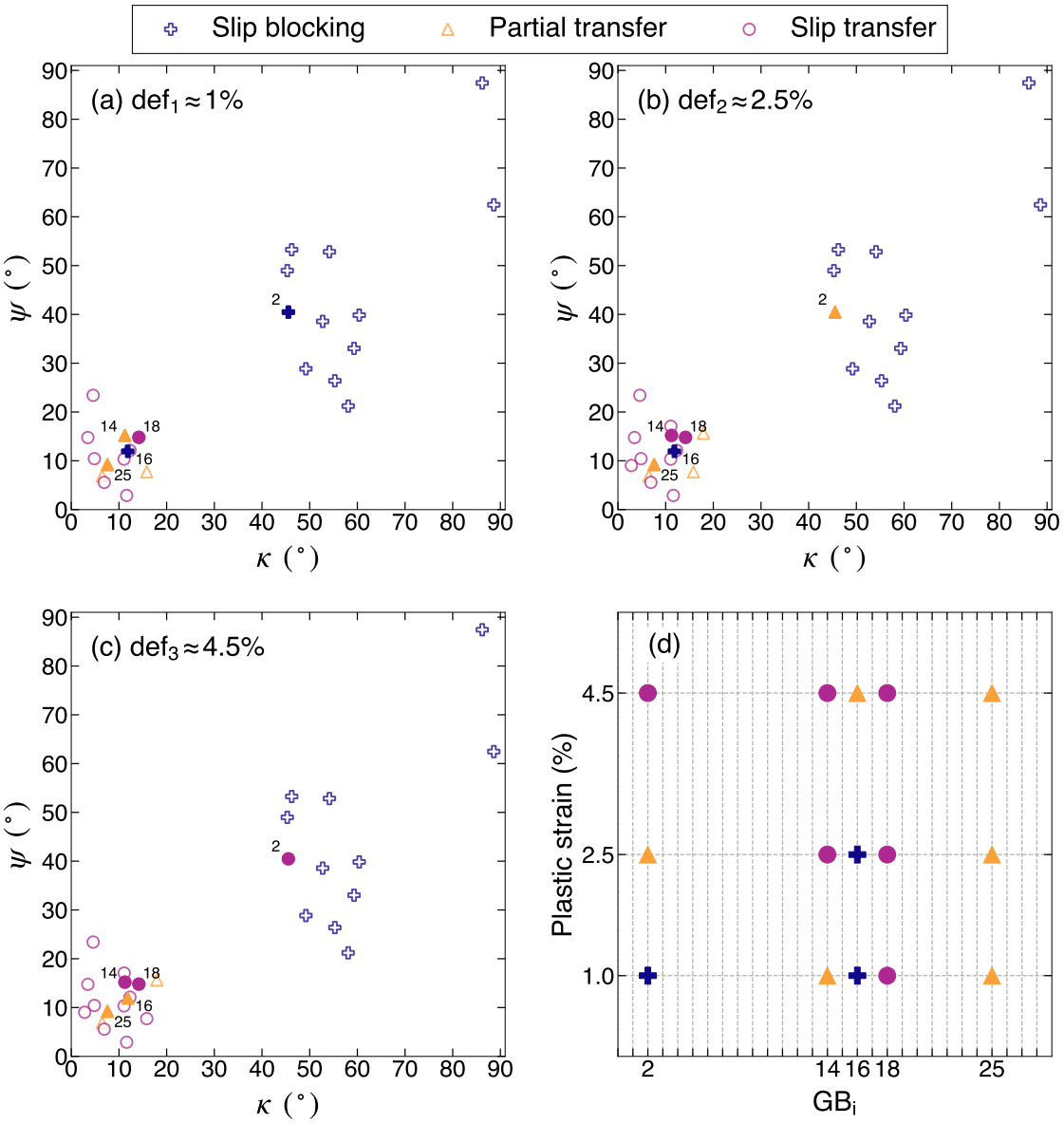

Figure 5.7: Influence of κ and ψ on slip transfer/blocking across the GBs as a function of the applied plastic deformation. (a) $\mathrm{def}_1 \approx 1\%$, (b) $\mathrm{def}_2 \approx 2.5\%$, and (c) $\mathrm{def}_3 \approx 4.5\%$. The GBs labeled with solid symbols will be analyzed in more detail in the next sections due to their unexpected slip transfer behavior. (d) Summary of the changes in the occurrence of slip transfer with plastic deformation in the selected GBs.

Once the active prismatic slip systems are identified, all the geometrical parameters that

characterize the alignment between the incoming and outgoing slip systems can be determined. The angles κ and ψ are obtained from the identification of the active prismatic slip planes, with κ as the angle between Burgers vectors and ψ as the angle between slip planes. However, the twist angle θ cannot be determined from surface observation only but needs the GB normal, which can only be obtained by 3D information about the orientation of the GB within the sample provided by DCT. The influence of κ and ψ on the occurrence of slip transfer across the GBs within the ROI as a function of plastic deformation is plotted in Fig. 5.7. The slip transfer events are indicated with dark pink circles, partial slip transfer with orange triangles, and slip blocking with blue crosses. Solid symbols indicate GBs that will be analyzed in more detail in Section 5.3.3.

The effect of the twist angle θ against the angle κ between Burgers vectors on slip transfer is plotted in Fig. 5.8 as a function of the applied plastic deformation. Most slip transfer and partial slip transfer events are located at low θ and κ, whereas slip blocking is associated with higher values. As already reported [131], the twist angle does not seem to play an important role in the occurrence of slip transfer, compared to the effect of the angle κ. .

As observed in Figs. 5.7 (a)-(c), most of the studied GBs fulfill the slip transfer criteria extensively reported in the literature for all applied deformations: slip transfer is favored when the slip systems across the GB are well aligned (low κ and low ψ). The partial slip transfer events are also located within the slip transfer region, which seems reasonable since these GBs can transfer slip to some extent.

Nevertheless, several GBs present an unforeseen slip transfer behavior depending on the applied plastic deformation. Five GBs have been selected for a deeper analysis due to this abnormal behavior. They are labeled in Figs. 5.7(a)-(c) and depicted with solid symbols. The summary of the slip transfer state (blocking, partial, or transfer) for these selected GBs is presented in Fig. 5.7(d) for the three applied deformations. GB_2, GB_{14}, and GB_{16} represent GBs whose slip transfer state evolves with plastic deformation. For instance, GB_2 evolves from slip blocking to partial slip transfer to full slip transfer with the applied plastic strain, even though there is a significant misalignment between the active slip systems. On the contrary, partial slip transmission is found in GB_{25} for all applied strain, even though the geometrical alignment makes it suitable for perfect slip transfer. Finally, although GB_{18} presents clear slip transfer from the lowest strain level, it has been selected for further analysis due to some unexpected plastic deformation mechanisms in its neighborhood due to its location within the macro-strain band influence region. These results suggest that the geometrical alignment between slip systems is not the only factor that plays a role in the occurrence or absence of slip transfer across GBs.

5.3.2 When slip transfer geometrical criteria work

Slip transfer was analyzed in more detail in some GBs where the classical geometrical criteria are fulfilled: slip transfers when the incoming and outgoing slip systems are well aligned, and slip is blocked when they are not. Several detailed sections of the effective shear strain maps within the ROI are depicted in Fig. 5.9, showing a close-up view of two different GBs (by rows) for the three applied deformations (by columns). The theoretical

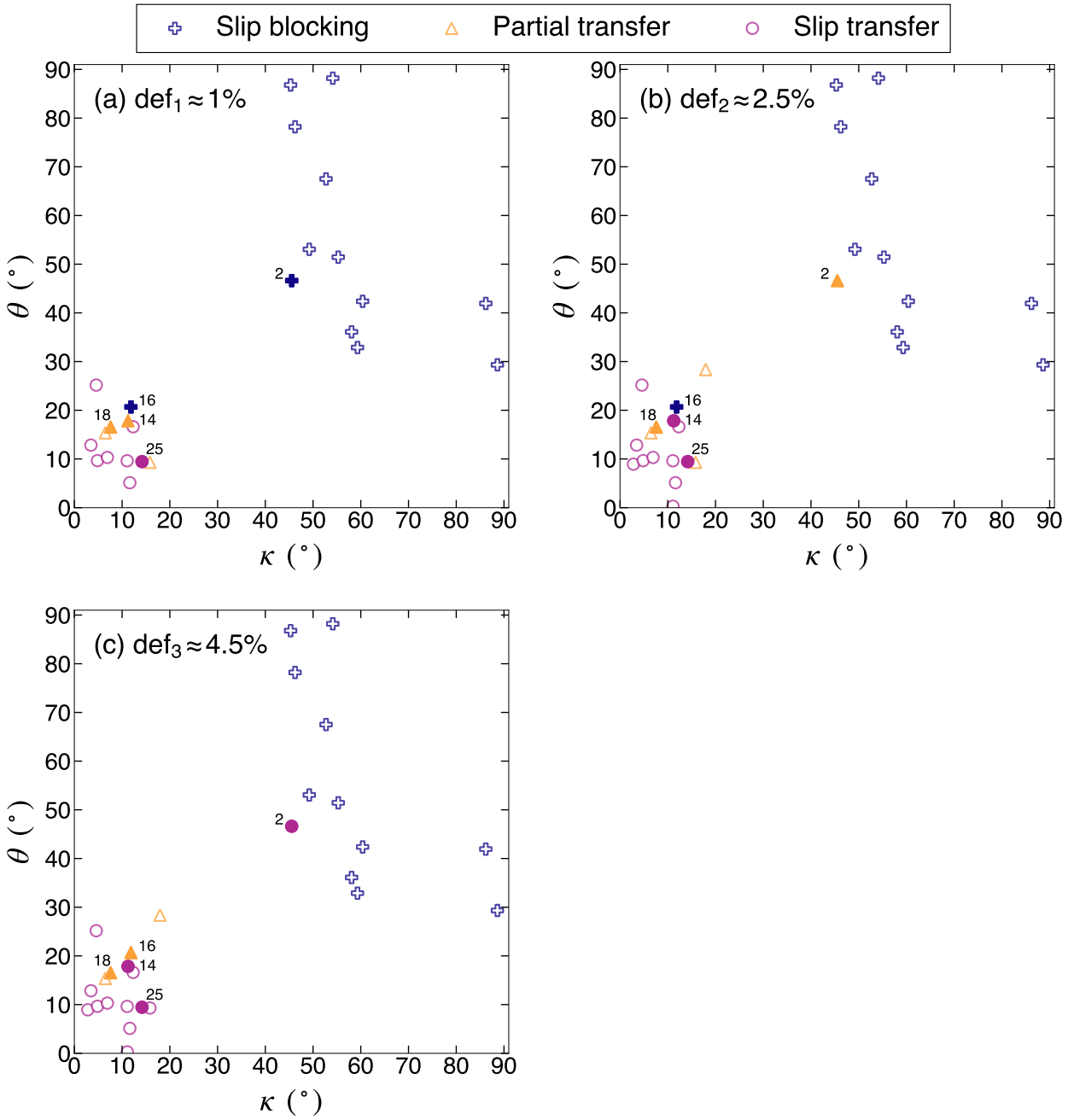

Figure 5.8: Influence of κ and θ on the occurrence of slip transfer/blocking across the analyzed GBs as a function of the applied plastic deformation. (a) $\mathrm{def}_1 \approx 1\%$, (b) $\mathrm{def}_2 \approx 2.5\%$, and (c) $\mathrm{def}_3 \approx 4.5\%$.

slip traces of the active prismatic planes have been drawn on top of the maps for slip system identification. The geometrical parameters and the values of selected slip transfer criteria (m', Δb, and LRB) have been calculated for the observed pairs of active slip systems across each GB (Table 5.1).

The first row of micrographs in Fig. 5.9 shows a case of convincing slip transfer across GB_4

from the lowest applied deformation (Fig. 5.9 (a)), where a pair of traces presents continuity across the boundary. The active slip systems in both grains across the boundary are uniquely identified as the $(01\bar{1}0)[2\bar{1}\bar{1}0]$ prismatic slip system, which is ranked first among the three possible prismatic slip systems according to their SF, as shown in Table 5.1. Due to its small misorientation angle, the slip systems across GB_4 are very well aligned, and κ and ψ are small, leading to high m' and low $\Delta b/b$. Furthermore, the twist angle θ calculated from the active slip planes and the GB normal is also low ($< 20°$), and so the LRB factor is also high. As observed in other studies [7, 24, 82, 130, 154], these results are all indicators of slip transfer across this GB. After the second applied deformation (Fig. 5.9 (b)), the number of slip bands and their intensity increase in both grains, especially in grain G_7, and hence more slip bands can go through the GB. In the third step of plastic deformation, the effective shear strain in the slip bands increases, and slip transfer is fairly evident all over the GB length. Moreover, there is no strain concentration at the GB (Fig. 5.9 (c)).

A clear slip blocking event is observed across GB_{27} in Fig. 5.9 (d)-(f), that presents a high misorientation angle Θ, as reported in Table 5.1. Double prismatic slip is observed in G_{18} and G_{19} after the first deformation step, and the active slip systems in each grain are the first and second according to their SF and all > 0.38. The slip bands that meet at the GB are the pink prismatic slip system $(\bar{1}010)[\bar{1}2\bar{1}0]$ in G_{19} (ranked second) and the blue prismatic slip system $(01\bar{1}0)[2\bar{1}\bar{1}0]$ (ranked first) in G_{18}. However, these slip systems are not adequately oriented for slip transmission, as shown in the angular parameters in Table 5.1, and slip transfer does not occur for any applied deformation. Furthermore, despite presenting slip blocking, there is only a slight strain concentration at the bottom region of this GB, which decreases as the distance to the triple point increases.

Table 5.1: Geometrical parameters and slip transfer criteria between the active prismatic slip systems for GB_4, and GB_{27}. The rank of the SF of the active prismatic slip system among the three possible planes is indicated between parenthesis and the SF is colored according to the active slip systems indicated in the legend in Fig. 5.9.

GB_i	$\mathrm{G_A}$	$\mathrm{G_B}$	$\mathrm{SF_A(R)}$	$\mathrm{SF_B(R)}$	Θ	κ	ψ	θ	m'	$\Delta b/b$	LRB
GB_4	7	12	0.45(1)	0.5(1)	13°	12.3°	12.1°	16.6°	0.96	0.21	0.94
GB_{27}	18	19	0.47(1)	0.43(2)	74.2°	54.1°	52.8°	88.2°	0.35	0.91	0.02

In summary, the likelihood of slip transfer across a GB increases when the active slip systems are geometrically well-aligned; otherwise, slip is blocked at the GB. Thus, the well-known geometrical criteria, m', Δb, and LRB, are generally good predictors for slip transfer across GBs.

5.3.3 When slip transfer geometrical criteria fail: the influence of local stress

As indicated in Fig. 5.7, several GBs within the ROI present an unexpected slip transfer behavior according to the conventional geometrical slip transfer criteria. As observed

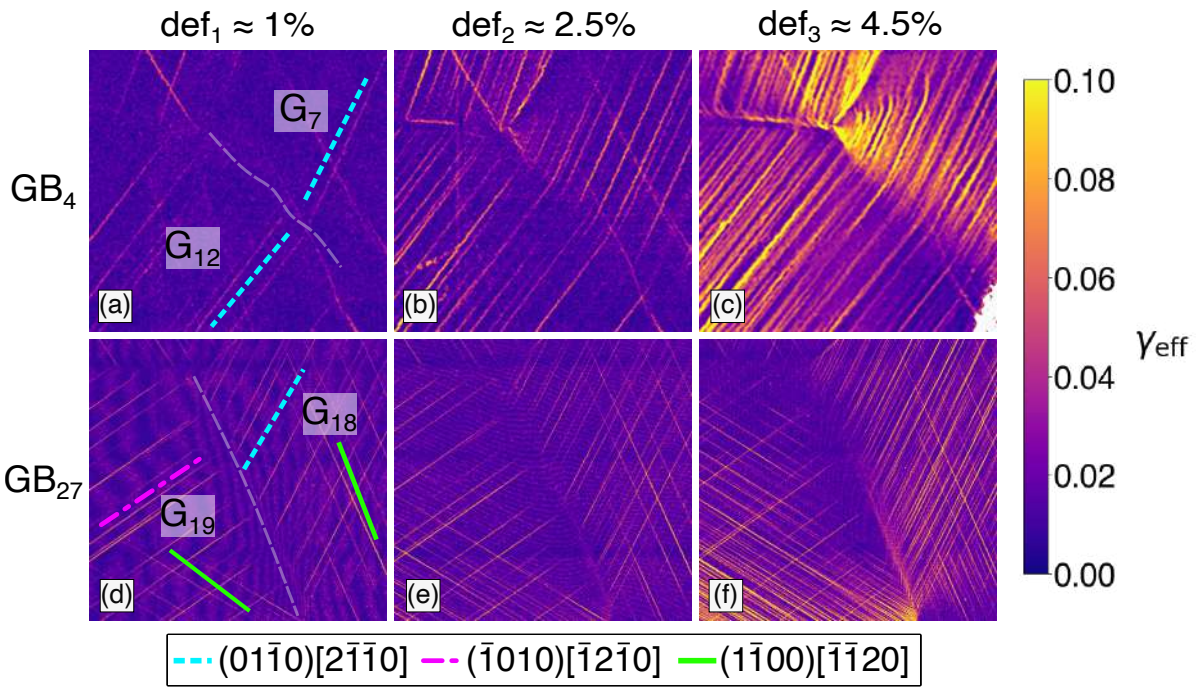

Figure 5.9: Effective shear strain maps of two GB that fulfill the classical slip transfer criteria. (a), (b), and (c): slip transfer across GB_4 after 1%, 2.5%, and 4.5% plastic deformation, respectively. (d), (e), and (f): slip blocking across GB_{27} after 1%, 2.5%, and 4.5% plastic deformation, respectively. The theoretical prismatic slip traces of the active slip systems have been drawn for each GB, and the GB trace has been indicated with a fine dashed gray line in the first deformation map.

from the effective shear strain maps, there are several GBs where the combination of active slip systems presents a suitable alignment for convincing slip transfer. However, some of them present partial slip transfer with just a few slip bands crossing through the GB that may evolve, or not, to convincing slip transfer. A close-up view of three different GBs that present an abnormal slip transfer behavior is shown in Fig. 5.10. The geometrical parameters and the values of m', Δb, and LRB have been calculated for the observed pairs of slip systems across each GB and are depicted in Table 5.2).

The first row in Fig. 5.10 displays the effective shear strain maps for GB_{25} for the three applied deformations. As observed in Fig. 5.10 (a), the neighbor grains G_{18} and G_{26} show double prismatic slip from the lowest applied deformation, activating both $(01\bar{1}0)[2\bar{1}\bar{1}0]$ and $(1\bar{1}00)[\bar{1}\bar{1}20]$ with $SF > 0.38$. The geometrical alignment between the corresponding pairs of prismatic slip systems (blue-to-blue and green-to-green) is very good due to the small misorientation angle (Table 5.2), and so are the slip transfer indicators. However, just one $(01\bar{1}0)[2\bar{1}\bar{1}0]$ slip band goes through GB_{25} after 1% deformation (blue prismatic slip systems, indicated with a white arrow in 5.10 (a) and (b)), while most of the $(1\bar{1}00)[\bar{1}\bar{1}20]$ slip bands show convincing slip transfer. At 2.5% plastic deformation, the prismatic slip activity increases in the neighbor grains, especially in G_{26}, and more green-to-green slip transfer occurrences are visible at the right section of the GB. Yet, slip trans-

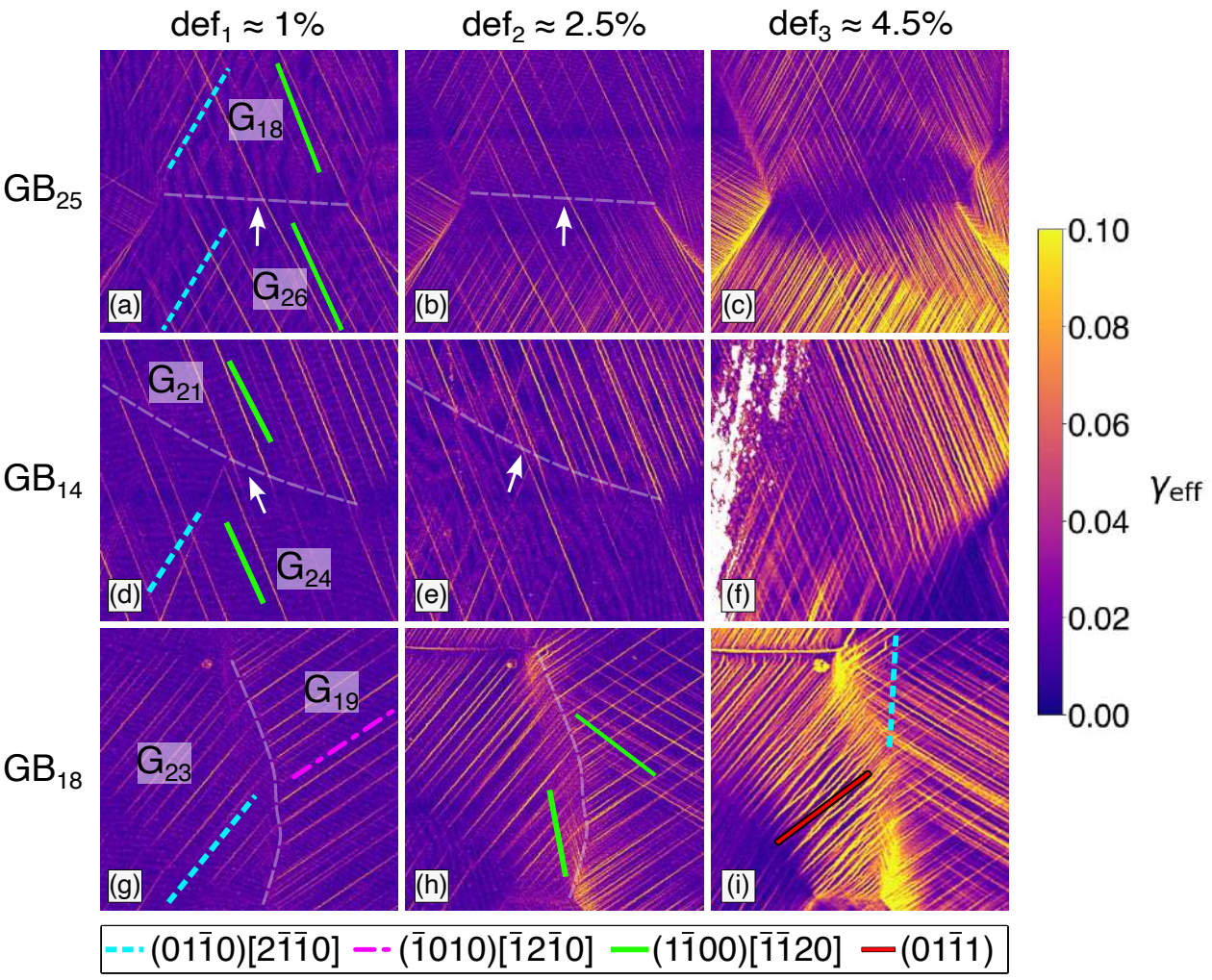

Figure 5.10: Effective shear strain maps after 1%, 2.5%, and 4.5% plastic deformation in the neighborhood of three GBs that do not fulfill the classical slip transfer criteria. (a), (b), and (c): GB_{25}. (d), (e), and (f): GB_{14}. (g), (h), and (i): GB_{18}. The theoretical prismatic slip traces of the observed active slip systems have been drawn for each GB, and the GB trace has been indicated with a fine dashed gray line at the first deformation map. An additional first-order pyramidal theoretical slip trace has been added in G_{23}.

fer does not progress between the blue slip bands even though these slip systems are well aligned. This difference in the slip transmission behavior may be attributed to the difference between the twist angles θ between the active pairs of prismatic slip systems ($\theta = 16.5°$ for the blue $(01\bar{1}0)[2\bar{1}\bar{1}0]$ versus $\theta = 5.1°$ for the green $(1\bar{1}00)[\bar{1}\bar{1}20]$ slip systems), which might favor slip transfer along the $(1\bar{1}00)[\bar{1}\bar{1}20]$ slip systems. There is an evident rise in the number of active slip bands in both grains at 4.5% deformation in both prismatic slip systems (Fig. 5.10 (c)), as well as significant strain concentrations at the neighbor GBs at the sides of G_{26}. Nonetheless, there is a lack of shear strain at the GB_{25} region and a limited number of visible shear bands going through it, in contrast to its neighborhood. Hence, the lack of slip transfer events between the pairs of active slip systems may be

attributed to the local strain heterogeneity, which locally reduces the driving force for slip. Both blue-to-blue and green-to-green prismatic slip transfer across GB_{25} seemed, in principle, very likely. However, the reduction in the effective shear strain, together with the absence of slip bands at the GB region, reveals that resolved shear stress for dislocation slip was very low near the GB, hindering slip transfer.

Table 5.2: Geometrical parameters and slip transfer criteria between the active prismatic slip systems for GB_{25}, GB_{14}, and GB_{18}. The rank of the SF of the active prismatic slip system among the three possible planes is indicated between parenthesis, and the SF is colored according to the active slip system indicated in the legend in Fig. 5.10.

GB_i	G_A	G_B	$SF_A(R)$	$SF_B(R)$	Θ	κ	ψ	θ	m'	$\Delta b/b$	LRB
GB_{25}	18	26	0.47(1)	0.46(1)	11.7°	7.6°	9.2°	16.5°	0.98	0.13	0.95
GB_{25}	18	26	0.38(2)	0.4(2)	11.7°	11.6°	2.9°	5.1°	0.98	0.2	0.98
GB_{14}	21	24	0.44(1)	0.37(2)	17.3°	11.2°	15.2°	17.8°	0.95	0.2	0.93
GB_{18}	19	23	0.43(2)	0.5(1)	15°	14.2°	14.8°	9.5°	0.94	0.25	0.96

GB_{14} presents partial slip transfer between green $(1\bar{1}00)[\bar{1}\bar{1}20]$ prismatic slip systems from 1% plastic deformation. The slip activity in grains G_{21} and G_{24} is dominated by the highest SF for the first and second deformations (green prismatic), but with increasing activity of the blue prismatic slip system $(01\bar{1}0)[2\bar{1}\bar{1}0]$ (ranked first in SF) in G_{24} from 2.5% deformation. As observed in Fig. 5.10 (d), a few slip bands reach the boundary and then fade towards the interior of G_{24} as indicated by the white arrow, but with no extended slip transfer behavior throughout the length of GB_{14}. The geometrical alignment between the pair of green slip systems is rather good, as shown in Table 5.2, except for the θ angle, which might be slightly larger than that of other GBs. Nevertheless, several slip bands can go through the GB and penetrate through the neighbor grain at the second deformation (Fig. 5.10 (e)). In this case, the white arrow points at a slip band in G_{24} which was already present at 1% deformation, and that goes through GB_{14} at 2.5% towards G_{21}. Moreover, several new slip bands reach the boundary from G_{21} and clearly fade after going through it, as observed at the first deformation step. Finally, there is convincing slip transfer from green-to-green prismatic slip systems across GB_{14} at 4.5% plastic deformation (Fig. 5.10 (f)), which may be driven from G_{21} to G_{24} according to the gradient in the effective shear strain. This observation might also be supported by the fact that the green prismatic system in G_{21} has a higher SF than that of G_{24} (0.44 against 0.37), where it is ranked second. The $(01\bar{1}0)[2\bar{1}\bar{1}0]$ slip system activity increases in G_{24} (ranked first in SF with value 0.47) after 2.5% deformation and dominates at 4.5%, compared to the green prismatic slip system. This might cause the green-to-green slip transfer not to progress that much towards the interior of G_{24}, where the blue prismatic dominates over the green. In summary, the dominant prismatic slip systems (green in G_{21} and blue in G_{24}) are not properly aligned for slip transfer, in contrast to the green prismatic slip systems which are suitably aligned. However, partial slip transfer is observed until 4.5% applied deformation, where convincing slip transfer is finally observed. This may be attributed to a lack of driving force to transfer slip from a dominant to a non-dominant slip system at low strains.

The case of GB_{18} is somewhat different from the previous two cases since there is convincing slip transfer between the blue $(01\bar{1}0)[2\bar{1}\bar{1}0]$ in G_{23} and the pink $(\bar{1}010)[\bar{1}2\bar{1}0]$ in G_{19} prismatic slip systems from the lowest deformation. The SF of the involved slip systems are both high (> 0.43), and the geometrical alignment is excellent, as shown in Table 5.2. The slip transfer process between this pair of prismatic slip systems does not significantly change with the applied deformation. However, the location of GB_{18} within the region of the macro-strain band (Fig. 5.5) induces the activation of additional deformation mechanisms necessary to accommodate the local stress. After 2.5% plastic deformation, the green $(1\bar{1}00)[\bar{1}\bar{1}20]$ prismatic slip system is activated in G_{23} with SF 0.23 (ranked third) and in G_{19} with SF 0.43 (ranked first), as shown in Fig. 5.10 (h). In the former, the activation of this prismatic slip system seems unlikely owing to its low SF, and yet it appears as thin slip bands near the proximity of the triple junction at the bottom, where plastic deformation is accumulated. The strain concentrations that appear at the triple points and at the GB itself after the third deformation step give rise to the activation of other plastic deformation mechanisms (Fig. 5.10 (i)). The large plastic deformation in G_{23} induces the appearance of wavy slip bands that arise from the $(01\bar{1}0)[2\bar{1}\bar{1}0]$ prismatic traces, that correlate with the theoretical slip trace direction of the first-order pyramidal slip system $(01\bar{1}1)$. Two possible slip systems share this pyramidal plane, $[1\bar{2}13]$ with SF 0.31 and $[\bar{1}\bar{1}23]$ with SF 0.08, therefore the former could be assumed to be active. Slip transfer is not observed between the first-order pyramidal slip system and any slip system active in G_{19}. Moreover, L-shaped slip bands are observed near the top triple junction among G_{23}, G_{19}, and G_{22}. They are associated with a slip plane change between the pink and the blue (SF 0.006, ranked third) prismatic slip systems in G_{19}. Consequently, after 4.5% plastic deformation, three slip systems have been activated in each grain at each side of GB_{18} despite being considerably unlikely and caused by the large strain concentration in this area. In brief, the large local strains observed around GB_{18} lead to the activation of multiple slip systems regardless of their macroscopic SF to accommodate the high plastic deformation in the neighborhood.

Overall, the two GBs analyzed in Fig. 5.10 (GB_{25} and GB_{14}) do not fulfill the classical slip transfer geometrical criteria because the local stresses affect the driving force for slip transfer across the GB. This leads to the observation of either limited slip transfer events or even partial slip transfer that only evolves to convincing slip transfer when the applied deformation is sufficient to drive slip toward the adjacent grain. In contrast, GB_{18} illustrates that, even when slip transfer is clearly observed, it is not enough to accommodate the large plastic deformation, and other plastic deformation mechanisms emerge.

Two additional GBs have been analyzed to showcase to which extent the local stress distribution can affect the occurrence or absence of slip transfer across a GB. First, GB_{16} has been selected as an example of how slip transfer can be impeded by insufficient local stress despite the good alignment between the active slip systems. As shown in the first row of Fig. 5.11, the dominant slip systems in G_{25} and G_{23} are the blue prismatic $(01\bar{1}0)[2\bar{1}\bar{1}0]$ with the highest SF (> 0.47). These slip systems are very well aligned regarding the angles κ and ψ, while the twist angle θ is slightly higher ($20.7°$). This leads to high m' and LRB values and low $\Delta b/b$, which indicate a great probability of slip transfer between the active prismatic slip systems. However, slip transfer is not observed after 1% deformation,

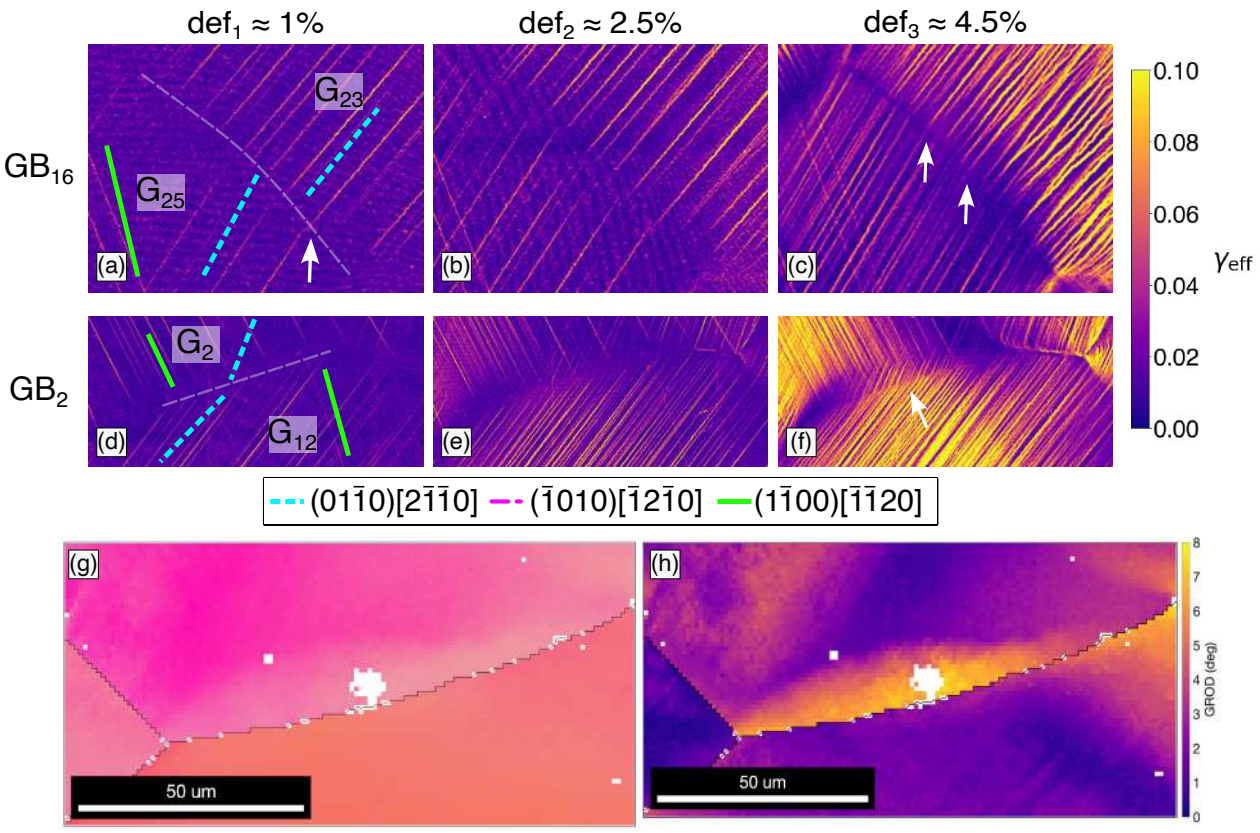

Figure 5.11: Detail shear strain HRDIC maps of two GBs that do not follow the classical slip transfer criteria. (a), (b), and (c): GB_{16} shear strain maps after 1%, 2.5%, and 4.5% plastic deformation, respectively. (d), (e), and (f): GB_2 shear strain maps after 1%, 2.5%, and 4.5% plastic deformation, respectively. For each GB, the theoretical prismatic slip traces of the observed active slip systems have been drawn, and the GB trace has been indicated with a translucent dashed gray line at the first deformation map. (g) and (h): G_2 EBSD and grain reference orientation deviation (GROD) maps after 4.5% plastic deformation, respectively.

Table 5.3: Geometrical parameters and slip transfer criteria between the active prismatic slip systems for GB_{16} and GB_2. The rank of the SF of the active prismatic slip system among the three possible planes is indicated between parenthesis, and the SF is colored according to the active slip systems indicated in the legend in Fig. 5.10.

GB_i	G_A	G_B	$SF_A(R)$	$SF_B(R)$	Θ	κ	ψ	θ	m'	$\Delta b/b$	LRB
GB_{16}	23	25	0.5(1)	0.47(1)	12.8°	11.9°	11.9°	20.7°	0.96	0.21	0.92
GB_2	12	2	0.5(1)	0.45(1)	61.4°	45.5°	40.5°	46.6°	0.53	0.77	0.48
GB_2	12	2	0.28(2)	0.41(2)	61.4°	58.1°	21.2°	36.1°	0.49	0.97	0.43

where only one trace matches across the GB but with a small curvature (indicated with a

white arrow in Fig. 5.11 (a)), suggesting that the continuity across the boundary may not be ideal. The slip band intensity increases in both grains at 2.5% plastic strain, but the number of active slip bands does not increase, and slip transfer is not yet clearly observed for any pair of bands (Fig. 5.11 (b)). After 4.5% plastic deformation, the slip activity in the prismatic blue slip systems significantly increases, and several instances of slip transfer across GB_{16} are observed, as highlighted by the white arrows in Fig. 5.11 (c). However, the continuity across the traces is not visible over the GB trace, which presents near-zero shear strain, suggesting that slip transfer across this GB might not be perfect. This may be attributed to insufficient local stresses to drive plastic deformation from one grain to the other, unlike those GBs located in other highly stressed regions.

Conversely, the local stresses could also assist the slip transfer process even if the slip systems across the GB are poorly aligned. The second row of Fig. 5.11 shows the effective shear strain distribution in GB_2, located within the macro-strain band region. As shown in Fig. 5.11 (d), there is double slip activation of the two highest SF prismatic slip systems in G_2 and G_{12}. The geometrical parameters and slip transfer criteria for the two pairs of prismatic slip systems (blue-to-blue and green-to-green) indicate that slip transfer across this GB would be unlikely due to their poor alignment (Table 5.3). Nevertheless, there are several visible blue-to-blue prismatic slip transfer events at 2.5% plastic deformation, and the process is possibly driven from G_{12} to G_2, given the intensity of the shear bands. At 4.5% deformation, there is convincing slip transfer between the blue prismatic slip systems across GB_2. The slip bands do not progress much through G_2 but extinguish a few microns away from the GB, where $(1\bar{1}00)[\bar{1}\bar{1}20]$ is dominant. Taking a closer look at the EBSD map acquired after 4.5% deformation (Fig. 5.11 (g)), it is clear that there is a local crystal rotation in G_2 close to GB_2. The grain reference orientation deviation (GROD) map is provided in Fig. 5.11 (h) as a measure of the misorientation between every pixel in the EBSD map and G_2 average orientation. The GROD distribution points out a significant crystal rotation near GB_2 of about 8°, probably caused by the large plastic deformation induced by the local stresses. This case proves that, even though the alignment between the active slip systems across a GB seems inadequate for slip transfer, large local stresses can provide enough driving force to overcome the GB energy barrier and induce slip transmission to the neighbor grain.

5.4 Conclusions

Slip transfer/blocking across 28 GBs was analyzed as a function of the applied plastic deformation in a pure Ti sample with strong rolling texture by means of slip trace analysis and high-resolution digital image correlation. The grain structure was determined in 3D using diffraction contrast tomography, so all the geometrical parameters that describe the alignment between the active slip systems across a grain boundary were known. Prismatic slip was practically the only plastic deformation mechanism, and the active prismatic slip systems presented high SF.

It was found that classical slip transfer geometrical criteria (m', Δb, or LRB) are generally good predictors for the likelihood of slip transmission across grain boundaries, indicating

that the probability of slip transfer across a grain boundary is strongly correlated with the geometrical alignment between the active slip systems. Thus, those grain boundaries where the active prismatic slip systems were well-aligned presented either full or partial slip transfer, and, conversely, slip blocking was observed when the alignment was poor. However, the information provided by high-resolution digital image correlation showed that local strain concentrations could affect the slip transfer process regardless of the geometrical alignment between the slip systems. In particular:

• Slip transfer between a pair of well-oriented slip systems can be impeded (leading to either partial slip transfer or even blocking) if there is another dominant slip system that is more favorable in terms of the SF to accommodate the plastic deformation across the boundary.

• Slip transfer between well-aligned slip systems across the boundary can be blocked as a result of the lack of driving force to transfer deformation due to the strain heterogeneity in the microstructure.

• Slip transfer may occur across a highly misoriented grain boundary due to the local stress concentrations, which provide sufficient driving force to overcome the energy barrier induced by the grain boundary and transmit dislocations to the adjacent grain.

In any case, despite the effect of the local stress concentrations, well-known slip transfer geometrical criteria, such as m', Δb, or LRB, can be used as a good first approximation for predicting slip transfer across grain boundaries. Moreover, these criteria can be easily implemented within the framework of crystal plasticity simulations of the mechanical behavior of polycrystals. This task will be accomplished in the following chapters.

6 Simulation of polycrystal deformation including slip transfer/blocking at grain boundaries

6.1 Introduction

The strength of pure metals is very low as a result of the development of plastic deformation by dislocation slip. Hence, they have to be strengthened by obstacles that hinder dislocation motion, and grain boundaries (GBs) stand among the strongest barriers to dislocation slip in polycrystals. As shown in previous chapters, the interaction of dislocations with GBs can be grouped into three categories. Opaque or impenetrable GBs do not allow the propagation of dislocation slip through the boundary, leading to the formation of dislocation pile-ups and local stress concentrations [26, 58]. Conversely, transparent GBs are found when all the active slip systems are suitably aligned, and the dislocations gliding in the incoming grain can be transmitted to the neighbor grain. Finally, dislocations in some active slip systems can easily propagate through the boundary, while others are blocked in the case of translucent GBs. This phenomenon leads to stress concentrations at the GB that depend on the number and intensity of slip in the systems blocked at the GB.

The effect of GBs on the strength of polycrystals was recognized in the 1950s, leading to the phenomenological Hall-Petch law [72, 143] that relates the yield strength of the polycrystal, σ_y with the average grain size, $\bar{D}_g$, according to

$$\sigma_y = \sigma_\infty + C_{HP}\,\bar{D}_g^{-x} \tag{6.1}$$

where σ_∞ is the yield stress of a polycrystal with very large grain size, C_{HP} a material constant and x a scaling exponent in the range -0.5 to -1 [47, 48, 112, 147].

Understanding the mechanical behavior of polycrystals has progressed rapidly in recent years through the combination of computational homogenization and crystal plasticity constitutive models [158]. As explained in Section 1.4, two different strategies have been used to study the effect of GBs on the strength of polycrystals based on either strain-gradient or physically-based crystal plasticity models. In the context of physically-based models, Haouala *et al.* [77] determined the effect of grain size on the strength of different

FCC polycrystals by means of computational homogenization of RVEs containing several hundred grains using a Fast Fourier Transform in combination with a strain gradient crystal plasticity model. The simulation results were in good agreement with the experimental data for Cu, Al, Ag, and Ni polycrystals for grain sizes $> 20\ \mu m$. Similar results were also obtained by Rubio *et al.* [151] through computational homogenization of equivalent RVEs using the finite element method and a physically-based crystal plasticity model that takes into account the storage of dislocations near the grain boundaries, following the approach developed by Haouala *et al.* [78]. Interestingly, the predictions of the physically-based model also overestimated the strength of the polycrystals when the average grain size was $< 20\ \mu m$. It was argued that the differences between experimental data and simulation results (using either strain gradient or physically-based models) arose because all GBs were assumed to be opaque in the simulations.

There is ample experimental evidence (presented in the previous chapters of this thesis) indicating that slip transfer through the GBs can take place when there is good alignment between incoming and outgoing slip systems across the boundary. Thus, geometrical criteria based on the orientation of the grains and slip systems across the boundary (Δb, or m') can be used to analyze slip transfer. The effect of these geometrical criteria on slip transfer was included in a physically-based crystal plasticity model used to study stress concentrations in either transparent, translucent, or opaque GBs in bicrystals oriented for single and double slip [76]. The results of the numerical simulations were in good agreement with experimental observations of slip transfer and slip activation on Al GBs, indicating that this approach was able to capture the effect of GBs on the slip behavior of FCC polycrystals.

This strategy is employed in this chapter to determine the flow strength of different FCC polycrystals by means of computational homogenization of an RVE of the microstructure. Different geometrical slip transfer criteria were implemented, and the predictions of the simulations were compared with experimental data in the literature on the Hall-Petch effect in both FCC (Al, Cu, Ni, Ag) and HCP (Ti, Mg) metallic polycrystals. Moreover, the influence of the GB character (either transparent, translucent, or opaque) on the local stresses that may trigger damage was also highlighted.

6.2 Physically-based crystal plasticity model

6.2.1 FCC metallic crystals

The mechanical behavior of the single crystals in the polycrystal is governed by a physically based, rate-dependent crystal plasticity model [78], which was modified to include the effect of slip blocking or transfer between slip systems concurring at a GB [76]. The model was developed within the framework of finite deformations using the multiplicative decomposition of the deformation gradient, following standard crystal plasticity implementations [158].

The relationship between the plastic shear deformation rate in the slip system α, $\dot{\gamma}^{\alpha}$, and the corresponding resolved shear stress, τ^{α}, is expressed by

$$\dot{\gamma^{\alpha}} = \dot{\gamma_0} \left(\frac{|\tau^{\alpha}|}{\tau_c^{\alpha}} \right)^{\frac{1}{m}} sgn(\tau^{\alpha}) \tag{6.2}$$

where $\dot{\gamma_0}$ is the reference shear strain rate, m the strain rate sensitivity parameter, and ${\tau_c}^{\alpha}$ is the CRSS in the slip system α. Standard values of $\dot{\gamma_0}$ and m for FCC polycrystals can be found in Table 6.1 [78].

The evolution of the CRSS during deformation follows a particularization of the Taylor model [175] by Franciosi *et al.* [57], which includes the contribution between dislocations in different slip systems to the hardening according to

$$\tau_c^{\alpha} = \mu b \sqrt{\sum_{\beta} q^{\alpha\beta} \rho^{\beta}} \tag{6.3}$$

where μ, b, and ρ^{β} stand for the shear modulus parallel to the slip plane, the Burgers vector, and the dislocation density in slip system β, respectively. The dimensionless coefficients $q^{\alpha\beta}$ stand for the different interactions between pairs of slip systems and were obtained by means of discrete dislocation dynamics simulations for FCC lattices where dislocation slip occurs in 12 {111}<110> systems [22, 44]. Due to symmetry considerations, only six independent coefficients are necessary to determine the 12 $\times$ 12 coefficients of $q^{\alpha\beta}$, and they are depicted in Table 6.1.

Table 6.1: Parameters of the dislocation-based crystal plasticity model for FCC single crystals.

Viscoplastic parameters	
Reference shear strain rate $\dot{\gamma_0}$ (s^{-1})	0.001
Strain rate sensitivity coefficient m	0.05
Dislocation interaction coefficients ($q^{\alpha\beta}$)	
Self interaction	0.122
Coplanar interaction	0.122
Collinear interaction	0.657
Glissile junction	0.137
Hirth lock	0.084
Lomer-Cottrell lock	0.118

The evolution of the dislocation density in each slip system, $\dot{\rho^{\alpha}}$, follows the Kocks-Mecking law [97, 98] that takes into account the balance between the generation and annihilation of dislocations. Nevertheless, the original idea of Kocks-Mecking was modified by Haouala *et al.* [76] to account for the formation of dislocation pile-ups in the slip system near a GB that does not allow for slip transfer leading to

$$\dot{\rho}^{\alpha} = \frac{1}{b}\left(\frac{1}{\ell^{\alpha}} - 2y_c\rho^{\alpha}\right)|\dot{\gamma}^{\alpha}| \quad \text{if slip transfer is allowed for any } \beta \tag{6.4}$$

$$\dot{\rho}^{\alpha} = \frac{1}{b}\left(\max\left(\frac{1}{\ell^{\alpha}}, \frac{K_s}{d_b}\right) - 2y_c\rho^{\alpha}\right)|\dot{\gamma}^{\alpha}| \text{ if slip transfer is blocked } \forall\beta \tag{6.5}$$

where β stands for any slip system in the nearest neighbor grain. Eq. 6.4 stands for the standard Kock-Mecking law that includes two terms that control the generation and annihilation of dislocations. Dislocation generation in the slip system α depends on the dislocation Mean Free Path (MFP), ℓ^{α}, which stands for the distance traveled by a dislocation segment before it is stopped by an obstacle, and it is given by

$$\ell^{\alpha} = \frac{K}{\sqrt{\sum_{\beta\neq\alpha}\rho^{\beta}}} \tag{6.6}$$

where ρ^{β} is the dislocation density in the slip system β and K is a dimensionless constant, known as the similitude coefficient, that relates the flow stress with the average wavelength of the characteristic dislocation pattern. It was estimated by Sauzay *et al.* [155] and Rubio *et al.* [151] for different FCC polycrystals.

Dislocation annihilation is controlled by the current dislocation density in the system α and y_c, the effective annihilation distance between dislocations. This latter parameter was estimated for different FCC metals [151], assuming equal densities of edge and screw dislocations. The annihilation distance for edge dislocations y_e is very small ($\approx 6b$) and independent of the metal, while that for screw dislocations y_s is a function of the stacking fault energy, temperature, and strain rate [51, 100]. The values of the critical annihilation distance for screw dislocations are taken from experimental investigations for Cu and Al [8, 100] and from dislocation dynamics simulations for Ni and Ag [141]. Assuming an equal fraction of edge and screw dislocations, the effective annihilation distance y_c is calculated as the average between y_e and y_s.

Eq. 6.4 establishes the dislocation accumulation rate at any slip system in any Gauss point of the polycrystal that is either far away from any GB boundary or when -even if the Gauss point is close to a GB- slip transfer to another slip system β is possible across the GB according to a geometrical criteria that has to be defined.

In contrast, Eq. 6.5 provides the dislocation accumulation rate for a slip system at a Gauss point near a GB when slip transfer across the boundary is blocked according to the geometrical criteria. The critical distance at the GB that leads to an increase in the dislocation generation rate (and, thus, to the formation of a dislocation pile-up) is given by the condition $K_s/d_b > 1/\sqrt{\ell^{\alpha}}$ where K_s is another dimensionless constant that determines the storage of dislocations at the GB and d_b is the distance from the Gauss point to the nearest GB along the slip direction. K_s was also determined by means of 3D dislocation dynamics simulations in the presence of impenetrable grain boundaries in FCC polycrystals [153] while d_b depends on the location of the Gauss point and on the orientation of the crystal.

The different coefficients of the crystal plasticity model for FCC Al, Ni, Cu, and Ag, as well as the elastic constants, are depicted in Table 6.2.

Table 6.2: Parameters of the dislocation-based crystal plasticity model for FCC materials [78, 151]

	Cu	Al	Ni	Ag
Elastic constants (GPa)				
C_{11}	168.4	108	249	124
C_{12}	121.4	61.3	155	93.7
C_{44}	75.4	28.5	114	46.1
Shear modulus μ	30.5	25.0	58.4	19.5
Dislocation parameters				
Burgers vector b (nm)	0.256	0.286	0.250	0.288
Effective annihilation distance y_c (nm)	15	56	14	12.5
Dislocation storage coefficient K	6	9	11	5
Grain boundary storage coefficient K_s	5	5	5	5

6.2.2 HCP metallic crystals

The physically-based crystal plasticity model for FCC metals presented in Section 6.2.1 was extended to HCP metallic crystals, namely Ti and Mg. To this end, the different slip systems active during the plastic deformation of HCP crystals have to be included in the model. Following Table 1.2, they are three (0001) basal slip systems and three $\{10\bar{1}0\}$ prismatic slip systems for both Ti and Mg, plus twelve first-order pyramidal $\{10\bar{1}1\}$ slip systems for Ti, and six second-order pyramidal $\{10\bar{2}2\}$ slip systems for Mg. Thus, there are 18 different slip systems in Ti and 12 in Mg that can be categorized into three families: basal, prismatic, and pyramidal (I or II). It should be noted that deformation twinning is another important plastic deformation mechanism in HCP metallic crystals, particularly in Mg, but it will not be included in this implementation. Thus, the comparison of the simulations for the Hall-Petch effect with experimental data in Ti and Mg will be carried out under conditions where deformation twinning can be neglected, such as high temperature and low strain rates [34].

The c/a ratio (that determines the orientation of the pyramidal slip planes as well as the distance between compact hexagonal planes) and the elastic constants of Ti and Mg single crystals used in the crystal plasticity model are shown in Table 6.3. $c/a \sim 1.63$ in pure Mg and the CRSS for basal slip is very low because the basal planes are the most compact ones. Conversely, $c/a < 1.63$ in Ti and prismatic glide will be dominant with respect to basal slip [106].

Table 6.3: Parameters of the dislocation-based crystal plasticity model for Ti and Mg (HCP) single crystals. The values of the stiffness constants (expressed in GPa) are taken from [81] for Ti and from [194], whereas the values of c/a are taken from [128] for Ti and from [23] for Mg.

	Ti	Mg
c/a	1.587	1.633
C_{11}	160	59.4
C_{12}	90	25.6
C_{44}	46.5	16.4
C_{13}	66	21.4
C_{33}	181	61.6
C_{66}	46.5	16.9

The relationship between the plastic shear deformation rate in the slip system α, $\dot{\gamma}^{\alpha}$, and the corresponding resolved shear stress, τ^{α}, can be expressed (as in FCC metals) as

$$\dot{\gamma^{\alpha}} = \dot{\gamma_0} \left(\frac{|\tau^{\alpha}|}{\tau_c^{\alpha}} \right)^{\frac{1}{m}} sgn(\tau^{\alpha}) \tag{6.7}$$

where $\dot{\gamma_0}$ is the reference shear strain rate, m the strain rate sensitivity parameter, and ${\tau_c}^{\alpha}$ is CRSS in the slip system α. Standard values of $\dot{\gamma_0}$ and m for HCP polycrystals can be found in Table 6.4.

Table 6.4: Parameters of the dislocation-based crystal plasticity model for HCP Ti and Mg single crystals.

Viscoplastic parameters	Ti	Mg
Reference shear strain rate $\dot{\gamma_0}$ (s^{-1})	0.001 [37]	0.001 [68]
Strain rate sensitivity coefficient m	0.02 [37]	0.05 [68]
Dislocation interaction coefficients ($q^{\alpha\delta}$)		
Same-hardening [23]	0.15	0.15

The evolution of the CRSS per slip system during deformation (Eq. 6.3) was modified for HCP metals to consider different CRSS for each slip system family as follows,

$$\tau_c^{\alpha} = \tau_{c_0}^{\alpha} + \mu^{\alpha} b^{\alpha} \sqrt{\sum_{\beta} q^{\alpha\beta} \rho^{\beta}}, \tag{6.8}$$

where τ_{c0}^{α} stands for the lattice resistance of the particular slip system family, and μ^{α} and b^{α} are the shear modulus parallel to the slip plane and the Burgers vector of the corresponding slip system family, respectively. It should be noted that the lattice resistance τ_{c0}^{α} of the only slip system family in FCC crystals ({111}<110>) is very small and can be neglected in Eq. 6.3 but this is not the case in HCP crystals. The introduction of different lattice resistances τ_{c0}^{α} for the different slip system families (basal, prismatic, or pyramidal) allows capturing the plastic anisotropy of HCP lattices.

The latent hardening due to the interactions of the dislocations gliding in different slip systems is accounted for through the coefficients of the dislocation interaction matrix $q^{\alpha\beta}$. Bertin *et al.* [23] estimated the 19 different latent-hardening coefficients of the different dislocation interactions in pure Mg, taking into account basal, prismatic, and second-order pyramidal $<c+a>$ slip. However, no information was found for the different dislocation interactions in pure Ti. Given that the active pyramidal slip systems are different for Ti and Mg, it was assumed that the latent hardening parameters were the same for all the dislocation-dislocation interactions in Ti and Mg (see Table 6.4). The influence of this hypothesis on the results was checked in the case of Mg, in which the 19 latent-hardening coefficients are available from [23], and the differences were not relevant.

The shear modulus μ^{α} and the Burgers vector b^{α} per slip system family were found in the literature for Ti and Mg (see Table 6.7). There is, however, no general agreement about the values of the CRSS per slip system because it is very difficult to measure accurately these quantities, and different techniques lead to different results. For instance, compression of single crystal micropillars manufactured by focused ion beam and oriented for single slip has become popular in recent years [67, 94, 152, 180, 181]. However, the small specimen size and the effect of free surfaces induce artifacts that lead to disparities among the results reported in the literature. Conventional slip trace analysis has also been employed to estimate the contribution of different slip systems to the overall plastic deformation in HCP polycrystals [34] but this procedure cannot provide absolute values of the CRSS but the ratios between the different slip system families. Wang *et al.* [183] presented a thorough literature review about the CRSS values and ratios in Ti from different experimental investigations and used high-energy X-ray diffraction microscopy to estimate the CRSS for the different slip systems in pure Ti. However, there is no general agreement in the literature about the actual CRSS for the different slip systems in Ti due to the large scatter in the available data.

Hence, the CRSS per slip system τ_{c0}^{α} is typically treated as a fitting parameter in crystal plasticity models of HCP metals. In this work, the values of τ_{c0}^{α} were fitted to experimental data found in the literature for the flow stress of Ti and Mg as a function of grain size. In the case of pure Ti, the experiments were carried out at room temperature and at $2.8 \cdot 10^{-4}$ s^{-1} for grain sizes from 6 to 100 μm and different applied strains [107]. The experimental data used to fit the CRSS for pure polycrystals Mg with grain sizes in the range 43 to 172 μm were obtained at $200°\mathrm{C}$ and a strain rate of $1.7 \cdot 10^{-4}$ s^{-1} [135]. High temperature was chosen to neglect the effect of deformation twinning, which is not included in the current crystal plasticity model and can have an important effect at room temperature. The fitting process of the lattice resistance τ_{c0}^{α} started by trying to fit the lattice resistance

values of the dominant slip systems, i.e. prismatic slip in Ti and basal slip in Mg. Then, the τ_{c0}^{α} for the other slip systems were chosen in order to keep reasonable CRSS ratios according to the data found in the literature. The results of the flow stress of each set of τ_{c0}^{α} values were validated against the experimental data of flow stress as a function of the grain size, employing the estimated flow stress for a very large grain size. To obtain this value, the intersection of the linear fit of the experimental data with the y-axis was calculated (see Fig. 6.16). This value was compared to the simulation of the polycrystals with fully transparent GBs, that represent the behavior of an "infinite" grain size. The selected values for the CRSS per slip system are shown in Table 6.5, together with the calculated CRSS ratios with respect to prismatic slip for Ti and with respect to basal slip for Mg. These ratios are in agreement with the observed ranges reported by Wang *et al.* [183] for pure Ti, and Chapuis *et al.* [36] and Sánchez-Martín *et al.* [120] for pure Mg at high temperature.

Table 6.5: Lattice resistance and CRSS values for the Ti and Mg polycrystals, calculated with Eq. 6.8. The CRSS ratios with respect to prismatic slip are indicated between parenthesis for Ti, and the CRSS ratios with respect to basal slip are indicated between parenthesis for Mg.

	Ti			Mg		
	basal	*prism*	*pyr (I)*	*basal*	*prism*	*pyr (II)*
Lattice resistance $\tau_{c_0}^{\alpha}$ (MPa)	52.9	24.4	76.3	0	10	25
CRSS τ_c^{α} (MPa)	60 (2)	30	90 (3)	0.7	10.7 (15)	26.3 (38)

The modified Kocks-Mecking law that controls the evolution of dislocation density (Eqs. 6.4 and 6.5) during deformation in HCP metals is equivalent to the one in FCC metals,

$$\dot{\rho}^{\alpha} = \frac{1}{b^{\alpha}}\left(\frac{1}{\ell^{\alpha}} - 2y_c^{\alpha}\rho^{\alpha}\right)|\dot{\gamma}^{\alpha}| \quad \text{if slip transfer is allowed for any } \beta \tag{6.9}$$

$$\dot{\rho}^{\alpha} = \frac{1}{b^{\alpha}}\left(\max\left(\frac{1}{\ell^{\alpha}}, \frac{K_s}{d_b}\right) - 2y_c^{\alpha}\rho^{\alpha}\right)|\dot{\gamma}^{\alpha}| \quad \text{if slip transfer is blocked } \forall\beta, \tag{6.10}$$

where β stands for any slip system in the nearest neighbor grain. Eq. 6.9 stands for the standard Kock-Mecking law that includes two terms that control the generation and annihilation of dislocations. Dislocation generation in the slip system α depends on the dislocation MFP, ℓ^{α} given by Eq. 6.6, where K was estimated by Alankar *et al.* [6] for α-Ti. No information was found about K for pure Mg was found in the literature, and the value for Ti was used.

Dislocation annihilation is controlled by the current dislocation density in the system α ρ^{α} and y_c^{α}, which stands for the effective annihilation distance between dislocations for the current slip system family. The critical annihilation distance for screw dislocations y_{edge}^{α} is estimated as $6b^{\alpha}$, as in FCC polycrystals. In the case of screw dislocations, Essmann *et al.* [51] proposed a relation between the critical annihilation distance and the CRSS for

dislocation glide. The assumption is that, in the absence of external stresses, two screw dislocations of opposite sign, separated by a distance y_c, experience an attractive shear stress of $\mu b/2\pi y_c$, where μ is the shear modulus and b the magnitude of the Burgers vector. These dislocations will mutually annihilate if the stress exceeds the stress τ_c required for dislocation glide, i.e. the CRSS. Hence, the critical dislocation annihilation distance assuming equal densities of edge and screw dislocations can be calculated according to

$$2y_c^\alpha = y_e^\alpha + y_s^\alpha = 6b^\alpha + \frac{\mu^\alpha b^\alpha}{2\pi\tau_c^\alpha}, \tag{6.11}$$

where the shear modulus μ^α, the Burgers vector b^α, and the CRSS τ_c^α depend on the slip system. In HCP metals, cross-slip can take place between <a> dislocations gliding in the basal and the prismatic slip planes. Hence, the smallest y_c^α among basal and prismatic slip is imposed for both slip system families because cross slip is controlled by the slip system with the highest CRSS (and, thus, the smallest y_c). The calculated values of y_c^α for each slip system family are presented in Table 6.6, and the smallest y_c between <a> basal and prismatic slip are chosen and highlighted in bold.

Table 6.6: Calculated and chosen critical annihilation distance between dislocations y_c^α for the Ti and Mg polycrystals, calculated with Eq. 6.11. The smallest y_c^α among basal and prismatic slip is highlighted in bold and will be chosen for both slip systems to account for basal-prismatic cross-slip.

	Ti			Mg		
	basal	*prism*	*pyr (I)*	*basal*	*prism*	*pyr (II)*
Calculated y_c^α (nm)	**19**	29	26	840	**40**	32
Chosen y_c^α (nm)	19	19	26	40	40	32

Eq. 6.10 provides the dislocation accumulation rate for a slip system at a Gauss point near a GB when slip transfer across the boundary is blocked. The critical distance at the GB that leads to an increase in the dislocation generation rate (and, thus, to the formation of a dislocation pile-up) is given by the condition $K_s/d_b > 1/\sqrt{\ell^\alpha}$. Due to the lack of information about K_s for HCP polycrystals, it was assumed to be the same used for FCC polycrystals [153], while d_b depends on the location of the Gauss point and on the orientation of the crystal. The different parameters of the crystal plasticity model for HCP Ti and Mg are included in Table 6.7.

6.3 Polycrystal homogenization framework

6.3.1 RVE generation

The mechanical behavior of polycrystals with different grain sizes was determined by means of the finite element simulation of the deformation of an RVE of the microstructure

Table 6.7: Parameters of the dislocation-based crystal plasticity model depending on the slip systems for the Ti and Mg (HCP) crystals.

	Ti			Mg		
	basal	*prism*	*pyr (I)*	*basal*	*prism*	*pyr (II)*
Shear modulus μ^α (GPa) [23, 81]	46.5	35	47.7	16.4	16.4	16.4
Burgers vector b^α (nm) [23, 128]	2.95	2.95	5.53	3.21	3.21	6.12
Dislocation storage coefficient K [6]	20	20	20	20	20	20
Grain boundary storage coefficient K_s [153]	5	5	5	5	5	5

under uniaxial tension, following the standard procedures in full-field computational homogenization [158].

The RVE was generated using the open-source software Neper [146]. The crystals within the RVE are generated using Laguerre-Voronoi tessellations, which lead to polyhedra with flat interfaces. The generation of the RVE involves three distinct processes: tessellation, meshing, and visualization. The tessellation module constructs the geometry of the polycrystal within a convex domain from user-defined crystal properties. Tessellations can be created from morphological microstructural properties such as grain size and shape. The seeds and weights attributes of the tessellation are set by optimization to obtain the desired cell properties. Crystal orientations can be randomly distributed in the 3D space or directly provided by the user from the information obtained by EBSD or X-ray diffraction. Moreover, RVEs with periodic or non-periodic microstructures can be created.

Once the microstructure has been tessellated, it can be discretized with tetrahedral or hexahedral elements for the finite element simulations using Gmsh [63], either with linear or quadratic interpolation. The discretization approach follows a bottom-up scheme that consists of meshing the 0D, 1D, 2D, and 3D entities (vertices, edges, faces, and polyhedra) successively [146]. Each entity is meshed independently of the other entities of the same dimension to ensure good mesh quality. The mesh properties are controlled by several parameters selected by the user, such as the target characteristic length of the elements, c_l, and the gradient parameter, p_l, which is the maximum ratio between the lengths of two adjacent elements. Finally, the visualization module generates images of both the geometry and the mesh of the created RVE.

The RVE was made up of grains with random crystallographic orientations and discretized with second-order modified tetrahedra (C3D10M elements with ten nodes in Abaqus). The shape of the grains was equiaxed, and the grain size followed a lognormal distribution with average grain size $\bar{D}_g$ and standard deviation of $0.2\bar{D}_g$ (Fig. 6.1).

6.3.2 Boundary conditions

The microstructure of the RVE was periodic along the three directions of the space, and periodic boundary conditions were applied to all the nodes on the boundary of the do-

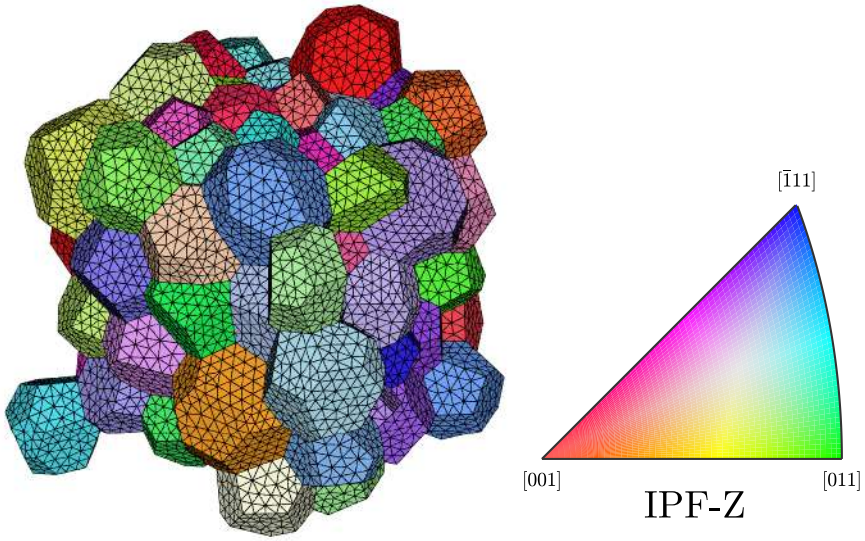

Figure 6.1: RVE of the microstructure including 100 grains discretized with 150000-second order tetrahedra. The grains are colored according to the crystal orientation relative to the Z axis, as indicated in the inverse pole figure.

main. The displacements of each pair of nodes A and B located on opposite surfaces of the domain were linked according to

$$\mathbf{u}_B - \mathbf{u}_A = (\bar{\mathbf{F}} - \mathbf{I})L \tag{6.12}$$

where L is the length of the cubic domain. The far-field deformation gradient $\bar{\mathbf{F}}$ applied to the RVE is obtained by prescribing the displacements of three master nodes M_i.

$$\mathbf{u}(M_i) = (\bar{\mathbf{F}} - \mathbf{I})\mathbf{e}_i \tag{6.13}$$

where $\mathbf{e}_i$ with $i = 1, 2, 3$ stand for the orthogonal basis along the three Cartesian axes x, y, z. The master nodes are linked to the microstructure by three springs of negligible stiffness, joined to a fixed node inside the RVE. The displacement of the master nodes is prescribed by applying a nodal force P_j to the master node M_i and degree of freedom j according to

$$P_j(M_i) = (\bar{\boldsymbol{\sigma}}\mathbf{e}_i)_j A_i \tag{6.14}$$

where $\bar{\boldsymbol{\sigma}}$ is the far-field stress tensor, and A_i is the projection of the current area of the face perpendicular to the $\mathbf{e_i}$ in this direction.

6.3.3 GB distance calculation

In order to apply Eqs. 6.4 and 6.5, it is necessary to calculate the distance d_b from each Gauss integration point to the nearest GB along the slip direction corresponding to each

slip system and to identify the grain across the boundary. This latter information is necessary to apply the geometrical criteria (LRB, m', Δb, or any combination thereof) to assess whether slip transfer across the GB is possible for each slip system. This information only depends on the geometry of the RVE and the discretization, and the values of d_b for each slip system in each Gauss point are calculated and stored before the numerical analysis.

The strategy to determine d_b is schematically presented in Fig. 6.2, which shows a simplified 2D representation of a section of a polycrystal in which grain A is surrounded by grains B, C, and D. The integration point P_0 that belongs to a tetrahedral element of grain A (shaded in grey) is plotted in green in Fig. 6.2 and the slip direction corresponding to the slip system α is plotted as a dashed blue line. The first step to calculate the distance d_b is to identify positions P_0 to P_1 along the positive slip direction (indicated by α^+ in the figure) using the distance $0.5R_{eq}$, where R_{eq} is the equivalent radius of grain A (determined from the volume of the grain assuming that it is spherical). If P_1 belongs to grain A (which is easily determined from the coordinates of the vertices of grain A, which is a convex polyhedron), the process is repeated until the position of P_i is outside grain A and within grain B. Then, a bisection method is used to determine the position of the GB between P_i and P_{i-1} with a given tolerance and to determine d_b along the positive slip direction. The same procedure is repeated for the negative slip direction, and the corresponding distance to the opposite GB, as well as the grain across this boundary, is determined (grain D in this case). The minimum value of d_b from both directions is stored as d_b together with the identifier for the nearest neighbor grain. It was assumed that d_b is constant throughout the analysis, a reasonable assumption because of the small applied far-field strain in the simulations (5%).

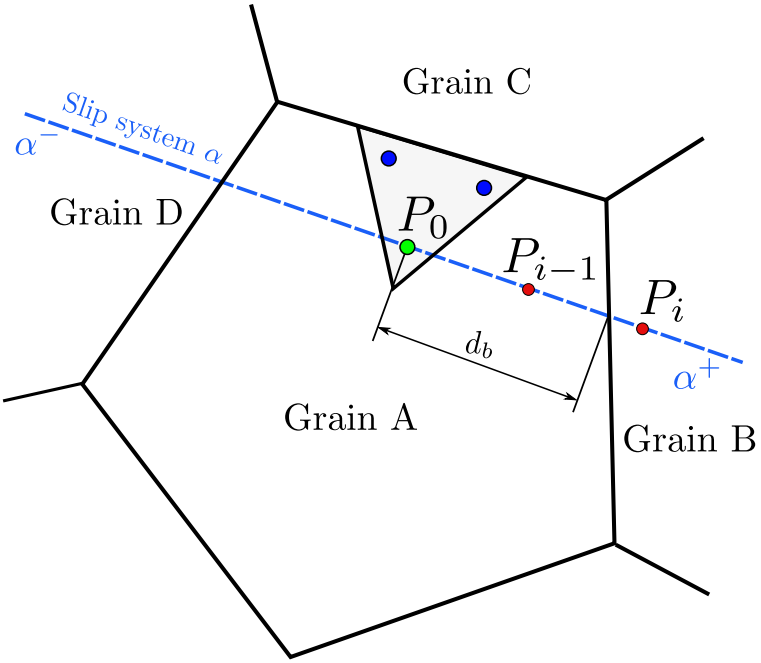

Figure 6.2: Schematic of the calculation of the distance from a Gauss point to the nearest GB along one slip direction.

An exception appears when the integration point is lying next to the outer boundary of the RVE because a point P_i outside the RVE does not lie in the convex hull of any grain. In this case, the grain across the boundary along any slip system has to be determined, taking into account the periodicity of the RVE. The point P_i outside the RVE is shifted in the three directions of the space by a distance $\pm L$, which is the length of the RVE. Because of the periodicity of the RVE, one of the new positions of P_i necessarily falls within one grain, which is the nearest neighbor along such a slip system.

6.3.4 Slip transfer criteria calculation

Once the neighbor grain across the boundary has been identified for each slip system α at each Gauss integration point in grain A, the likelihood of slip transfer from the slip system α in grain A to any of the slip systems β in the neighbor grain B can be assessed using any of the geometrical criteria detailed in the introduction. Two of them, based on the Luster-Morris geometric compatibility criterion m' and on the residual Burgers vector Δb, have been used in this investigation because they are supported by experimental evidence. They can be computed as [19] (Fig. 1.5),

$$m'_{\alpha\beta} = (\boldsymbol{n}_\alpha \cdot \boldsymbol{n}_\beta)(\boldsymbol{b}_\alpha \cdot \boldsymbol{b}_\beta) \quad \text{and} \quad \Delta b_{\alpha\beta} = |\boldsymbol{b}_\alpha - \boldsymbol{b}_\beta| \tag{6.15}$$

where $\boldsymbol{n}_\alpha$ and $\boldsymbol{n}_\alpha$ are unit vectors perpendicular to the slip plane α in grain A and slip plane β in grain B. Obviously, all the vectors in Eq. 6.15 have to be expressed in the same reference frame. The orientation of grain A with respect to the Cartesian reference frame of the RVE is given by the Euler angles (φ_1^A, ϕ^A, φ_2^A) while that of grain B is given by (φ_1^B, ϕ^B, φ_2^B). The vectors $\boldsymbol{n}'_\alpha$ and $\boldsymbol{b}'_\alpha$ expressed in the reference frame of crystal A can be transformed to the reference frame of crystal B, $\boldsymbol{n}_\alpha$ and $\boldsymbol{b}_\alpha$, according to

$$\boldsymbol{n}_\alpha = \boldsymbol{n}'_\alpha \boldsymbol{G}_A^{-1} \boldsymbol{G}_B \quad \text{and} \quad \boldsymbol{b}_\alpha = \boldsymbol{b}'_\alpha \boldsymbol{G}_A^{-1} \boldsymbol{G}_B \tag{6.16}$$

where $\boldsymbol{G}_A$ and $\boldsymbol{G}_B$ stand for the orientation matrices of grains A and B, where, again, orientations are expressed relative to the Cartesian reference frame of the RVE as a function of the Euler angles of each grain, according to [157].

$$\boldsymbol{G} = \begin{pmatrix} \cos\varphi_1 \cos\varphi_2 - \sin\varphi_1 \sin\varphi_2 \cos\phi & \sin\varphi_1 \cos\varphi_2 + \cos\varphi_1 \sin\varphi_2 \cos\phi & \sin\varphi_2 \sin\phi \\ -\cos\varphi_1 \sin\varphi_2 - \sin\varphi_1 \cos\varphi_2 \cos\phi & -\sin\varphi_1 \sin\varphi_2 + \cos\varphi_1 \cos\varphi_2 \cos\phi & \cos\varphi_2 \sin\phi \\ \sin\varphi_1 \sin\phi & -\cos\varphi_1 \sin\phi & \cos\phi \end{pmatrix}.$$

Slip transfer between slip systems α and β is allowed when m' is above (or $\Delta b_{\alpha\beta}$ is below) a threshold value. If the condition of slip transfer is fulfilled for any β slip system in the neighbor grain, Eq. 6.4 is used as the constitutive equation of slip system α at the Gauss integration point of the crystal. Otherwise, slip transfer from α to β is not possible due to the geometric incompatibility, and the constitutive equation is expressed by Eq. 6.5.

It should be noted that these changes in the slip behavior due to the presence of impenetrable GBs are only active near GBs (as dictated by the condition $K_s/d_b > 1/\sqrt{\ell^\alpha}$). Moreover,

the geometrical analysis of slip transfer at each GB indicates how many pairs of slip systems are suitably oriented to transfer slip across the boundary, leading to a classification of GBs from fully opaque (slip transfer is not possible for any pair of slip systems) to translucent (slip transfer is possible for some pairs of slip systems) to fully transparent (slip transfer is allowed for all 12 pairs of slip systems in the case of FCC crystals).

The mechanical behavior of the RVEs under uniaxial tension was simulated using Abaqus Standard [163] within the framework of the finite deformations theory with the initial unstressed state as reference. The constitutive behavior of each crystal was governed by the crystal plasticity model presented in Section 6.2.1, which was implemented in Abaqus through a user-defined material model (UMAT).

6.4 Results and discussion

6.4.1 RVE selection

Different sets of simulations were carried out in FCC Cu RVEs with 20 μm grain size and fully opaque GBs to assess the effect of the number of grains, the discretization, and the random set of orientations on the mechanical behavior of the polycrystals. The mechanical response of RVEs with 50, 100, and 200 grains and random texture was calculated using approximately the same discretization ($\approx$ 50k elements). As shown in Fig. 6.3 (a), the differences in the flow strength between the RVEs with 50 and 100 grains were about 5% and only 2% between the RVEs with 100 and 200 grains. Subsequently, RVEs with 100 grains were discretized with 12000 (coarse mesh), 150000 (medium mesh), and 350000 (fine mesh) second-order tetrahedral elements (C3D10M in Abaqus), to assess the mesh sensitivity in the tensile response of the polycrystals. The coarse discretization overestimated the flow strength of the polycrystal by $\approx$ 10% while the difference in flow strength between the medium and fine discretizations was only 2% (Fig. 6.3 (b)). Thus, RVEs with 100 grains discretized with 150000 elements were selected for the analysis in order to optimize the balance between time and accuracy (final RVE displayed in Fig. 6.1). Finally, simulations of the same RVE with three different sets of random orientations showed differences of 4% between the maximum and minimum flow stress (Fig. 6.3 (c)). Hence, the texture that led to the intermediate flow stress was selected for the simulations presented in this work.

6.4.2 Effect of slip transfer on the flow strength of FCC metals

The effect of grain size and grain boundary character on the mechanical response of Al and Cu polycrystals was analyzed using the crystal plasticity model and the computational homogenization scheme presented above. To this end, RVEs with four different grain sizes $\bar{D}_g$ (10, 20, 40, and 80 μm) and the same set of randomly generated orientations were generated. Simulations were performed at quasi-static strain rates ($\approx 10^{-3}\ s^{-1}$) under uniaxial tension up to 5% applied strain. The initial dislocation density was $\approx 10^{12}$ m^{-2}, evenly distributed among the 12 slip systems, which corresponds to well-annealed

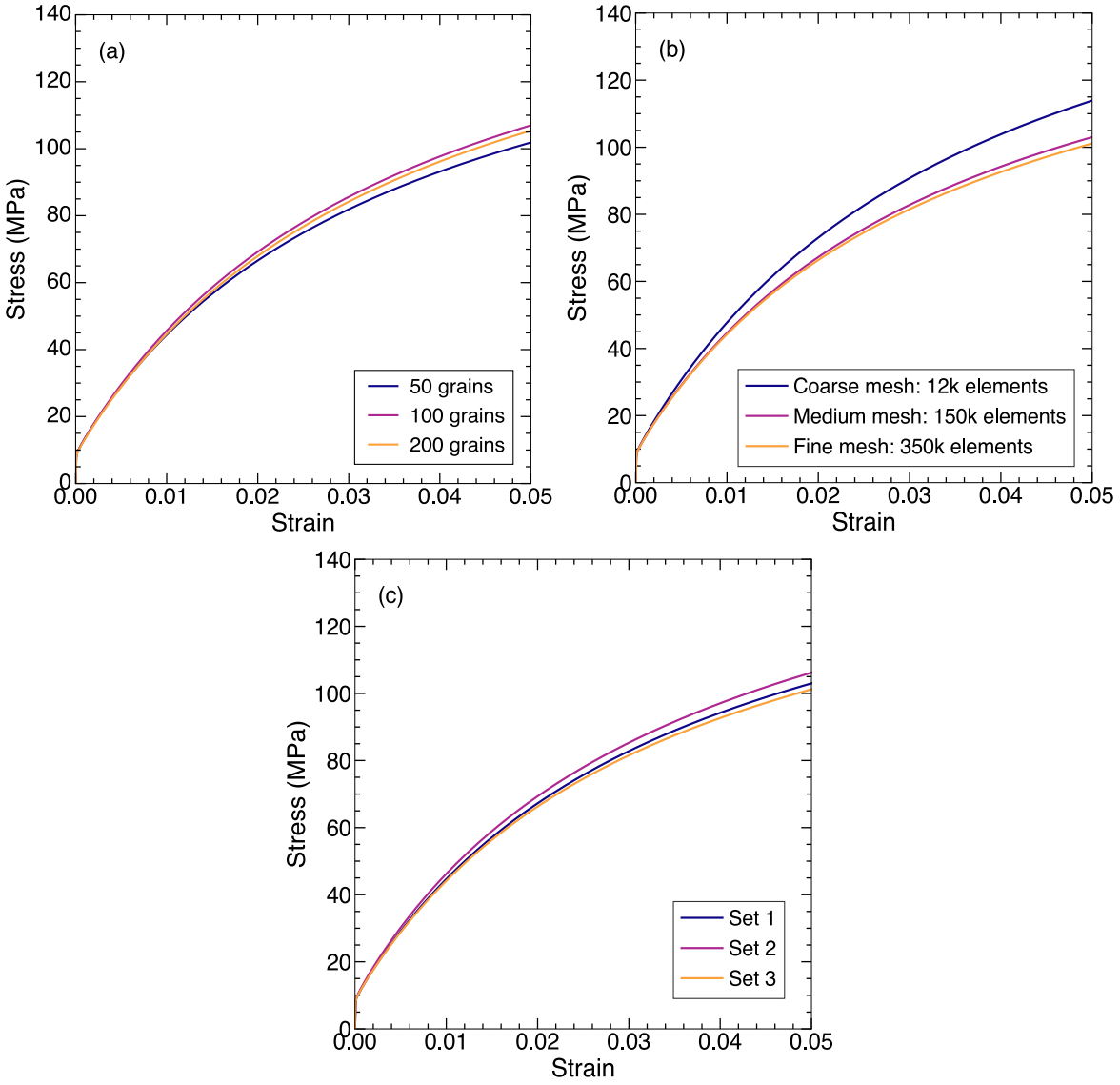

Figure 6.3: RVE selection analysis performed in Cu RVEs with 20 μm grain size and fully opaque GBs. (a) Effect of the number of grains on the tensile response. (b) Effect of the discretization on the tensile response. (c) Effect of the set of random orientations on the tensile response.

polycrystals. The parameters of the crystal plasticity model for both Al and Cu can be found in Tables 6.1 and 6.2.

The effect of grain boundary character on the engineering stress-strain curves under tension of Al and Cu polycrystals with different average grain sizes ($\bar{D}_g$ = 10 μm and 40 μm) is presented in Figs. 6.4 (a)-(d). The stress in these plots has been normalized by μb to reveal the differences in strain hardening between Al and Cu as a result of the interaction, accumulation, and annihilation of dislocations and to compensate for the effect of the differences in elastic constants. Five different curves are plotted in each figure: the strongest

polycrystals correspond to simulations in which all GBs are assumed to be opaque and, thus, the constitutive equation of the material is given by Eq. 6.5. In contrast, the softest response is given by the dashed black curves that were obtained, assuming that all GBs were fully transparent. The constitutive equation of the polycrystal, in this case, is given by Eq. 6.4, and the results of the simulations are independent of $\bar{D}_g$ and stand for the behavior of a polycrystal with an "infinite" grain size. Obviously, the differences in the flow stress between polycrystals with fully opaque and fully transparent GBs increase as the average grain size decreases, in agreement with the Hall-Petch effect. It should be noted that the stress-strain curves of Al polycrystals with either opaque or transparent GBs in Figs. 6.4 (a) and (b) show very little strain hardening for strains $> 2\%$, and this behavior is associated with the high values of K and y_c in the constitutive model. Dislocation multiplication is responsible for the strain hardening in the bulk crystals and decreases as the similitude coefficient K increases because the dislocation MFP is proportional to K. Moreover, dislocation annihilation -which reduces strain hardening- is more efficient for higher y_c. in contrast, the stress-strain curves of Cu polycrystals present continuous strain hardening because K and y_c are smaller. Thus, Al and Cu represent two FCC polycrystals with different strain-hardening behavior.

The three curves between those corresponding to fully opaque and fully transparent GBs in Figs. 6.4 (a)-(d) show the behavior of polycrystals where slip transfer is allowed between slip systems that intersect at a GB when the Luster-Morris parameter m' is higher than a threshold given by 0.9, 0.75 or 0.5. The higher the threshold, the closer the stress-strain curves are to the fully opaque case. On the other hand, the stress-strain curves obtained with a threshold $m' > 0.5$ are almost the same as those obtained with fully transparent GBs for both Al and Cu. The effect of slip transfer on the formation of dislocation pile-ups near the GBs can be ascertained from the spatial distribution plots of the dislocation density in a cross-section of the RVEs corresponding to Al (Figs. 6.5 (a), (c) and (e)) and Cu polycrystals (Fig. 6.5 (b), (d) and (f)) with an average grain size of 10 μm deformed up to 5%. Obviously, high dislocation densities are found at all of GBs if they are assumed to be opaque (Figs. 6.5 (a) and (b)), leading to a large increase in the flow stress observed in Figs. 6.4 (a) and (c) for Al and Cu polycrystals with $\bar{D}_g = 10\ \mu m$. As slip transfer is allowed, some opaque GBs become translucent or transparent as slip transfer is allowed, as shown in Figs. 6.5 (c) and (e) for Al and in (d) and (e) for Cu, and the number of GBs in which dislocation pile-ups have disappeared increases as the geometrical threshold for slip transfer is reduced in the model. In the case of $m' > 0.5$ (not shown in the figure), practically all GBs are transparent, and no dislocation pile-ups can be found.

The formation of pile-ups at GBs is directly associated with an increase in the local stresses, as shown in the spatial distribution plots of the Von Mises stress in the cross-section of the RVEs of Al (Fig. 6.6 (a), (c) and (e)) and Cu polycrystals (Fig. 6.6 (b), (d) and (f)) with an average grain size of 10 μm deformed up to 5%. The more transparent the GB, the lower the stress concentration, and thus, slip transfer may play a dominant role in the determination of the GBs at which damage may develop in polycrystals.

The results presented above show how slip transfer influences the local dislocation density and flow stress at GBs. Obviously, the reduction in the strength of the polycrystal

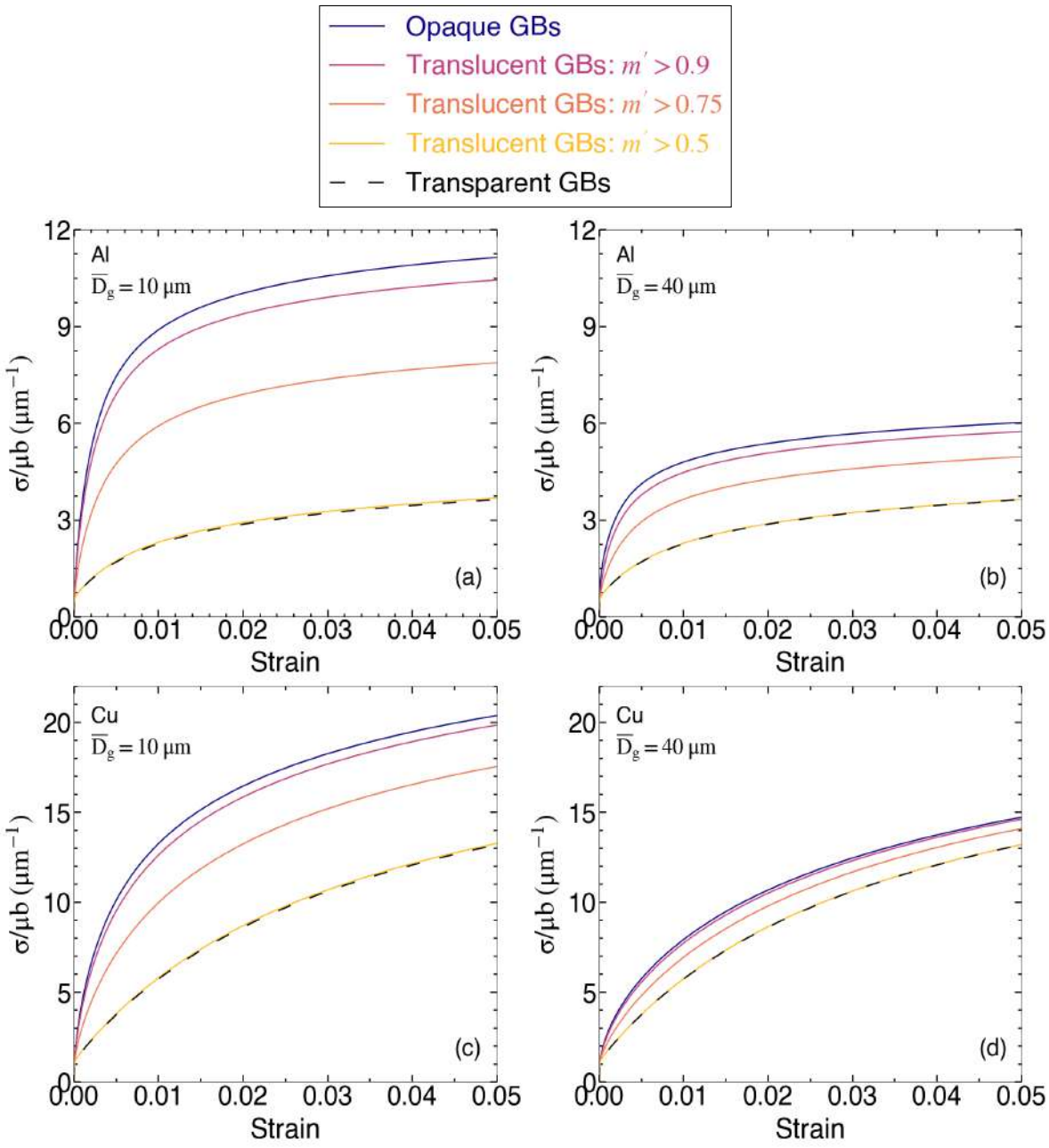

Figure 6.4: Engineering stress-strain curves of Al and Cu polycrystals as a function of grain boundary type: (a) Al $\bar{D}_g$ =10 μm, (b) Al $\bar{D}_g$ = 40 μm, (c) Cu $\bar{D}_g$ = 10 μm and (d) Cu $\bar{D}_g$ = 40 μm.

should be related to the threshold for translucent GBs in the RVE. This information can be obtained from the geometrical analysis to determine the nearest neighbor grain for each slip system α presented in section 6.3 and the corresponding m' values for all the β slip systems in the nearest neighbor grain. Then, a GB between grains A and B is characterized from the viewpoint of slip transfer by all the m' values between all the slip systems in grains A and B. The translucency of the grain boundary can be assessed by analyzing the

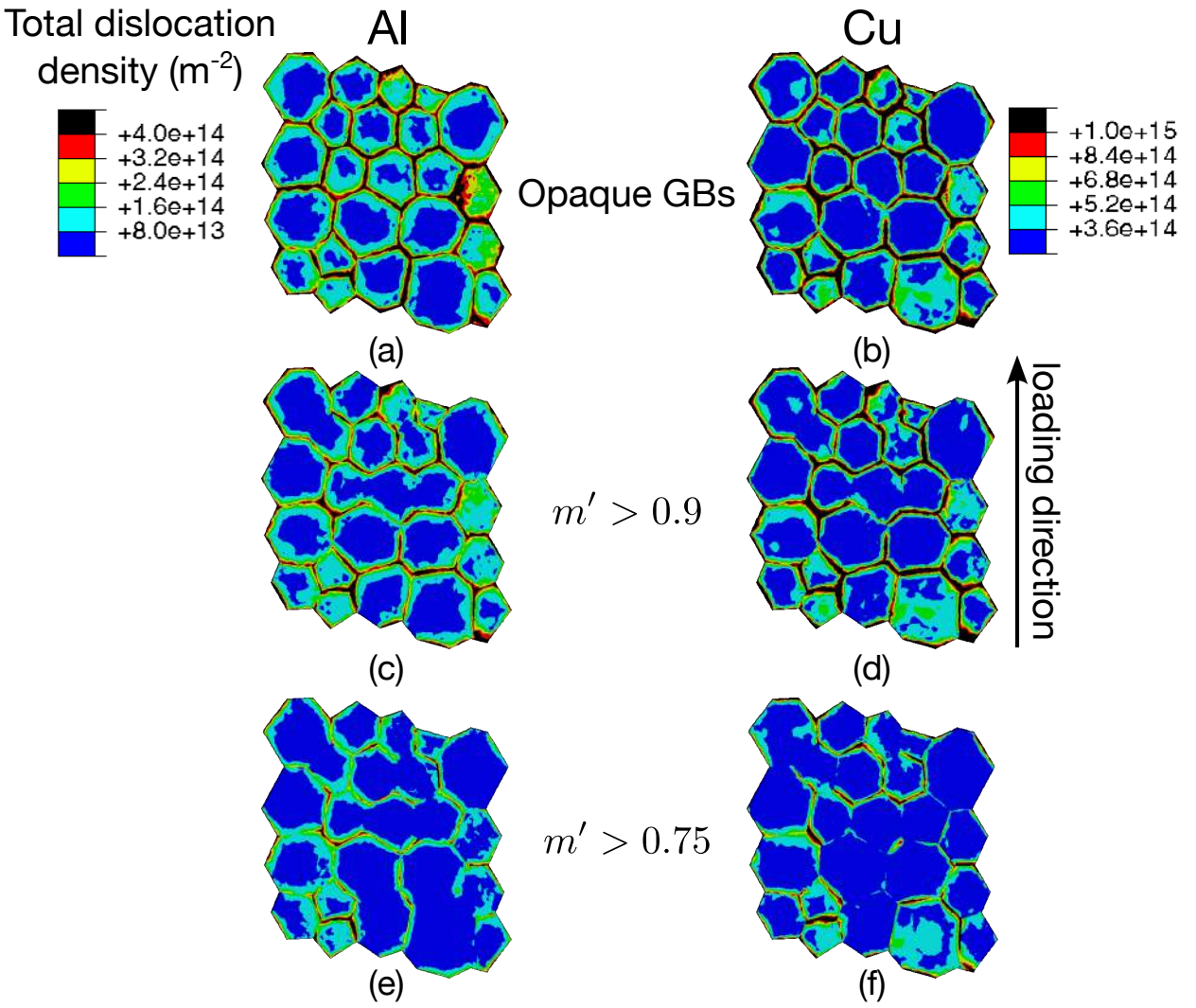

Figure 6.5: Spatial distribution of the total dislocation density (in m^{-2}) in a cross-section of the RVE of the Al and Cu polycrystals with an average grain size of 10 μm deformed up to 5%. (a) Al, opaque GBs. (b) Cu, opaque GBs. (c) Al, translucent GBs with $m' > 0.9$. (d) Cu, translucent GBs with $m' > 0.9$. (e) Al, translucent GBs with $m' > 0.75$. (f) Cu, translucent GBs with $m' > 0.75$.

number of slip systems that fulfill a slip transfer criterion. Taking into account that FCC crystals have 12 slip systems from the $\{111\} < 110 >$ family, a 12×12 m' matrix is calculated for pairs of neighbor grains, where each row relates the geometric compatibility of the lattice from a given incoming slip system α. In this context, slip transfer is considered possible along a certain slip system, for instance, $\alpha = 1$, when any of the $m'_{1\beta}$ values for the 12 possible outgoing slip systems β in the nearest neighbor grain is above the threshold for slip transfer. Thus, the number of slip systems in grain A that can transfer slip can be determined for each grain boundary, and the grain boundaries in the RVE can be classified according to their translucency to dislocations in three distinct groups: opaque GBs (slip transfer is not allowed for any pair of slip systems), translucent or partially-transparent

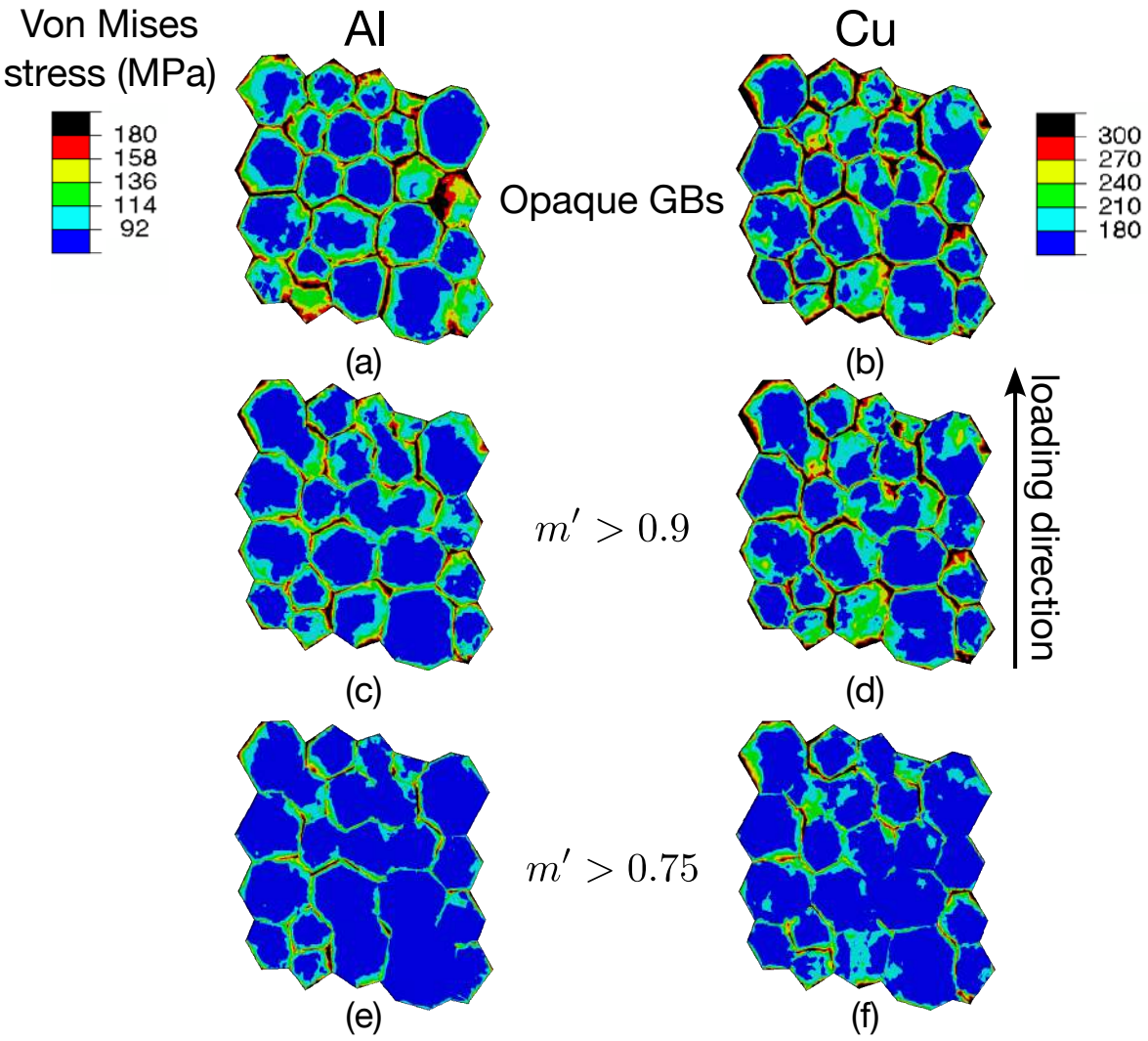

Figure 6.6: Spatial distribution of the Von Mises stress (in MPa) in a cross-section of the RVE of the Al and Cu polycrystals with an average grain size of 10 μm grain size deformed up to 5%. (a) Al, opaque GBs. (b) Cu, opaque GBs. (c) Al, translucent GBs with $m' > 0.9$. (d) Cu, translucent GBs with $m' > 0.9$. (e) Al, translucent GBs with $m' > 0.75$. (f) Cu, translucent GBs with $m' > 0.75$.

GBs (slip transfer is allowed along several pairs of slip systems) and fully transparent GBs (slip transfer is allowed in all slip systems).

The fraction of GBs in the RVE as a function of the number of transparent slip systems across the boundary is plotted in Figs. 6.7 (a) to (c) for different values of the threshold m' for slip transfer. If the threshold for slip transfer is very high, $m' > 0.9$ (Fig. 6.7 (a)), 48% of the GBs are fully opaque while only 3.4% of the GB are fully transparent (all slip systems in one grain can transfer slip to -at least- one slip system in the neighbor grain). Most of the remaining slip systems are translucent and contain 1 to 4 slip systems that can transfer slip to the neighbor grain. The number of GBs where 5 to 11 slip systems can transfer slip is negligible. When the threshold for slip transfer is reduced to $m' > 0.75$, the fraction

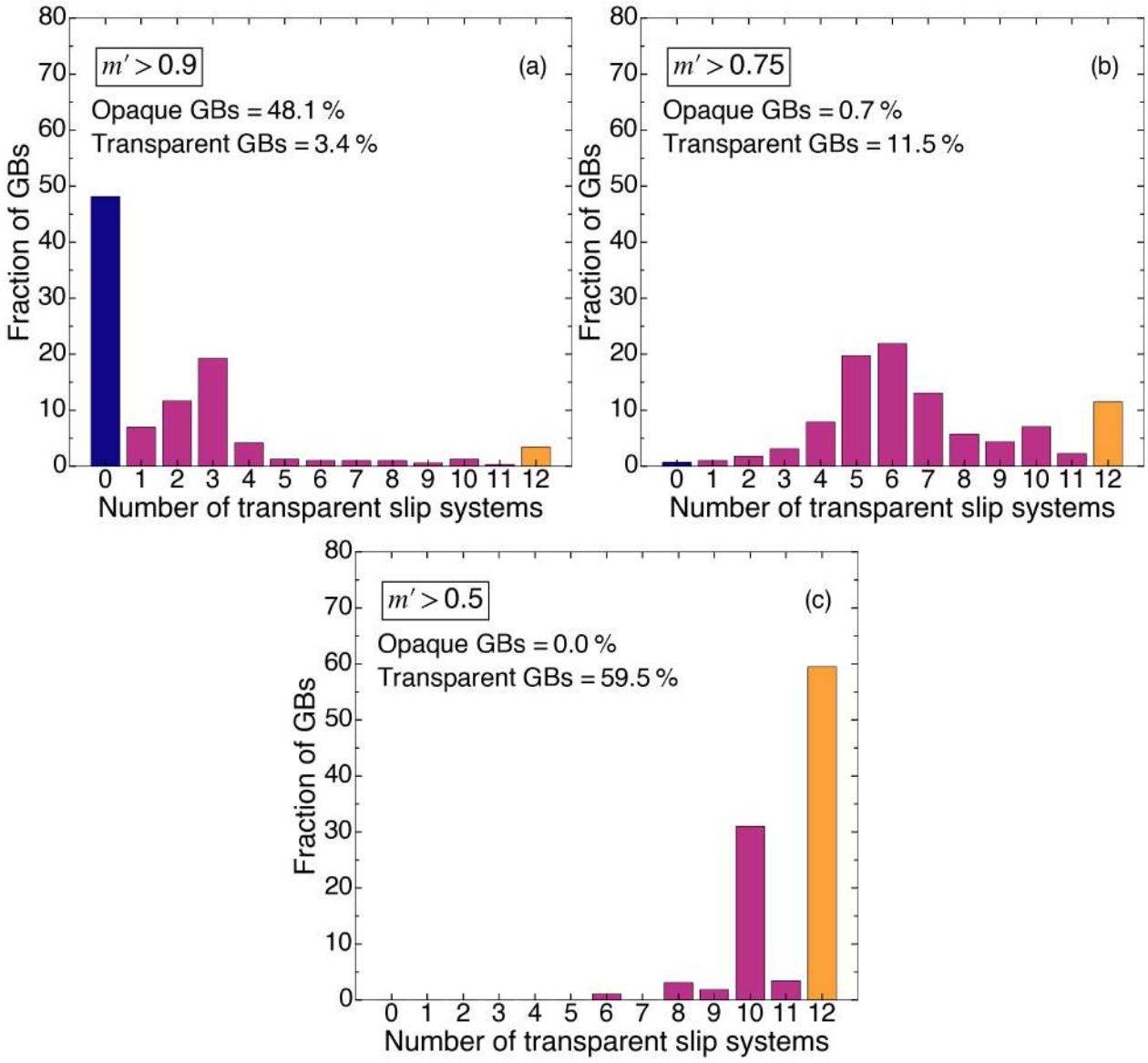

Figure 6.7: Fraction of GBs in the RVE as a function of the number of transparent slip systems. (a) $m' > 0.9$. (b) $m' > 0.75$. (c) $m' > 0.5$.

of fully opaque GBs drops to $< 1\%$ while the number of fully transparent GBs increases to 11.5%. Moreover, most of the GBs can transfer slip across the GB along four or more slip systems. Finally, if the threshold for slip transfer is further reduced to $m' > 0.5$ (Fig. 6.7 (c)), almost 60% of the GBs are fully transparent, and the remaining ones can transfer slip along many slip systems, leading to a polycrystal in which the effect of GBs on the strength can be neglected.

So far, slip transfer in the simulations has been characterized by the Luster-Morris compatibility factor, but any other geometrical factor can be used in the model. For instance, the engineering stress-strain curves for Al and Cu polycrystals with an average grain size of 10 μm are plotted in Figs. 6.8 (a) and (b), respectively, when slip transfer across the

GB was allowed when the residual Burgers vector $\Delta b < 0.45b$. The curves corresponding to fully opaque and fully transparent GBs (as well as those obtained with a slip transfer threshold defined by $m' > 0.75$) are also plotted for comparison. It is worth noting that the stress-strain curves corresponding to $m' > 0.75$ and $\Delta b < 0.45b$ are almost identical for both Al and Cu, suggesting that the reduction in the flow stress due to slip transfer is mainly controlled by the fraction of opaque, translucent and transparent GBs and not by the particular criterion used. This assumption is confirmed by the histograms of the different types of GBs in the RVE from the viewpoint of slip transfer plotted in Fig. 6.9 for both slip transfer thresholds. The fraction of fully opaque and fully transparent GBs is very similar in both cases, and most of the GBs are translucent. Thus, slip transfer is allowed in a wide number of slip systems (from 2 to 10) for both slip transfer thresholds. It is interesting to notice that pairs of slip systems of an FCC crystal share the same Burgers vectors and, thus, the number of transparent or opaque slip systems in the case of the residual Burgers vector criterion is always an even number.

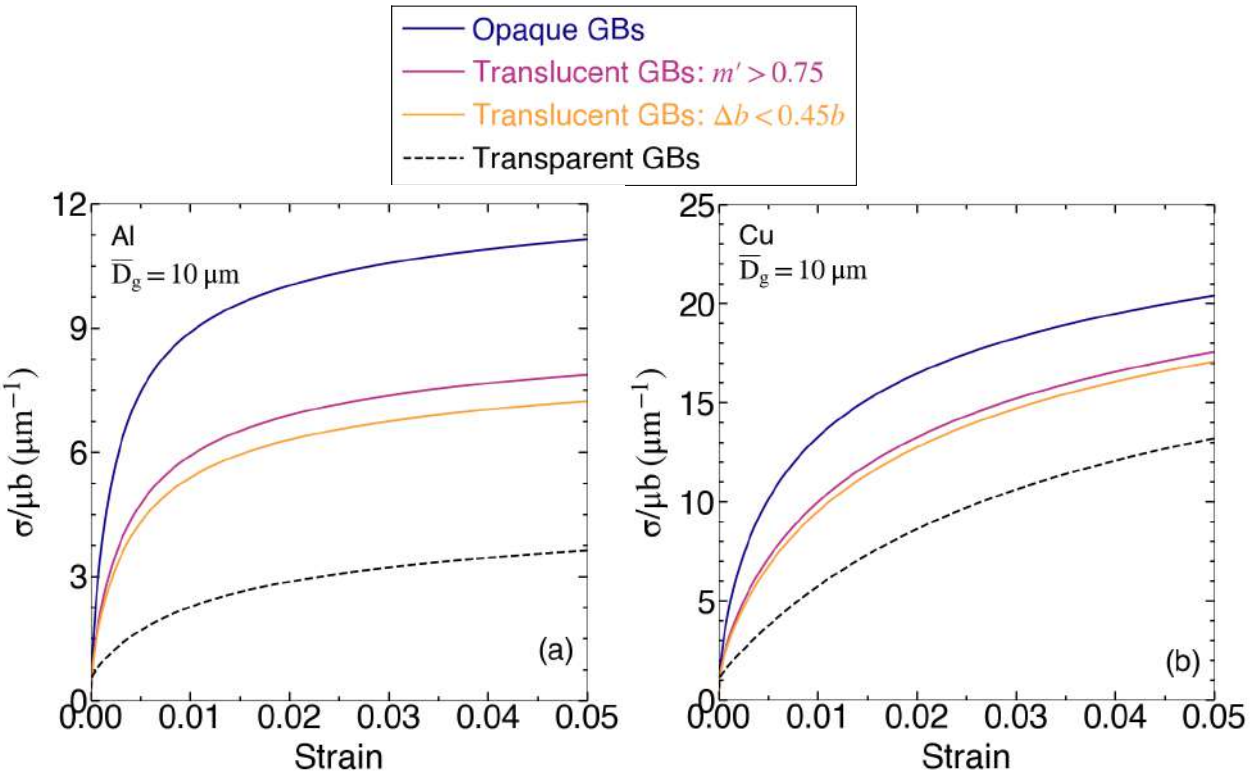

Figure 6.8: Engineering stress-strain curves of polycrystals with an average grain size of 10 μm for opaque and transparent GBs as well as slip transfer criteria of $m' > 0.75$ or $\Delta b < 0.45b$. (a) Al. (b) Cu.

6.4.3 Effect of slip transfer on the Hall-Petch law of FCC metals

The experimental evidence indicates that the strength of polycrystals increases as the grain size decreases following a power-law of the grain size. Based on theoretical results [192]

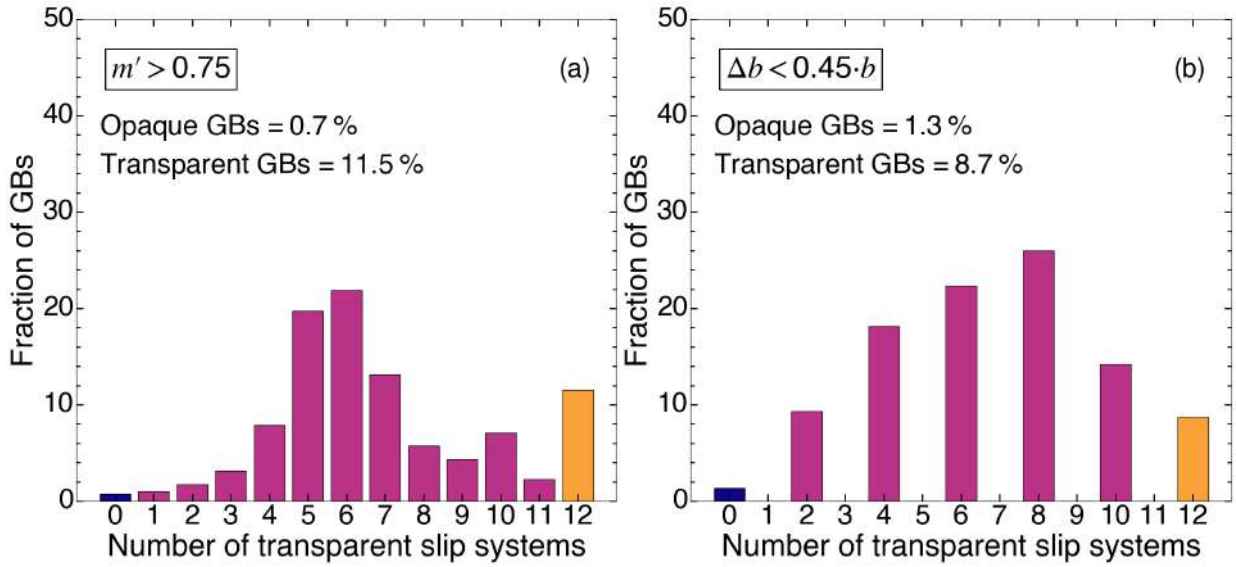

Figure 6.9: Fraction of GBs in the RVE as a function of the number of transparent slip systems. (a) $m' > 0.75$. (b) $\Delta b_{\alpha\beta} < 0.45b$.

and on dislocation dynamics simulations [11], the strengthening caused by GBs, $\sigma_y - \sigma_\infty$, has been proposed to scale with the average grain size $\bar{D}_g$ and the square root of the initial dislocation density in the polycrystal $\sqrt{\rho_i}$ according to [78]

$$\sigma_y/\sigma_\infty - 1 = C(\bar{D}_g\sqrt{\rho_i})^{-x} \tag{6.17}$$

where σ_y is the flow strength of the polycrystal, σ_∞ the flow stress of a polycrystal with "infinite" grain size, and C and x are material constants that depend on the physical parameters of the model for each FCC metal, mainly the similitude constant K and the effective annihilation distance y_c. Eq. 6.17 was in very good agreement with the results of the simulations for Al, Cu, Ni, and Ag FCC polycrystals under the assumption that all GBs were opaque [151] leading to similar values of the exponent (in the range 0.7 to 0.9) when the applied strain was 1%. The effect of slip transfer on the flow strength of Al and Cu polycrystals with different grain sizes (in the range 10 μm to 80 μm) deformed up to ε =1% and 5% is plotted in Fig 6.10. The initial dislocation density in all cases was of the order of 10^{12} m^{-2}.

The results of the simulations show that slip transfer reduces the strengthening provided by GBs but does not modify the exponent of Eq. 6.17 when values of the threshold m' for slip transfer are similar to those reported experimentally [7, 82, 198]. The exponent depends on the FCC metal and on the applied strain. It is slightly lower (more negative) for Cu than for Al and decreases in both cases when the strain to determine the flow strength of the polycrystal is increased from 1% to 5% due to the effect of annihilation of dislocations near the GBs where the dislocation density is maximum. Moreover, the reduction in GB strengthening for Al is always higher than that for Cu when the thresholds for slip transfer are set to $m' > 0.9$ or $m' > 0.75$, although the differences are not huge. They can be attributed to changes in the dislocation accumulation and annihilation of dislocations

near the GBs as a result of the differences in the physical parameters that control these phenomena in each metal.

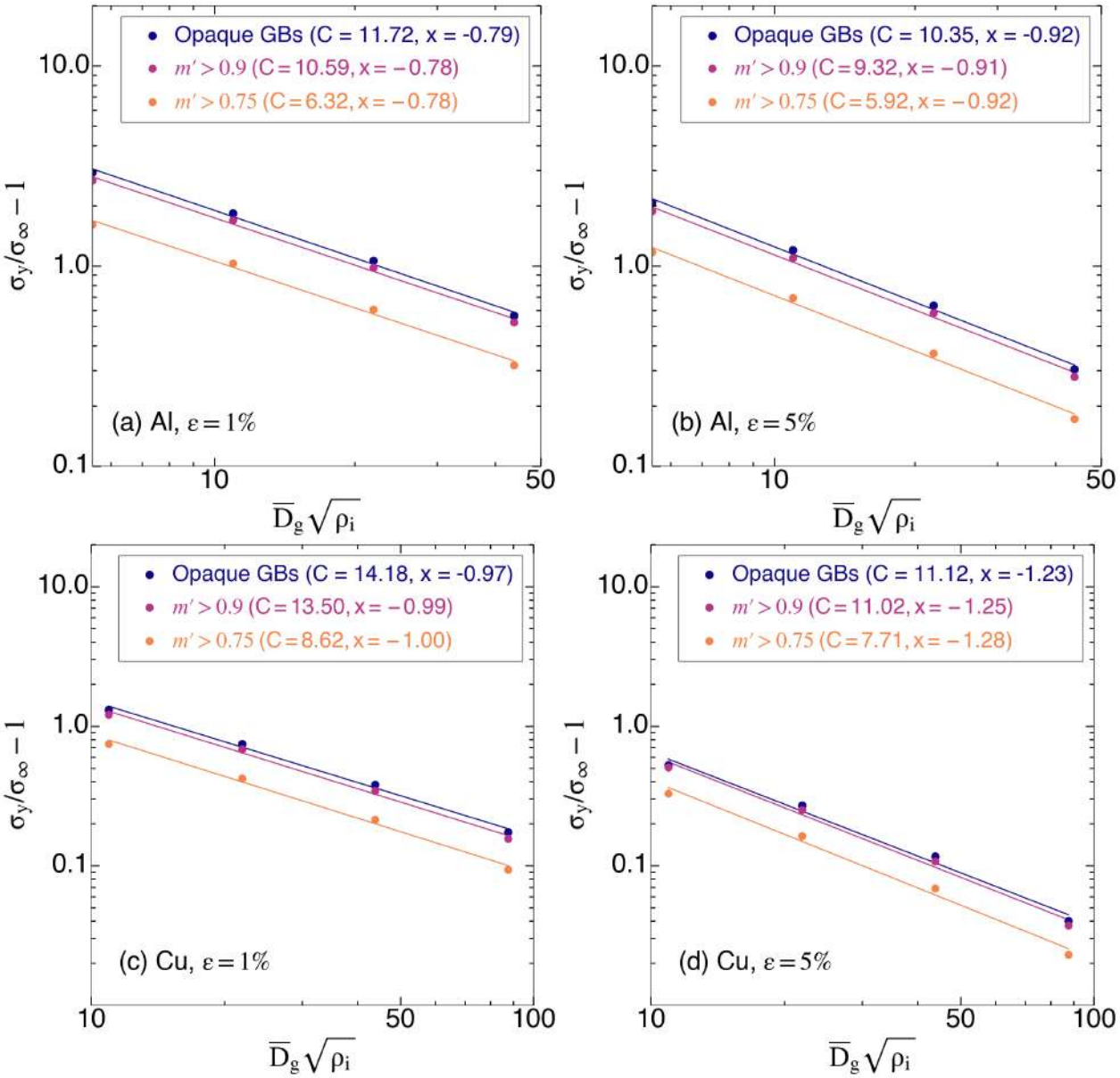

Figure 6.10: Grain boundary strengthening in Al and Cu polycrystals as a function of the adimensional parameter $\bar{D}_g\sqrt{\rho_i}$. (a) Al, $\varepsilon = 1\%$. (b) Al, $\varepsilon = 5\%$. (c) Cu, $\varepsilon = 1\%$. (d) Cu, $\varepsilon = 5\%$. The results of the simulations with fully opaque GBs and with thresholds $m' > 0.9$ and $m' > 0.75$ for slip transfer are plotted in each figure.

6.4.4 Comparison with experiments (FCC)

In order to assess the validity of the modeling strategy presented above, numerical simulations of the flow stress as a function of the grain size were carried out for Al, Cu, Ni,

and Ag polycrystals and compared with experimental data in the literature [33, 74, 75, 127]. The experiments in the literature were carried out at room temperature under quasi-static loading conditions, and, therefore, the effect of the strain rate on the flow stress was considered negligible. Due to the lack of information about the initial experimental dislocation density, it was assumed to be of the order of $10^{12}\ m^{-2}$ in all cases, which is a typical value for well-annealed polycrystals. The parameters of the crystal plasticity model for Al, Cu, Ni, and Ag were obtained by [151] and can be found in Tables 6.1 and 6.2. All the simulations were carried out using the RVE shown in Fig. 6.1 with random texture and average grain sizes in the range 10 μm to 80 μm.

The experimental results of the flow stress in tension are plotted as a function of the inverse of the average grain size, $\bar{D}_g^{-1}$ in Figs. 6.11 (a), (b), (c), and (d) for Al, Cu, Ni, and Ag polycrystals, respectively. Data for two different strain values are shown in each figure. Two simulation results assuming fully opaque GBs (open red circles) and translucent GBs with a threshold for the Luster-Morris parameter (open blue circles) are compared. The thresholds for m' were chosen for each metal to get the best fit of the experimental data because accurate experimental information is unavailable. Nevertheless, they are in the range of the values reported by different experimental investigations of slip transfer [7, 82, 198]. More importantly, good agreement between experiments and simulations is found when the average grain size is large ($\bar{D}_g^{-1} < 25$ mm^{-1}, $\bar{D}_g > 40\ \mu m$), regardless of the inclusion of slip transfer in the simulations, but the trend of the experimental data follows the predictions of the simulations including slip transfer when the grain sizes are smaller than 20 μm ($\bar{D}_g^{-1} > 50$ mm^{-1}). It should be noted, however, that the experimental data set of Ag is smaller than those of Al, Cu, and Ni and presents a larger scatter in the flow stress values, especially for 0.2% applied strain.

The relative errors between the experimental and simulated slopes of the scattered data plotted in Figs. 6.11 (a)-(d) for the studied metals and the different applied strains are displayed in Table 6.8. The relative error assessment shows that, except for the case of Ag at 0.2% strain, the relative error between the translucent GBs simulations and the experimental data is always smaller than that provided by the opaque GBs simulations. Hence, considering the effect of slip transfer in the deformation of polycrystalline materials achieves more realistic results in the tensile response than considering fully opaque GBs. It should be noted that the experimental measurement of the initial dislocation density is complex and time-consuming, usually leading to a lack of information about the dislocation density in the experimental data, which limits the quality of the fittings. This fact, together with the smaller size of the Ag data set, hinders the conclusion that the predictions with translucent GBs are more accurate than those carried out with opaque GBs for Ag at small strains.

It is also important to notice that slip transfer not only influences the overall strength of the polycrystal but also leads to dramatic changes in the stresses at the GBs as a function of the GB orientation (Fig. 6.6). These differences in GBs as a function of orientation are likely to play a dominant role in the nucleation of damage by GB cracking during monotonic and cyclic deformation or in aggressive environments [113, 126] as well as in the development of GB sliding during creep deformation [186]. The combination of the crystal plasticity

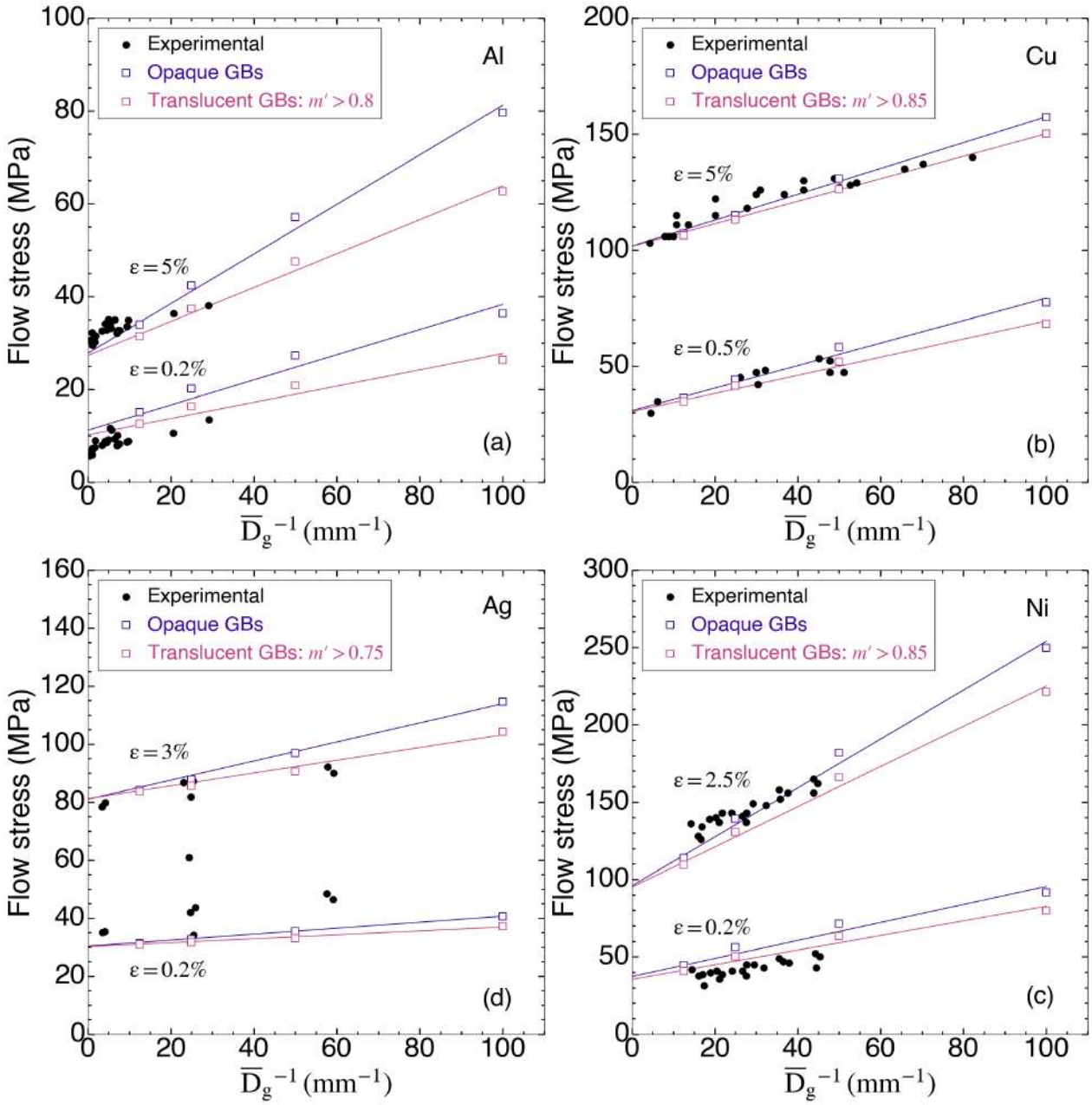

Figure 6.11: Experimental data from the literature and simulation results of the flow stress of Al, Cu, Ni, and Ag polycrystals as a function of $\bar{D}_g^{-1}$ for different applied strains. (a) Al. (b) Cu. (c) Ni. (d) Ag. Experimental results are indicated by black circles, while simulation results without and with slip transfer are represented by open red and blue circles. The linear fittings for the simulated results are indicated in red (opaque GBs) and blue (translucent GBs) solid lines.

model presented in this chapter together with cohesive elements at the GBs [5] would provide a novel way to explore the role of opaque, translucent, and transparent GBs on the ductility, formability, and forming limits of polycrystalline materials.

Material	Strain	m_{exp}	m_{opaque}	$\mathrm{RE}_{\mathrm{opaque}}$	$m_{translucent}$	$\mathrm{RE}_{\mathrm{translucent}}$
Al	0.2%	0.2	0.27	36%	0.18	12.2%
	5%	0.25	0.53	111%	0.37	44.4%
Cu	0.5%	0.39	0.48	22.8%	0.39	1.1%
	5%	0.46	0.56	21.9%	0.49	6.2%
Ag	0.2%	0.2	0.1	47.9%	0.07	65.7%
	3%	0.21	0.33	56.9%	0.22	4.8%
Ni	0.2%	0.41	0.58	42.9%	0.47	16.1%
	2.5%	1.03	1.58	54%	1.3	26.5%

Table 6.8: Flow stress slope error assessment between experimental data and simulation results for different strains for Al, Cu, Ag, and Ni (Fig. 6.11(a)-(d)). m_{exp}, m_{opaque}, and $m_{translucent}$ are the slopes of the scattered data for the experiments, opaque GBs simulation and translucent GBs simulation, respectively. $\mathrm{RE}_{\mathrm{opaque}}$ and $\mathrm{RE}_{\mathrm{translucent}}$ are the relative errors between the experiments and the opaque GBs simulation and between the experiments and the translucent GBs simulation, respectively.

6.4.5 Effect of slip transfer on the flow strength of HCP metals

Numerical simulations of the flow stress as a function of the grain size were carried out for Ti and Mg polycrystals, assuming fully opaque and fully transparent GBs. The same periodic RVE used for FCC polycrystals was employed, with random texture and average grain sizes of 10 μm, 20 μm, 40 μm, and 80 μm (see Fig. 6.1). The simulations were carried out at quasi-static strain rates of $\approx 10^{-4}\ s^{-1}$ to 1% plastic deformation. The initial dislocation density was $\approx 10^{12}\ m^{-2}$, evenly distributed among the slip systems, which corresponds to well-annealed polycrystals. The parameters of the crystal plasticity model adapted for Ti and Mg can be found in Tables 6.3, 6.4, 6.5, 6.6 and 6.7.

The engineering tensile stress-strain curves of Ti and Mg polycrystals up to 1% strain are plotted in Fig. 6.12 as a function of grain size. The simulations with fully opaque GBs are represented by solid lines, and the simulations with transparent GBs are plotted with dashed black lines. The simulations that assume that all GBs are transparent to dislocations are independent of the grain size and stand for the behavior of a polycrystal with an "infinite" grain size. As observed for FCC polycrystals, the differences in the flow stress between polycrystals with fully opaque and fully transparent GBs increase as the average grain size decreases, in agreement with the Hall-Petch effect. The stress in Fig. 6.12 (a) and (b) has been normalized by μb to highlight the differences in the strain hardening rate between Ti and Mg as a result of the interaction, accumulation, and annihilation of dislocations. μ^{prism} and b^{prism} have been used for Ti, whereas μ^{basal} and b^{basal} were used for Mg. This choice is supported by the fact that these slip systems possess the lowest CRSS values and thus will be dominant over the others for the numerical simulations (see Fig. 6.15).

As observed in Fig. 6.12 (d), Mg shows limited strain hardening for strains $> 0.8\%$, and this behavior can be attributed to the higher values of y_c^α in the constitutive model, since dislocation annihilation starts sooner as y_c^α increases. As a result, the dislocation accumulation and annihilation rates tend to balance, and the hardening rate reaches a steady state.

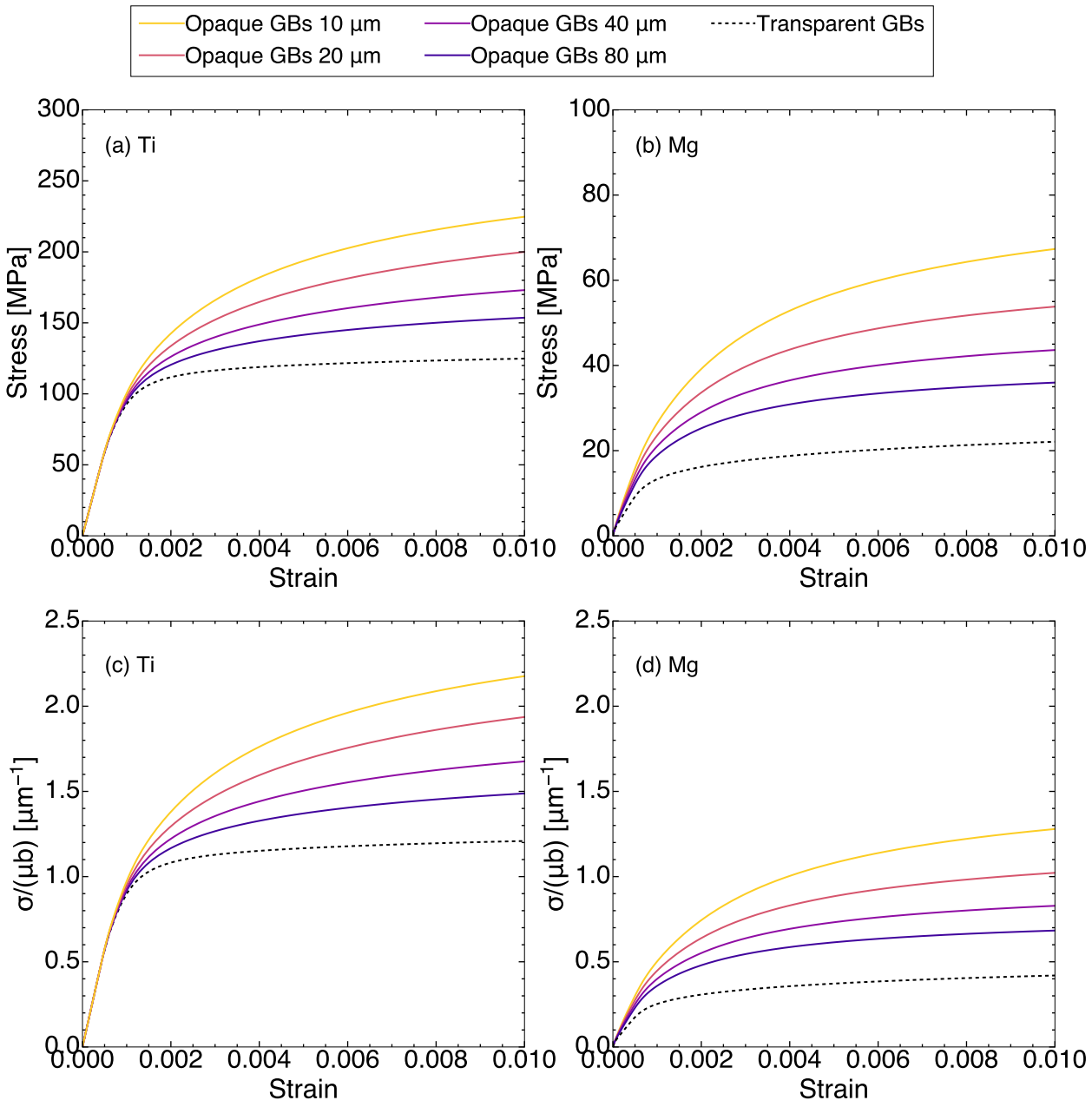

Figure 6.12: Engineering stress-strain curves of polycrystals with transparent GBs and opaque GBs with grain sizes between 10 and 80 μm for (a) Ti, and (b) Mg.

Conversely, the tensile response of Ti still presents strain hardening at 1% because the values of y_c^α are slightly smaller, and dislocation accumulation is dominant over dislocation annihilation.

The spatial distribution of the Von Mises stress (in MPa) and the total dislocation density (in m^{-2}) are plotted Figs. 6.13 and 6.14 for a cross-section of the Ti and Mg RVE polycrystals with transparent and fully-opaque GBs. High dislocation densities are found when GBs are opaque due to the formation of dislocation pile-ups, while smaller dislocation

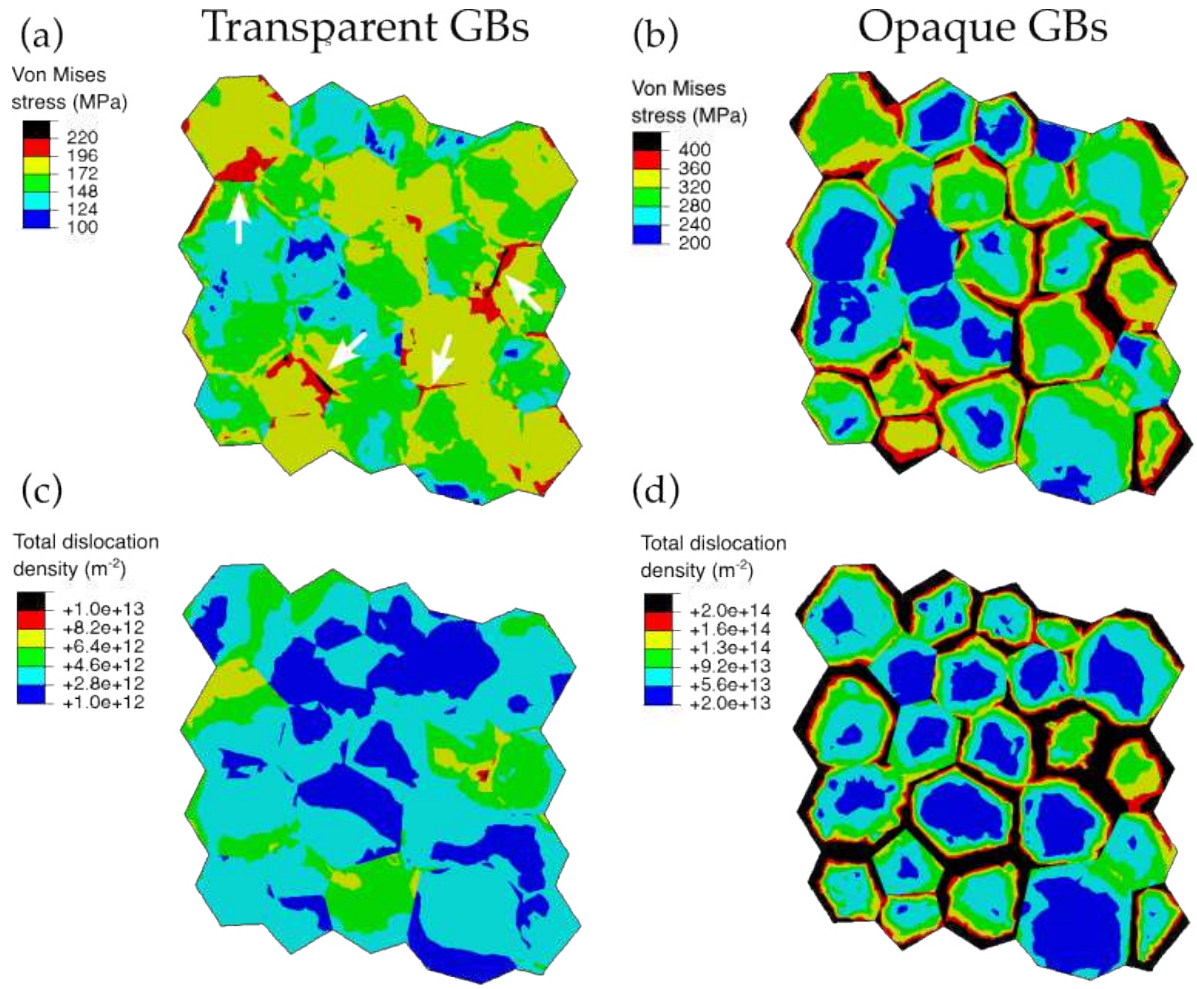

Figure 6.13: Spatial distribution of the Von Mises stress in MPa and the total dislocation density (in m^{-2}) in a cross-section of the Ti polycrystals with transparent GBs (a) and (c), and opaque GBs with an average grain size of 10 μm (b) and (d) deformed up to 1% in tension. Notice the different legend ranges for the stresses and dislocation densities between transparent GBs and opaque GBs. The white arrows in (a) indicate some stress concentrations present at GBs for the simulation with fully transparent GBs.

densities are observed at the bulk of the grains (Figs. 6.13 (d) and 6.14 (d)). However, in contrast to the contour plots obtained for FCC polycrystals (Fig. 6.5 and Fig. 6.6), not all GBs present large dislocation densities despite all GBs being opaque to dislocations. Furthermore, this local increase in dislocation density in some GBs does not necessarily lead to a significant increase in the flow stress, as observed in Figs. 6.13 (b) and 6.14 (b). Instead, the stress is found to be rather homogeneous in some regions, regardless of the location within the bulk of the grain or the GB. This behavior may be attributed to the deformation incompatibility between the grains with different orientations, which is enhanced by the plastic anisotropy of the HCP lattice, where the slip systems contribute differently to plastic deformation. The effect of the plastic anisotropy in HCP metals leads to large variations in the stress fields, which are much larger than in FCC polycrystals. The result is that

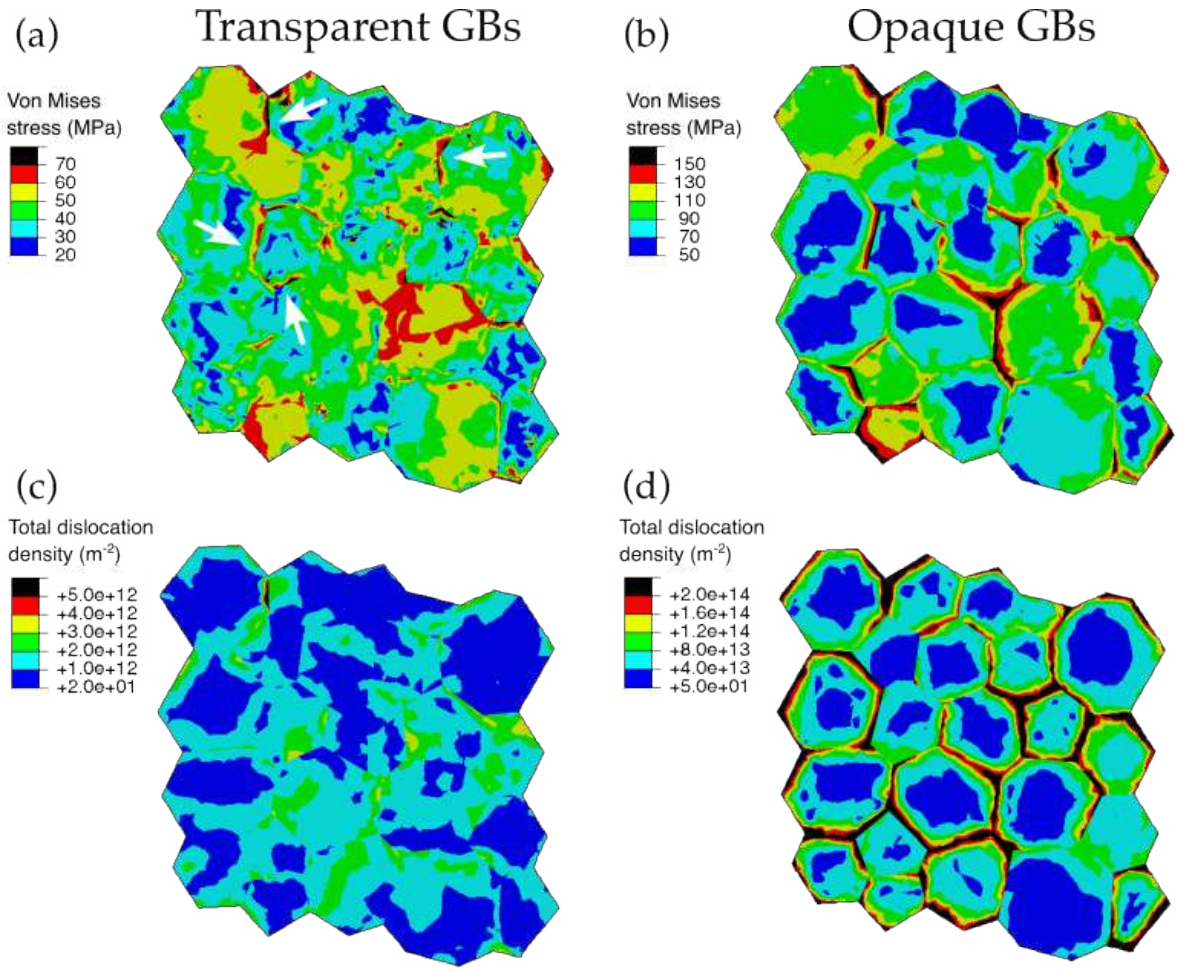

Figure 6.14: Spatial distribution of the Von Mises stress in MPa and the total dislocation density (in m^{-2}) in a cross-section of the Mg polycrystals with transparent GBs (a) and (c), and opaque GBs with an average grain size of 10 μm (b) and (d) deformed up to 1% in tension. Notice the different legend ranges for the stresses and dislocation densities between transparent GBs and opaque GBs. The white arrows in (a) indicate some stress concentrations present at GBs for the simulation with fully transparent GBs.

while some GBs are free of stress concentrations, they are very large in others. In the case of the simulations with transparent GBs, despite GBs not piling up dislocations, there are small stress concentrations observed at a few GBs as compared to the bulk (marked with white arrows in Figs. 6.13 (a) and 6.14 (a)). These stress concentrations are associated with the plastic anisotropy of HCP materials, which leads to deformation incompatibility when deforming grains with different crystal orientations. However, the stresses are generally more homogeneously distributed within the bulk, with some contrasts between adjacent grains, in the simulations with transparent GBs.

The relative activity of slip systems in terms of the accumulated plastic slip γ as a function of the applied strain is shown in Fig. 6.15 for Ti (a) and Mg (b) with 10 μm grain size with fully-opaque (solid lines) and fully transparent GBs (dashed lines). Prismatic slip,

which has the smallest CRSS, presents the greater contribution to plastic slip for the entire simulation, followed by basal and first-order pyramidal slip. The contribution of basal slip increases as the stresses become enough to activate basal slip, whose CRSS is twice that of prismatic slip (Table 6.5). The contribution of the first-order pyramidal slip systems is less than 10% at the end of the simulation, owing to its high CRSS, which is three times that of prismatic slip. The activation of basal slip is delayed in the case of fully transparent GBs in comparison with fully opaque GBs. This effect is caused by the softer tensile response with fully transparent GBs, which leads to lower stresses. Thus, the higher stresses needed to activate basal and pyramidal slip are only reached at higher strains. Conversely, basal slip presents the predominant contribution to γ in Mg (Fig. 6.15 (b)), followed by prismatic and second-order pyramidal, which agrees with the CRSS values set for the simulations. When the GBs are assumed to be fully transparent, the activation of prismatic and pyramidal slip is delayed to higher strains, and their contribution to the accumulated plastic slip is lower.

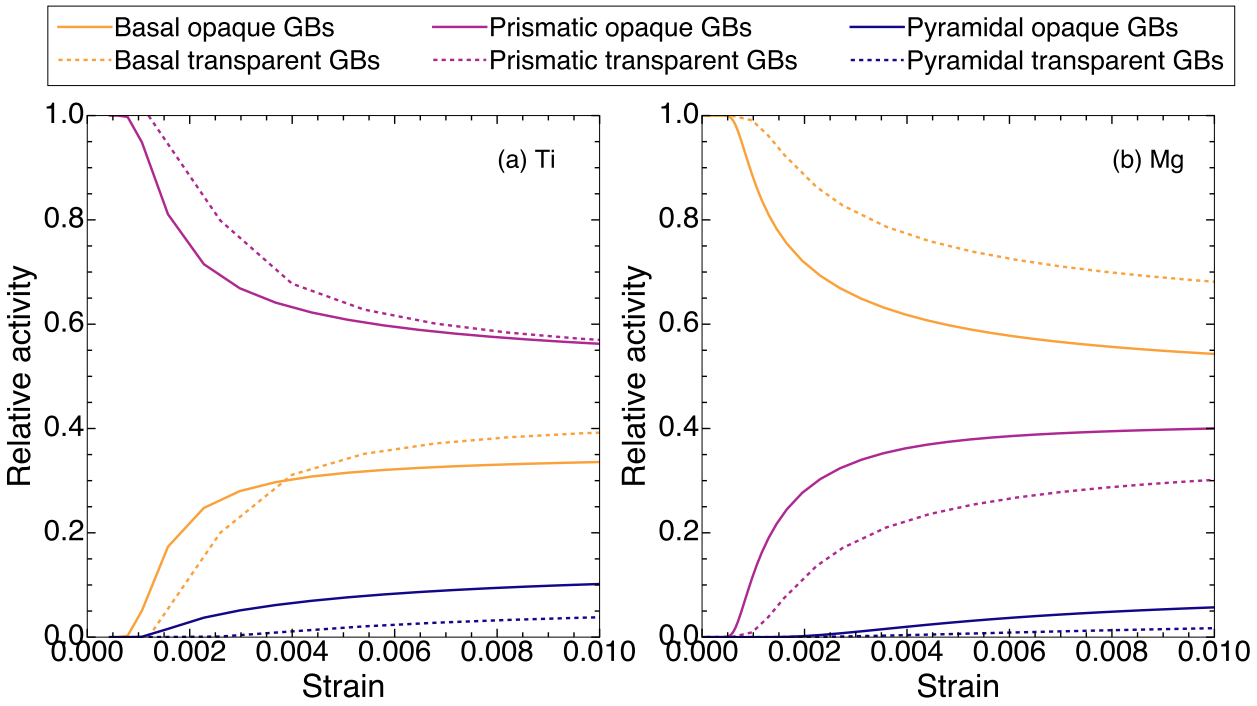

Figure 6.15: Relative activity of the different slip systems to the accumulated plastic slip γ as a function of the applied strain for the 10 μm RVE with opaque GBs and the RVE with transparent GBs for (a) Ti, and (b) Mg.

6.4.6 Comparison with experiments (HCP)

The numerical predictions of the effect of grain size on the flow strength of Ti and Mg were validated against the experimental data found in the literature [107, 135]. The experiments were carried out under quasi-static loading conditions ($\approx 10^{-4}\ s^{-1}$), and, therefore, the effect of the strain rate on the flow stress was considered negligible. The experiments in Ti were carried out at room temperature, while the ones in Mg were performed at $200°C$

[135], where deformation twinning can be neglected. As well as in the case of FCC metals, the dislocation density was assumed to be of the order of $10^{12}\ m^{-2}$ in both cases. The parameters of the crystal plasticity model for Ti and Mg can be found in Tables 6.4, 6.3, 6.5, 6.6 and 6.7. All the simulations were carried out using the periodic RVE shown in Fig. 6.1 with random texture and average grain sizes in the range 10 μm to 80 μm.

The experimental results of the flow stress in tension are plotted as a function of the inverse of the square root of the average grain size, $\bar{D}_g^{-1/2}$ in Figs. 6.16 (a) and (b), for Ti and Mg, respectively. The simulation results assume fully opaque GBs in both cases. The relative errors between the experimental and simulated slopes of the scattered data plotted in Fig. 6.16 (a) and (b) for Ti and Mg for the applied strains are displayed in Table 6.9. The relative error assessment shows that the relative error between the numerical simulations with opaque GBs and the experimental data for the Ti polycrystals at 1% deformation is very small for the fitted CRSS values. The error in the slope is larger in Mg at the yield stress (0.2% deformation), but the lack of information for the flow stress for small grain sizes (< 40 μm) and about the initial dislocation density impedes drawing conclusions about the effect of grain size on the flow stress of Mg. Moreover, slip transfer has not been considered in this model, which could improve the predictions of the flow stress as a function of $\bar{D}_g^{-1/2}$, especially for Mg.

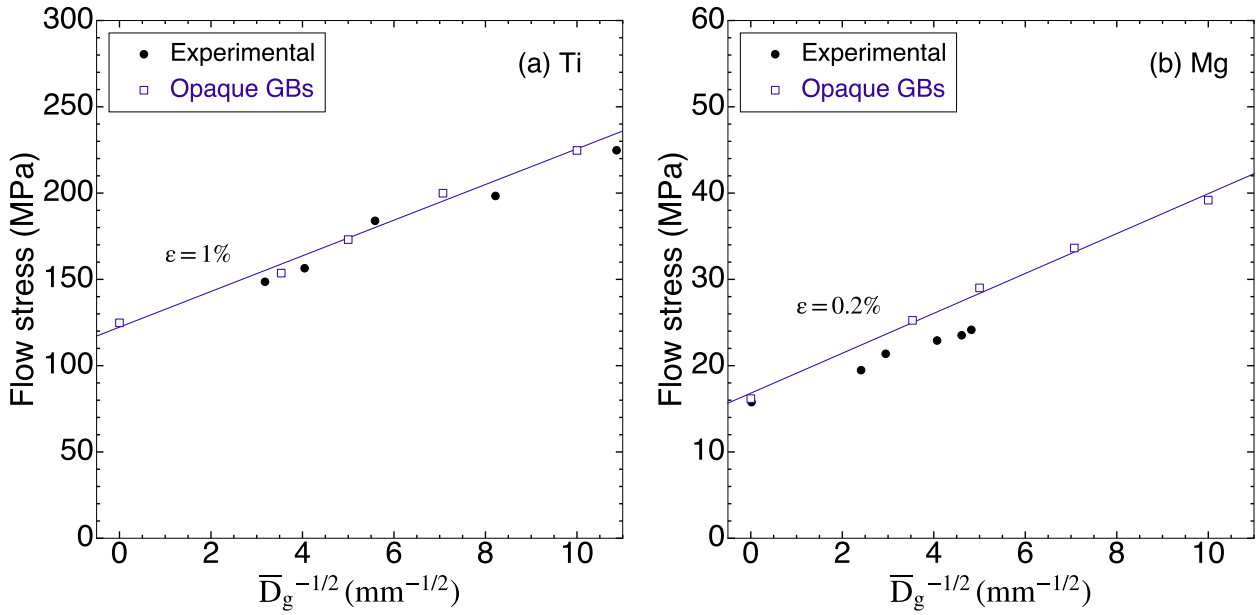

Figure 6.16: Experimental data from the literature and simulation results of the flow stress of HCP polycrystals as a function of $\bar{D}_g^{-1/2}$ for different applied strains for (a) Ti and (b) Mg. The experimental results are indicated by black circles, and simulation results with opaque GBs are indicated by open purple squares. The linear fittings for the simulated results are indicated in purple solid lines.

Material	Strain	m_{exp}	m_{opaque}	$\mathrm{RE}_{\mathrm{opaque}}$
Ti	1%	9.72	10.33	6.3%
Mg	0.2%	1.74	2.31	32.8%

Table 6.9: Flow stress slope error assessment between experimental data and simulation results for different strains for Ti and Mg (Fig. 6.16(a) and (b)). m_{exp} and m_{opaque} are the slopes of the scattered data for the experiments, opaque GBs simulation and translucent GBs simulation, respectively. $\mathrm{RE}_{\mathrm{opaque}}$ is the relative error between the experiments and the opaque GBs simulation.

6.5 Conclusions

The effect of slip transfer on the flow strength of FCC and HCP polycrystals has been analyzed by means of full-field computational homogenization in combination with a physically based crystal plasticity model. The critical resolved shear stress for plastic slip in each slip system follows the modified Taylor model, while the generation and annihilation of dislocations in each slip system in the bulk during deformation is described by a Kocks–Mecking law. This law is modified near the grain boundaries to discriminate between slip systems that can or cannot transfer slip across the boundary using geometrical criteria based on the orientation and activity of the slip systems of both grains near the boundary. This model leads to a classification of the grain boundaries as fully opaque (slip transfer is not possible for any slip system), fully transparent (slip transfer is possible for all slip systems), and translucent (slip transfer is possible for several slip systems). The model was extended to capture the anisotropy of the HCP lattice, including different values for the CRSS for each slip system family (basal, prismatic, and pyramidal).

The mechanical behavior of Al and Cu polycrystals with grain sizes in the range 10 μm to 80 μm and random texture was determined assuming that all grain boundaries were opaque and transparent or that slip transfer was possible for different thresholds of the Luster–Morris geometric compatibility parameter m' or of the residual Burgers vector Δb. Slip transfer between suitably oriented neighbor grains led to a clear reduction in the flow stress of the polycrystals (as compared with the simulations with opaque grain boundaries), which was dependent on the fraction of translucent and transparent grain boundaries in the microstructure, as given by the threshold in the slip transfer geometrical criterion. Moreover, dislocation densities and Von Mises stresses were much higher around opaque grain boundaries, which are potential places for damage nucleation. The strengthening provided by grain boundaries in Al and Cu polycrystals was well described by $C(\bar{D}_g\sqrt{\rho_i})^{-x}$ where $\bar{D}_g$ is the average grain size and ρ_i the initial dislocation density. C depended on the material and on the fraction of translucent and transparent boundaries while x was a function of the material and of the applied strain but was independent of slip transfer at grain boundaries. Finally, the predictions of the simulations were compared with experimental data in the literature on the effect of grain size on the strength of Al, Cu, Ni, and Ag polycrystals. It was found that the inclusion of slip transfer in the model led to more accurate predictions of the Hall–Petch effect, particularly for small grain sizes (< 20 μm).

The crystal plasticity model was extended to HCP metals and employed to carry out numerical simulations of the mechanical behavior of Ti and Mg RVEs under uniaxial tension. The grain boundaries were assumed to be fully opaque and fully transparent to dislocations. The effect of the grain size on the flow stress was accurately captured for both Ti and Mg, which presented different strain hardening behaviors due to the difference between the dislocation annihilation distance. The spatial distribution of the Von Mises stress and the total dislocation density stress concentrations at the GBs were a consequence in HCP polycrystals of both the formation of dislocation pile-ups and of the accommodation of the deformation between grains with different crystallographic orientations and, thus, large anisotropy in the plastic deformation. The contribution of the different slip systems to the accumulated plastic strain agreed with the CRSS values set for each metal, with prismatic and basal slip being dominant for Ti and Mg, respectively.

Finally, the numerical simulations were validated against experimental data of the flow stress for different grain sizes for conditions where deformation twinning could be neglected. The effect of grain boundaries on the flow stress could be accurately captured for Ti, whereas it was slightly overestimated for Mg. Nevertheless, slip transfer was not accounted for in these simulations, which could improve the agreement with the experimental data, especially for Mg. This fact, together with the lack of data for small grain sizes for the experimental data, impedes drawing conclusions about the effect of GBs on pure Mg. Notwithstanding, the crystal plasticity model efficiently captures the anisotropy existing in the HCP lattice and opens the door to more complex simulations where the effect of the stress concentrations at GBs on damage nucleation is included.

7 Simulation of the deformation of polycrystals including intergranular fracture

7.1 Introduction

Ductile fracture of polycrystalline metals takes place by the propagation of a crack throughout the microstructure after significant plastic deformation. Crack propagation may take place through the grains (transgranular fracture) or along the GBs (intergranular fracture). In particular, intergranular cracking has been often identified as one of the mechanisms responsible for the reduced ductility of many metallic alloys [125] due to either microstructural or environmental effects. The former involves the segregation of impurities during solidification and/or the precipitation of brittle phases during heat treatments while GB embrittlement may be caused by liquid metal embrittlement [129], hydrogen embrittlement [21, 150], stress corrosion cracking [90, 161], and neutron irradiation [18, 49]. In all cases, the local stresses at the GB are key factors to trigger intergranular fracture, and they depend on the dislocation interaction with GBs.

The mechanisms and modeling of ductile fracture of metallic polycrystals have been extensively studied in the past, assuming that the material behaves as an elastoplastic solid following the J2 theory of plasticity [61, 177] or strain gradient plasticity models [121] but the analysis of ductile fracture at the mesoscale has not received similar attention. Frodal *et al.* [59] recently presented a crystal plasticity model to assess fracture in smooth and notched tensile specimens where each grain was explicitly modeled. Fracture was introduced using a continuum damage approach based on a damage parameter that reduces the strength of the material as damage progresses. Clayton and McDowell [42] and Alabort *et al.* [5] analyzed intergranular fracture in polycrystalline metals through the combination of crystal plasticity and cohesive elements at the grain boundaries. Both investigations confirmed that the strength and ductility of polycrystalline metals can be dramatically affected by GB damage. Furthermore, Alabort *et al.* [5] reported that GBs perpendicular to the loading axis tended to fail prematurely at strengths well below the macroscopic yield stress. Nevertheless, these simulations were carried out in 2D or in specimens containing a few grains, and the overall influence of the microstructure (grain

size, texture, etc.) on the mechanisms of GB cracking could not be analyzed. Moreover, the effect of slip blocking was not included in the crystal plasticity model.

As shown in Chapter 6, crystal plasticity can take into account the strengthening effect of GBs. Moreover, the effect of slip transfer can also be included to simulate the local stress concentration/relief induced by dislocation pile-up/transmission at GBs, leading to more realistic representations of dislocation-GB interactions. In this chapter, the effect of GB character (fully opaque, fully transparent, and translucent GBs) on the mechanisms of intergranular fracture is analyzed in polycrystalline thin foils of Al (FCC) and Mg (HCP). These two metals were selected to study the effect of plastic isotropy (FCC) versus plastic anisotropy (HCP) on fracture. The tensile response of foils with different crystal orientations and GB characteristics under different loading conditions (plane stress and plane strain) was simulated, and the effect of the GB features on fracture was assessed.

7.2 Constitutive behavior

7.2.1 Crystal plasticity model

The physically-based crystal plasticity model presented in Chapter 6 was used to simulate the behavior of the grains. The mechanical behavior of the Al (FCC) single crystals was governed by the crystal plasticity model presented in Section 6.2.1. Plastic deformation was dictated by dislocation slip along the 12 slip systems from the {111} family in Table 1.1. The viscoplastic parameters and the dislocation interaction coefficients are included in Table 6.1, and the parameters of the crystal plasticity model are referred to in Table 6.2.

The mechanical behavior of the Mg (HCP) single crystals was governed by the same physically-based crystal plasticity model presented in Section 6.2.2. A total of 12 slip systems were considered for Mg, distributed in three $<a>$ basal, three $<a>$ 4 prismatic, and six second-order $<a+c>$ pyramidal slip systems (Table 1.2). The parameters of the viscoplastic law for Mg are the same as those presented in Table 6.4. The stiffness constants for pure Mg can be found in Table 6.3, and the parameters of the dislocation-based crystal plasticity model in 6.7. Nevertheless, the matrix $q_{\alpha\beta}$ was modified to account for the interactions between dislocations on different slip systems in the hardening. Instead of the same-hardening assumption employed in Chapter 6, the latent-hardening coefficients obtained by Bertin *et al.* through dislocation dynamics simulations for Mg were used (Table 7.1).

7.2.2 Slip transfer/blocking at GBs

The behavior of GBs from the viewpoint of slip transfer (either transparent, translucent, or opaque) was taken into account through Eqs. 6.4 and 6.5 for FCC Al and Eqs. 6.9 and 6.10 for HCP Mg. To account for the effect of GBs in the numerical simulations, the distance to the nearest GB from each Gauss point needs to be calculated, as explained in Section 6.3. Then, the neighbor grain across the boundary can be identified for each slip system α at each Gauss integration point. The likelihood of slip transfer from the slip system α in

Table 7.1: Latent-hardening coefficients for the dislocation interaction matrix $q_{\alpha\beta}$ for pure Mg [23].

Interaction	Value
Basal self-interaction	0.15
Prismatic self-interaction	0.15
Pyramidal $<c+a>$ self-interaction	0.15
Coplanar basal/basal	0.15
Prismatic/prismatic	0.038
Collinear basal/prismatic	0.707
Non-collinear basal/prismatic	0.054
Collinear prismatic/basal	0.535
Non-collinear prismatic/basal	0.06
Semi-collinear basal/pyramidal $<c+a>$	0.367
Non-collinear basal/pyramidal $<c+a>$	0.293
Semi-collinear prismatic/pyramidal $<c+a>$	0.068
Non-collinear prismatic/pyramidal $<c+a>$	0.088
Semi-collinear pyramidal $<c+a>$/basal	0.017
Non-collinear pyramidal $<c+a>$/basal	0.011
Semi-collinear pyramidal $<c+a>$/prismatic	0.025
Non-collinear pyramidal $<c+a>$/prismatic	0.015
Semi-collinear pyramidal $<c+a>$/pyramidal $<c+a>$	0.018
Non-collinear pyramidal $<c+a>$/pyramidal $<c+a>$	0.042

grain A to any of the slip systems β in the neighbor grain B was assessed according to the Luster-Morris geometrical parameter m' as

$$m'_{\alpha\beta} = (\boldsymbol{n}_\alpha \cdot \boldsymbol{n}_\beta)(\boldsymbol{b}_\alpha \cdot \boldsymbol{b}_\beta) \tag{7.1}$$

where $\boldsymbol{n}_\alpha$ and $\boldsymbol{n}_\alpha$ are unit vectors perpendicular to the slip plane α in grain A and slip plane β in grain B. All the vectors involved in this calculation have to be expressed in the same reference frame, as explained in Section 6.3.

In the case of FCC metals, slip transfer between slip systems α and β is allowed when $m' > 0.8$. If the condition of slip transfer is fulfilled for any β slip system in the neighbor grain, Eq. 6.4 is used as the constitutive equation of slip system α at the Gauss integration point of the crystal. Otherwise, slip transfer from α to β is not possible due to the geometric incompatibility, and the constitutive equation is expressed by Eq. 6.5. The same strategy was for Mg (HCP), regardless of the slip system family. This means that, for instance, slip transfer will be possible for an incoming basal slip system α if $m' > 0.8$ for any outgoing β slip system, regardless of whether it is basal, prismatic, or pyramidal. If this condition is fulfilled, Eq. 6.9 would be used for the dislocation accumulation; otherwise, Eq. 6.10 is used to indicate slip blocking. It should be noted that the model is general and

allows to use of different thresholds for slip transfer for each combination of incoming and outgoing slip system families (either basal, prismatic, or pyramidal) and impedes slip transfer between two different slip system families. However, for the sake of simplicity, this possibility was not included in the simulations.

The geometrical analysis of slip transfer at each GB indicates how many pairs of slip systems are suitably oriented to transfer slip across the boundary, leading to a classification of GBs from fully opaque (slip transfer is not possible for any pair of slip systems) to translucent (slip transfer is possible for some pairs of slip systems) to fully transparent (slip transfer is allowed for all slip systems).

7.2.3 Intergranular fracture modeling

Cohesive zone modeling is a numerical technique used in the field of computational mechanics to simulate the behavior of materials, particularly in the context of fracture and delamination [50, 139]. It represents the interaction between adjacent material surfaces by defining a cohesive zone with its own material properties, such as fracture energy and stiffness. Cohesive zone modeling is widely employed in engineering and materials science to analyze and predict the behavior of materials under various loading conditions, especially in applications involving adhesive bonding, composites, and structural integrity assessments [27, 32, 111, 187].

Cohesive zone modeling can be performed through the use of either cohesive elements or cohesive surfaces [163]. The choice between cohesive elements and surfaces-based cohesive behavior depends on the specific analysis requirements and the desired balance between computational simplicity and modeling accuracy. Cohesive elements are recommended for more detailed analyses or complex constitutive behaviors at the cost of additional pre-processing effort and increased computational cost. In contrast, cohesive surfaces are computationally more efficient and accurate enough for analyses that assume negligible interface thickness. In the past, GB fracture has been modeled through the insertion of both cohesive surfaces [5, 162] and cohesive elements [159].

The cohesive zone approach [16, 46] for damage initiation and evolution is used as the constitutive law for GBs. In this context, a traction-separation law is typically used to define the relationship between the forces (traction t) and relative displacements (separation δ) between two material surfaces along the cohesive zone. The typical bilinear cohesive traction-separation law is represented in Fig. 7.1, where the behavior of the cohesive surfaces before damage is linear-elastic, and there is a linear stiffness decrease after damage initiation until the final failure. The subindices n, s, and t denote the normal and the two orthogonal shear directions in the cohesive surface. The area under the curve represents the total fracture energy of the cohesive surface G_C.

Thus, the evolution of the tractions of a cohesive surface with a bilinear traction-separation law can be mathematically described by:

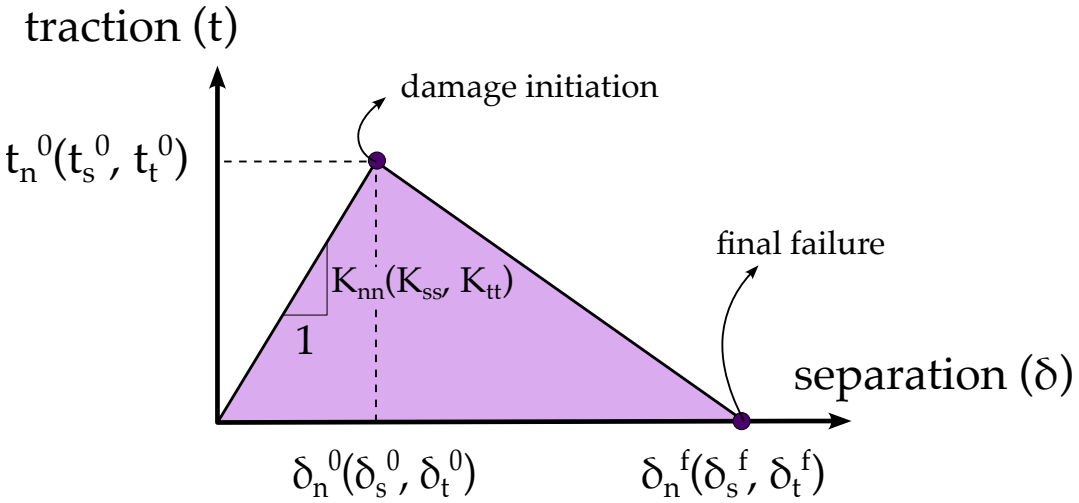

Figure 7.1: Bilinear traction-separation law, where damage initiation is indicated by the superindex 0 and failure is indicated by the superindex f.

$$\begin{Bmatrix} t_n \\ t_s \\ t_t \end{Bmatrix} = \begin{bmatrix} K_{nn}[1-D(\delta)] & 0 & 0 \\ 0 & K_{ss}[1-D(\delta)] & 0 \\ 0 & 0 & K_{tt}[1-D(\delta)] \end{bmatrix} \begin{Bmatrix} \delta_n \\ \delta_s \\ \delta_t \end{Bmatrix} \tag{7.2}$$

where K_{nn}, K_{ss}, and K_{tt} represent the stiffness constants, and δ_n and δ_s and δ_t stand for the normal opening and the two shear displacements between both cohesive surfaces, respectively. $D(\delta)$ is a scalar damage variable, which represents the overall damage in a cohesive surface. The damage evolution is typically represented by a decreasing linear stiffness law as follows:

$$D(\delta) = \begin{Bmatrix} 0; & \delta < \delta^0 \\ \dfrac{\delta^f(\delta - \delta^0)}{\delta(\delta^f - \delta^0)}; & \delta \geq \delta^0 \end{Bmatrix} \tag{7.3}$$

where δ is defined as an effective displacement, and δ_n, δ_s and δ_t stand for the separations in the different directions. The effective displacement δ was defined by Camanho *et al.* [31] as

$$\delta = \sqrt{\delta_n^2 + \delta_s^2 + \delta_t^2} \tag{7.4}$$

The damage initiation point δ^0 is defined according to the selected damage initiation law. A maximum stress criterion was selected for the damage initiation according to,

$$\text{MAX}\left\{\frac{t_n}{t_n^0}, \frac{t_s}{t_s^0}, \frac{t_t}{t_t^0}\right\}, \tag{7.5}$$

where t_n^0, t_s^0, and t_t^0 are the critical stresses that lead to the onset of damage in the cohesive surface. The damage evolution in a cohesive surface in Abaqus can be controlled by either

an energy-based or a separation-based law. A maximum separation criterion based on δ_n^f, δ_s^f, and δ_t^f was selected in this investigation.

Depending on how the user defines these six variables (critical stresses and critical displacements), the behavior of the cohesive surfaces will be more or less anisotropic. In this investigation, the behavior of the cohesive surfaces was assumed to be isotropic, and thus the stiffness, the stress for damage initiation, and the maximum separations were equally set for the three directions and depended only on two parameters, t_i^0 and δ_i^f. Damage initiation is determined by t_i^0 and the damage evolution by δ_i^f. Both parameters control the area under the traction-separation law and, hence, the total fracture energy of the cohesive surfaces. Moreover, the initial stiffness of the cohesive surfaces is set to a very large value, so the separation between the cohesive surfaces at the GB is negligible until the onset of damage.

First, the stress for damage initiation, t_i^0, was chosen for each metal (either Al or Mg) according to stresses at the GBs in a simulation without considering intergranular fracture (without cohesive surfaces) for the strongest case, which corresponds to the fully opaque GBs. Then, the maximum separation, δ_i^f, was selected to reach a fracture energy of 1.5 J/m^2 for both Al and Mg, which is a reasonable value for GB energy in metals [29, 199]. The cohesive surface interaction parameters used for Al and Mg are indicated in Table 7.2.

Table 7.2: Interaction properties for the cohesive surfaces introduced at GBs in the Al and Mg thin foils.

Material	K_{ii} [MPa]	t_i^0 [MPa]	δ_i^f [μm]	G_C [J/m^2]
Al (FCC)	$3 \cdot 10^7$	15	20	1.5
Mg (HCP)	$3 \cdot 10^7$	20	15	1.5

7.3 Numerical model

7.3.1 Finite element model

The effect of GBs on the deformation and fracture of FCC and HCP polycrystals was determined by means of the finite element simulation of pseudo-3D foils of Al (FCC) and Mg (HCP) polycrystals under uniaxial tension. Thus, the columnar GBs perpendicular to the foil were included between the grains.

The microstructures were generated using Neper [146]. The grains within the foils were generated using Laguerre-Voronoi tessellations, which lead to polyhedra with flat interfaces. The foil dimensions in the sample reference frame are shown in Fig. 7.2, where $L_x = 0.3$ mm, $L_y = 0.15$ mm, and $L_x = 0.015$ mm. In other words, $L_x = 20 \cdot L_z$, and $L_y = 10 \cdot L_z$. The notation of the boundary faces is provided on the left in Fig. 7.2, with z_0 and z_1 being the bottom and top surfaces of the foil, respectively, and x_0, x_1, y_0, and y_1 the lateral faces in the x and y directions.

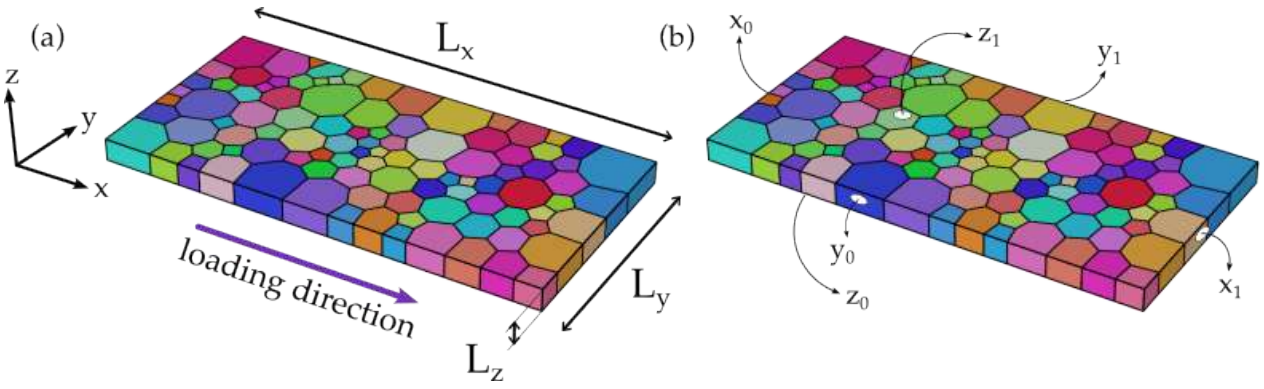

Figure 7.2: Thin foil with columnar grains to simulate the effect of GBs in FCC and HCP metals. The reference frame and the loading direction are indicated in (a), and the notation employed for the foil boundary faces is indicated in (b).

Two different realizations with 100 grains, R_1 and R_2, respectively, were generated. Microstructure R_1 is composed of 263 GBs, while R_2 includes 268 GBs. The grain size in both realizations followed a lognormal distribution with a mean grain size of 20 μm and a standard deviation of 4 μm. The grain shape was equiaxed in the xy plane and columnar along z (see reference frame in Fig. 7.3).

Three foils were employed to simulate the mechanical behavior in Al (Fig. 7.3). Foils 1 and 2 have the same grain distribution (R_1) and different random crystal orientations, whereas foil 3 has a different microstructure (R_2) as well as random crystal orientations. In contrast, four different foils were employed for the numerical simulation of Mg. The same two geometrical realizations, R_1 and R_2, were used, and two sets of crystal orientations were assigned to each of them: one with random crystal orientations and the other with a strong basal texture. This texture was obtained from X-ray diffraction of an AZ31 Mg alloy reported by Jamali *et al.* [87]. 100 representative orientations were extracted from the orientation distribution function (ODF) with MTEX [15] for R_1 and R_2, and the basal pole figure is provided in Fig. 7.4.

Once the microstructure was tessellated, it was discretized with $\approx 40k$ second-order modified tetrahedra (C3D10M elements with ten nodes in Abaqus) for the finite element simulations using Gmsh [63].

7.3.2 Cohesive surfaces

Cohesive surfaces were chosen to model intergranular fracture. This approach was chosen rather than cohesive elements for the sake of simplicity and given that no special constitutive fracture behavior is attributed to GBs. The shared nodes between the adjacent grains were duplicated, and the contact pairs between each master and slave cohesive surface were defined through an in-house Matlab code. An example of the cohesive surfaces generated in one of the thin foils is presented in Fig. 7.5. The cohesive surfaces were generated for both microstructure realizations R_1 and R_2, regardless of the crystal orientations. The constitutive behavior of the cohesive surfaces for Al and Mg is indicated in Section 7.2.3.

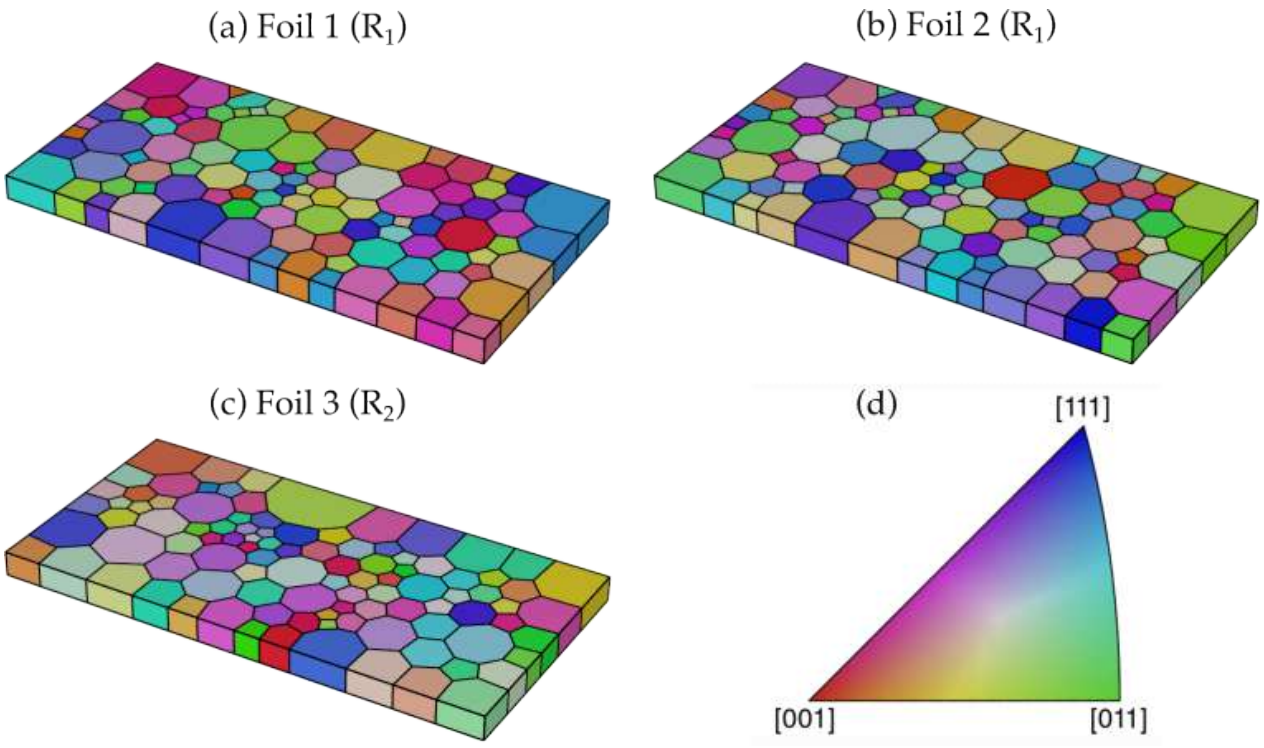

Figure 7.3: Thin foils used to simulate the effect of GBs in Al (FCC) (a)-(c). The grains within the foils are colored according to the inverse pole figure along z, provided in (d). Note that foils 1 and 2 have the same grain distribution (R_1) but different crystal orientations, while foil 3 has a different grain distribution (R_2).

7.3.3 Boundary conditions

The thin foils were subjected to uniaxial loading along the x direction. The displacements at the surface x_0 were set to 0 along the x direction while an increasing displacement was applied in the opposite face x_1 in the loading direction, which is parallel to x. The thin foils were deformed up to 5% under a quasi-static strain rate of 10^{-3} s^{-1}. The stresses on the lateral surfaces, given by $y = y_0$ and y_1, were 0 to simulate uniaxial tension along x.

Two different loading scenarios were considered: plane stress and plane strain. In the plane stress condition, the stresses on the bottom (z_0) and top (z_1) surfaces were set to 0, leading to an approximation of the stress state on the surface of the polycrystal. In a plane strain condition, the out-of-plane displacements along the z axis are restricted and set to 0. This stress state is a (crude) approximation of the stress state within the bulk of the polycrystal under uniaxial loading when the displacements perpendicular to the loading axis are hindered by the neighbor grains.

Three different GB characters were employed for each foil: fully opaque GBs, fully transparent GBs, and translucent GBs, where slip transfer is allowed when $m' > 0.8$ between any family of slip systems. Hence, twelve simulations were carried out for each foil, six including intergranular fracture and six without intergranular fracture. Three GB characters and the two loading conditions were carried out for each foil with or without intergranu-

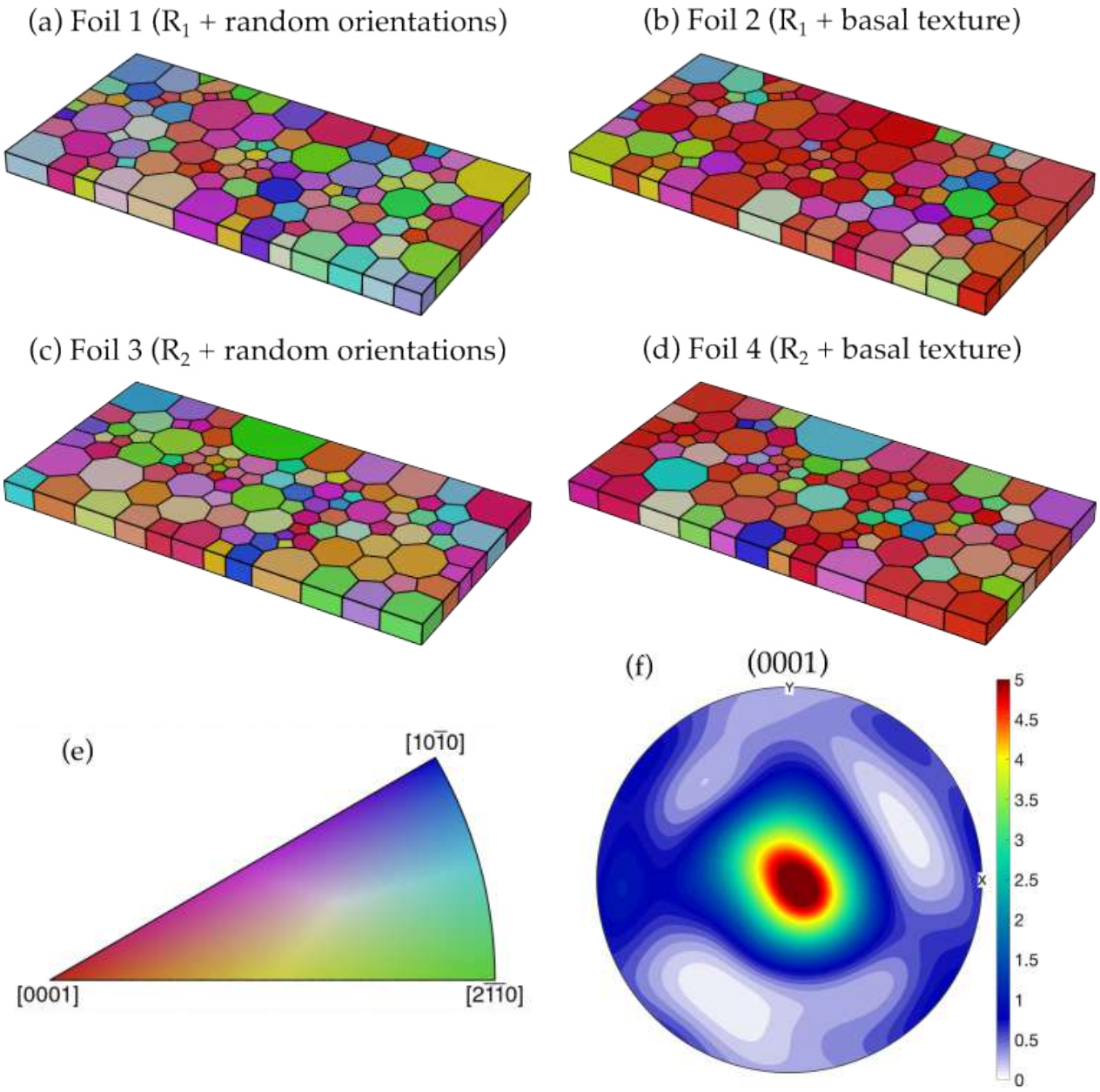

Figure 7.4: Thin foils used to simulate the effect of GBs in Mg (HCP) (a)-(d). The grains within the foils are colored according to the inverse pole figure along z, provided in (e). Note that two different grain realizations were generated (R_1 and R_2), and two different sets of crystal orientations were used for each foil: random orientation and a strong basal texture. The basal pole figure for the microstructures with basal texture is shown in (f).

lar fracture.

The mechanical behavior of the foils under uniaxial tension was simulated using Abaqus Standard [163] within the framework of the finite deformations theory with the initial unstressed state as reference. The crystal plasticity models were implemented in Abaqus through a user-defined material model (UMAT).

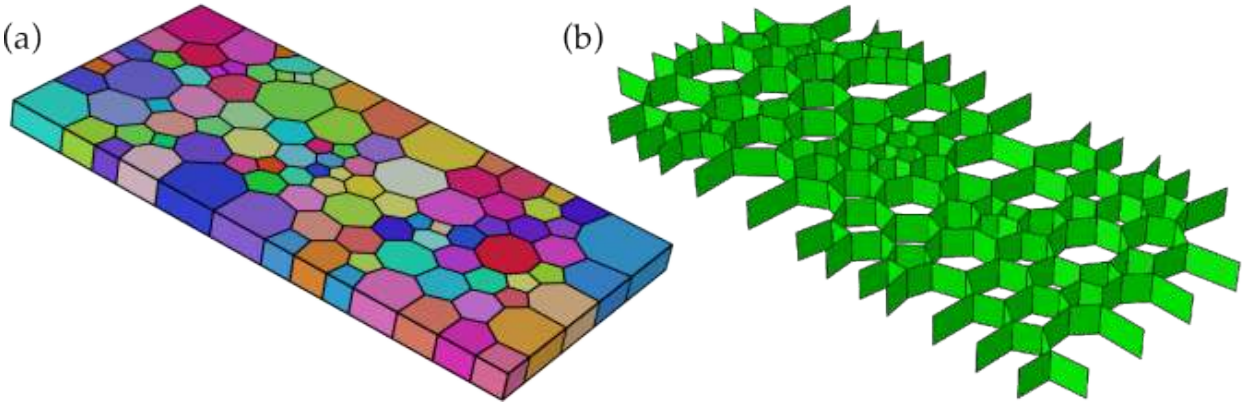

Figure 7.5: Example of thin foil polycrystal (left), together with the sample reference frame and loading direction, and cohesive surfaces generated at the GBs of the same polycrystal (right).

7.4 GB damage analysis

The effect of different GB features on damage nucleation and propagation was analyzed from the results of the numerical simulations, including cohesive surfaces. Different GB characteristics were considered for the analysis, namely geometrical and crystallographic. Regarding the geometrical factors, the GB length $\mathrm{L_{GB}}$ and the angle between the GB and the loading axis α_x ($0 < \alpha_x < 90°$) were included. From the crystallographic point of view, the GB misorientation angle Θ was also considered. The number of transparent slip systems per GB $\mathrm{n_{Trs}}$ was included to analyze the effect of GB character on intergranular fracture. Given that 12 slip systems were considered for both Al and Mg, $\mathrm{n_{Trs}}$ was equal to 12 for the simulations with fully transparent GBs and equal to 0 for the simulations with fully opaque GBs. The simulations with translucent GBs incorporated the Luster-Morris parameter as the slip transfer criterion, and slip transfer was allowed for an incoming slip system as long as there was at least one outgoing slip system with $m' > 0.8$. In that case, such incoming slip system would be considered transparent. Thus, $\mathrm{n_{Trs}}$ could range from 0 to 12 per GB for the simulations with translucent GBs.

An additional parameter named the slip activation factor SA was defined in order to account for the probability of each grain to deform along a certain slip system family. This parameter depends on the Schmid factors of the possible active slip systems in the family according to

$$\mathrm{SA}_{ss} = \frac{\sum_{i=1}^{n_{ss}} \mathrm{SF}_i}{n_{ss} \cdot \mathrm{SF}_{max}}, \tag{7.6}$$

where n_{ss} is the number of slip systems in the family considered, SF_i is the Schmid factor of each slip system i, and SF_{max} is the maximum value that the Schmid factor can take, which is 0.5. Thus, the slip activation factor gives a measure of how well the slip systems of a certain family are oriented to generate dislocation slip. In the case of Al (FCC), there is only one family of {111} slip systems. Thus, the number of slip systems n_{ss} is equal to

12, and there is only SA per grain. In contrast, three different slip activation factors can be determined in Mg (HCP). They are SA_b, SA_p, and SA_{py}, which stand for the corresponding slip activation factors for basal, prismatic, and second-order pyramidal slip. The different values of n_{ss} per slip system family (three for basal, three for prismatic, and six for pyramidal slip) are considered to calculate the respective slip activation factors.

The variables $\mathrm{L_{GB}}$, α_x, Θ, and $\mathrm{n_{Trs}}$ are related to the GB while the slip activation factor SA is linked to the grain. The connection of SA with a GB was carried out through the arithmetic mean of the SA of the grains across the GB. In the case of Mg (HCP), three SA were calculated for each GB, and they correspond to the arithmetic mean of the basal, prismatic, and pyramidal SA of the grains across the GB. Hence, $\overline{\mathrm{SA}}_\mathrm{b}$, for instance, would represent the arithmetic mean of the slip activation factor for basal slip in the two grains at either side of a GB while $\overline{\mathrm{SA}}_\mathrm{p}$ and $\overline{\mathrm{SA}}_\mathrm{py}$ have the same meaning for prismatic and pyramidal slip.

The strain for damage initiation ε^0_{dmg} was used as GB damage indicator. The Pearson correlation coefficient (r) was used to assess the correlation between the different GB features and ε^0_{dmg}. The Pearson correlation measures the degree of the linear relationship between two variables [99]. It ranges between -1 to 1, where a value of -1 means a total negative linear correlation, 0 means no correlation, and +1 means a total positive correlation. A schematic representation of the Pearson correlation is provided in Fig. 7.6, presenting a strong positive correlation $r > 0$ in (a), no linear correlation $r = 0$ in (b), and strong negative correlation $r < 0$ in (c).

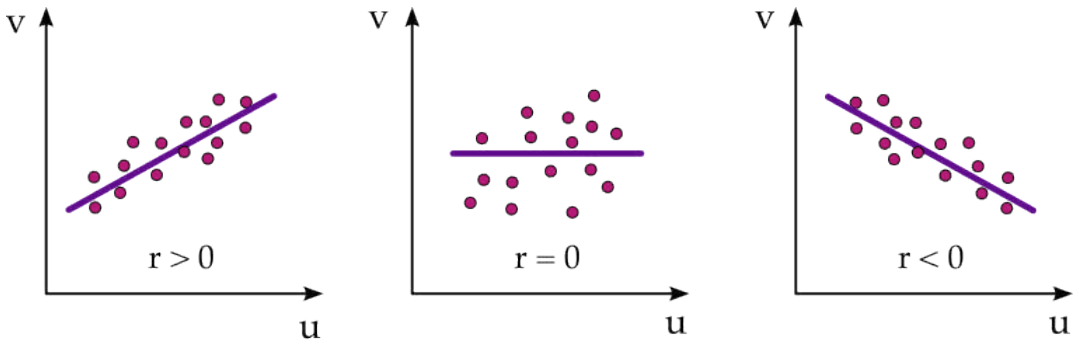

(a) Strong positive correlation (b) No correlation (c) Strong negative correlation

Figure 7.6: Schematic representation of Pearson correlation between two variables u and v: (a) strong positive correlation with $r > 0$, (b) no correlation with $r = 0$, and (c) strong negative correlation.

The Pearson correlation coefficient between two variables u and v can be mathematically expressed as

$$r(u, v) = \frac{s_{uv}}{s_u \times s_v}, \tag{7.7}$$

where s_{uv} is the covariance between the variables u and v, and s_u and s_v stand for the standard deviations of u and v, respectively [99]. This coefficient was computed to analyze

the effect of the different GB features on damage initiation ε^0_{dmg} for the different thin foils in which intergranular fracture was considered.

7.5 Results and discussion

7.5.1 Intergranular fracture of Al foils in tension

The numerical simulations of the tensile response of the three Al thin foils with and without intergranular fracture are plotted as a function of GB character under plane stress in Fig. 7.7 (a), and under plane strain in Fig. 7.7 (b).

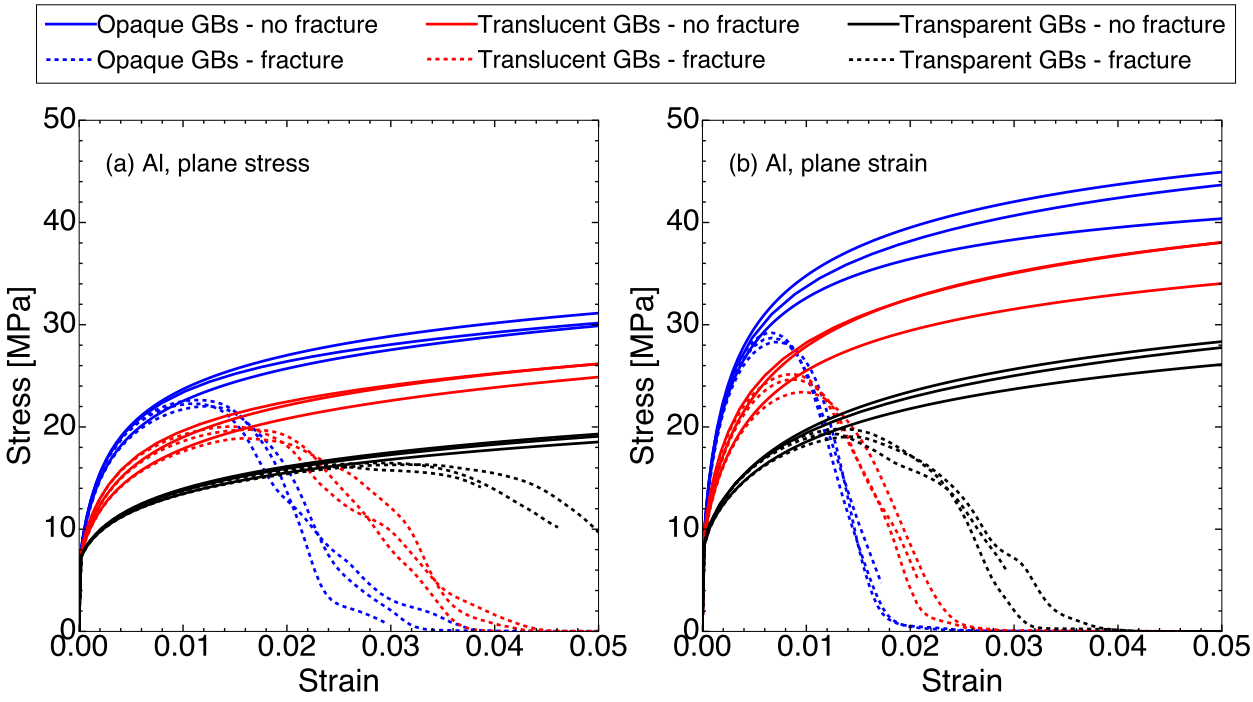

Figure 7.7: Engineering stress-strain curves of the Al (FCC) foils as a function of grain boundary type under (a) plane stress and (b) plane strain loading conditions. The solid lines correspond to the mechanical behavior without fracture, and the dashed lines correspond to simulations that include fracture at the GBs.

As observed in Chapter 6, the simulations with opaque GBs present the strongest tensile response, followed by those with translucent GBs, and finally by the simulations with fully transparent GBs. The simulations under plane strain generally present higher stresses than those under plane stress as a result of the restriction in the out-of-plane deformation, which leads to higher triaxiality. The simulations under plane stress present lower differences in the stress-strain curves between them for any GB character as compared with those carried out under plane strain (of the order of 5 MPa). These differences can also be attributed to the triaxiality.

The tensile stress-strain curves of the foils, including intergranular fracture, are super-

posed to those without cohesive surfaces until the onset of damage. While continuous strain hardening is observed in the foils without damage, the nucleation and growth of intergranular cracks lead to a maximum in the stress-strain curves, followed by a progressive reduction in the load-carrying capacity of the foil until complete fracture. The nucleation and progress of damage depended on the stress state (either plane stress or plane strain) and on the GB character. Fracture occurs sooner and progresses more rapidly under plane strain than under plane stress because of the higher stresses that facilitate the early fracture of the GBs. Moreover, damage initiation occurs sooner in the simulations with fully opaque GBs, followed by translucent GBs and fully transparent GBs simulations. This sequence is also repeated for the strain at the maximum stress as well as for the strain to failure.

The contour plots of the Von Mises stress (in MPa) and of the total dislocation density (in m^{-2}) are plotted in Fig. 7.8 for Al foil 1 under plane stress without fracture at ε = 2%. The results with fully opaque GBs are presented in the first row, with translucent GBs with slip transfer when $m' > 0.8$ in the second row, and with fully transparent GBs in the third row. Stress concentrations are found at the GBs along the center of the foil when all GBs are opaque, and they are associated with dislocation pile-up, as observed in the corresponding dislocation density contour plot. The stress concentrations gradually decrease for the translucent GBs, in which those GBs suitably oriented for slip transfer do not lead to stress concentrations, and the dislocation densities vary accordingly. Finally, high stress concentrations and dislocation pile-ups are not found in the case of fully transparent GBs. Stresses and dislocation densities are more homogeneous in this case, and moderate stress concentrations are found in smaller grains.

The effect of including intergranular fracture via cohesive surfaces in Al is plotted in Fig. 7.9 for foil 1 under plane stress at ε = 2%. The foils where intergranular fracture is not included are displayed on the left column, and the foils that incorporate intergranular fracture are displayed on the right column. As observed in the tensile curves for plane stress condition (Fig. 7.7 (a)), at ε = 2%, the foils with fully opaque GBs with intergranular fracture present a significant drop in the strength. As shown in the contour plots in the first row of Fig. 7.9, multiple cracks can already be observed at this strain, most of them in highly stressed GBs. The decrease in stiffness for the foils with translucent GBs at 2% deformation is not that dramatic, but there are some cracks with observable separation, also located at GBs with large local stresses. In the case of the foils with fully transparent GBs, the tensile test presents a negligible drop in the mechanical properties, and in fact, no evident cracks can be observed in the foil contour plots at this stage.

The final crack paths in the Al foil 1 are depicted in Fig. 7.10 as a function of GB character and loading conditions (plane stress or plane strain). The region most affected by fracture in the foils under plane stress is the left region, and fracture occurs in this region regardless of GB character. The foils with fully opaque and fully transparent GBs present almost the same crack path but not exactly the same. However, the foil with translucent GBs presents another crack at the middle-right region of the foil that does not appear in the other two cases. Regarding plane strain, the crack paths are very different for the three GB characters. Two main cracks appear at the two left and right ends of the foil in the foil with opaque

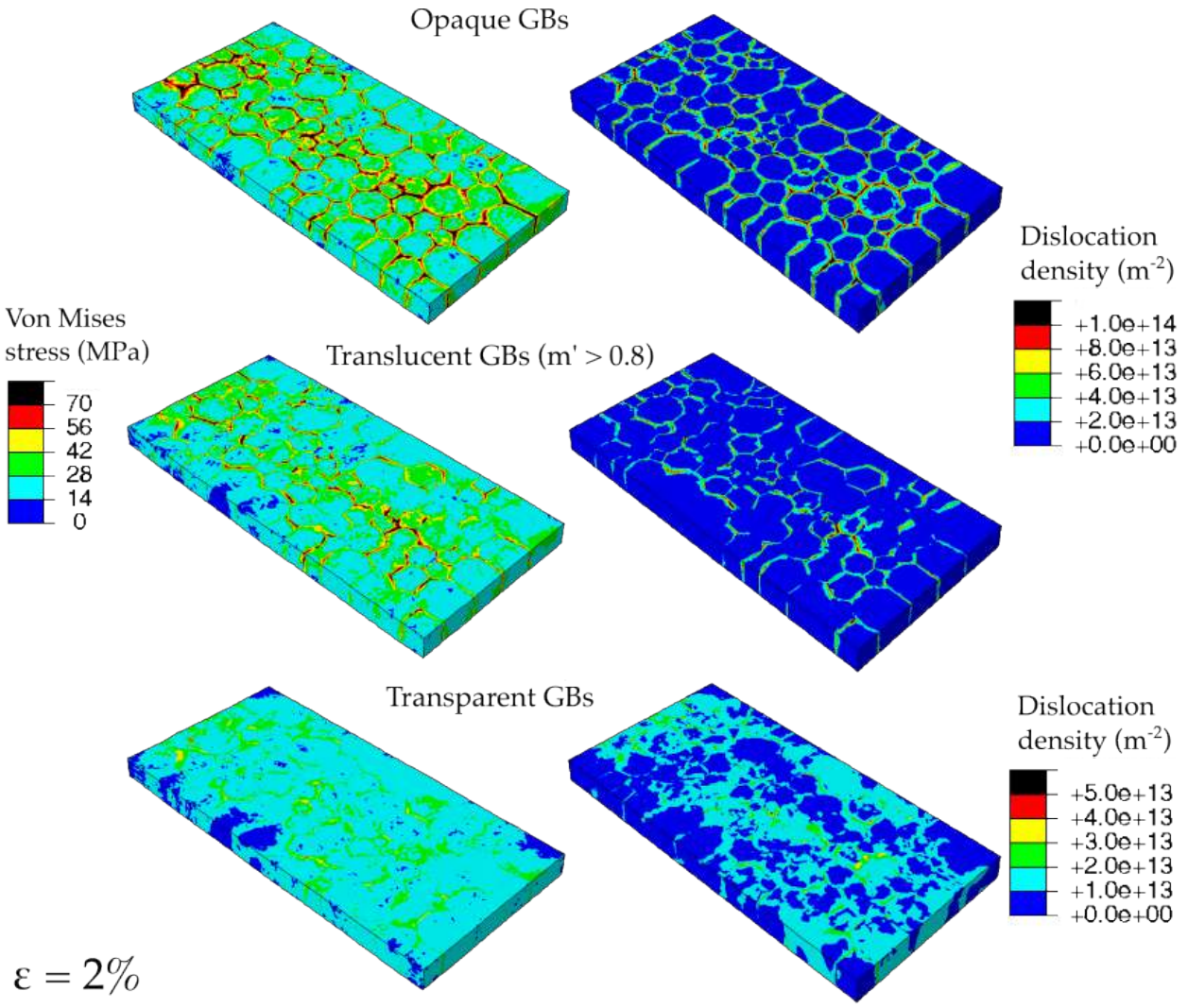

Figure 7.8: Contour plot of the Von Mises stress in MPa (left column) and of total dislocation density in m^{-2} (right column) at ε = 2% as a function of GB character in Al foil 1 under plane stress without fracture. The contour plots with fully opaque GBs are represented on the first row, with translucent GBs where slip transfer is allowed for $m' > 0.8$ on the second row and with transparent GBs on the third row. Note that a different scale is employed for the dislocation density for the foils with opaque and translucent GBs than that used for fully transparent GBs.

GBs, while the final crack appears at the right end (indicated with arrows in Fig. 7.10) with the translucent GBs, but the associated crack opening is very limited. Finally, the simulation with transparent GBs presents a complete separation from a catastrophic crack right in the middle of the foil. It should be noticed that many other GBs were damaged before the final fracture, but their fracture is not that evident in the contour plots in each foil. The final cracks of the other two Al foils also presented different paths depending on the GB character and loading conditions, but they are not provided for the sake of brevity.

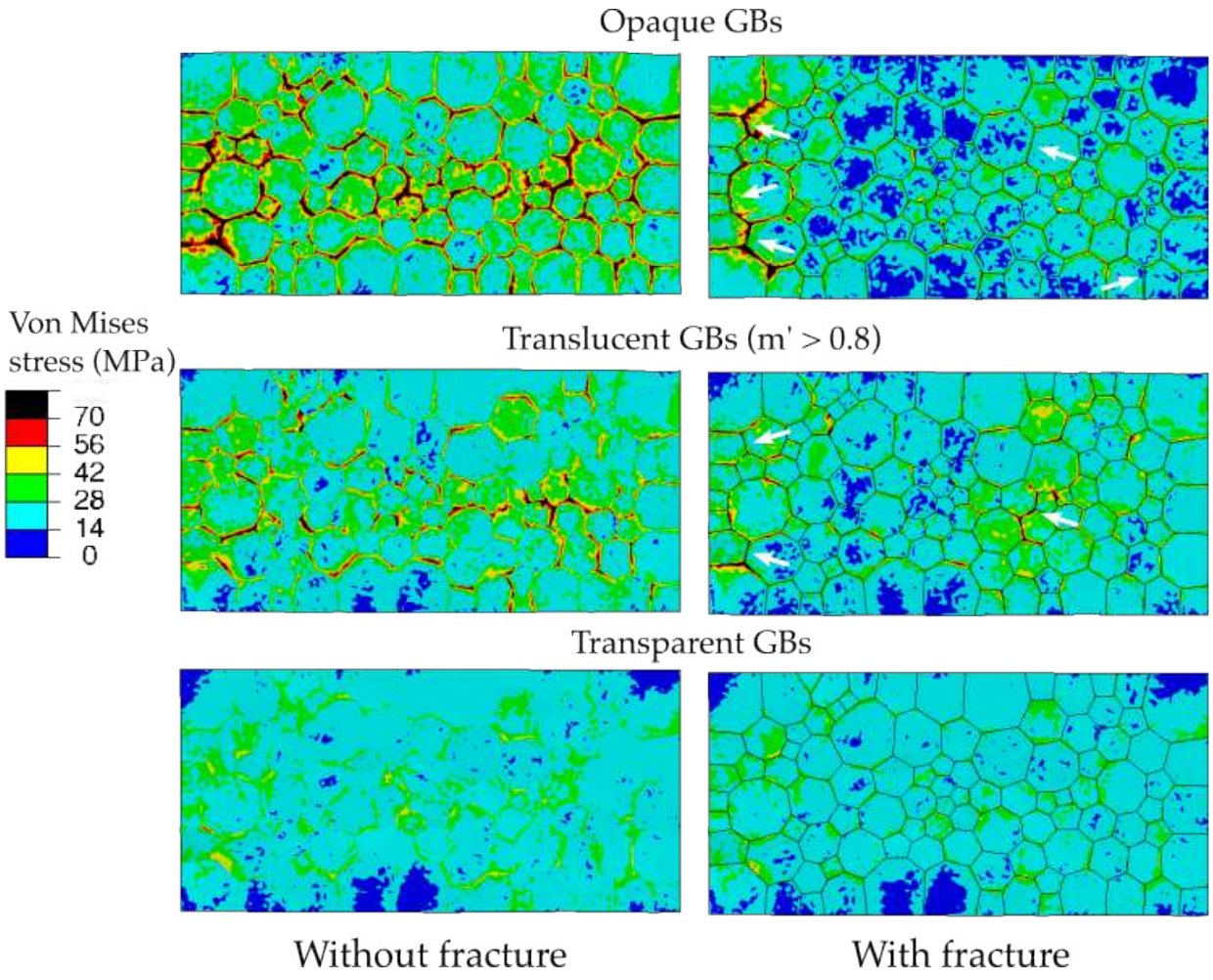

Figure 7.9: Contour plots of the Von Mises stress in MPa at ε = 2% without including fracture (left) and including intergranular fracture (right) as a function of GB character in Al foil 1 under plane stress. The contour plots with fully opaque GBs are represented on the first row, with translucent GBs where slip transfer is allowed for $m' > 0.8$ on the second row and with transparent GBs on the third row. Cracks are indicated by white arrows.

The effect of the different GB features –presented in Section 7.4– on the strain for damage initiation ε^0_{dmg} in the GBs was analyzed. To this end, the strain at which the first damage appeared in each GB was recorded and stored together with the GB features: α_x, $\mathrm{L_{GB}}$, Θ, $\overline{\mathrm{SA}}$, and $\mathrm{n_{Trs}}$. This database for the three Al thin foils is composed of 4760 damaged GBs, 2380 under plane stress, and 2380 under plane strain. The Pearson correlation coefficient matrix is plotted for ε^0_{dmg} and the different GB features in Fig. 7.11 for plane stress (a) and plane strain (b). The value of the Pearson correlation coefficient r is indicated at the center of each cell and also used as a heat map variable, ranging from -1 (pink) to +1 (orange), as indicated by the color bar on the right.

The Pearson coefficients r for the length of the GB $\mathrm{L_{GB}}$, the misorientation angle Θ, and the mean slip activation factor $\overline{\mathrm{SA}}$ are close to zero, indicating that there is no correlation

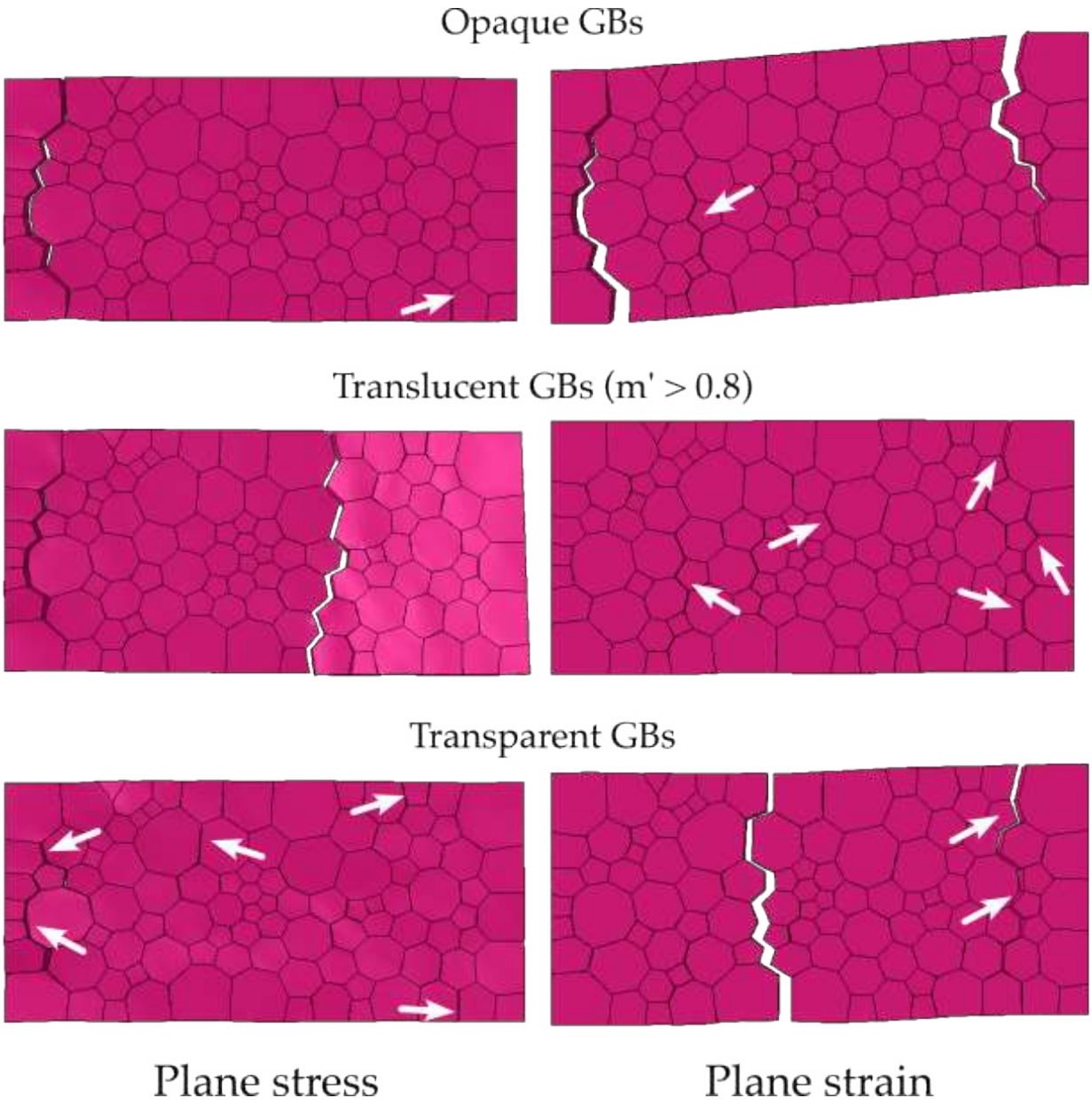

Figure 7.10: Crack path at the end of the simulations of Al foil 1 under plane stress (left column) and plane strain (right column) with fully opaque GBs (first row), translucent GBs where slip transfer is allowed for $m' > 0.8$ (second row), and transparent GBs (third row). The white arrows indicate the location of several intergranular cracks that are not evident in the figure.

between these variables and damage initiation. However, the angle between the GB and the loading axis α_x presents a moderate negative correlation with ε^0_{dmg} for both plane stress and plane strain. This indicates that the strain for damage initiation ε^0_{dmg} decreases when the angle α_x increases. In other words, those GBs perpendicular to the loading axis ($\alpha_x \approx 90°$) are prone to show damage nucleation at lower strains. The number of transparent slip systems $\mathrm{n_{Trs}}$ presents a moderate positive correlation with ε^0_{dmg}, and ε^0_{dmg} increases with

n_{Trs}. Hence, slip transfer delays the nucleation of damage in GBs, and conversely, those GBs with less transparent slip systems (or even opaque GBs with $n_{Trs} = 0$) will present premature damage initiation. The r values for α_x and n_{Trs} are of the same order for plane stress and plane stress. However, the strength of the correlation between n_{Trs} and ε^0_{dmg} is slightly higher than that of α_x for plane stress. This behavior could be explained by the fact that the GBs can couple the deformation with out-of-plane displacements under plane stress, and thus, the geometrical effect, governed by α_x, is not as important as the effect of GB character. Conversely, α_x presents the same correlation as n_{Trs} under plane strain, probably because the constraint of the out-of-plane motion enhances the effect of the geometry.

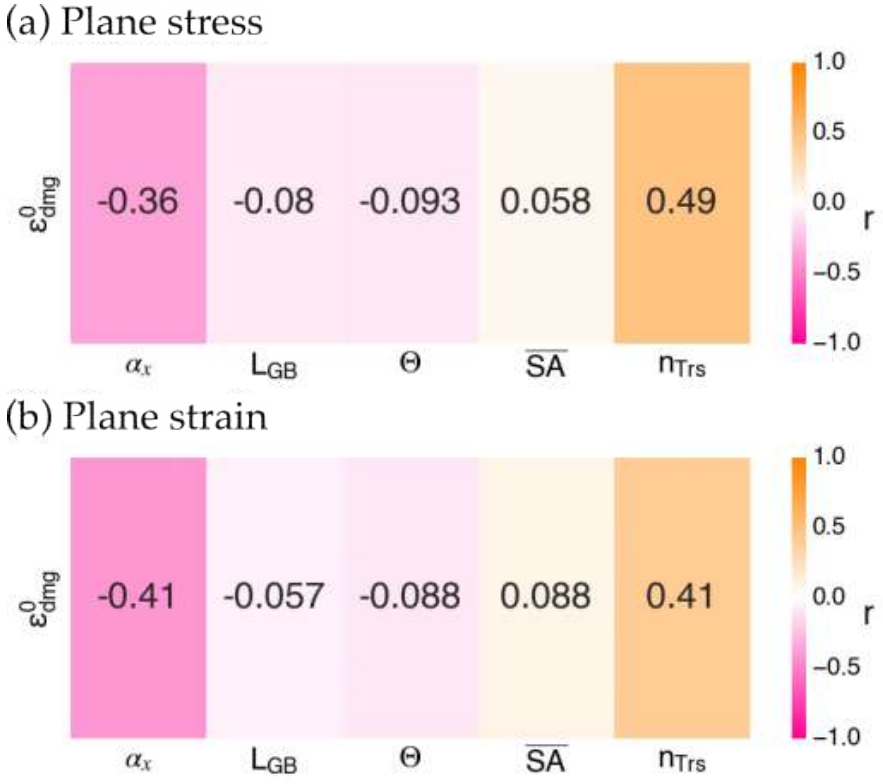

Figure 7.11: Pearson correlation matrix for GB fracture in the Al foils. (a) Plane stress, (b) plane strain.

In summary, the two GB features that have an effect on damage nucleation in FCC Al foils are the angle between the GB and the loading axis α_x and the number of transparent slip systems in a GB, n_{Trs}. The GBs that may lead to premature damage nucleation are those nearly perpendicular to the loading axis and those opaque or nearly opaque to dislocations. On the contrary, the GB length L_{GB}, the misorientation angle Θ, and the slip activation factor $\overline{SA}$ are not correlated with the onset of damage at GBs.

7.5.2 Intergranular fracture of Mg foils in tension (random texture)

The tensile stress-strain curves of the two Mg foils with random crystal orientations (foils 1 and 3 in Fig. 7.4), with and without fracture, are plotted in Fig. 7.12 as a function of GB character under plane stress (a), and plane strain (b) loading conditions. The simulations without fracture are represented with solid lines, and the simulations that include fracture through cohesive surfaces are plotted with dashed lines.

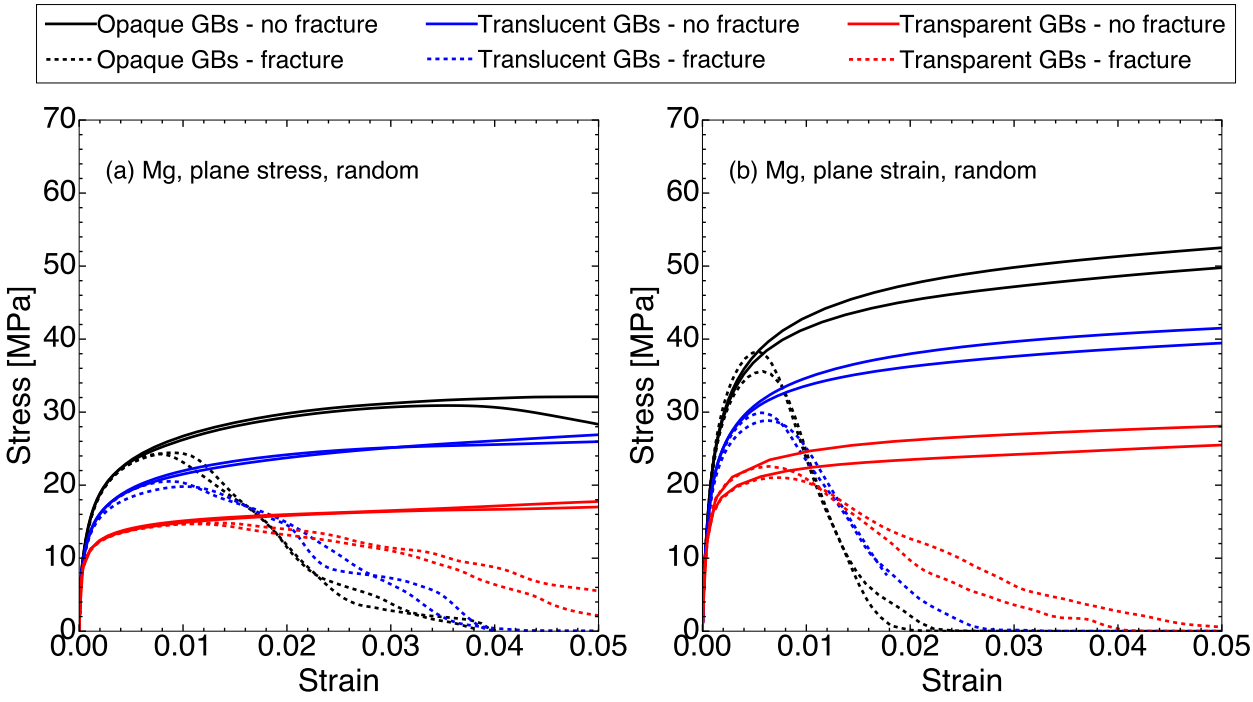

Figure 7.12: Engineering stress-strain curves of the Mg thin foils with random orientations (foils 1 and 3) as a function of GB type under (a) plane stress and (b) plane strain loading conditions. The solid lines correspond to the mechanical response of the foils without fracture, while the dashed lines include fracture at GBs.

As in the case of FCC Al, the HCP Mg foils with fully opaque GBs present the strongest tensile response, followed by translucent GBs and transparent GBs. Similarly, the stress-strain curves obtained under plane strain are displaced towards higher stresses because of the larger triaxiality. The curves of the two foils do not present great differences between them, but this difference increases under plane strain loading conditions. When GBs are assumed to be translucent or fully transparent in HCP metals, stress concentrations mainly arise because of the deformation incompatibility between grains with different crystal orientations. This behavior applies to both loading conditions, plane stress (Fig. 7.12 (a)) and plane strain (Fig. 7.12 (b)).

Regarding fracture, damage is nucleated early and evolves faster for plane strain than for plane stress, as in the case of the Al foils, because of the enhanced triaxiality. In addition, the GB character (opaque, translucent, or transparent) has an effect on damage nucleation and propagation, but it is clearly smaller than in the case of FCC Al. For instance, the strain

at the maximum stress is very similar for the three types of GBs in both plane stress and plane strain, although the maximum stress is significantly higher for the opaque GBs. This may suggest that HCP materials are not as sensitive to the GB character as FCC materials.

The contour plots of the Von Mises stress (in MPa) and of the total dislocation density (in m^{-2}) are plotted in Fig. 7.13 for Mg foil 1 under plane stress without fracture at 2% deformation. The results with fully opaque GBs are presented in the first row, with translucent GBs with slip transfer when $m' > 0.8$ in the second row, and with fully transparent GBs in the third row. The contour plots of the Von Mises stress in the foil with opaque shows that stress concentrations at the GBs are localized in a limited number of GBs while they were more homogeneously distributed in the FCC Al foil. Similar differences between HCP Mg and FCC Al can be found in the foils with translucent and transparent GBs, although the number of GBs with stress concentrations decreases in both cases as slip transfer is allowed through the GB. These results indicate that the deformation incompatibility between adjacent grains in HCP Mg leads to the development of stress concentrations at GBs, even in the case of the foil with fully transparent GBs. Regarding dislocation density, dislocation pile-ups appear at GBs when they are assumed as fully opaque, but the distribution of GBs with large dislocation densities is more inhomogeneous than in the case of the FCC Al foil, and the dislocation density in some GBs in HCP Mg foils is only slightly higher than that in the bulk. When slip transfer is allowed, more GBs become transparent to dislocations, and the total dislocation density decreases. Finally, the dislocation density is approximately one order of magnitude smaller for the foil with fully transparent GBs, but there are still some regions with high dislocation density that are associated with stress concentrations at GBs due to the incompatibility of deformation between grains. Hence, stress concentrations at GBs in HCP Mg foils are determined by the GB character (either opaque, translucent, or transparent) and by the orientation of the grains around the GB that may lead to the development of stress concentrations to accommodate the incompatibility of plastic deformation between grains.

The effect of including intergranular fracture via cohesive surfaces in Mg is plotted in Fig. 7.14 for foil 1 (with random crystal orientations) under plane stress at ε = 2%. The foils without intergranular fracture are displayed on the left column, and the foils that incorporate intergranular fracture are displayed on the right column. As observed in the tensile stress-strain curves under plane stress (Fig. 7.12 (a)), at ε = 2%, all the three foils (fully opaque, translucent, and fully transparent GBs) present a significant drop in the strength when interface fracture is included. Multiple cracks are observed for the foil with opaque GBs at this strain (Fig. 7.14), most of them located within the most stressed region. This is also the case for translucent GBs, where the number of cracks is smaller, but they are also located in regions where the stresses are higher. Finally, the foil with fully transparent GBs just presents a few cracks because, as shown in the tensile test (Fig. 7.12 (a)), the fracture is delayed to higher strains.

The final crack paths in the Mg foil 1 with random texture are depicted in Fig. 7.15 as a function of GB character and loading conditions (plane stress or plane strain). Cracking occurs in different locations depending on the GB character and the loading conditions, as in the Al foil. Fracture generally occurs at the left region of the foils under plane stress,

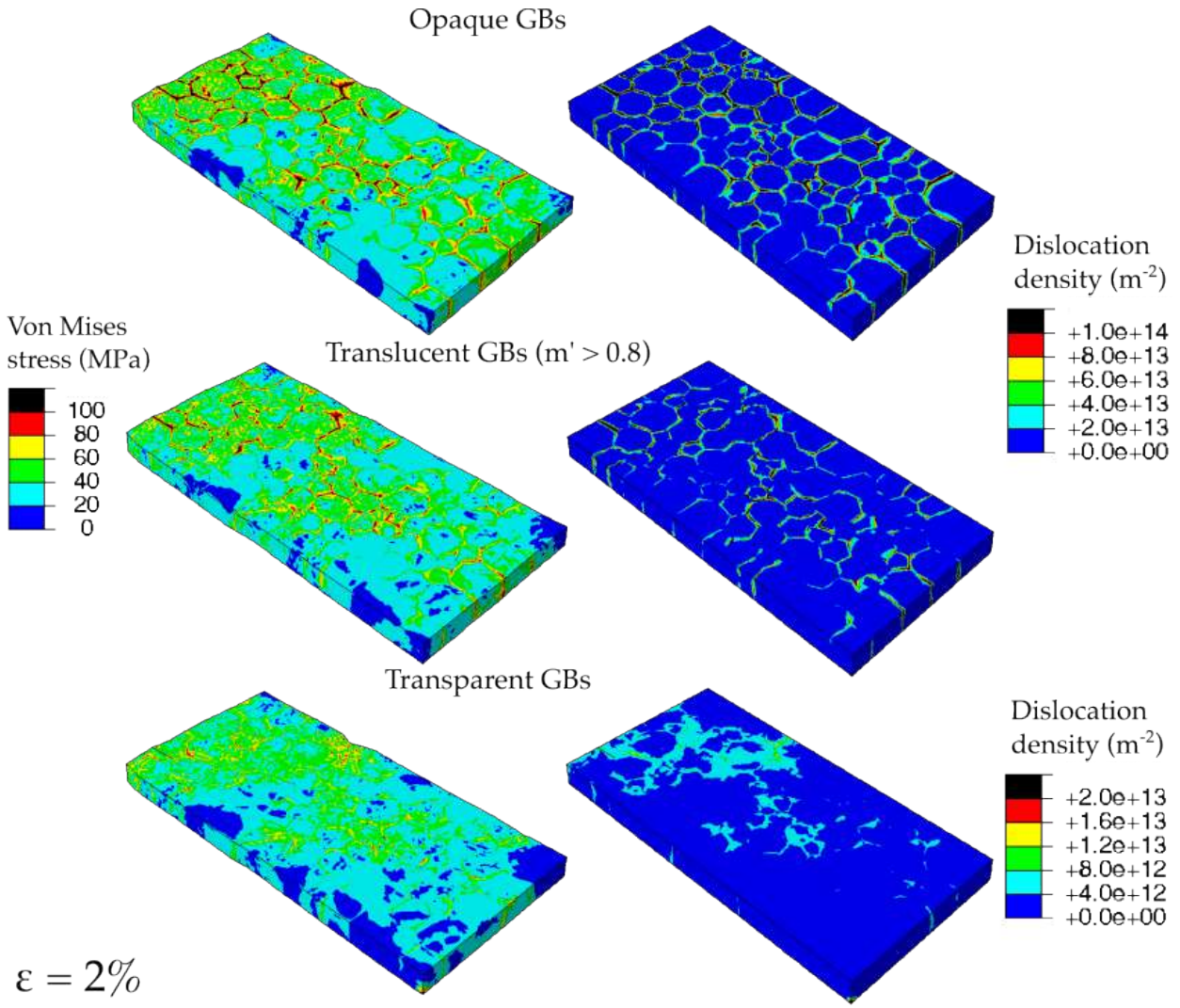

Figure 7.13: Contour plot of the Von Mises stress in MPa (left column) and of total dislocation density in m^{-2} (right column) at ε = 2% as a function of GB character in Mg foil 1 (random texture) under plane stress without fracture. The contour plots with fully opaque GBs are represented on the first row, with translucent GBs where slip transfer is allowed for $m' > 0.8$ on the second row and with transparent GBs on the third row. Note that a different scale is used for the dislocation density of the foils with opaque and translucent GBs and for the fully transparent GBs.

but the crack path differs depending on the GB character. However, there is a significant number of damaged GBs that are common to the three GB characters. Regarding the simulations under plane strain, the foils with opaque and translucent GBs present a very similar crack path along the central section of the foil. However, the foil with transparent GBs presents a different crack path, more similar to the ones found under plane stress.

The effect of the different GB features on the strain for damage initiation ε^0_{dmg} was also analyzed in the HCP Mg foils with random texture following the same strategy used in

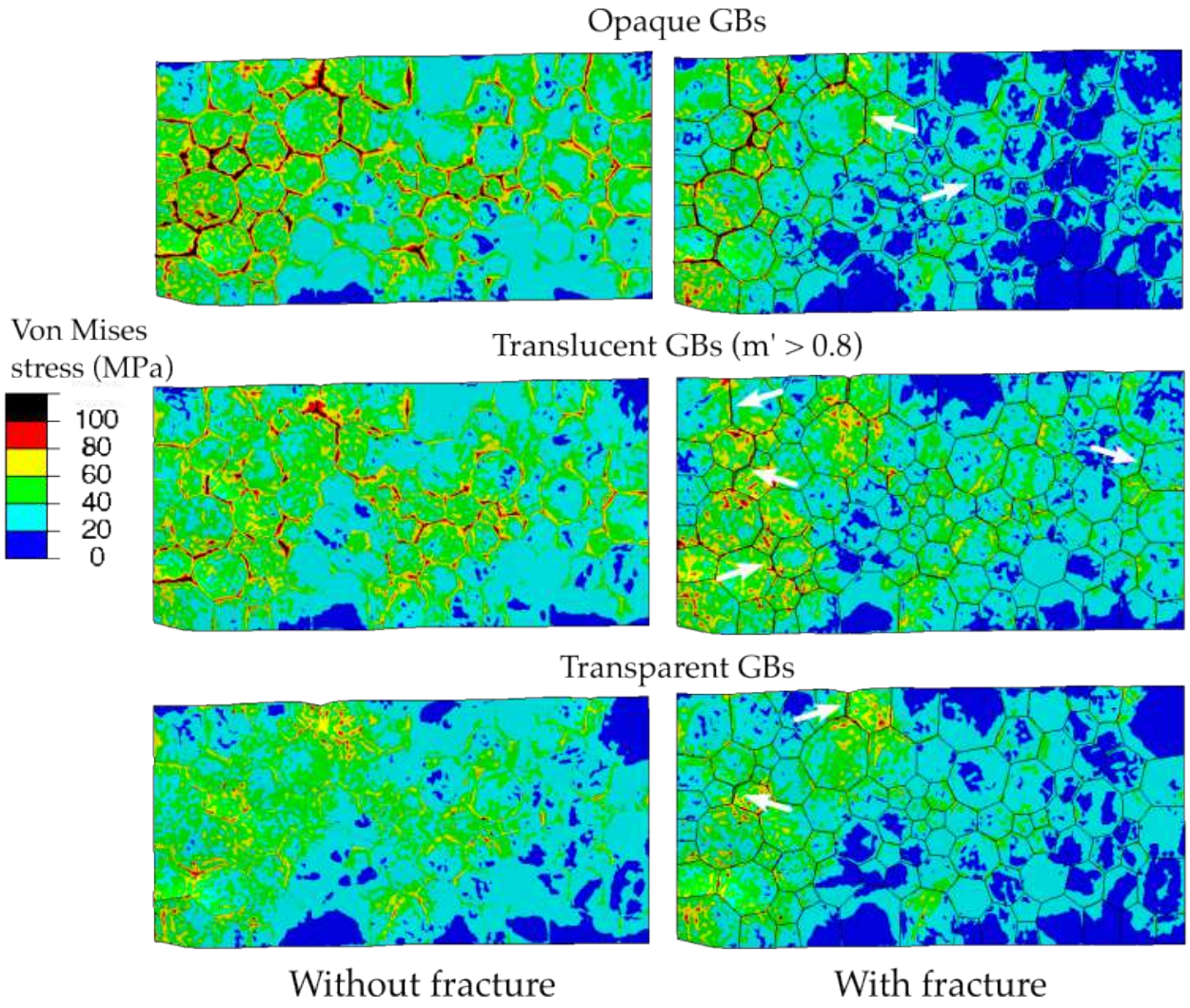

Figure 7.14: Contour plots of the Von Mises stress in MPa at ε = 2% without intergranular fracture (left) and with intergranular fracture (right) as a function of GB character in the Mg foil 1 under plane stress. The contour plots with fully opaque GBs are represented on the first row, with translucent GBs where slip transfer is allowed for $m' > 0.8$ on the second row and with transparent GBs on the third row. The white arrows indicate the location of intergranular cracks.

the Al foils. Besides the GB features used for FCC Al (α_x, $\mathrm{L_{GB}}$, Θ, and $\mathrm{n_{Trs}}$), the mean slip activation factors for basal, prismatic, and pyramidal slip, $\overline{\mathrm{SA}}_{\mathrm{b}}$, $\overline{\mathrm{SA}}_{\mathrm{p}}$, and $\overline{\mathrm{SA}}_{\mathrm{py}}$, respectively, were included in the analysis. The dataset for Mg with random texture is composed of 3141 fractured GBs for the two thin foils, classified as 1562 under plane stress and 1579 under plane strain. The Pearson correlation matrices for plane stress and plane strain are presented in Fig. 7.16 and visually display the influence of the GB features on ε^0_{dmg}.

The damage analysis for the simulations under plane stress indicated that the angle α_x between the GB and the loading axis presents a moderate negative correlation with the strain for damage initiation ε^0_{dmg}. This means that GBs that are perpendicular to the loading axis

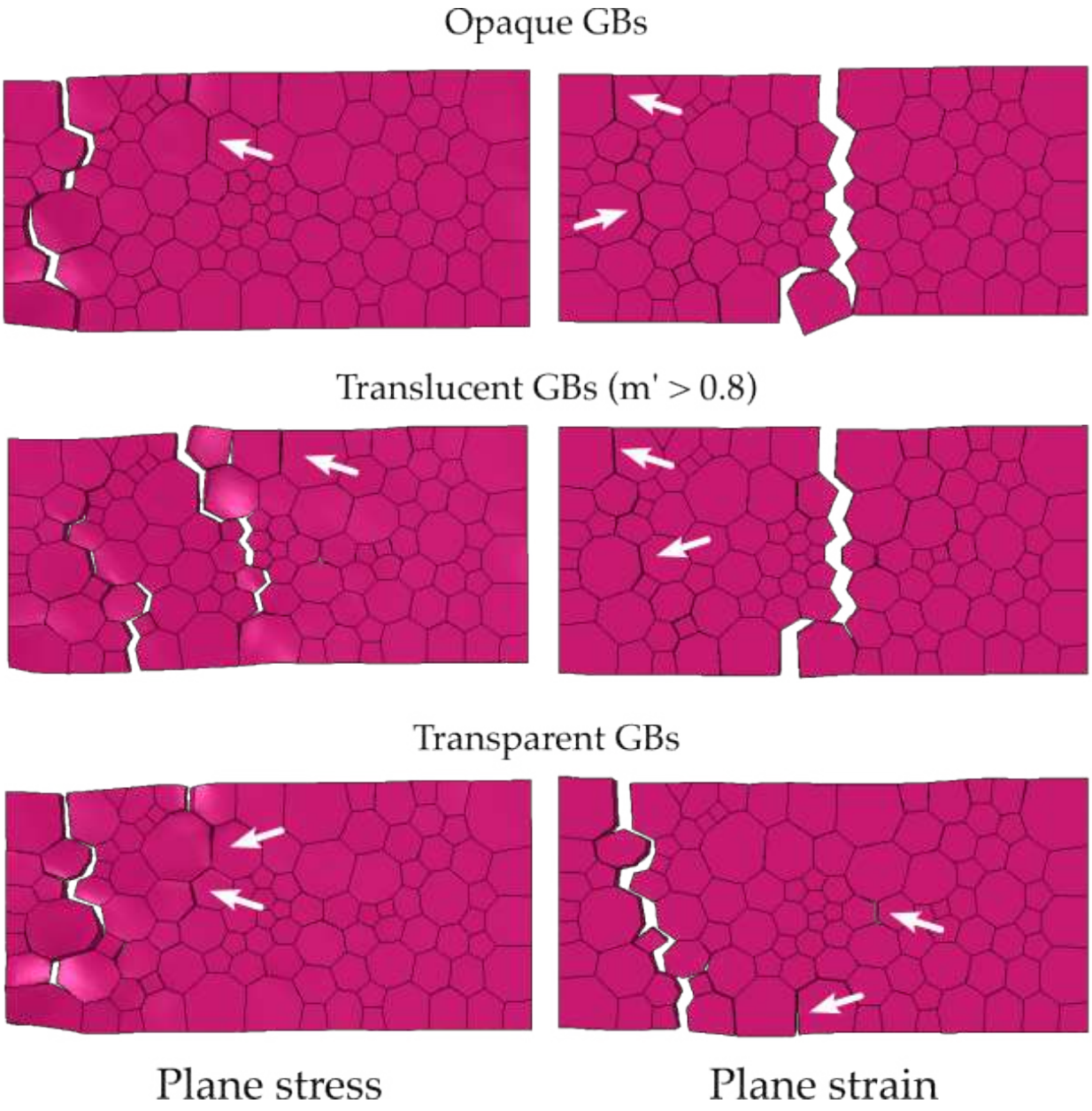

Figure 7.15: Crack path at the end of the simulations of Mg foil 1 with random crystal orientations under plane stress (left column) and plane strain (right column) with fully opaque GBs (first row), translucent GBs where slip transfer is allowed for $m' > 0.8$ (second row), and transparent GBs (third row).

are prone to damage nucleation at lower strains. $\mathrm{L_{GB}}$, Θ, and $\overline{\mathrm{SA}}_{\mathrm{py}}$ show a near-zero correlation on ε^0_{dmg}, and thus, they do not influence damage nucleation. However, a noticeable linear correlation between $\overline{\mathrm{SA}}_{\mathrm{b}}$ with ε^0_{dmg}, comparable to that observed for α_x, is noticed in the HCP Mg foils. This result is different from the one reported in FCC Al foils, where the average slip activation factor showed negligible correlation with damage initiation. The Pearson correlation values of the basal and the prismatic slip activation factors have

Figure 7.16: Pearson correlation matrix for GB fracture in the Mg foils with random crystal orientations. (a) Plane stress, (b) plane strain.

opposite signs, with negative Pearson correlation for $\overline{\mathrm{SA}}_{\mathrm{b}}$ and positive for $\overline{\mathrm{SA}}_{\mathrm{p}}$. This is in agreement with the geometry of the hexagonal lattice because basal and prismatic planes are perpendicular, and when one is well-oriented for slip, the other is not. According to the Pearson correlation values, damage at GBs occurs earlier when the grains across a GB are well-oriented for basal slip, and thus $\overline{\mathrm{SA}}_{\mathrm{b}}$ is high. Taking into account that the CRSS for basal slip is very low, plastic deformation will be localized in the grains with high $\overline{\mathrm{SA}}_{\mathrm{b}}$ across the GB, and the accommodation of the large plastic deformation in these grains with other stiffer grains in the neighborhood may lead to the appearance of stress concentrations at the GBs and, eventually, to fracture. Finally, the number of transparent slip systems $\mathrm{n}_{\mathrm{Trs}}$ presents a weak positive correlation with ε^0_{dmg}, meaning that those GBs opaque to dislocations could be more likely to early damage nucleation. This correlation is significantly smaller than in Al and may suggest that GB character has a lower effect on damage initiation in HCP Mg than in FCC Al.

This analysis was also performed for the foils under plane strain, and the results are similar. A stronger (but moderate) correlation is observed for α_x, higher than in the case of plane stress. Apart from this, the effect of the slip activation factor $\overline{\mathrm{SA}}_{\mathrm{b}}$ decreases with respect to the plane stress conditions, and its Pearson correlation coefficient is now comparable to that of the number of transparent slip systems $\mathrm{n}_{\mathrm{Trs}}$. This means the texture and the effect of the GB character play minor roles in damage nucleation under plane strain because the higher stress levels favor the stronger effect of the angle between GB and the loading axis.

7.5.3 Intergranular fracture of Mg foils in tension (basal texture)

The tensile stress-strain curves of the two Mg foils with strong basal texture (foils 2 and 4 in Fig. 7.4), with and without fracture, are plotted in Fig. 7.17 as a function of GB character under plane stress (a), and plane strain (b) loading conditions. The simulations without fracture are represented with solid lines, while those with fracture through cohesive surfaces are plotted with dashed lines.

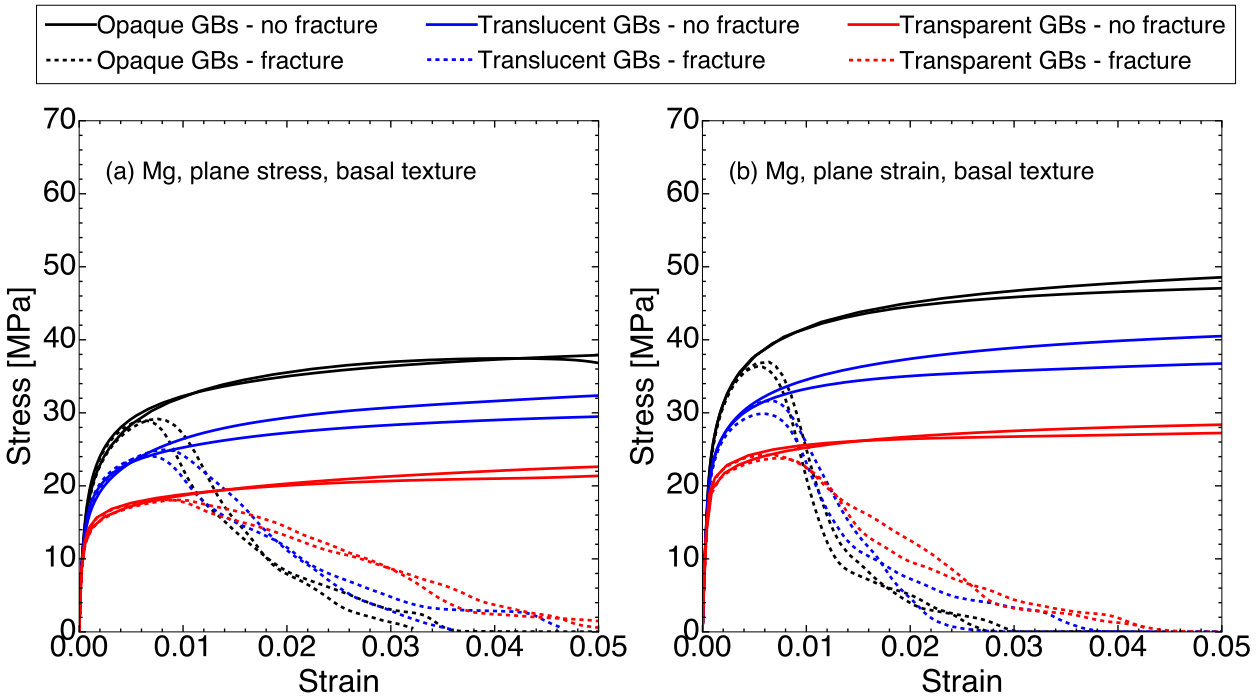

Figure 7.17: Engineering stress-strain curves of the Mg thin foils with basal texture (foils 2 and 4) as a function of GB type under (a) plane stress and (b) plane strain loading conditions. The solid lines correspond to the mechanical response of the foils without fracture, while the dashed lines include fracture at GBs.

The foils with fully opaque GBs present the strongest mechanical response, followed by translucent GBs and transparent GBs, as reported in the two previous cases (FCC Al and HCP Mg with random texture). Similarly, the stress-strain curves under plane strain are displaced towards higher stresses because of the triaxiality. The curves of the different foils do not present great differences in the case of strong basal texture, especially when GBs are fully opaque or fully transparent.

Regarding fracture, damage initiates early and grows at a faster rate for plane strain than for plane stress, as observed in the Mg foils without texture. The GB character (opaque, translucent, or transparent) does not seem to affect damage nucleation and propagation since the strain at the maximum stress and the damage propagation are very similar for the three types of GBs in both plane stress and plane strain. This reinforces the idea that HCP materials are not as sensitive to the GB character as FCC materials.

The contour plots of the Von Mises stress (in MPa) and of the total dislocation density (in

m^{-2}) are plotted in Fig. 7.18 for Mg foil 2 with basal texture under plane stress without fracture at 2% deformation. The results with fully opaque GBs are presented in the first row, with translucent GBs with slip transfer when $m' > 0.8$ in the second row, and with fully transparent GBs in the third row. As observed in the contour plots, stress concentrations are found at some GBs in the foils with opaque GBs but not in all of them. The stress concentrations decrease as the GBs become translucent and transparent, but they appear even in the latter due to the deformation incompatibility between adjacent grains. These stress concentrations appear at the regions where the crystal orientations between the adjacent grains are very different, like the left region of the foil (see Fig. 7.4 (b)). Conversely, when the grain orientations and the dominant deformation mechanisms are compatible, as in the central section of the foil, no large stress concentrations appear, regardless of the GB character.

The effect of intergranular fracture is depicted in the contour plots in Fig. 7.19 for foil 2 (with strong basal texture) under plane stress at ε = 2%. The foils without fracture are displayed on the left column, and the foils that incorporate intergranular fracture are displayed on the right column. As observed in the tensile stress-strain curves for plane stress (Fig. 7.17 (a)), at ε = 2%, all the three foils (fully opaque, translucent, and fully transparent GBs) present a significant drop in the strength. Multiple cracks are observed for the foil with opaque GBs at this strain (Fig. 7.19), and most of them are located on the left side of the foil, in which large stress concentrations at GBs can be found. This is also the case for translucent GBs, where the number of cracks is smaller, but they are also located in regions where the stresses are higher. Finally, the foil with fully transparent GBs just presents a few cracks because, as shown in the tensile test (Fig. 7.17 (a)), fracture is delayed to larger applied strains.

The final crack paths in Mg foil 2 with basal texture are depicted in Fig. 7.20 as a function of GB character and loading conditions (plane stress or plane strain). Cracking occurs in more similar locations depending on the GB character and the loading conditions in comparison to the Mg foil without texture (see Fig. 7.15). In this case, the fracture is localized on the left region of the foils regardless of the GB character and the loading conditions, but the crack path is different for plane stress and plane strain. Nevertheless, the GB character seems to have a smaller effect on the location of the final crack in comparison to that observed in the foil with random texture.

Due to the plastic anisotropy of HCP Mg, crystallographic texture may have an important effect on the tensile response of the foil. The tensile stress-strain curves of the Mg foils with random texture (foils 1 and 3) and with strong basal texture (foils 2 and 4) with and without intergranular fracture are presented in Fig. 7.21 (a) for fully opaque GBs and plane stress. The stress-strain curves with and without texture present a similar shape, but the foils with basal texture are displaced towards slightly higher stresses (about 5 MPa difference). The stiffer response of the foils with basal texture can be explained by the enhanced activation of prismatic slip, which requires higher CRSS and thus hardens the material. Conversely, when the crystal orientations are random, basal slip will be facilitated due to its small CRSS, which provides a softer response.

To illustrate this, the relative contributions of the different slip systems in the HCP lattice

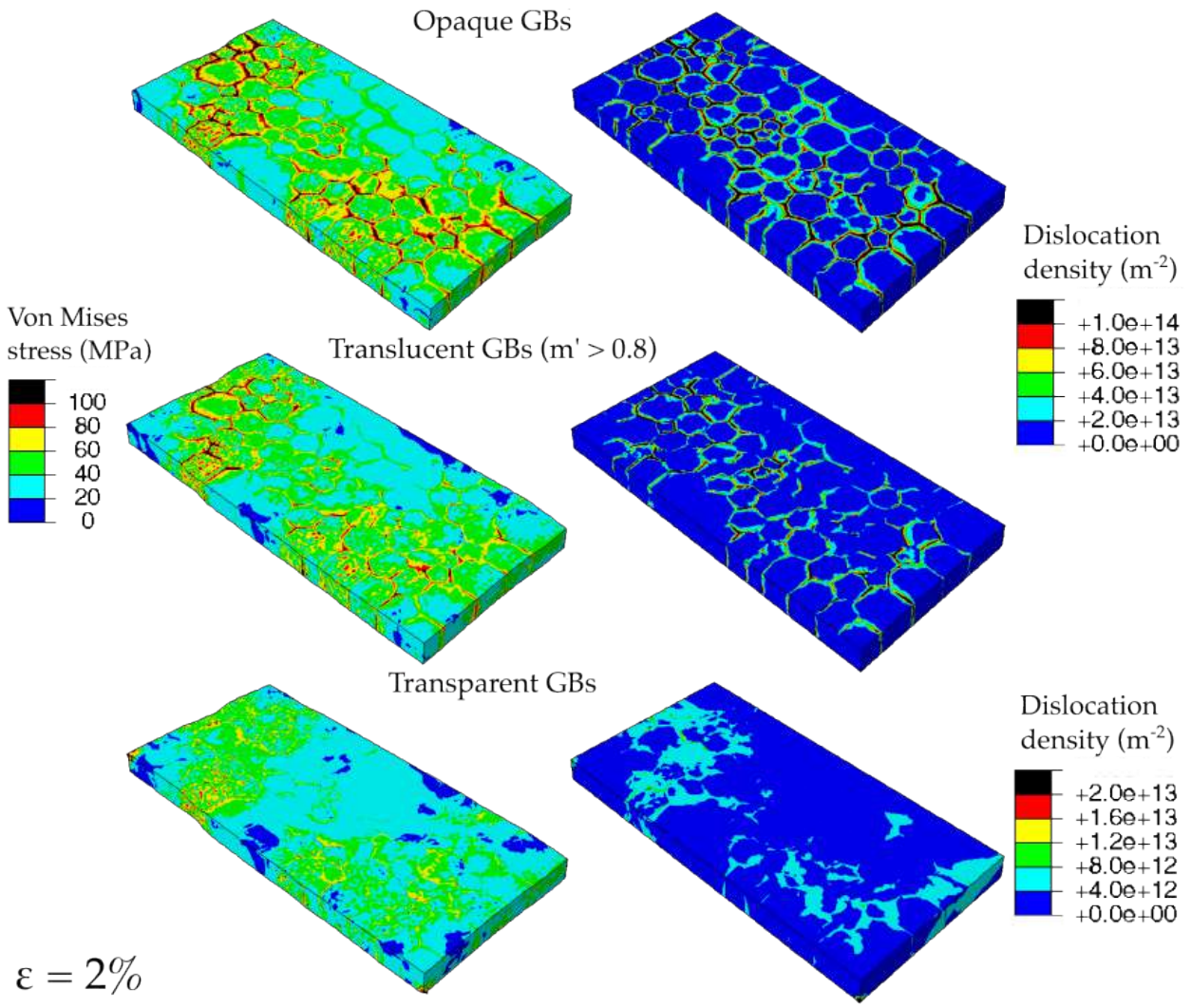

Figure 7.18: Contour plot of the Von Mises stress in MPa (left column) and of total dislocation density in m^{-2} (right column) at ε = 2% as a function of GB character in Mg foil 2 (strong basal texture) under plane stress without fracture. The contour plots with fully opaque GBs are represented on the first row, with translucent GBs where slip transfer is allowed for $m' > 0.8$ on the second row and with transparent GBs on the third row. Note that a different scale is employed for the dislocation density for the foils with opaque and translucent GBs and for those with fully transparent GBs.

to the accumulated plastic slip γ are plotted in Fig. 7.21 (b) for foils 1 (random orientations, solid lines) and 2 (basal texture, dashed lines) and plane stress. The strong effect of texture on the deformation mechanisms is shown in this figure. In general, basal slip dominates over the other slip systems at the early stages of deformation when the stresses are low. The contribution of prismatic slip increases with applied strain as the stresses are large enough to overcome its CRSS (refer to Table 6.5). The contribution of pyramidal slip is always very small. The main contribution to the plastic deformation under plane stress and random texture always comes from basal slip in the whole strain range (about 65%),

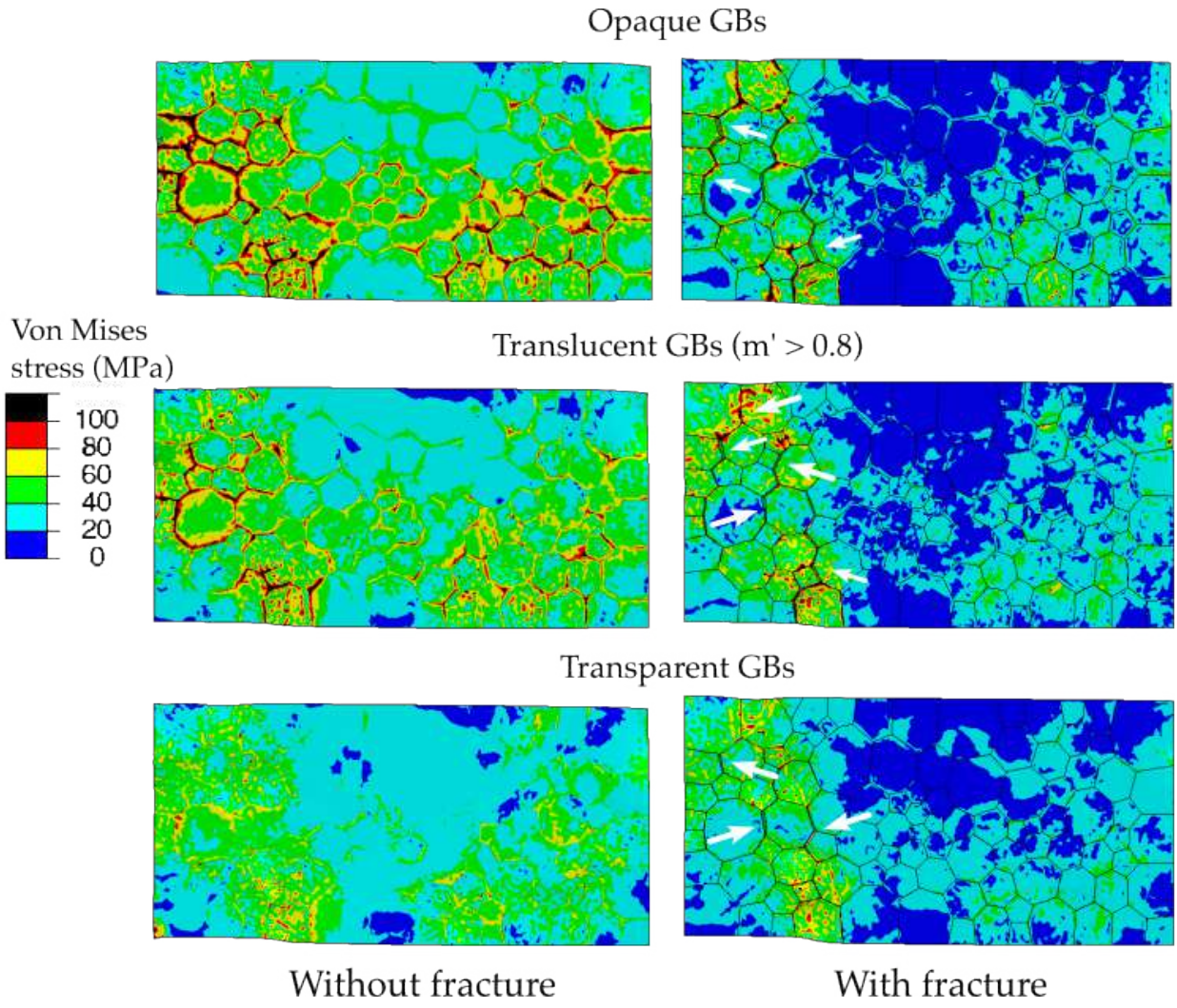

Figure 7.19: Contour plots of the Von Mises stress in MPa at ε = 2% without including fracture (left) and including intergranular fracture (right) as a function of GB character in Mg foil 2 under plane stress. The contour plots with fully opaque GBs are represented on the first row, with translucent GBs where slip transfer is allowed for $m' > 0.8$ on the second row and with transparent GBs on the third row. Intergranular cracks are indicated with white arrows.

followed by prismatic (about 30%) and pyramidal slip (less than 5%). However, basal slip and prismatic slip contribute equally to plastic slip (about 50% each) in the foil with strong basal texture, while the contribution of pyramidal slip is negligible. It should be noticed that the basal texture promotes the activation of prismatic slip instead of basal slip because the basal planes are nearly parallel to the loading axis. Thus, the activation of prismatic slip, which requires higher CRSS, induces a strengthening effect on the tensile response of the foils with a strong basal texture. However, the CRSS for basal slip in Mg is very small -as compared to those of prismatic and pyramidal – so basal slip is always active. These two factors lead to a competitive process between basal and prismatic slip activation, whose contributions would probably be balanced above 5% strain.

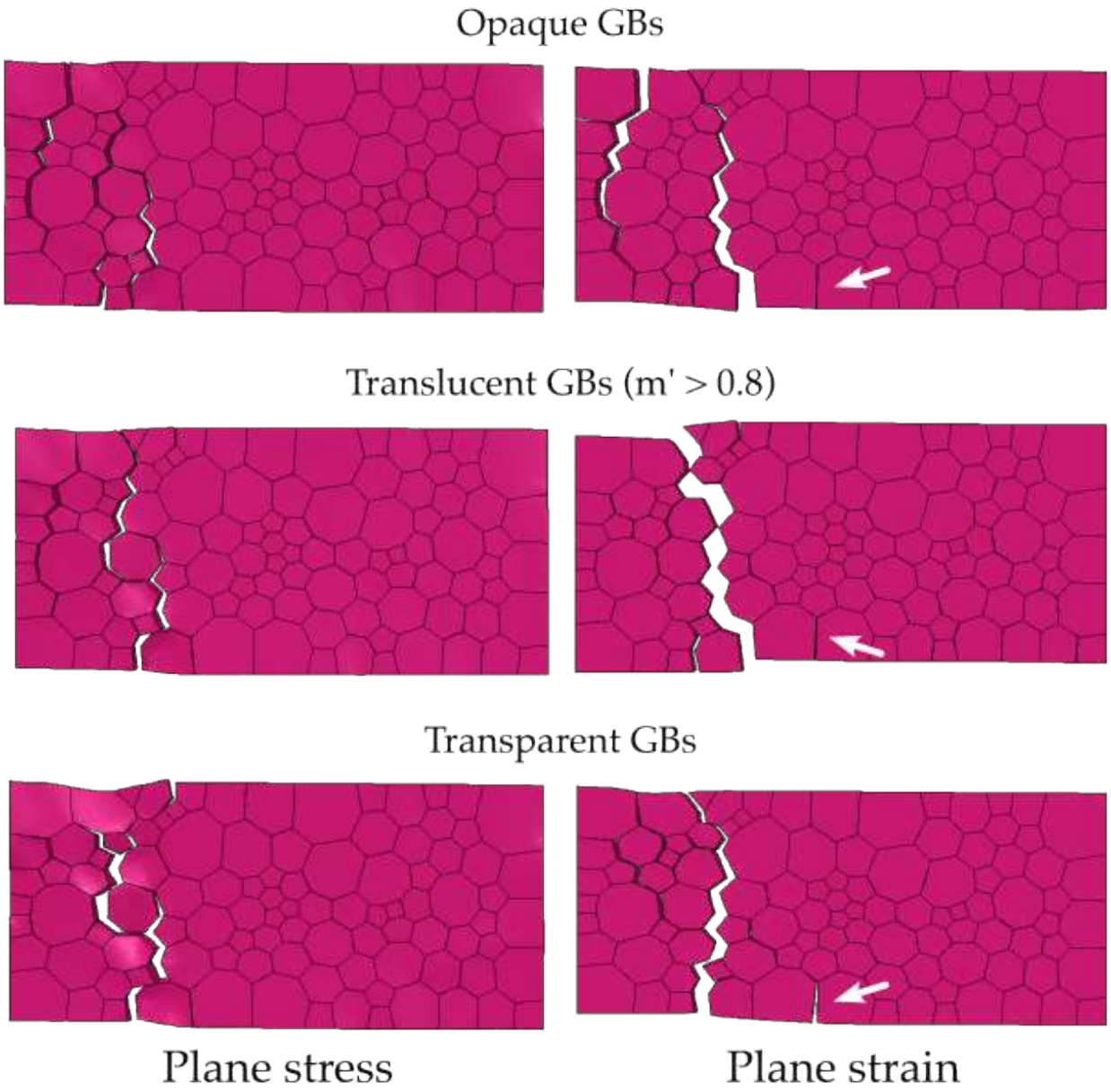

Figure 7.20: Crack path at the end of the simulations of Mg foil 1 with basal texture under plane stress (left column) and plane strain (right column) with fully opaque GBs (first row), translucent GBs where slip transfer is allowed for $m' > 0.8$ (second row), and transparent GBs (third row).

The effect of texture on the strength of the foils is different under plane strain (Fig. 7.22 (a)), and the foils with random texture are slightly stronger than those with random texture. Plane strain leads to a greater increase in the strength of the foils with random texture than in those with basal texture because the out-of-plane displacements necessary to accommodate the deformation incompatibility between adjacent grains with very different crystal orientations are hindered. On the contrary, out-of-plane displacements are less crit-

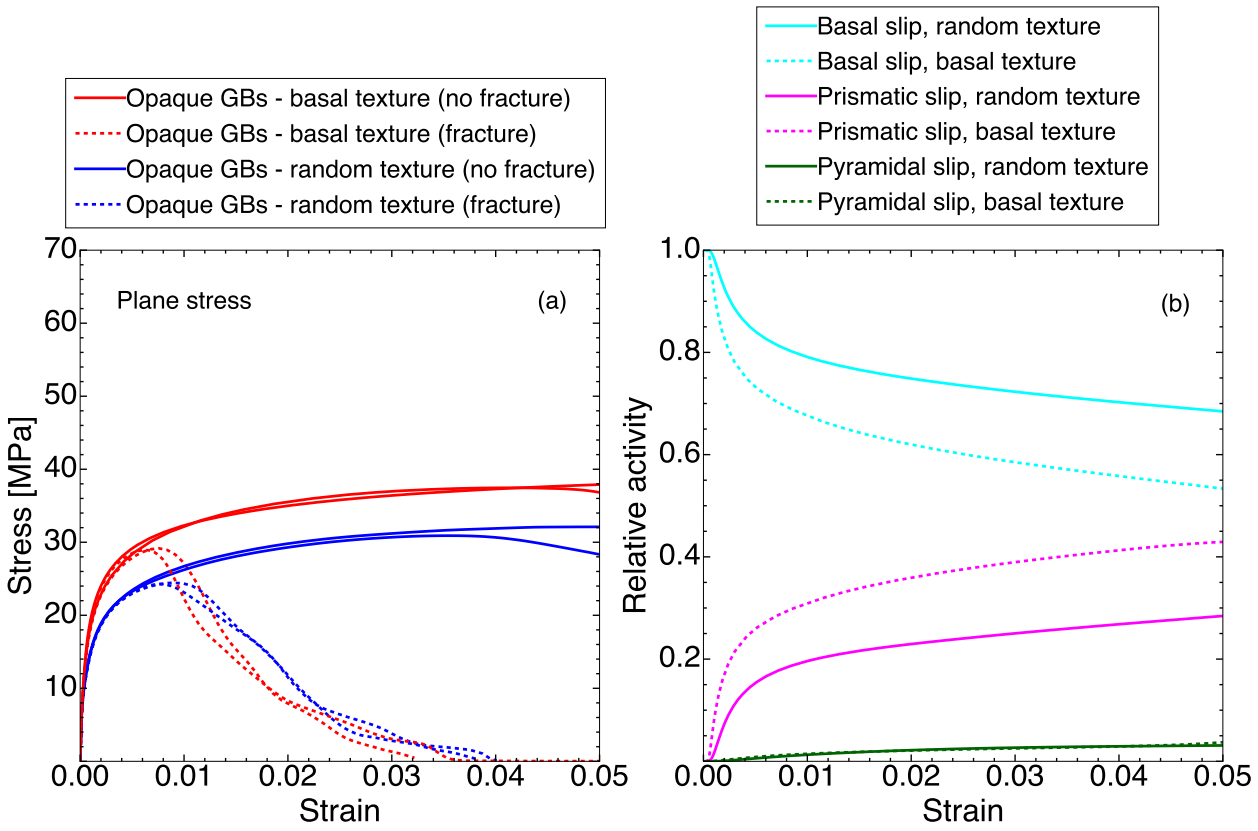

Figure 7.21: (a) Engineering stress-strain curves of Mg thin foils with random crystal orientations (foils 1 and 3, in blue) and with strong basal texture (foils 2 and 4, in red) with opaque GBs under plane stress. The solid lines correspond to the foils without fracture, and the dashed lines correspond to the foils with fracture. (b) Relative contribution of the basal, prismatic, and pyramidal slip systems to the accumulated plastic slip γ as a function of the crystallographic texture in Mg thin foils 1 (random orientations, solid lines) and 2 (basal texture, dashed lines) with fully opaque GBs under plane stress conditions.

ical in the foils with basal texture because of the orientation similarity between neighbor grains. Hence, the difference in the tensile response under plane stress and plane strain between random and basal texture could be attributed to the conjoint effect of the out-of-plane constraint, which increases triaxiality, and the crystallographic texture. Regarding intergranular fracture, the presence of crystallographic texture does not seem to play any role since the tensile responses for foils 1 and 2 are very similar in terms of both the strain for damage nucleation and the damage propagation rate.

Regarding slip system activity, the plane strain simulations present a similar behavior to that observed under plane stress but modified by the higher stresses applied on the foils (Fig. 7.22 (b)). They promote a significant contribution of prismatic slip from the early stages of deformation. Moreover, the contribution of pyramidal slip is also greater than for plane stress, but it is still negligible as compared to basal or prismatic. Basal slip is dominant for the simulations with random texture (about 60%), followed by prismatic

with about 30% contribution to γ. However, prismatic slip clearly dominates over basal slip –even below 1% deformation– in the foil with strong basal texture. The effect of crystallography and texture is once again enhanced by the plane strain constraint to the foil plane, which drastically increases the stress level and the activation of prismatic slip. On one hand, the basal texture promotes the dominant activation of prismatic slip with higher CRSS, which provides a strengthening effect in the tensile response. On the other hand, in the foils with random orientations, the main contribution to the accumulated plastic slip comes from the softer basal slip due to its ease of activation. Nevertheless, the out-of-plane constraint, together with the orientation differences between adjacent grains, increases the stress triaxiality, thus providing a harder tensile response. Summing all these effects, the tensile curves of the foils with and without texture look very similar despite the fact that the plastic deformation mechanisms are significantly different.

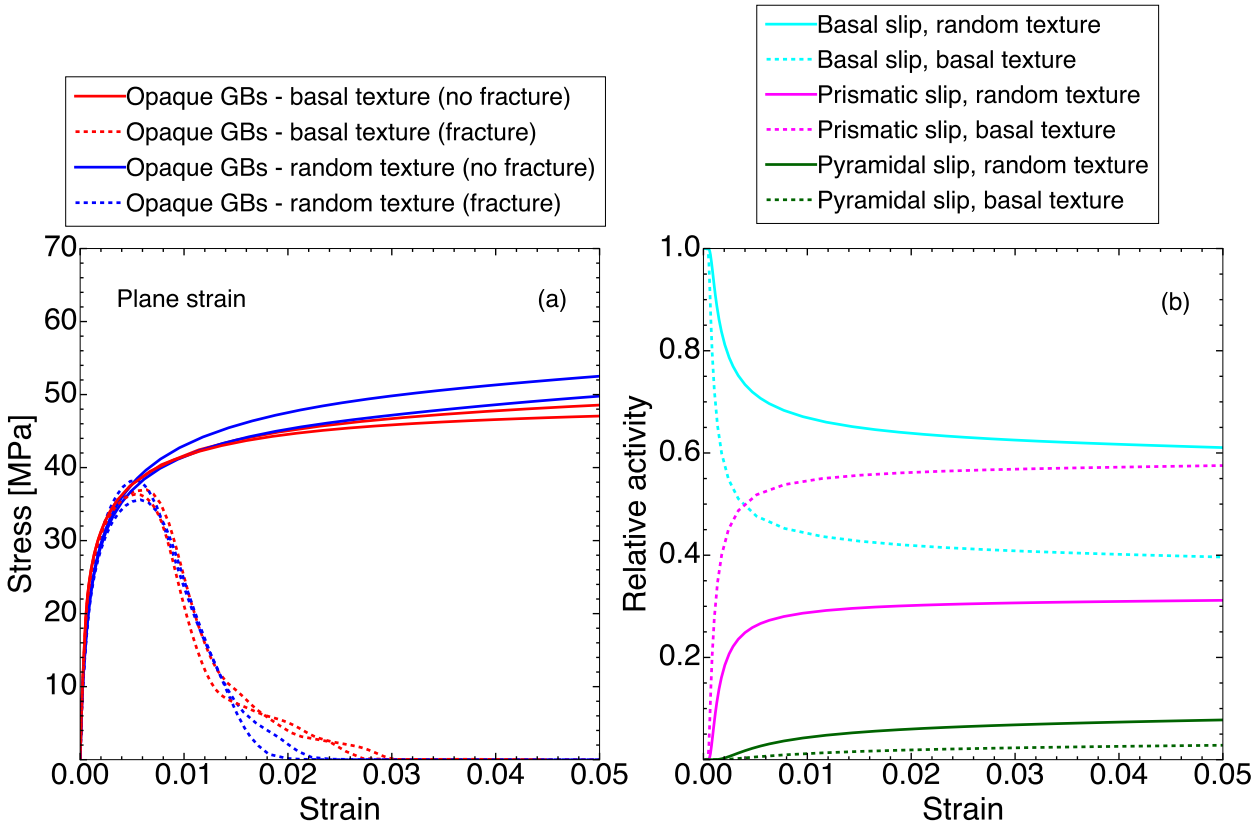

Figure 7.22: (a) Engineering stress-strain curves of Mg thin foils with random crystal orientations (foils 1 and 3, in blue) and with strong basal texture (foils 2 and 4, in red) with opaque GBs under plane strain. The solid lines correspond to the foils without fracture, and the dashed lines correspond to the foils with fracture. (b) Relative contribution of the basal, prismatic, and pyramidal slip systems to the accumulated plastic slip γ as a function of the crystallographic texture in Mg thin foils 1 (random orientations, solid lines) and 2 (basal texture, dashed lines) with fully opaque GBs under plane strain conditions.

The influence of the different GB features on the strain for damage initiation ε^0_{dmg} was also analyzed in the HCP Mg foils with basal texture (foils 2 and 4). The analyzed GB features

were again α_x, $\mathrm{L_{GB}}$, Θ, and $\mathrm{n_{Trs}}$, together with the mean slip activation factors for basal, prismatic, and pyramidal slip, $\overline{\mathrm{SA}}_\mathrm{b}$, $\overline{\mathrm{SA}}_\mathrm{p}$, and $\overline{\mathrm{SA}}_\mathrm{py}$. The dataset for the Mg foils with basal texture (foils 2 and 4) is composed of 3102 fractured GBs for the four analyzed thin foils, classified as 1543 under plane stress and 1559 under plane strain. The Pearson correlation matrices for plane stress and plane strain are presented in Fig. 7.23, which display the influence of the GB features on ε^0_{dmg}.

Figure 7.23: Pearson correlation matrix for GB fracture in the Mg foils with strong basal texture. (a) Plane stress, (b) plane strain.

The damage analysis for the simulations under plane stress indicated that the angle α_x presents a moderate negative correlation with ε^0_{dmg}, which means that GBs that are perpendicular to the loading axis are prone to damage at lower strains. This correlation is slightly stronger than in the case of the foils with random orientations. The misorientation angle Θ, and $\overline{\mathrm{SA}}_\mathrm{py}$ show a near-zero correlation on ε^0_{dmg}, and thus, they do not have any influence on damage nucleation. The number of transparent slip systems $\mathrm{n_{Trs}}$ presents a weak positive correlation with ε^0_{dmg}, higher than that observed for the foils with random orientation. This suggests that the GB character has a greater effect on damage initiation in HCP Mg in the presence of texture since grain orientations are more alike and the deformation incompatibility is reduced.

The linear correlation between $\overline{\mathrm{SA}}_\mathrm{b}$ with ε^0_{dmg} for the foils with basal texture is smaller than for the foils with random texture, whereas the r value for $\overline{\mathrm{SA}}_\mathrm{p}$ remains the same. In this case, the Pearson coefficients of the basal and the prismatic slip activation factors are nearly identical but with opposite signs, with negative Pearson correlation for $\overline{\mathrm{SA}}_\mathrm{b}$ and positive for $\overline{\mathrm{SA}}_\mathrm{p}$. This is in agreement with the geometry of the hexagonal lattice because

basal and prismatic planes are perpendicular, and when one is well-oriented for slip, the other is not. According to them, damage at GBs occurs earlier when the grains across a GB are well-oriented for basal slip ($\overline{\mathrm{SA}}_{\mathrm{b}}$ is high), and conversely, damage nucleation is delayed if the grains are well-oriented for prismatic slip. Unlike the foils with random orientations, the GB length L_{GB} also presents a weak negative correlation with ε^0_{dmg}, comparable to that observed for the slip activation factors for basal and prismatic slip.

This analysis was also performed for the foils under plane strain, and the results are similar to those observed for the foils with random texture. A stronger (but moderate) correlation is observed for α_x, slightly higher than in the case of plane stress. Furthermore, the slip activation factor for basal slip $\overline{\mathrm{SA}}_{\mathrm{b}}$ presents a greater (but still very weak) correlation, whereas $\overline{\mathrm{SA}}_{\mathrm{p}}$ has no influence on ε^0_{dmg} as compared to plane stress. Apart from this, the effect of the other GB features on damage initiation is nearly identical to those presented for plane stress, with the slip activation factors for basal and prismatic and the number of transparent slip systems presenting some correlation with damage nucleation.

7.6 Conclusions

The tensile deformation of FCC Al and HCP Mg thin foils, including intergranular fracture at GBs, was simulated by means of a dislocation-based crystal plasticity model that allows for slip transfer. Intergranular fracture was introduced through cohesive surfaces governed by a bilinear traction-separation law. Polycrystalline foils with columnar grains with different textures were generated, and the effect of GB character on intergranular fracture was assessed by considering three types of simulations: foils with fully opaque GBs, foils with fully transparent GBs, and foils with translucent GBs where slip transfer is allowed when $m' > 0.8$. Two loading cases were used for each foil: plane stress and plane strain. The tensile stress-strain curves and the analysis of the onset of damage at the GB database led to the following conclusions:

- The microstructural features that influence damage initiation in FCC Al thin foils are the angle between the GB and the loading axis α_x and the number of transparent slip systems $\mathrm{n}_{\mathrm{Trs}}$, i.e., GBs perpendicular or nearly perpendicular to the loading axis and that opaque from the viewpoint of slip transfer will be damaged earlier during deformation. In the case of HCP Mg, damage nucleation is also dominated by the GB angle with the loading axis α, but the slip activation factor of the GBs also plays an important role. Thus, GBs nearly perpendicular to the loading direction whose neighboring grains are suitably oriented for basal slip will probably initiate damage. Unlike FCC Al, the HCP Mg simulations proved to be less sensitive to the GB character (fully opaque, translucent, or fully transparent GBs).
- GB character (opaque, translucent, or transparent GBs) has an important effect on damage nucleation in Al. Opaque GBs, in which dislocation pile-ups are formed, are more prone to present premature damage nucleation than translucent or transparent GBs, in which damage is delayed. Damage also propagates faster when GBs are opaque than when GBs are transparent. On the contrary, GB character has limited influence on damage nucleation in HCP Mg because stress concentrations at

GBs (that lead to damage nucleation) are controlled in HCP Mg by the anisotropic behavior of grains with different orientations.

- The loading conditions (either plane stress or plane strain) also influence the onset and propagation of intergranular damage. GB fracture under plane stress conditions depends more on the GB character (fully opaque, translucent, or fully transparent GBs), whereas the microstructural features (the angle between GB and loading axis, or the slip activation factor) are more relevant in the case of plane strain. This latter behavior is attributed to constraint induced by the plane strain condition that forces the deformation to occur in the foil plane and increases the triaxiality.
- Texture has a remarkable effect on the deformation of Mg thin foils due to their plastic anisotropy, especially on the slip system contribution to the accumulated plastic slip. Basal slip was dominant over prismatic and pyramidal slip when in the presence of random texture. Conversely, the presence of a strong basal texture promoted the activation of the better-oriented prismatic slip systems despite its greater CRSS. This led to a competitive process with the conjoint activation of both slip systems, one that is energetically favorable (basal) against one that is geometrically favorable (prismatic). In all cases, the contribution of pyramidal slip was negligible ($< 10\%$) owing to its high CRSS.

8 General discussion, conclusions and future work

8.1 General discussion and conclusions

The thesis has analyzed the mechanisms of dislocation/grain boundary interaction in metallic polycrystals from the experimental and simulation viewpoints. The experimental characterization was carried out using state-of-the-art techniques (including slip trace analysis in combination with electron backscatter diffraction, diffraction contrast tomography, and high-resolution digital image correlation) to assess the validity of different geometrical criteria to predict dislocation slip transfer/blocking at grain boundaries in FCC (Ni) and HCP (Ti) polycrystals. Then, the slip transfer criteria were implemented in a physically-based crystal plasticity model to predict the effect of grain boundaries (and, thus, of the grain size) on the strength of metallic polycrystals, taking into account the existence of different types of grain boundaries from the viewpoint of slip transmission: transparent, translucent and opaque. Finally, intergranular fracture was included in the simulations through cohesive surfaces along the grain boundaries to understand the influence of the microstructure on the nucleation and growth of damage in polycrystals.

The starting point for the experimental assessment of slip transfer is the well-known EBSD-based slip trace analysis technique. As presented in Chapter 2, this technique has been implemented and validated in pure Ni (FCC). The experimental results revealed that slip transfer at coherent and incoherent annealing twin boundaries in pure Ni is controlled by the residual Burgers vector and takes place when $\Delta b \approx 0$, regardless of the angle between slip normals and the twist angle (which is known for twin boundaries) between the incoming and outgoing slip planes. Moreover, slip transfer seems to be controlled by dislocation cross-slip in this case. Slip transfer across regular grain boundaries is very likely to occur across low-angle regular grain boundaries when the active slip systems are geometrically well-aligned, and unlikely to occur otherwise. However, there is a significant number of slip blocking instances where the classical geometrical criteria indicate high likelihood for slip transfer, that can be attributed to some of the main inherent limitations of the conventional slip trace analysis methodology. First, they could be caused by the error induced by the assumption that the active slip system is the one with the high-

est Schmid factor. As explained in Section 1.3, this technique can only ascertain the slip plane from the observation of the slip bands on the sample surface. The existence of three different slip systems per $\{111\}$ slip plane in FCC materials (see Table 1.1) induces a significant uncertainty on the active slip system identification. Furthermore, this methodology lacks information about the 3D GB geometry, which is directly related to the twist angle θ. Hence, these outliers could be a consequence of a large value of the twist angle θ between the active slip systems, which is not known for regular grain boundaries because there was no information about the grain boundary orientation within the sample. Finally, the conventional EBSD-based slip trace analysis technique does not provide any insights into the local stress distribution near grain boundaries, which could affect the driving force to transfer slip between neighboring grains.

The limitation of the unequivocal active slip system identification was overcome with the use of pure Ti (HCP) samples with a strong rolling texture. As a consequence of the strong texture, only prismatic slip was observed after plastic deformation. Due to the existence of three prismatic slip systems with distinct slip planes, the active slip systems could be identified from the slip trace direction on the surface with no associated error. Then, Laboratory-scale Diffraction Contrast Tomography (Lab-DCT) was used to solve the limitation of the lack of information about the 3D geometry of grain boundaries (Chapter 3). This novel technique was able to provide detailed information about the microstructure (grain size, shape, and orientation as well as grain boundary orientation) of pure Ti foils in 3D prior to deformation. The data obtained by means of Lab-DCT were compared to those obtained on the sample surface by EBSD and were of similar quality for grains $> 50\ \mu m$. Hence, this technique has proved to be a great alternative to EBSD, achieving very similar results for medium to coarse grain sizes while providing a three-dimensional microstructure reconstruction.

Two Ti samples were scanned by Lab-DCT to obtain all the information about the GB geometry through the thickness of the samples and, therefore, allow the calculation of the twist angle θ between the active slip systems. The analysis of prismatic-to-prismatic slip transfer in the first sample was carried out by coupling conventional slip trace analysis for the slip system identification and slip transfer observation and Lab-DCT for the 3D microstructural characterization, as presented in Chapter 4. This allowed the acquisition of an extensive and robust database of slip transfer and blocking occurrences across more than 300 grain boundaries, where the twist angle could be characterized. This data was employed to evaluate the performance of different slip transfer metrics such as the Luster-Morris parameter m', the residual Burgers vector Δb, or the Lee Robertson and Birnbaum parameter LRB, via a categorical model. The efficacy of each slip transfer criterion as a slip transfer predictor was measured through the F1 score, and the results pointed that the highest F1 scores were attained by m' and Δb. However, the LRB criterion which directly depends on the twist angle θ (Eq. 1.3) presented the worst accuracy to predict the likelihood of slip transfer, suggesting that the twist angle plays a minor role on prismatic-to-prismatic slip transfer.

Nevertheless, despite the high performance of some of the geometrical slip transfer criteria, some slip blocking events were still observed when slip transfer across the GB was

expected. This abnormal behavior could be caused by the local stress state near those grain boundaries, which could not be ascertained with the current experimental methodology. For this reason, high-resolution digital image correlation (HRDIC) was used to obtain the strain heterogeneity distribution after deformation in the second Ti sample and overcome the last limitation of the conventional slip trace analysis technique (Chapter 5). The effective shear strain maps were obtained at different applied strains to observe the plastic deformation mechanisms and the evolution of the slip transfer process across 28 grain boundaries. The slip bands and the occurrence of slip transfer, partial slip transfer and slip blocking, as well as strain concentrations were accurately resolved in the HRDIC maps. Despite most of the grain boundaries fulfilled the expected slip transfer behavior dictated by the classical geometrical criteria, some of them presented an unforeseen behavior. A detailed analysis on these grain boundaries revealed that the local stress state around the GB can hinder or assist the occurrence of slip transfer. The heterogeneous strain distribution within the studied area together with the competition between different slip systems led to different slip transfer behaviors depending on the applied strain, which directly affected the driving force to transfer slip to the neighbor grains regardless of the geometrical alignment between the active slip systems.

Overall, the experimental work performed in Ni (FCC) and Ti (HCP) revealed that classical slip transfer geometrical criteria (m', Δb, or LRB) are generally good predictors for the likelihood of slip transmission across grain boundaries, indicating that the probability of slip transfer across a grain boundary is strongly correlated with the geometrical alignment between the active slip systems. Thus, those grain boundaries where the active slip systems were well-aligned presented either full or partial slip transfer, and, conversely, slip blocking was observed when the alignment was poor. The few grain boundaries where an abnormal slip transfer behavior was observed (slip transfer where there should be blocking according to the geometrical criteria and vice-versa) could be explained when examining the local stress state around grain boundaries. The experimental methodology for slip transfer assessment employed in this thesis is presented as an alternative to the conventional EBSD-based slip trace analysis, traditionally used to analyze slip transfer across grain boundaries. By means of different state-of-the-art techniques such as Lab-DCT and HRDIC the main limitations of the conventional slip trace analysis method were overcome, thus providing a reliable slip transfer database.

As indicated by the experimental evidence, slip transfer through the grain boundaries can take place when there is good alignment between incoming and outgoing slip systems across the boundary. However, despite some numerical models can account for the effect of grain boundaries on the mechanical behavior of polycrystalline materials, the effect of slip transfer across grain boundaries is not usually included and all grain boundaries are assumed as opaque to dislocations. This led to an overestimation in the flow stress predictions for different grain sizes, which was attributed to the stress concentrations associated to dislocation pile-ups at the grain boundaries. Therefore, the purpose of the simulation work in this thesis was to introduce the effect of slip transfer in a physically-based crystal plasticity model via different geometrical criteria such as m' or Δb (Chapter 6). This led to different GB characters according to their ability to transfer dislocations to the neighbor grain, namely transparent, translucent, or opaque grain boundaries. The crystal plasticity

model was able to capture the different stress concentrations depending on the degree of translucency of each GB according to any imposed geometrical slip transfer criteria. Furthermore, the model was adapted to capture the anisotropy present in HCP metals by including different critical resolved shear stress values (CRSS) depending on the slip system family (basal, prismatic or pyramidal). The crystal plasticity model was employed to analyze the Hall-Petch effect through computational homogenization of a representative volume element in different FCC and HCP materials including slip transfer. The predictions of the flow stress for different grain sizes were compared to experimental data found in the literature, and it was found that the simulations incorporating slip transfer aligned more closely with the experimental findings than the simulations assuming opaque grain boundaries.

The grain boundaries in polycrystalline materials are susceptible areas for damage initiation and propagation, and hence have a strong influence on the lifespan of critical structural components. For this reason, the effect of grains boundaries on intergranular fracture was analyzed in Chapter 7. The crystal plasticity model presented in Chapter 6 was used to model the grains constitutive behavior in thin foils with columnar grains. Cohesive surfaces governed by a traction-separation law were inserted at the grain boundaries to simulate intergranular fracture. Different Al (FCC) and Mg (HCP) foils were tested under uniaxial tension and the effect of grain boundary character (transparent, translucent, or opaque grain boundaries) was analyzed under plane stress and plane strain conditions. Moreover, the influence of different grain boundary features on damage nucleation were studied for both materials. As a consequence, the grain boundaries more susceptible to damage initiation can be identified according to their geometrical and crystallographic characteristics depending on their crystal lattice and loading conditions.

The computational work presented in this thesis was able to capture the physics behind grain boundary strengthening and intergranular fracture, which is of great importance for metallic materials with structural applications, where grain boundaries suppose potential damage initiation sites. The significance of numerical simulation is amplified in the context of multiscale modeling, allowing researchers to bridge the gap between micro-scale interactions and macroscopic material behavior. This capability enables a thorough exploration of tailored materials, optimization of design parameters, contributing to the field of grain boundary engineering.

The main conclusions of this thesis can be summarized as follows:

- Slip transfer at coherent and incoherent annealing twin boundaries in pure Ni is controlled by the residual Burgers vector and takes place when $\Delta b \approx 0$, regardless of the angle between slip normals and the twist angle between the incoming and outgoing slip planes. Moreover, slip transfer seems to be controlled by dislocation cross-slip in this case. Slip transfer across regular grain boundaries is very likely to occur across low-angle regular grain boundaries if the Luster–Morris parameter $m' > 0.8$, and it is unlikely to take place otherwise. However, there is a significant number of slip blocking instances when $0.75 < m' < 0.9$. They could be due to an error induced by the assumption that the active slip system is the one with the highest Schmid factor or to a large value of the twist angle θ, which is not known

because there was no information about the grain boundary orientation within the sample.

- The Laboratory-scale Diffraction Contrast Tomography (Lab-DCT) technique is able to provide detailed information about the microstructure (grain size, shape, and orientation as well as grain boundary orientation) of pure Ti foils in 3D prior to deformation. The data obtained by laboratory-scale diffraction contrast tomography are of similar quality to those obtained on the sample surface by electron backscatter diffraction on the sample surface for grains > 50 μm.
- Prismatic-to prismatic slip transfer in Ti occurs when $\Delta b/b < 0.43$ or $m' > 0.8$ and both geometrical criteria give an F1 score of 0.993. They were associated with low-angle grain boundaries and with good alignment between the incoming and outgoing slip directions and slip planes. Surprisingly, the twist angle θ did not play a clear role in slip transfer/blocking and, thus, the LRB geometrical criteria was not a good predictor of slip transfer/blocking at grain boundaries. Thus, geometrical criteria based on $\Delta b/b$ or m' can be confidently used in crystal plasticity simulations to account for slip transfer/blocking at grain boundaries.
- Nevertheless, slip transfer/blocking in a few grain boundaries in Ti did not follow the geometrical criteria indicated in the previous point. Their behavior was studied as a function of the applied strain by means of high-resolution digital image correlation to take into account the effect of the local stress near grain boundaries on slip transfer. It was found that slip transfer between a pair of well-oriented slip systems can be impeded (leading to either partial slip transfer or even blocking) if there is another dominant slip system that is more favorable in terms of the Schmid factor to accommodate the plastic deformation across the boundary. In addition, slip transfer between well-aligned slip systems across the boundary can be blocked as a result of the lack of driving force to transfer deformation due to the strain heterogeneity in the microstructure. Finally, slip transfer may occur across a highly misoriented grain boundary due to the local stress concentrations, which provide sufficient driving force to overcome the energy barrier induced by the grain boundary and transmit dislocations to the adjacent grain.
- The experimental Hall-Petch effect on FCC (Al, Cu, Ni, Ag) and HCP (Ti, Mg) polycrystals can be captured by means of computational homogenization of a representative volume element of the microstructure through a crystal plasticity model that accounts for slip transfer/blocking at grain boundaries through geometrical criteria. This result opens the path to include size effects in crystal plasticity simulations without the need for (computationally) costly strain gradient plasticity formulations.
- Numerical simulations of thin foils of FCC Al polycrystals with columnar microstructures showed that damage by grain boundary fracture is triggered at lower strains when the grain boundary is oriented perpendicularly to the loading axis and slip transfer is blocked, leading to the formation of stress concentrations. In the case of HCP Mg polycrystals, the main microstructural parameters controlling damage nucleation were the orientation of the grain boundary with respect to the loading

axis (as in FCC) and the crystallographic orientation of the grains, and those grain boundaries where the adjacent grains were well-oriented for basal slip were more prone to fracture.

This thesis has been able to fulfill the two main objectives presented in Chapter 1. First, the experimental methodology for slip transfer assessment has been implemented and validated as an alternative to the conventional slip trace analysis technique. The application of novel techniques such as Lab-DCT and HRDIC has provided valuable information to analyze the plastic deformation mechanisms near grain boundaries. This experimental workflow solves the main limitations of the classical technique, allowing the acquisition of more reliable data that can be used to establish sound criteria for slip transfer across grain boundaries. The experimental work has revealed that the geometrical alignment between the active slip systems across a grain boundary generally controls the likelihood to transfer slip to the neighbor grain. The few outliers found in the data that did not follow the geometrical criteria could be explained by the heterogeneous strain distribution acquired by means of HRDIC, and supposed less than 10% of the dataset. Therefore, geometrical slip transfer criteria based on m', Δb, or LRB serve as good predictors for slip transfer. An existing dislocation-based crystal plasticity model has been updated to account for slip transfer according to any of these geometrical criteria in FCC and HCP materials. Thus, slip transfer can be taken into account in the mechanical behavior of 3D FCC and HCP polycrystals, providing a more realistic tensile response to the experimental data than when all grain boundaries are assumed as opaque to dislocations. Finally, intergranular fracture was modeled in FCC and HCP thin foils, where the updated crystal plasticity model governed the constitutive behavior of the grains and cohesive surfaces were inserted at the grain boundaries to model fracture. The intergranular fracture simulations provided valuable insights on the grain boundaries that may potentially initiate fracture depending on the crystal lattice, the microstructural features, and the loading conditions. All together, the numerical simulations provide more realistic representations of the physics behind slip transfer and intergranular fracture, serving as a useful tool to identify the critical grain boundaries that can trigger damage.

8.2 Future work

Future work will be focused on the application of the presented methodologies to investigate the effect of slip transfer in other scenarios and complement the acquired information. The following lines of work are proposed:

1. The effect of the twist angle on the occurrence of slip transfer/blocking across annealing twin boundaries in pure Ni could be effectively addressed through slip trace analysis and electron backscatter diffraction because of the twin-matrix crystallographic relationship. However, this analysis should be extended to regular grain boundaries through the application of diffraction contrast tomography (to obtain the grain boundary inclination through the sample), high-resolution digital image correlation, and electron backscatter diffraction to determine the actual active slip systems.

2. The crystallographic texture of the Ti samples only analyzed the effect of geometrical criteria to predict prismatic-to-prismatic slip transfer. It would be interesting to extend the methodology to other samples with different grain sizes and random textures to validate or disprove the geometrical criteria for basal-to-basal and pyramidal-to-pyramidal slip transfer as well as for slip transfer between different slip systems. In particular, it would be important to assess the effect of the twist angle on these cases.

3. Use the 3D information of the microstructure of one Ti sample obtained by diffraction contrast tomography to create a one-to-one model of the microstructure. The mechanical deformation of the sample will be simulated using the crystal plasticity model, including the effect of slip transfer/blocking at grain boundaries, and compared with experimental data: the macroscopic stress-strain curve as well as the deformation fields on the sample surface obtained by high-resolution digital image correlation. This task will close the experimental/simulation loop and will also shed light on the mechanisms of slip transfer/blocking in grain boundaries that do not fulfill the geometrical criteria.

4. Create 3D representative volume elements of different metals with different microstructures (grain size, texture, etc.) and carry out numerical simulations of the mechanical behavior in tension, including slip transfer/blocking at grain boundaries as well as grain boundary fracture. The simulations will provide information about the nucleation and growth of grain boundary damage that will be used to train a machine learning model that should be able to identify the local microstructural features that trigger intergranular damage during deformation. This information will be useful in designing novel microstructures that have optimum damage tolerance to intergranular cracking.

Bibliography

[1] W. V. Aarle, W. Ludwig, A. King, and D. Penumadu, "An accurate projection model for diffraction image formation and inversion using a polychromatic cone beam", Journal of Applied Crystallography **48**, 334 (2015).

[2] W. Z. Abuzaid, M. D. Sangid, J. D. Carroll, H. Sehitoglu, and J. Lambros, "Slip transfer and plastic strain accumulation across grain boundaries in hastelloy x", Journal of the Mechanics and Physics of Solids **60**, 1201 (2012).

[3] W. Z. Abuzaid, H. Sehitoglu, and J. Lambros, "Localisation of plastic strain at the microstructurlal level in hastelloy x subjected to monotonic, fatigue, and creep loading: the role of grain boundaries and slip transmission", Materials at High Temperatures **33**, 384 (2016).

[4] A. Acharya and A. J. Beaudoin, "Grain-size effect in viscoplastic polycrystals at moderate strains", Journal of the Mechanics and Physics of Solids **48**, 2213 (2000).

[5] E. Alabort, D. Barba, S. Sulzer, M. Lißner, N. Petrinic, and R. C. Reed, "Grain boundary properties of a nickel-based superalloy: characterisation and modelling", Acta Materialia **151**, 377 (2018).

[6] A. Alankar, P. Eisenlohr, and D. Raabe, "A dislocation density-based crystal plasticity constitutive model for prismatic slip in α-titanium", Acta Materialia **59**, 7003 (2011).

[7] R. Alizadeh, M. Peña-Ortega, T. R. Bieler, and J. LLorca, "A criterion for slip transfer at grain boundaries in al", Scripta Materialia **178**, 408 (2020).

[8] A. Arsenlis and D. M. Parks, "Modeling the evolution of crystallographic dislocation density in crystal plasticity", Journal of the Mechanics and Physics of Solids **50**, 1979 (2002).

[9] M. F. Ashby, "The deformation of plastically non-homogeneous materials", The Philosophical Magazine: A Journal of Theoretical Experimental and Applied Physics **21**, 399 (1970).

[10] M. Atkinson, R. Thomas, A. Harte, P. Crowther, and J. Q. da Fonseca, *Defdap: deformation data analysis in python - v0.92*, 2020.

[11] J. A. El-Awady, "Unravelling the physics of size-dependent dislocation-mediated plasticity", Nature Communications 2015 6:1 **6**, 1 (2015).
[12] U. Ayachit, *The paraview guide: a parallel visualization application* (Kitware, Inc., 2015).
[13] F. Bachmann, H. Bale, N. Gueninchault, C. Holzner, and E. M. Lauridsen, "3d grain reconstruction from laboratory diffraction contrast tomography", J Appl Crystallogr **52**, 643 (2019).
[14] F. Bachmann, R. Hielscher, and H. Schaeben, "Texture analysis with mtex- free and open source software toolbox", Solid State Phenomena **160**, 63 (2010).
[15] F. Bachmann, R. Hielscher, and H. Schaeben, "Grain detection from 2d and 3d ebsd data–specification of the mtex algorithm", Ultramicroscopy **111**, 1720 (2011).
[16] G. I. Barenblatt, "The mathematical theory of equilibrium cracks in brittle fracture", Advances in Applied Mechanics **7**, 55 (1962).
[17] S. Bargmann, M. Ekh, K. Runesson, and B. Svendsen, "Modeling of polycrystals with gradient crystal plasticity: a comparison of strategies", Philosophical Magazine **90**, 1263 (2010).
[18] C. M. Barr, E. Y. Chen, J. E. Nathaniel, P. Lu, D. P. Adams, R. Dingreville, B. L. Boyce, K. Hattar, and D. L. Medlin, "Irradiation-induced grain boundary facet motion: in situ observations and atomic-scale mechanisms", Science Advances **8**, 900 (2022).
[19] E. Bayerschen, A. T. McBride, B. D. Reddy, and T. Böhlke, "Review on slip transmission criteria in experiments and crystal plasticity models", Journal of Materials Science **51**, 2243 (2016).
[20] C. J. Bayley, W. A. M. Brekelmans, and M. G. D. Geers, "A three-dimensional dislocation field crystal plasticity approach applied to miniaturized structures", Philosophical Magazine **87**, 1361 (2007).
[21] S. Bechtle, M. Kumar, B. P. Somerday, M. E. Launey, and R. O. Ritchie, "Grain-boundary engineering markedly reduces susceptibility to intergranular hydrogen embrittlement in metallic materials", Acta Materialia **57**, 4148 (2009).
[22] N. Bertin, L. Capolungo, and I. J. Beyerlein, "Hybrid dislocation dynamics based strain hardening constitutive model", International Journal of Plasticity **49**, 119 (2013).
[23] N. Bertin, C. N. Tomé, I. J. Beyerlein, M. R. Barnett, and L. Capolungo, "On the strength of dislocation interactions and their effect on latent hardening in pure magnesium", International Journal of Plasticity **62**, 72 (2014).
[24] T. R. Bieler, R. Alizadeh, M. Peña-Ortega, and J. Llorca, "An analysis of (the lack of) slip transfer between near-cube oriented grains in pure al", International Journal of Plasticity **118**, 269 (2019).
[25] T. R. Bieler, P. Eisenlohr, F. Roters, D. Kumar, D. E. Mason, M. A. Crimp, and D. Raabe, "The role of heterogeneous deformation on damage nucleation at grain boundaries in single phase metals", International Journal of Plasticity **25**, 1655 (2009).
[26] T. R. Bieler, S. C. Sutton, B. E. Dunlap, Z. A. Keith, P. Eisenlohr, M. A. Crimp, and B. L. Boyce, "Grain boundary responses to heterogeneous deformation in tantalum polycrystals", JOM **66**, Bieler, slip transfer in Ta BCC using m', 121 (2014).
[27] B. R. Blackman, H. Hadavinia, A. J. Kinloch, and J. G. Williams, "The use of a cohesive zone model to study the fracture of fibre composites and adhesively-bonded joints", International Journal of Fracture **119**, 25 (2003).

[28] N. Bozzolo and M. Bernacki, "Viewpoint on the formation and evolution of annealing twins during thermomechanical processing of fcc metals and alloys", Metallurgical and Materials Transactions A 2020 51:6 **51**, 2665 (2020).
[29] V. V. Bulatov, B. W. Reed, and M. Kumar, "Grain boundary energy function for fcc metals", 10.1016/j.actamat.2013.10.057 (2013).
[30] W. D. Callister, *Fundamentals of materials science and engineering*, Vol. 471660817 (Wiley, 2000), pp. 115–117.
[31] P. P. Camanho and C. G. Davila, *Mixed-mode decohesion finite elements for the simulation of delamination in composite materials*, 2002.
[32] R. D. Campilho, M. D. Banea, J. A. Neto, and L. F. D. Silva, "Modelling adhesive joints with cohesive zone models: effect of the cohesive law shape of the adhesive layer", International Journal of Adhesion and Adhesives **44**, 48 (2013).
[33] R. P. Carreker, "Tensile deformation of silver as a function of temperature, strain rate, and grain size", The Journal of The Minerals, Metals & Materials Society (JOM-TMS) **9**, 112 (1957).
[34] C. M. Cepeda-Jiménez, J. M. Molina-Aldareguia, and M. T. Pérez-Prado, "Origin of the twinning to slip transition with grain size refinement, with decreasing strain rate and with increasing temperature in magnesium", Acta Materialia **88**, 232 (2015).
[35] C. M. Cepeda-Jiménez, J. M. Molina-Aldareguia, and M. T. Pérez-Prado, "Ebsd-assisted slip trace analysis during in situ sem mechanical testing: application to unravel grain size effects on plasticity of pure mg polycrystals", JOM **68**, 116 (2016).
[36] A. Chapuis and J. H. Driver, "Temperature dependency of slip and twinning in plane strain compressed magnesium single crystals", Acta Materialia **59**, 1986 (2011).
[37] R. Chatterjee and A. A. Alankar, "Crystal plasticity modeling of dynamic recrystallization in cp ti", in , Vol. 14 (2019), pp. 251–258.
[38] J. Chen, J. Lu, W. Cai, Y. Zhang, Y. Wang, W. Jiang, M. Rizwan, and Z. Zhang, "In-situ study of adjacent grains slip transfer of inconel 718 during tensile process at high temperature", International Journal of Plasticity **163**, 10.1016/j.ijplas.2023.103554 (2023).
[39] Z. Chen and S. H. Daly, "Active slip system identification in polycrystalline metals by digital image correlation (dic)", Experimental Mechanics **57**, 115 (2017).
[40] K. S. Cheong, E. P. Busso, and A. Arsenlis, "A study of microstructural length scale effects on the behaviour of fcc polycrystals using strain gradient concepts", International Journal of Plasticity **21**, 1797 (2005).
[41] W. Clark, R. Wagoner, Z. Shen, T. Lee, I. Robertson, and H. Birnbaum, "On the criteria for slip transmission across interfaces in polycrystals", **26**, Shen Robertson. Slip transmission FCC deltab, 203 (1992).
[42] J. D. Clayton and D. L. McDowell, "Homogenized finite elastoplasticity and damage: theory and computations", Mechanics of Materials **36**, 799 (2004).
[43] M. Dao, L. Lu, R. J. Asaro, J. T. D. Hosson, and E. Ma, "Toward a quantitative understanding of mechanical behavior of nanocrystalline metals", Acta Materialia **55**, 4041 (2007).
[44] B. Devincre, T. Hoc, and L. Kubin, "Dislocation mean free paths and strain hardening of crystals", Science **320**, 1745 (2008).

[45] S. J. Dillon and G. S. Rohrer, "Characterization of the grain-boundary character and energy distributions of yttria using automated serial sectioning and ebsd in the fib", Journal of the American Ceramic Society **92**, 1580 (2009).
[46] D. S. Dugdale, "Yielding of steel sheets containing slits", Journal of the Mechanics and Physics of Solids **8**, 100 (1960).
[47] D. J. Dunstan and A. J. Bushby, "The scaling exponent in the size effect of small scale plastic deformation", International Journal of Plasticity **40**, 152 (2013).
[48] D. J. Dunstan and A. J. Bushby, "Grain size dependence of the strength of metals: the hall–petch effect does not scale as the inverse square root of grain size", International Journal of Plasticity **53**, 56 (2014).
[49] P. D. Edmondson, Y. Zhang, S. Moll, F. Namavar, and W. J. Weber, "Irradiation effects on microstructure change in nanocrystalline ceria - phase, lattice stress, grain size and boundaries", Acta Materialia **60**, 5408 (2012).
[50] M. Elices, G. V. Guinea, J. Gómez, and J. Planas, "The cohesive zone model: advantages, limitations and challenges", Engineering Fracture Mechanics **69**, 137 (2002).
[51] U. Essmann and H. Mughrabi, "Annihilation of dislocations during tensile and cyclic deformation and limits of dislocation densities", Philosophical Magazine A **40**, 731 (1979).
[52] G. Esteban-Manzanares, R. Santos-Güemes, I. Papadimitriou, E. Martínez, and J. LLorca, "Influence of the stress state on the cross-slip free energy barrier in al: an atomistic investigation", Acta Materialia **184**, 109 (2020).
[53] L. P. Evers, D. M. Parks, W. A. M. Brekelmans, and M. G. D. Geers, "Crystal plasticity model with enhanced hardening by geometrically necessary dislocation accumulation", Journal of the Mechanics and Physics of Solids **50**, 2403 (2002).
[54] H. Fang, D. J. Jensen, and Y. Zhang, "An efficient method to improve the spatial resolution of laboratory x-ray diffraction contrast tomography", IOP Conference Series: Materials Science and Engineering **580**, 10.1088/1757-899x/580/1/012030 (2019).
[55] H. Fang, D. J. Jensen, and Y. Zhang, "Improved grain mapping by laboratory x-ray diffraction contrast tomography", IUCrJ **8**, 559 (2021).
[56] M. Feser, C. Holzner, and E. Lauridsen, *Laboratory x-ray micro-tomography system with crystallographic gran orientation mapping capabilities*, 2015.
[57] P. Franciosi, M. Berveiller, and A. Zaoui, "Latent hardening in copper and aluminium single crystals", Acta Metallurgica **28**, 273 (1980).
[58] L. H. Friedman and D. C. Chrzan, "Continuum analysis of dislocation pile-ups: influence of sources", Philosophical Magazine A **77**, 1185 (1998).
[59] B. H. Frodal, S. Thomesen, T. Børvik, and O. S. Hopperstad, "On the coupling of damage and single crystal plasticity for ductile polycrystalline materials", International Journal of Plasticity **142**, 102996 (2021).
[60] E. Ganju, E. Nieto-Valeiras, J. LLorca, and N. Chawla, "A novel diffraction contrast tomography (dct) acquisition strategy for capturing the 3d crystallographic structure of pure titanium", Tomography of Materials and Structures **1**, 100003 (2023).
[61] W. M. Garrison and N. R. Moody, "Ductile fracture", Journal of Physics and Chemistry of Solids **48**, 1035 (1987).

[62] J. Genée, L. Signor, and P. Villechaise, "Slip transfer across grain/twin boundaries in polycrystalline ni-based superalloys", Materials Science and Engineering: A **701**, 24 (2017).

[63] C. Geuzaine and J. F. Remacle, "Gmsh: a 3-d finite element mesh generator with built-in pre- and post-processing facilities", International Journal for Numerical Methods in Engineering **79**, 1309 (2009).

[64] A. Ghosh, A. Singh, and N. P. Gurao, "Effect of rolling mode and annealing temperature on microstructure and texture of commercially pure-titanium", Materials Characterization **125**, 83 (2017).

[65] F. D. Gioacchino, T. E. Edwards, G. N. Wells, and W. J. Clegg, "A new mechanism of strain transfer in polycrystals", Scientific Reports **10**, 10.1038/s41598-020-66569-7 (2020).

[66] F. D. Gioacchino and J. Q. da Fonseca, "Plastic strain mapping with sub-micron resolution using digital image correlation", Experimental Mechanics **53**, 743 (2013).

[67] J. Gong and A. J. Wilkinson, "Anisotropy in the plastic flow properties of single-crystal α titanium determined from micro-cantilever beams", Acta Materialia **57**, 5693 (2009).

[68] S. Graff, W. Brocks, and D. Steglich, "Yielding of magnesium: from single crystal to polycrystalline aggregates", International Journal of Plasticity **23**, 1957 (2007).

[69] M. A. Groeber and M. A. Jackson, *Dream.3d: a digital representation environment for the analysis of microstructure in 3d*, 2014.

[70] Y. Guo, T. B. Britton, and A. J. Wilkinson, "Slip band-grain boundary interactions in commercial-purity titanium", Acta Materialia **76**, 1 (2014).

[71] Y. Guo, D. M. Collins, E. Tarleton, F. Hofmann, J. Tischler, W. Liu, R. Xu, A. J. Wilkinson, and T. B. Britton, "Measurements of stress fields near a grain boundary: exploring blocked arrays of dislocations in 3d", Acta Materialia **96**, 229 (2015).

[72] E. O. Hall, "The deformation and ageing of mild steel: ii characteristics of the lüders deformation", Proceedings of the Physical Society. Section B **64**, 742 (1951).

[73] S. Han and M. A. Crimp, "Ecci analysis of shear accommodations at grain boundaries in commercially pure alpha titanium", International Journal of Plasticity **131**, 10.1016/j.ijplas.2020.102731 (2020).

[74] N. Hansen, "The effect of grain size and strain on the tensile flow stress of aluminium at room temperature", Acta Metallurgica **25**, 863 (1977).

[75] N. Hansen and B. Ralph, "The strain and grain size dependence of the flow stress of copper", Acta Metallurgica **30**, 411 (1982).

[76] S. Haouala, R. Alizadeh, T. R. Bieler, J. Segurado, and J. Llorca, "Effect of slip transmission at grain boundaries in al bicrystals", International Journal of Plasticity **126**, 10.1016/j.ijplas.2019.09.006 (2020).

[77] S. Haouala, S. Lucarini, J. LLorca, and J. Segurado, "Simulation of the hall-petch effect in fcc polycrystals by means of strain gradient crystal plasticity and fft homogenization", Journal of the Mechanics and Physics of Solids **134**, 10.1016/j.jmps.2019.103755 (2020).

[78] S. Haouala, J. Segurado, and J. LLorca, "An analysis of the influence of grain size on the strength of fcc polycrystals by means of computational homogenization", Acta Materialia **148**, 72 (2018).

[79] A. Harte, M. Atkinson, M. Preuss, and J. Q. da Fonseca, "A statistical study of the relationship between plastic strain and lattice misorientation on the surface of a deformed ni-based superalloy", Acta Materialia **195**, 555 (2020).
[80] A. Harte, M. Atkinson, A. Smith, C. Drouven, S. Zaefferer, J. Q. da Fonseca, and M. Preuss, "The effect of solid solution and gamma prime on the deformation modes in ni-based superalloys", Acta Materialia **194**, 257 (2020).
[81] R. F. S. Hearmon, "The elastic constants of crystals and other anisotropic materials", Landolt-Börnstein Tables **3**, 559 (1984).
[82] S. Hémery, P. Nizou, and P. Villechaise, "In situ sem investigation of slip transfer in ti-6al-4v: effect of applied stress", Materials Science and Engineering: A **709**, 277 (2018).
[83] J. P. Hirth, "Influence of grain boundaries on mechanical properties.", Metall Trans **3**, 3047 (1972).
[84] C. Holzner, L. Lavery, H. Bale, A. Merkle, S. McDonald, P. Withers, Y. Zhang, D. J. Jensen, M. Kimura, A. Lyckegaard, P. Reischig, and E. M. Lauridsen, "Diffraction contrast tomography in the laboratory – applications and future directions", Microscopy Today **24**, 34 (2016).
[85] D. A. Hughes, N. Hansen, and D. J. Bammann, "Geometrically necessary boundaries, incidental dislocation boundaries and geometrically necessary dislocations", Scripta Materialia **48**, 147 (2003).
[86] D. Hull and D. Bacon, *Introduction to dislocations*, Fifth Edition, Vol. 37 (Elsevier, 2011).
[87] A. Jamali, A. Ma, and J. LLorca, "Influence of grain size and grain boundary misorientation on the fatigue crack initiation mechanisms of textured az31 mg alloy", Scripta Materialia **207**, 114304 (2022).
[88] S. Jiang, Y. Jia, and X. Wang, "In-situ analysis of slip transfer and heterogeneous deformation in tension of mg-5.4gd-1.8y-1.5zn alloy", Journal of Magnesium and Alloys **8**, 1186 (2020).
[89] G. Johnson, A. King, M. G. Honnicke, J. Marrow, and W. Ludwig, "X-ray diffraction contrast tomography: a novel technique for three-dimensional grain mapping of polycrystals. ii. the combined case", Journal of Applied Crystallography **41**, 310 (2008).
[90] R. Jones, "Stress-corrosion cracking", in , Vol. 13A (ASM International, 2003), pp. 346–366.
[91] J. Kacher, B. P. Eftink, B. Cui, and I. M. Robertson, "Dislocation interactions with grain boundaries", Current Opinion in Solid State and Materials Science **18**, 227 (2014).
[92] R. Keinan, H. Bale, N. Gueninchault, E. M. Lauridsen, and A. J. Shahani, "Integrated imaging in three dimensions: providing a new lens on grain boundaries, particles, and their correlations in polycrystalline silicon", Acta Materialia **148**, 225 (2018).
[93] A. King, P. Reischig, J. Adrien, and W. Ludwig, "First laboratory x-ray diffraction contrast tomography for grain mapping of polycrystals", Journal of Applied Crystallography **46**, 1734 (2013).

[94] K. Kishida, J. G. Kim, T. Nagae, and H. Inui, "Experimental evaluation of critical resolved shear stress for the first-order pyramidal c+a slip in commercially pure ti by micropillar compression method", Acta Materialia **196**, 168 (2020).
[95] S. Kobayashi, S. Ogou, and S. Tsurekawa, "Grain boundary engineering for control of fatigue fracture in 316l austenitic stainless steel", Materials Transactions **60**, 623 (2019).
[96] U. F. Kocks, "The relation between polycrystal deformation and single-crystal deformation", Metallurgical and Materials Transactions **1**, 1121 (1970).
[97] U. F. Kocks, A. S. Argon, and M. F. Ashby, *Thermodynamics and kinetics of slip*, Vol. 19 (Pergamon press, 1975).
[98] U. F. Kocks and H. Mecking, "Physics and phenomenology of strain hardening: the fcc case", Progress in Materials Science **48**, 171 (2003).
[99] V. Kotu and B. Deshpande, "Data exploration", in , Second Edition (Morgan Kaufmann, Jan. 2019), pp. 39–64.
[100] L. P. Kubin, *Dislocations, mesoscale simulations and plastic flow*, First, Vol. 5 (Oxford University Press, 2013).
[101] K. S. Kumar, H. V. Swygenhoven, and S. Suresh, "Mechanical behavior of nanocrystalline metals and alloys", Acta Materialia **51**, 5743 (2003).
[102] M. A. Kumar, I. J. Beyerlein, R. A. Lebensohn, and C. N. Tomé, "Modeling the effect of neighboring grains on twin growth in hcp polycrystals", Modelling and Simulation in Materials Science and Engineering **25**, 064007 (2017).
[103] B. Larrouy, P. Villechaise, J. Cormier, and O. Berteaux, "Grain boundary–slip bands interactions: impact on the fatigue crack initiation in a polycrystalline forged ni-based superalloy", Acta Materialia **99**, 325 (2015).
[104] LaVision, *Davis software for intelligent imaging*, 2020.
[105] R. A. Lebensohn and A. Needleman, "Numerical implementation of non-local polycrystal plasticity using fast fourier transforms", Journal of the Mechanics and Physics of Solids **97**, 333 (2016).
[106] J. S. Lecomte, L. T. Nguyen, F. Abbès, C. Schuman, and J. M. Raulot, "Contribution of the nanoindentation to the study of hcp metals", Materials Science Forum **783-786**, 2327 (2014).
[107] R. J. Lederich, S. M. L. Sastry, J. E. O'neal, and B. B. Rath, "The effect of grain size on yield stress and work hardening of polycrystalline titanium at 295 k and 575 k", Materials Science and Engineering **33**, 183 (1978).
[108] T. C. Lee, I. M. Robertson, and H. K. Birnbaum, "Prediction of slip transfer mechanisms across grain boundaries", Scripta Metallurgica **23**, 799 (1989).
[109] T. C. Lee, I. M. Robertson, and H. K. Birnbaum, "Anin situ transmission electron microscope deformation study of the slip transfer mechanisms in metals", Metallurgical Transactions A **21**, 2437 (1990).
[110] S. F. Li and R. M. Suter, "Adaptive reconstruction method for three-dimensional orientation imaging", Journal of Applied Crystallography **46**, 512 (2013).
[111] S. Li, M. D. Thouless, A. M. Waas, J. A. Schroeder, and P. D. Zavattieri, "Use of a cohesive-zone model to analyze the fracture of a fiber-reinforced polymer–matrix composite", Composites Science and Technology **65**, 537 (2005).

[112] Y. Li, A. J. Bushby, and D. J. Dunstan, "The hall–petch effect as a manifestation of the general size effect", Proceedings of the Royal Society A: Mathematical, Physical and Engineering Sciences **472**, 10.1098/RSPA.2015.0890 (2016).
[113] D. Liang, J. Hure, A. Courcelle, S. E. Shawish, and B. Tanguy, "A micromechanical analysis of intergranular stress corrosion cracking of an irradiated austenitic stainless steel", Acta Materialia **204**, 116482 (2021).
[114] L. C. Lim and R. Raj, "The role of residual dislocation arrays in slip induced cavitation, migration and dynamic recrystallization at grain boundaries", Acta Metallurgica **33**, 2205 (1985).
[115] J. D. Livingston and B. Chalmers, "Multiple slip in bicrystal deformation", Acta Metallurgica **5**, 322 (1957).
[116] W. Ludwig, P. Reischig, A. King, M. Herbig, E. M. Lauridsen, G. Johnson, T. J. Marrow, and J. Y. Buffiere, "Three-dimensional grain mapping by x-ray diffraction contrast tomography and the use of friedel pairs in diffraction data analysis", Rev Sci Instrum **80**, 33905 (2009).
[117] W. Ludwig, S. Schmidt, E. M. Lauridsen, and H. F. Poulsen, "X-ray diffraction contrast tomography: a novel technique for three-dimensional grain mapping of polycrystals. i. direct beam case", Journal of Applied Crystallography **41**, 302 (2008).
[118] J. Luster and M. A. Morris, "Compatibility of deformation in two-phase ti-al alloys: dependence on microstructure and orientation relationships", Metallurgical and Materials Transactions A **26**, 1745 (1995).
[119] G. Martin, C. W. Sinclair, and R. A. Lebensohn, "Microscale plastic strain heterogeneity in slip dominated deformation of magnesium alloy containing rare earth", Materials Science and Engineering: A **603**, 37 (2014).
[120] R. S. Martín, J. M. Molina-Aldareguia, and M. T. P. Prado, "Micromechanics of magnesium and its alloys studied by nanoindentation", (2016).
[121] E. Martínez-Pañeda and C. Betegón, "Modeling damage and fracture within strain-gradient plasticity", International Journal of Solids and Structures **59**, 208 (2015).
[122] S. A. McDonald, C. Holzner, E. M. Lauridsen, P. Reischig, A. P. Merkle, and P. J. Withers, "Microstructural evolution during sintering of copper particles studied by laboratory diffraction contrast tomography (labdct)", Sci Rep **7**, 5251 (2017).
[123] S. A. McDonald, P. Reischig, C. Holzner, E. M. Lauridsen, P. J. Withers, A. P. Merkle, and M. Feser, "Non-destructive mapping of grain orientations in 3d by laboratory x-ray microscopy", Sci Rep **5**, 14665 (2015).
[124] S. A. McDonald, T. L. Burnett, J. Donoghue, N. Gueninchault, H. Bale, C. Holzner, E. M. Lauridsen, and P. J. Withers, "Tracking polycrystal evolution non-destructively in 3d by laboratory x-ray diffraction contrast tomography", Materials Characterization **172**, 10.1016/j.matchar.2020.110814 (2021).
[125] C. J. McMahon, "Intergranular fracture in steels", Materials Science and Engineering **25**, 233 (1976).
[126] M. D. McMurtrey, B. Cui, I. Robertson, D. Farkas, and G. S. Was, "Mechanism of dislocation channel-induced irradiation assisted stress corrosion crack initiation in austenitic stainless steel", Current Opinion in Solid State and Materials Science **19**, 305 (2015).

[127] T. Narutani and J. Takamura, "Grain-size strengthening in terms of dislocation density measured by resistivity", Acta Metallurgica et Materialia **39**, 2037 (1991).
[128] S. Nemat-Nasser, W. G. Guo, and J. Y. Cheng, "Mechanical properties and deformation mechanisms of a commercially pure titanium", Acta materialia **47**, 3705 (1999).
[129] M. G. Nicholas and C. F. Old, "Liquid metal embrittlement", Journal of Materials Science **14**, 1 (1979).
[130] E. Nieto-Valeiras and J. LLorca, "Criteria for slip transfer across grain and twin boundaries in pure ni", Materialia **21**, 10.1016/j.mtla.2021.101303 (2022).
[131] E. Nieto-Valeiras, E. Ganju, N. Chawla, and J. LLorca, "Assessment of slip transfer criteria for prismatic-to-prismatic slip in pure ti from 3d grain boundary data", Acta Materialia **262**, 119424 (2024).
[132] S. Niverty, J. Sun, J. Williams, F. Bachmann, N. Gueninchault, E. Lauridsen, and N. Chawla, "A forward modeling approach to high-reliability grain mapping by laboratory diffraction contrast tomography (labdct)", JOM **71**, 2695 (2019).
[133] J. F. Nye, "Some geometrical relations in dislocated crystals", Acta Metallurgica **1**, 153 (1953).
[134] J. Oddershede, F. Bachmann, J. Sun, and E. Lauridsen, "Advanced acquisition strategies for lab-based diffraction contrast tomography", Integrating Materials and Manufacturing Innovation **11**, 1 (2022).
[135] N. Ono, R. Nowak, and S. Miura, "Effect of deformation temperature on hall–petch relationship registered for polycrystalline magnesium", Materials Letters **58**, 39 (2004).
[136] A. Orozco-Caballero, D. Lunt, J. D. Robson, and J. Q. da Fonseca, "How magnesium accommodates local deformation incompatibility: a high-resolution digital image correlation study", Acta Materialia **133**, 367 (2017).
[137] G. Palumbo, D. Dunikowski, R. Wirecka, T. Mazur, U. Lelek-Borkowska, K. Wawer, and J. Banas, "Effect of grain size on the corrosion behavior of fe-3wt.%si-1wt.%al electrical steels in pure water saturated with co(2)", Materials (Basel) **14**, 10.3390/ma14175084 (2021).
[138] H. Pan, Y. He, and X. Zhang, "Interactions between dislocations and boundaries during deformation", Materials 2021, Vol. 14, Page 1012 **14**, 1012 (2021).
[139] K. Park and G. H. Paulino, "Cohesive zone models: a critical review of traction-separation relationships across fracture surfaces", Applied Mechanics Reviews **64**, 10.1115/1.4023110 (2011).
[140] L. Patriarca, W. Abuzaid, H. Sehitoglu, and H. J. Maier, "Slip transmission in bcc fecr polycrystal", Materials Science and Engineering A **588**, Slip transfer studied in BCC by HRDIC. They use the residual Burgers vector as criterion, and it works as usual., 308 (2013).
[141] P. Pauš, J. Kratochvíl, and M. Beneš, "A dislocation dynamics analysis of the critical cross-slip annihilation distance and the cyclic saturation stress in fcc single crystals at different temperatures", Acta Materialia **61**, 7917 (2013).
[142] J. Pelleg, *Mechanical properties of materials*, 1st ed. (Springer, 2013).
[143] N. J. Petch, "The cleavage strength of polycrystals", J. Iron Steel Inst. **174**, 25 (1953).

[144] H. Pirgazi, K. Glowinski, A. Morawiec, and L. A. I. Kestens, "Three-dimensional characterization of grain boundaries in pure nickel by serial sectioning via mechanical polishing", Journal of Applied Crystallography **48**, 1672 (2015).
[145] D. M. W. Powers, "Evaluation: from precision, recall and f-measure to roc, informedness, markedness and correlation", International Journal of Machine Learning Technology, 37 (2011).
[146] R. Quey, P. R. Dawson, and F. Barbe, "Large-scale 3d random polycrystals for the finite element method: generation, meshing and remeshing", Computer Methods in Applied Mechanics and Engineering **200**, 1729 (2011).
[147] S. V. Raj and G. M. Pharr, "A compilation and analysis of data for the stress dependence of the subgrain size", Materials Science and Engineering **81**, 217 (1986).
[148] K. D. Ralston, N. Birbilis, and C. H. J. Davies, "Revealing the relationship between grain size and corrosion rate of metals", Scripta Materialia **63**, 1201 (2010).
[149] W. T. Read and W. Shockley, "Dislocation models of crystal grain boundaries", Physical Review **78**, 275 (1950).
[150] I. M. Robertson, T. Tabata, W. Wei, F. Heubaum, and H. K. Birnbaum, "Hydrogen embrittlement and grain boundary fracture", Scripta Metallurgica **18**, 841 (1984).
[151] R. A. Rubio, S. Haouala, and J. Llorca, "Grain boundary strengthening of fcc polycrystals", Journal of Materials Research **34**, 2263 (2019).
[152] R. Sánchez-Martín, M. T. Pérez-Prado, J. Segurado, J. Bohlen, I. Gutiérrez-Urrutia, J. Llorca, and J. M. Molina-Aldareguia, "Measuring the critical resolved shear stresses in mg alloys by instrumented nanoindentation", Acta Materialia **71**, 283 (2014).
[153] C. D. Sansal, B. Devincre, and L. Kubin, "Grain size strengthening in microcrystalline copper: a three-dimensional dislocation dynamics simulation", Key Engineering Materials **423**, 25 (2010).
[154] M. Sarebanzadeh, A. Orozco-Caballero, and J. Llorca, "Accurate determination of active slip systems for improved geometrical criteria of basal-to-basal slip transfer at grain boundaries in pure mg", Acta Materialia **243**, https://doi.org/10.1016/j.actamat.2022.118536 (2023).
[155] M. Sauzay and L. P. Kubin, "Scaling laws for dislocation microstructures in monotonic and cyclic deformation of fcc metals", Progress in Materials Science **56**, 725 (2011).
[156] J. Schindelin, I. Arganda-Carreras, E. Frise, V. Kaynig, M. Longair, T. Pietzsch, S. Preibisch, C. Rueden, S. Saalfeld, B. Schmid, J. Y. Tinevez, D. J. White, V. Hartenstein, K. Eliceiri, P. Tomancak, and A. Cardona, "Fiji: an open-source platform for biological-image analysis", Nature Methods **9**, 676 (2012).
[157] A. J. Schwartz, M. Kumar, B. L. Adams, and D. P. Field, *Electron backscatter diffraction in materials science* (Springer US, 2009), pp. 1–403.
[158] J. Segurado, R. A. Lebensohn, and J. Llorca, "Computational homogenization of polycrystals", Advances in Applied Mechanics **51**, 1 (2018).
[159] S. E. Shawish, L. Cizelj, and I. Simonovski, "Modeling grain boundaries in polycrystals using cohesive elements: qualitative and quantitative analysis", Nuclear Engineering and Design **261**, 371 (2013).
[160] Z. Shen, R. H. Wagoner, and W. A. T. Clark, "Dislocation and grain boundary interactions in metals", Acta Metallurgica **36**, 3231 (1988).

[161] K. Sieradzki and R. C. Newman, "Stress-corrosion cracking", Journal of Physics and Chemistry of Solids **48**, 1101 (1987).
[162] I. Simonovski and L. Cizelj, "Cohesive zone modeling of intergranular cracking in polycrystalline aggregates", Nuclear Engineering and Design **283**, 139 (2015).
[163] D. S. Simulia, *Standard user's manual and abaqus cae manual 6.14*, Vol. 1 (2006).
[164] R. E. Smallman and A. H. W. Ngan, *Surfaces, grain boundaries and interfaces* (Butterworth-Heinemann, Aug. 2014), pp. 415–442.
[165] M. Soleimani, H. Mirzadeh, and C. Dehghanian, "Effect of grain size on the corrosion resistance of low carbon steel", Materials Research Express **7**, 10.1088/2053-1591/ab62fa (2020).
[166] R. Sperry, S. Han, Z. Chen, S. H. Daly, M. A. Crimp, and D. T. Fullwood, "Comparison of ebsd, dic, afm, and ecci for active slip system identification in deformed ti-7al", Materials Characterization **173**, 10.1016/j.matchar.2021.110941 (2021).
[167] R. Sperry, A. Harte, J. Q. da Fonseca, E. R. Homer, R. H. Wagoner, and D. T. Fullwood, "Slip band characteristics in the presence of grain boundaries in nickel-based superalloy", Acta Materialia **193**, 229 (2020).
[168] J. C. Stinville, W. C. Lenthe, M. P. Echlin, P. G. Callahan, D. Texier, and T. M. Pollock, "Microstructural statistics for fatigue crack initiation in polycrystalline nickel-base superalloys", International Journal of Fracture **208**, 221 (2017).
[169] J. C. Stinville, W. C. Lenthe, J. Miao, and T. M. Pollock, "A combined grain scale elastic–plastic criterion for identification of fatigue crack initiation sites in a twin containing polycrystalline nickel-base superalloy", Acta Materialia **103**, 461 (2016).
[170] J. C. Stinville, N. Vanderesse, F. Bridier, P. Bocher, and T. M. Pollock, "High resolution mapping of strain localization near twin boundaries in a nickel-based superalloy", Acta Materialia **98**, 29 (2015).
[171] J. Sun, F. Bachmann, J. Oddershede, and E. Lauridsen, "Recent advances of lab-based diffraction contrast tomography – reconstruction speed benchmark testing and validations", IOP Conference Series: Materials Science and Engineering **1249**, /10.1088/1757-899X/1249/1/012045 (2022).
[172] J. Sun, A. Lyckegaard, Y. B. Zhang, S. A. Catherine, B. R. Patterson, F. Bachmann, N. Gueninchault, H. Bale, C. Holzner, E. Lauridsen, and D. J. Jensen, "4d study of grain growth in armco iron using laboratory x-ray diffraction contrast tomography", IOP Conference Series: Materials Science and Engineering **219**, 10.1088/1757-899x/219/1/012039 (2017).
[173] J. Sun, Y. Zhang, A. Lyckegaard, F. Bachmann, E. M. Lauridsen, and D. J. Jensen, "Grain boundary wetting correlated to the grain boundary properties: a laboratory-based multimodal x-ray tomography investigation", Scripta Materialia **163**, 77 (2019).
[174] C. Suryanarayana, "Nanocrystalline materials", International Materials Reviews **40**, 41 (1995).
[175] G. I. Taylor, "The mechanism of plastic deformation of crystals. part ii.—comparison with observations", Proceedings of the Royal Society of London. Series A **145**, 388 (1934).
[176] A. Tharwat, "Classification assessment methods", Applied Computing and Informatics **17**, 168 (2018).
[177] P. F. Thomason, *Ductile fracture of metals. pergamon press, oxford* (1990).

[178] T. Vermeij, R. H. Peerlings, M. G. Geers, and J. P. Hoefnagels, "Automated identification of slip system activity fields from digital image correlation data", Acta Materialia **243**, 118502 (2023).
[179] F. Wang, S. Sandlöbes, M. Diehl, L. Sharma, F. Roters, and D. Raabe, "In situ observation of collective grain-scale mechanics in mg and mg–rare earth alloys", Acta Materialia **80**, 77 (2014).
[180] J. Y. Wang, N. Li, R. Alizadeh, M. A. Monclús, Y. W. Cui, J. M. Molina-Aldareguía, and J. LLorca, "Effect of solute content and temperature on the deformation mechanisms and critical resolved shear stress in mg-al and mg-zn alloys", Acta Materialia **170**, 155 (2019).
[181] J. Wang, Y. Chen, Z. Chen, J. Llorca, and X. Zeng, "Deformation mechanisms of mg-ca-zn alloys studied by means of micropillar compression tests", Acta Materialia **217**, 117151 (2021).
[182] L. Wang, Y. Yang, P. Eisenlohr, T. R. Bieler, M. A. Crimp, and D. E. Mason, "Twin nucleation by slip transfer across grain boundaries in commercial purity titanium", Metallurgical and Materials Transactions A: Physical Metallurgy and Materials Science **41**, 421 (2010).
[183] L. Wang, Z. Zheng, H. Phukan, P. Kenesei, J. S. Park, J. Lind, R. M. Suter, and T. R. Bieler, "Direct measurement of critical resolved shear stress of prismatic and basal slip in polycrystalline ti using high energy x-ray diffraction microscopy", Acta Materialia **132**, 598 (2017).
[184] M. G. Wang and A. H. Ngan, "Indentation strain burst phenomenon induced by grain boundaries in niobium", Journal of Materials Research **19**, 2478 (2004).
[185] Z. M. Wang, R. M. Osgood, and J. Parisi, *Grain boundaries: from theory to engineering*, Vol. 172 (Springer, 2013).
[186] Y. J. Wei and L. Anand, "Grain-boundary sliding and separation in polycrystalline metals: application to nanocrystalline fcc metals", Journal of the Mechanics and Physics of Solids **52**, 2587 (2004).
[187] D. Xie and A. M. Waas, "Discrete cohesive zone model for mixed-mode fracture using finite element analysis", Engineering Fracture Mechanics **73**, 1783 (2006).
[188] Xnovotech, *Grainmapper 3d user's guide*, 2022.
[189] X. Xu, D. Lunt, R. Thomas, R. P. Babu, A. Harte, M. Atkinson, J. Q. D. Fonseca, and M. Preuss, "Identification of active slip mode in a hexagonal material by correlative scanning electron microscopy", 10.1016/j.actamat.2019.06.024 (2019).
[190] B. Yang, C. Shi, R. Lai, D. Shi, D. Guan, G. Zhu, Y. Cui, G. Xie, Y. Li, A. Chiba, and J. LLorca, "Identification of active slip systems in polycrystals by slip trace - modified lattice rotation analysis (st-mlra)", Scripta Materialia **214**, 10.1016/j.scriptamat.2022.114648 (2022).
[191] B. Yavuzyegit, E. Avcu, A. D. Smith, J. M. Donoghue, D. Lunt, J. D. Robson, T. L. Burnett, J. Q. da Fonseca, and P. J. Withers, "Mapping plastic deformation mechanisms in az31 magnesium alloy at the nanoscale", Acta Materialia **250**, 118876 (2023).
[192] M. Zaiser and S. Sandfeld, "Scaling properties of dislocation simulations in the similitude regime", Modelling and Simulation in Materials Science and Engineering **22**, 65012 (2014).

[193] T. Zhai, A. J. Wilkinson, and J. W. Martin, "A crystallographic mechanism for fatigue crack propagation through grain boundaries", Acta Materialia **48**, 4917 (2000).

[194] J. Zhang and S. P. Joshi, "Phenomenological crystal plasticity modeling and detailed micromechanical investigations of pure magnesium", Journal of the Mechanics and Physics of Solids **60**, 945 (2012).

[195] Z. Zhang, Z. Yang, S. Lu, A. Harte, R. Morana, and M. Preuss, "Strain localisation and failure at twin-boundary complexions in nickel-based superalloys", Nature Communications **11**, 10.1038/s41467-020-18641-z (2020).

[196] Y. Zhao, S. Niverty, X. Ma, and N. Chawla, "Correlation between corrosion behavior and grain boundary characteristics of a 6061 al alloy by lab-scale x-ray diffraction contrast tomography (dct)", Materials Characterization **193**, 10.1016/j.matchar.2022.112325 (2022).

[197] Z. Zhao, M. Ramesh, D. Raabe, A. M. Cuitiño, and R. Radovitzky, "Investigation of three-dimensional aspects of grain-scale plastic surface deformation of an aluminum oligocrystal", International Journal of Plasticity **24**, 2278 (2008).

[198] Z. Zhao, T. R. Bieler, J. LLorca, and P. Eisenlohr, "Grain boundary slip transfer classification and metric selection with artificial neural networks", Scripta Materialia **185**, 71 (2020).

[199] H. Zheng, X. G. Li, R. Tran, C. Chen, M. Horton, D. Winston, K. A. Persson, and S. P. Ong, "Grain boundary properties of elemental metals", Acta Materialia **186**, 40 (2020).

[200] B. Zhou, Y. Li, L. Wang, H. Jia, and X. Zeng, "The role of grain boundary plane in slip transfer during deformation of magnesium alloys", Acta Materialia **227**, 10.1016/j.actamat.2022.117662 (2022).

[201] B. Zhou, L. Wang, P. Jin, H. Jia, H. J. Roven, X. Zeng, and Y. Li, "Revealing slip-induced extension twinning behaviors dominated by micro deformation in a magnesium alloy", International Journal of Plasticity **128**, 102669 (2020).